Technische Universität München
TUM School of Engineering and Design

External Stabilization of Robot Manipulators

Tobias Franz Christian Berninger, M. Sc.

Vollständiger Abdruck der von der TUM School of Engineering and Design der Technischen Universität München zur Erlangung eines

Doktors der Ingenieurwissenschaften (Dr.-Ing.)

genehmigten Dissertation.

Vorsitz: Prof. Dr.-Ing. Michael F. Zäh

Prüfer*innen der Dissertation:

1. Prof. dr.ir. Daniel J. Rixen
2. Prof. Dr.-Ing. Sami Haddadin

Die Dissertation wurde am 25. April 2022 bei der Technischen Universität München eingereicht und durch die TUM School of Engineering and Design am 13. September 2022 angenommen.

Acknowledgement

I am very grateful for all the opportunities and experiences that my time at the Chair of Applied Mechanics has granted me. Traveling to conferences all over the world, giving TV interviews for our CROPS robot, teaching in front of students in Munich and Singapore, managing and acquiring industry and research projects, arguing with the legal department, writing research proposals, spending all day and night at the chair to write papers, supervising student theses and student assistants, building my own mechatronic prototypes and see them fail and succeed, even being able to do a little bit of research on our humanoid robot LOLA or use thrash metal music as an excitation source for operational modal analysis as side projects. I do not think that there is single thing that I missed out on in my 'Ph.D. life'.

However, the most important part are the people that I was fortunate to meet and had a large positive impact on my time here. In the following, I want to thank each one of you:

Dear Daniel, one of the first things you ever said to me was during the interview process for the Ph.D. position: "Well, the grades aren't the best, but sometimes you also need people that are just capable of working". Despite of what others might think, I actually took that as a compliment. You immediately put a lot of trust in me by giving me the responsibility of managing the EXPERTISE project and gave me a significant amount of freedom to handle industry projects with *Boeing* and other partners. I am truly thankful for the amount of trust and freedom you gave me during various points of my time at the chair. You always tried to find time for me when needed and I always enjoyed our discussions. I am amazed by your willingness and ability to support each of your Ph.D.- and sometimes even master- and bachelor students. I am sure that if the day had 30 hours, you would try to spend even more time with us. I do not think I could have wished for a better Doktorvater.

Dear Thomas, it is fair to say that without you I would not have done my Ph.D. at the Chair of Applied Mechanics. I thoroughly enjoyed my time as a student assistant in the rotordynamics group under your supervision and I am very thankful for the opportunity to develop the turbo pump test rig. Thank you for recommending me to Daniel for the Ph.D. position and further supporting me in all kinds of administrative manners during my time at the chair.

Dear Simon, Georg, Schorsch, Andi, Daniela and Manuela, thank you for supporting me during many situations, from finding lost checks to doing emergency repairs on all kind of systems. The chair is in a unique position to have its own mechanical- and electrical workshop and we are all glad to have you. Without you, we would not be able to develop our prototypes and test rigs in such a short amount of time and quality.

My dear Ph.D. colleagues, unfortunately I can not thank everyone individually here. Thank you for listening to my stupid stories during lunch, thank you for doing live thrash metal gigs with me on our Christmas parties, thank you for letting me crash your office to complain about silly things (especially towards the end of my time at the chair). I have good memories with every single one of you, from going to international conferences together, over doing stupid mountain biking trips, to just hanging out in the coffee room. I am truly

thankful to have had the opportunity to work with such a talented group of people.

My dear students, when I decided to do my Ph.D., one of my main motivations was the possibility to continue to work with students. You all proved to me that I made the right choice, and I want to thank you individually in Appendix D.

Dear Tobias, I want to thank you and *the Boeing Company* for continuously putting your trust in me and my work. You basically motivated this entire thesis, and without you showing up in the beginning of 2017, I probably would have done my doctorate on a completely different topic. Thank you for your sustained effort to do projects with us despite all administrative hurdles. I am sure that our projects have enabled and strengthened the relationship between *Boeing* and TUM, and I hope that you continue to do projects with the chair and TUM in the future.

Dear Julia, this is normally the part where the Ph.D. student thanks their significant other for being supportive and understanding of their lack of time together. However, I sometimes joke that my side hustle is doing my Ph.D. and my main job is spending an amazing time with you. I do not know how many people can claim to have done a Ph.D. in four years, while also riding over 50.000 km of motorcycle with their girlfriend. Thank you for annoying me every weekend that we have to do something together, thank you for exploring other countries and cities with me, thank you for forcing me to regularly visit family and friends, thank you for going to concerts and playing video games with me, thank you for being my model when I want to shoot pictures. I have literally spent the last four years at full throttle with you to the point of complete exhaustion. I sometimes complain about that, but I would not have wanted it any other way. Thank you for the memories.

Munich, June 08, 2021 *Tobias*

Abstract

The continuous drive to automate increasingly complex and intricate manufacturing processes with robot manipulators also pushes manufacturers to further improve the path tracking accuracy of their robots. This is a quite challenging task, since commonly suggested methods for high-precision robot control require high-fidelity models of complex effects in the robot's drivetrain, as well as its flexible joints and flexible links.

The goal of this thesis is to accomplish a path tracking accuracy of below 20 μm with a robot manipulator. In order to achieve this, the influence of structural dynamics on the performance of robot manipulators is investigated, with the conclusion that it is quite unfeasible to achieve such a high accuracy by modifying the control system of an existing industrial robot.

Instead, this thesis investigates two different approaches of using an external device to stabilize the manufacturing tool for higher path accuracy. The first approach focuses on damping the pose dependent structural dynamics of a robot manipulator using active vibration damping methods applied via a proof-mass actuator and acceleration feedback. The second approach uses a highly precise positioning system to stabilize the process tool against any disturbances transferred over the robot's structure.

Both approaches are tested using a high-fidelity robot simulation model, which is developed throughout this thesis. The final prototypes are applied to two different robot manipulators, with the second external stabilization approach improving the path tracking accuracy of a UR10 robot from 1 mm to below 15 μm.

Zusammenfassung

Das anhaltende Bestreben immer komplexere und kompliziertere Fertigungsprozesse mit Robotermanipulatoren zu automatisieren drängt Hersteller auch dazu die Bahngenauigkeit ihrer Roboter weiter zu verbessern. Dies ist eine recht anspruchsvolle Aufgabe, da die üblicherweise vorgeschlagenen Methoden für eine hochpräzise Robotersteuerung sehr genaue Modelle der komplexen Effekte im Antriebsstrang des Roboters sowie seiner flexiblen Gelenke und Arme erfordern.

Das Ziel dieser Arbeit ist es mit einem Robotermanipulator eine Bahngenauigkeit von unter 20 μm zu erreichen. Hierzu wird zunächst der Einfluss der Strukturdynamik auf die Genauigkeit von Robotermanipulatoren untersucht, mit der Schlussfolgerung, dass es sehr unwahrscheinlich ist eine solch hohe Genauigkeit durch die Modifikation des Steuerungssystems eines bestehenden Industrieroboters zu erreichen.

Stattdessen werden in dieser Arbeit zwei verschiedene Ansätze zur Verwendung einer externen Vorrichtung zur Stabilisierung des Fertigungswerkzeugs für eine höhere Bahngenauigkeit untersucht. Der erste Ansatz konzentriert sich auf die Dämpfung der positionsabhängigen Strukturdynamik eines Robotermanipulators unter Verwendung aktiver Schwingungsdämpfungsmethoden, die über einen Proof-Mass-Aktuator und Beschleunigungsfeedback angewendet werden. Der zweite Ansatz nutzt ein hochpräzises Positioniersystem, um das Prozesswerkzeug gegen die über die Roboterstruktur übertragenen Störungen zu stabilisieren.

Beide Ansätze werden mit einem hochwertigen Robotersimulationsmodell getestet, das im Rahmen dieser Arbeit entwickelt wird. Die endgültigen Prototypen werden auf zwei verschiedenen Robotermanipulatoren angewendet, wobei der zweite externe Stabilisierungsansatz die Bahngenauigkeit eines UR10-Roboters von 1 mm auf unter 15 μm verbessert.

Contents

Chapter 1

Introduction

Starting with their first introduction into the industrial manufacturing landscape in 1961 in a *General Motors* factory for die casting handling and spot welding, robot manipulators had a large impact on increasing the productivity of manufacturing processes over the past decades [204]. The typical industrial robot manipulator consists of six or seven actuated rotational degrees of freedom (DOF) connected by theoretically rigid links in a tree-like structure [248]. Their general objective is to substitute a human arm by being able to reach a larger workspace in any orientation, carry larger loads, being more precise, faster and able to perform the same repetitive task in a predictable and reliable manner without tiring.

Typical applications for industrial robot manipulators are the automation of welding or cutting processes (e.g. MIG/MAG welding, spot welding, plasma cutting/welding, laser cutting/welding, etc.), material handling processes (e.g. pick-and-place, injection molding, machine loading, machine tending, order picking, packaging, etc.) and other applications like assembly, bonding/sealing, coating/painting, drilling/grinding/milling, etc. [73].

Because of their potential for high productivity and cost efficiency, it is only natural that the industrial market is driven to further automate increasingly complicated and intricate manufacturing processes. This also presents the robot manufactures with the challenge to further improve the performance of their robot manipulators to meet this demand of the industry. Over the past decade, one large trend has been to develop torque-controlled robot manipulators that are able to sense their environment, which are potentially more useful for assembly tasks and safe to work collaboratively with humans [121]. However, the other trend is to quite simply make the next generation of position-controlled robots faster and more precise in order to enable them to perform tasks like high-precision laser cutting or welding. For example, the topic of this theses was largely motivated by an R&D project between the *Chair of Applied Mechanics* at TUM and *Boeing Research and Technology Europe* that had the goal to automate a high-precision non-contact manufacturing process using a large industrial robot manipulator which needed to follow a trajectory path with 20 μm accuracy.

Robot Accuracy

The first step to further increase the accuracy of robot manipulators is to find a common definition and test scenario. This was done in 1990 with the norm ISO 9283, according to which the performance of a robot manipulator can be determined by conducting the following tests with a laser tracker or a similar device, Fig 1.1:

- The *pose repeatability* is the tolerance RP between the real tool center point (TCP) positions of the robot, after moving it into the same pose multiple times.
- The *pose accuracy* is the deviation AP between the mean of the real TCP positions B and the planned TCP position A, after moving the robot into the same pose multiple times.
- The *path repeatability* is the tolerance RT between the real paths of the robot's TCP, after tracking the same trajectory multiple times.

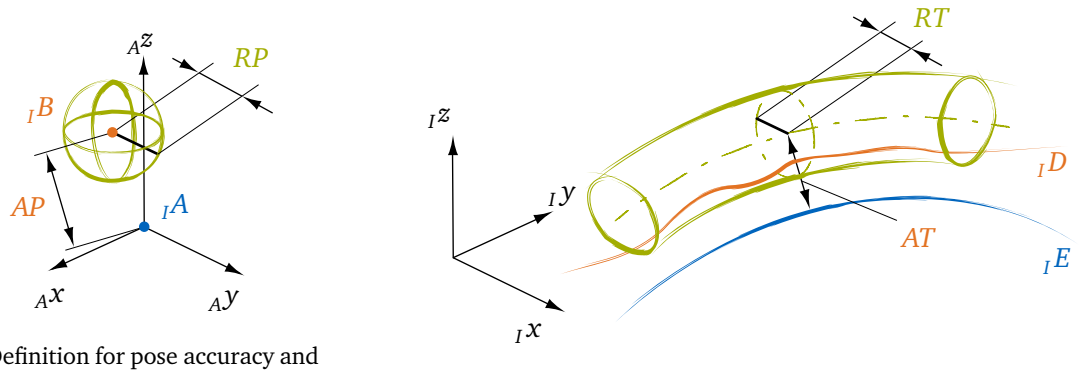

(a) Definition for pose accuracy and -repeatability.

(b) Definition for path accuracy and -repeatability.

Figure 1.1: Definitions for a robot accuracy test according to ISO 9283, adapted from [6].

- The *path accuracy* is the maximum deviation AT of the average real path to the planned path E, after tracking the same trajectory multiple times.

While ISO 9283 is the agreed industry standard to evaluate the performance of industrial manipulators, manufactures unfortunately often only disclose the pose repeatability of their robots[1]. The main reason for this is probably that it is often the best of the above mentioned accuracy measures. However, the pose repeatability only tells us that while the robot might not end up at the desired position, it is at least always wrong in a similar way. A good pose repeatability is therefore somewhat reassuring, and also a requirement to further improve the pose accuracy using volumetric calibration methods as I will discuss later. However, it gives us no real information about the real pose accuracy and definitely not about the path accuracy. Most larger robot manufacturers like *ABB*, *Kuka* and *Fanuc* claim a pose repeatability of up to 10 μm for their smaller sized robots with a reach below 1.0 m [3, 94, 162]. However, according to measured data published by *ABB*, the path repeatability and path accuracy is always at least one order of magnitude worse [3, 6, 7].

The important accuracy measures for this thesis are the path repeatability and path accuracy, which were both required to be below 20 μm. A brief market analysis shows that there are no manipulators with a reach over 2 m available that can even achieve a pose repeatability below 20 μm.

Fig. 1.2 shows the measured vertical path error at the TCP of a selection of commercially available robot manipulators, while following a horizontal trajectory. We can easily see that none of these robots are even close to achieving the desired path accuracy.

Error Sources of Robot Manipulators

In order to derive methods to improve the accuracy of robot manipulators, we can first have a look at typical sources of error. According to [145, 174, 206] these can be categorized as follows:

- *Environmental errors* such as the varying temperature of the joints during the warm up process, which can have an influence on the lubrication of the gears and therefore backlash and friction.

- *Parametric errors* which include kinematic parameter variation because of manufacturing and assembly tolerances, the influence of dynamic parameters like the flexibilities

[1] The only major robot manufacturer that publicly discloses the other accuracy measures as defined by ISO 9283 for their robot models seems to be *ABB*, see e.g. [6].

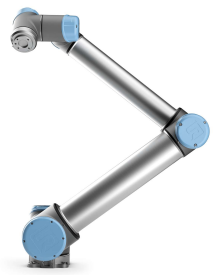

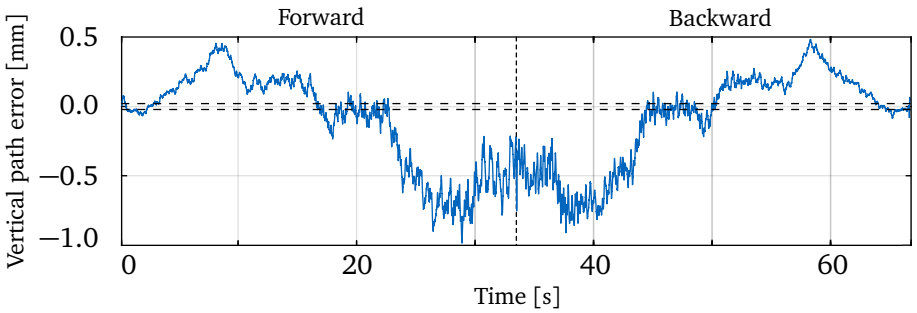

(a) The UR10 made by *Universal Robots* is a cheap, lightweight, position controlled robot. Its maximum payload is 10 kg and maximum reach is 1.3 m. The manufacturer only discloses a pose repeatability of ±0.1 mm according to ISO 9283 [279].
The measurements show the vertical path error while following a 1.0 m horizontal trajectory with 30 mm/s starting close to the base of the robot until it is almost completely stretched out. The measurements were performed using highly precise eddy-current sensors from *Micro-Epsilon* with a usable resolution of 3 μm. These measurements are published as part of my paper [51].

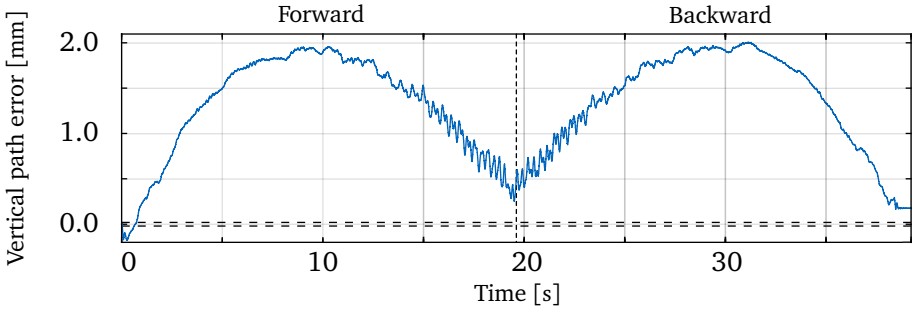

(b) The Panda made by *Franka Emika* is a cheap, lightweight, torque controlled robot. Its maximum payload is 3 kg and maximum reach is 0.85 m. The manufacturer discloses a pose repeatability of ±0.1 mm and path accuracy of ±1.25 mm according to ISO 9283 [98].
The measurements show the vertical path error while following a 0.8 m horizontal trajectory with 40 mm/s starting close to the base of the robot until it is almost completely stretched out. The measurements were also performed using highly precise eddy-current sensors from *Micro-Epsilon* with a usable resolution of 3 μm. These measurements were part of the master's thesis of my student PRAUTZSCH [217].

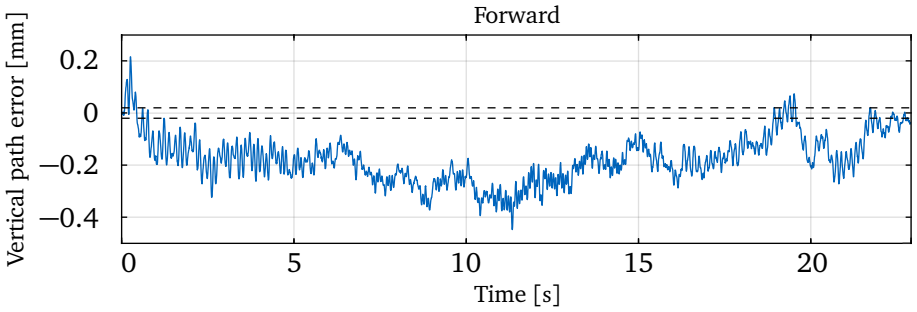

(c) The IRB 4600 made by *ABB* is a typical position controlled industrial robot manipulator. Its maximum payload is 40 kg and maximum reach is 2.05 m. The manufacturer discloses a pose repeatability of ±0.06 mm, pose accuracy of ±0.02 mm, path repeatability of ±0.28 mm and path accuracy of ±0.57 mm according to ISO 9283 [6].
The measurements show the vertical path error while following a 1.0 m horizontal trajectory with 45 mm/s. The measurements were performed using a AT960 laser tracker from *Leica*. These measurements were part of our R&D project with *Boeing Research and Technology Europe* and were performed by the WZL laboratory of the RWTH Aachen.

Figure 1.2: Measured vertical path error for a selection of robot manipulators with the accuracy requirement of 20 μm marked with dotted horizontal lines.

of the joints and links, as well as friction and other non-linearities like hysteresis and backlash.

- *Measurement errors* of the various sensors used in a robot manipulator, like incremental and absolute encoders or torque sensors.
- *Computational errors* caused by wrongly planned trajectories or control system errors.
- *Application errors* e.g. caused by installing the robot on a flexible mounting surface.

Regarding the accuracy of robot manipulators, it is generally agreed that the main sources of error are geometrical errors of the robot assembly and the compliance of the gears, joints and links that cause the robot to deform depending on the current pose and load [247, 252]. This is a problem, since a typical industrial robot manipulator can only measure the angles of its motors. It is then assumed that there is no deformation of the gears, joints and links to derive the needed motor angles to follow a desired trajectory at the TCP using inverse kinematics. However, depending on the load of the robot and its current position, the compliant components of the robot will deform and cause the TCP to sink below the desired position.

Investigating the measured vertical path error of e.g. the UR10 in a bit more detail (Fig. 1.3), we can see that the real behavior is even more complicated than this. The test trajectory starts with the TCP of the robot right next to its base in its most folded position. The robot should therefore experience the least amount of torque caused by its own weight in its starting position. The robot then moves its TCP away from its base following a horizontal trajectory. The moment arm, and therefore the load on the robots compliant components, can consequently only increase. This would imply that the TCP can only drop below its planned trajectory in vertical direction. However, we can see that the TCP of the robot actually starts to raise up for the first half of its trajectory. The rising of the robot is probably caused by a combination of a slightly miss-planned trajectory due to geometrical errors and backlash in the gears.

Additionally to this slowly changing 'quasi-static' error, there are also dynamic oscillations visible during the entirety of the robot's motion, with larger amplitudes towards the end of the trajectory while the robot is stretched out the most[2]. These dynamic phenomena are mainly caused by the torque ripple of the robot's drivetrain exciting the structural dynamics of its mechanical components and will be a significant part of this theses.

For now, we can try to separate the error into a 'quasi-static'- and 'dynamic' error[3]. We can see that the 'quasi-static' error (Fig. 1.3 green line), while probably quite hard to predict purely based on models, is at least repeatable, since the robot is following the same error profile while moving backwards and forwards. Provided that the robot otherwise has a good pose repeatability, this repeatable error can be compensated by using a volumetric calibration process [206]: The robot is moved into different poses while the real TCP position is measured using a laser tracker. The recorded pose accuracy data is then used to create a compensation map that uses slightly different joint angles for each pose to improve the pose accuracy.

However, even under the assumption that we can perform an almost perfect volumetric calibration, the 'dynamic' error (Fig. 1.3 orange line) would still be larger than our accuracy

[2] I want to emphasize here that these measurements were performed using highly accurate eddy-current sensors with a usable resolution of below 3 μm, the dynamic error shown in Fig. 1.3 is therefore not sensor noise, but real motion measured at the TCP of the robot.

[3] This is done here by performing a Fourier transform of the measured error signal and then plotting the result of an inverse Fourier transformation that only uses the frequency contributions below 0.25 Hz for the 'quasi-static' error and the frequency contributions higher than 0.25 Hz for the 'dynamic' error.

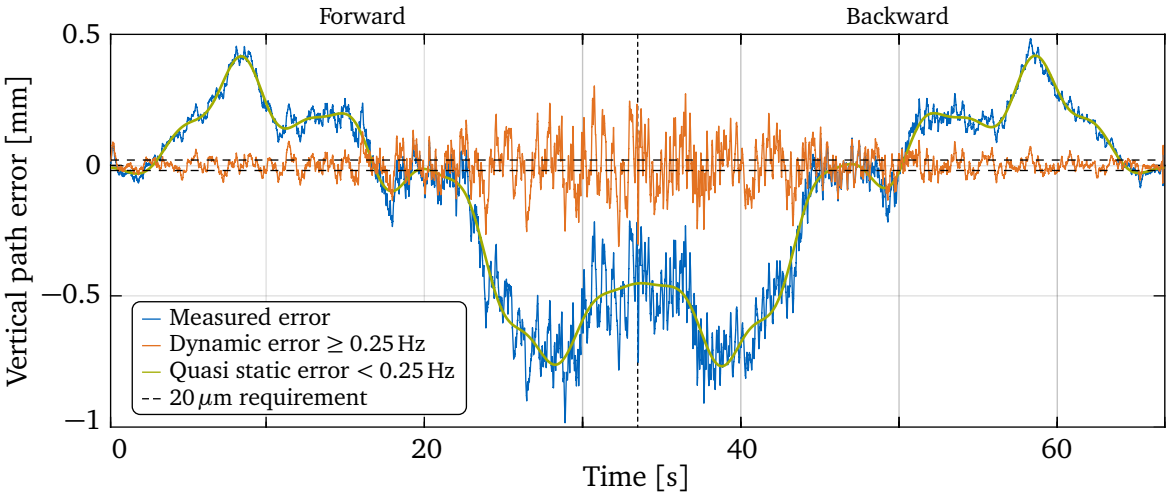

Figure 1.3: Detailed view of the measured vertical path error of the UR10 during a horizontal trajectory as also shown in Fig. 1.2a.

requirement. This leaves us with no choice, but to also somehow consider the structural dynamics of the robot to further improve its accuracy. Unfortunately, this is a vastly more complicated problem, since the error will in most cases not be as nicely repeatable as the 'quasi-static' error. While the vibration amplitudes will be similar when repeating the same trajectory, the exact motion is very dependent on the exact starting state of the system and how it is excited by the different possible excitation sources like torque-ripple, grinding of the gears and other external disturbances. Additionally, there is also the interaction between the joint controllers of the robot and its own structural dynamics to consider.

Over the past decades, quite a large amount of research effort has been dedicated to methods that try to modify the robot's own control system to compensate these dynamics effects caused be the excitation of the dynamics of the mechanical structure of a robot manipulator. However, the big disadvantage of these methods is that the available control variables for the robot are either the motor angles, or the joint-torques for torque-controlled robots[4]. Since we are interested in precise control of the robot's TCP, there are additional dynamics of the flexible gear, joints and links of the robot between the input (motor angle / joint-torque) and the output (actual TCP position) of this supplementary control system. Without direct feedback at the TCP of the robot, a control system like that would be entirely feedforward based and would require almost unachievable precise models of the plants between the joints of the robot and the TCP, see Fig. 1.4a green arrows. Some methods propose to use measured feedback at the TCP using additional sensors or camera systems. However, these methods also have to deal with the still non-collocated nature of the control problem which can be quite problematic in the field of structural control systems [219].

External Approaches

For the above mentioned reasons, we decided to approach the problem of reducing the dynamic error at the robot's TCP differently by using an additional set of actuators at the robots end effector. This makes the control problem collocated and, as we will see later, has some great advantages like not needing precise models of the system for good performance. In this thesis I will investigate two approaches:

[4]As we will see later, there is the additional problem that typical robot joint position-, as well as torque-controllers, have a quite limited bandwidth of usually around 10 Hz at the joint side, which will also inherently limit any kind of control system that will try to use these quantities as their control variable.

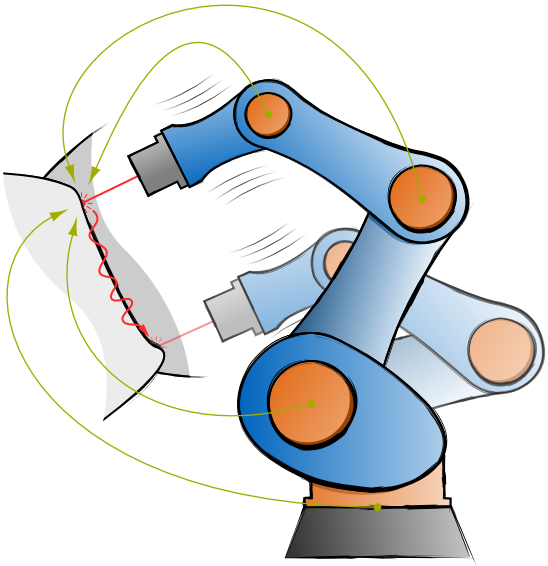

(a) High precision laser welding using a robot manipulator. The transfer paths needed for precise control of the TCP using the robot's joints are shown in green.

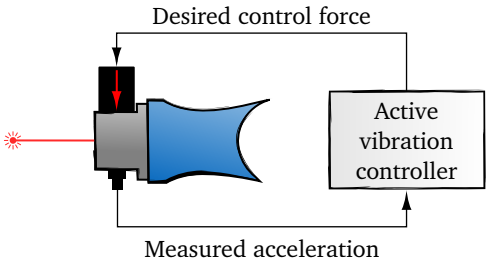

(b) Active vibration damping approach.

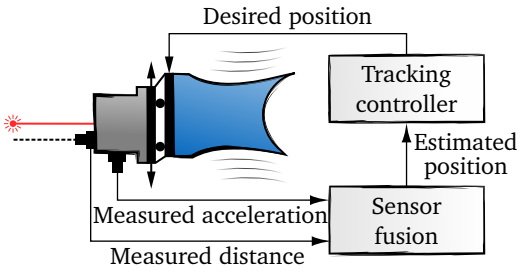

(c) Active stabilization approach.

Figure 1.4: Concepts for high-precision robot control.

- The first one uses an additional proof-mass actuator at the mounting flange of the robot, Fig. 1.4b. The reaction force created by the inertia of the moving proof-mass actuator is then used as the control variable. Using acceleration feedback at the same position, we can employ traditional active vibration techniques to damp the structural vibrations of the robot.
  The big challenge here is going to be the time-variability of the controlled structure, since the structural dynamics of the robot highly depend on its current position [46, 48]. Using exclusively measured accelerations also has some unique challenges like being more susceptible to instabilities due to control spillover when using modern control methods. However, since it is much more convenient to just attach a set of acceleration sensors near the robots end effector than to acquire position feedback using for example laser trackers, we wanted to stick to control designs that exclusively use acceleration feedback.

- The second approach uses an extra set of actuators at the mounting flange to move the process tool, Fig. 1.4c. The idea here is to decouple the tool from any disturbance coming from the robot, similar to in-body image stabilization (IBIS) systems in professional cameras. The concept is also sometimes called inertially stabilized platforms (ISP) and has been used for systems like camera tracking or laser guidance systems on warships [126]. The main challenge of this concept is the need for a good estimation of the real TCP position to counteract the undesired motion, as well as an adequate actuator design that is able to support the required bandwidth of the control system.

Since both of these approaches need no prior knowledge about the robot itself and can theoretically work completely independently of the robot's own control system, we named this thesis 'External Stabilization of Robot Manipulators'.

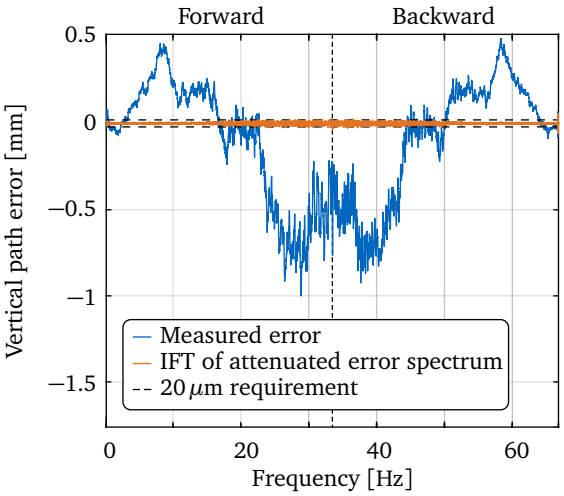

Figure 1.5: Measured vertical path error with the inverse Fourier transformation (IFT) of the attenuated spectrum.

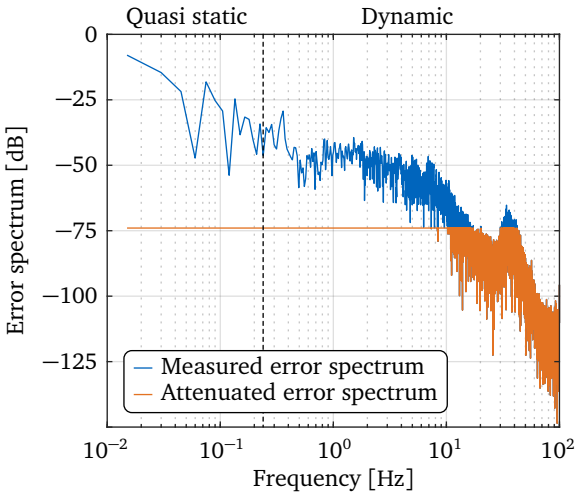

Figure 1.6: Spectrum of the measured vertical path error at the UR10 robot with an evenly attenuated spectrum. The reference value is 1 mm.

1.1 Goal, Methodology and Structure of the Thesis

The main goal of this thesis was to **develop an external stabilization device to increase the path accuracy of robot manipulators**.

This was largely motivated by an industrial project with *Boeing Research & Technology* which had the following requirements:

- The automated process works without contact to the process surface and requires a path accuracy of 20 μm.
- The prototype stabilization device is a proof-of-concept and needs to be able to stabilize a 200 g dummy tool with 20 μm precision and compensate a maximum path error of $\pm$2.5 mm.
- The prototype is tested on a UR10 robot tracking a horizontal process surface at various speeds.
- The complexity of the system should be as low as possible to ensure a more straightforward industrialization of the prototype system. The system should therefore work with the least amount of prior knowledge as possible. Meaning, without having to utilize complex models of the robot's structural dynamics and without having to interface with the control system of the robot. Ideally, the device can be mounted independently on any kind of robot manipulator and used with minimal tuning effort.
- The control system should be robust against additional unknown disturbances transferred over the robot's mechanical structure to the process tool.

Considering the frequency spectrum of the vertical path error measurements of the UR10 robot (Fig. 1.5), we can do a rough estimate of the minimum attenuation needed for the stabilization system. In order to keep the maximum error peaks below 20 μm[5], we need a minimum attenuation of up to −70 dB in the quasi-static frequency region and a minimum attenuation of up to −40 dB of the dynamic error, Fig. 1.6. Additionally, the control system

[5]For simplicity, I assume an even attenuation across the frequency spectrum.

needs a control bandwidth of at least 50 Hz to effect the necessary frequency range. As we will see in the following State of the Art chapter, these are quite extreme requirements for a mechatronic positioning system. Especially considering the system is mounted on a moving, vibrating robot manipulator with a flexible mechanical structure.

Methodology

Since this thesis was tightly coupled to an industrial project, my number one priority was to produce a working prototype that fulfills the above mentioned requirements. From experience, most of the time spent in the development of new mechatronic systems relates to implementation and hardware issues that do not make good topics for scientific publications. This also meant that I could not spend too much time on investigating exotic control methods that might not work on the real system, in order to not jeopardize the final goal of this thesis by running out of time. I therefore followed a strict methodology:

1. **Gain a better understanding of the influence of structural dynamics on robots and mechatronics systems in general.**
   In order to achieve this, we performed a series of tests on a UR10, *ABB* IRB 4600, *Franka* Panda and our own CROPS harvesting robot. We also did experiments on a robot joint test rig, a mechanical single harmonic oscillator test rig and our biped walking robot LOLA (Fig. 1.7 orange area). The results were then used to identify all relevant physical effects that needed to be considered for the development of the external stabilization prototypes.

2. **Built a full robot simulation model as a development platform** in Simulink based on this knowledge.

3. **Derive smaller models with higher levels of abstraction** for hierarchical testing of new stabilization concepts and control methods (Fig. 1.7 blue area).
   The full robot model was first reduced to a single flexible joint model with one flexible link, then further reduced to a flexible joint model with one rigid link and finally to a simple reduced linear transfer function model that represented the structural dynamics at the TCP of the flexible model with one link. This was an important step, since we could easily test new ideas on simple models in order to rule them out as quickly as possible to save time. For example, almost every control method worked on the linear transfer function model, however, roughly half of our tested control strategies could already be eliminated with the flexible single link models. Finally, only a small amount of methods proofed to be actually promising on the full robot manipulator model.

4. After deciding on a small number of worthwhile prototype concepts, **built small component test rigs** to separately tests subcomponents.
   This is also an important step to save development time. Immediately building a first version of the entire prototype makes it difficult to reiterate on separate subcomponents, since a small change to one component might have a large effect on another subcomponent that is otherwise already working as intended, causing unnecessary redesign effort. This proofed especially valuable for the mechanical system of the stabilization prototype, since we had to go through a few iterations to achieve the desired performance.

5. **Tune and test the prototypes on moving robot manipulators**.
   As described in the requirements, we tested the stabilization prototype on a UR10 robot. However, the active vibration damping prototype was tested on our CROPS harvesting

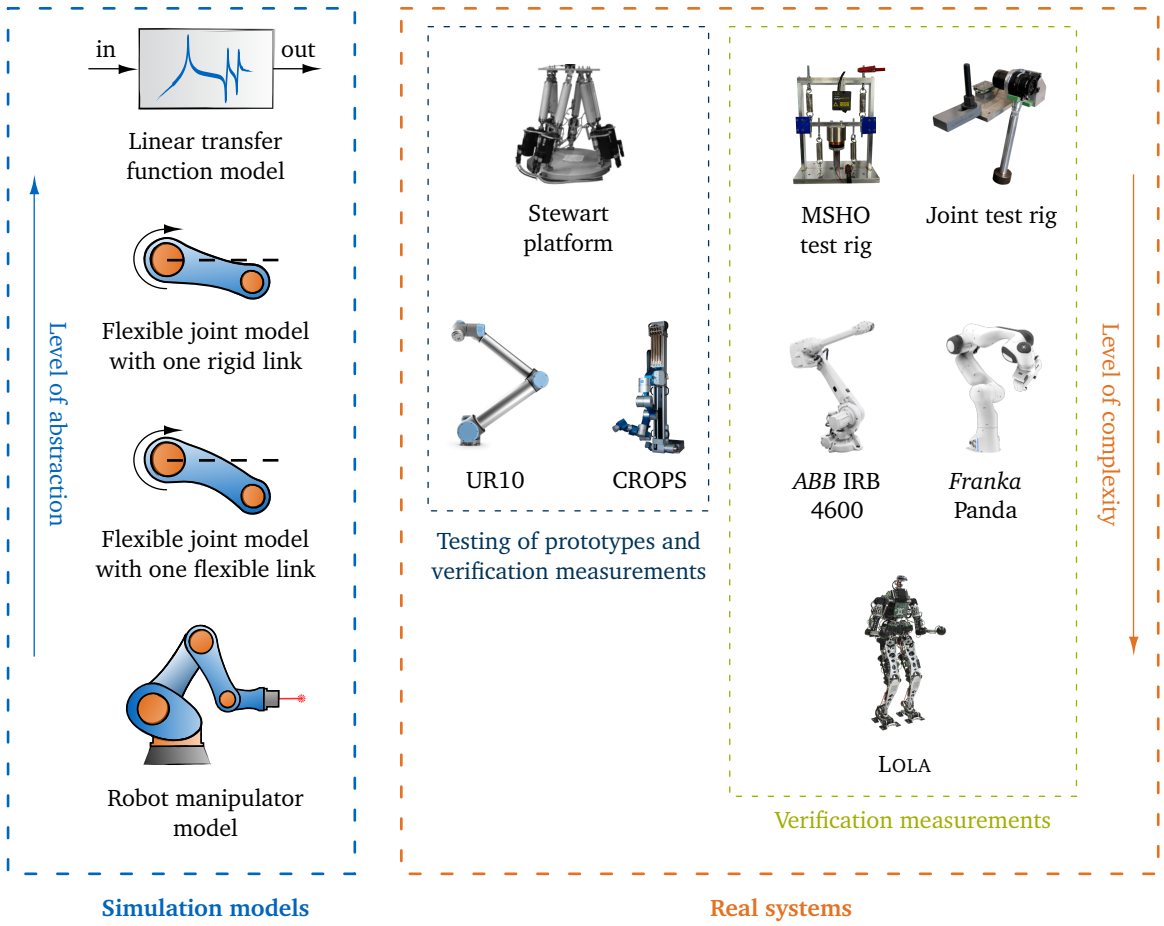

Figure 1.7: Simulation models and real systems used as development platforms or for verification measurements.

robot. The main reason for this is that these robots behave quite differently, which shows that different approaches might be more suitable for different types of robots.

In order to keep this thesis concise, I will only report on the final working prototypes, without mentioning specific reiterations or subcomponent tests. Nevertheless, I will still comment on important lessons-learned at the appropriate places.

Structure of the Thesis

The structure of the thesis aims to reflects this methodology. First, we will have a detailed look at the current state of the art in chapter 2. This includes a short analysis of the performance of currently available industrial robot manipulators, as well as common approaches to model robots and methods to improve their accuracy. Additionally, I will give a short overview of various stabilization systems and their performance, as well as active vibration damping approaches.

Chapter 3 will explain the fundamental theory needed to understand the following core chapters of the thesis. My assumption for the most likely type of reader is that they have a stronger background in typical robotics topics and a weaker background in structural dynamics and active vibration control. For this reason, I will start with a more thorough introduction of structural dynamics concepts, followed by classical active vibration damping methods and finally common joint control strategies for position- and torque-controlled robots.

Chapter 4 first showcases the Simulink based robot manipulator model, which we developed over the past years. The model is based on a flexible multibody simulation with flexible links and drivetrains. The multibody model also includes additional effects like motor-cogging, which is probably the main excitation source for moving robots. The model is verified using measurements from a UR10 robot. The robot model is then used to investigate pose dependent structural dynamics and the effects of structural dynamics on position- and torque controlled robots. Our findings are then also verified using measurements from our CROPS harvesting robot, a joint test rig and the torque-controlled *Franka* Panda robot. The chapter ends with an excursus about the influence of structural dynamics on our biped walking robot *Lola*. This section is not necessary for the following development of the external stabilization prototypes. However, it is still helpful to gain a deeper understanding about the influence of structural dynamics on the performance of complex mechatronic systems.

The final prototypes for the active vibration damping- and external stabilization approach are described in chapter 5. For both cases, I will first introduce the actuator and control design, and then show the simulated system performance. The active vibration damping approach is then tested on our CROPS harvesting robot and the stabilization unit is tested using a UR10 robot. For the active vibration damping approach, I will also use a section to comment on the performance of more modern control methods.

Finally, the overall conclusions and outlook are discussed in chapter 6.

The appendix first showcases many important implementation and hardware issues using a mechanical single harmonic oscillator test rig. I also give a quick summary of the first version of the stabilization unit. The rest of the appendix includes a full list of students I have had the pleasure to work with during my time at the chair, my full publication list and an overview of the Simulink blocks of the robot simulation model.

1.2 Thesis Contributions

The novel contributions of this thesis can be summarized as fallows:

- An experimental investigation of the pose dependent structural dynamics of robot manipulators using an experimental modal analysis of our CROPS harvesting robot. While this is not the first modal analysis of a robot manipulator, it is definitely the most detailed one to my knowledge. Most published results only use 5 to 10 sensors, while our analysis used 77 measurement points. The high level of detail also allowed us to observe that only certain mode shapes are controllable via the robots joint controllers. Furthermore, we were able to easily visualize the pose dependent structural dynamics of a robot manipulator by measuring the driving point dynamics at the TCP of the robot at 60 different poses. The results are also published in our paper [46].

- An investigation of the influence of structural dynamics on cascaded joint position controllers using a flexible multibody simulation with flexible drivetrains/links and experimental verification results on a joint test rig. We further investigated the feasibility of using a cascaded control structure with the position- and/or velocity-loop being closed behind the flexibility of the drivetrain using direct joint position/-velocity feedback. The results are also published in our paper [47].

- An investigation of the influence of structural dynamics on the performance of torque-controlled robots. Especially regarding the possible control-bandwidth of joint-torque controllers and their influence on passivity based control schemes for high-precision path tracking. The results are verified using experimental results from a *Franka* Panda

robot. The results are partially based on the master's thesis of my student[6] PRAUTZSCH [217] and are also published in our paper [218].

- A full procedure to simulate a robot manipulator in Simulink, including verified coupled models for the BLDC motors, motor-cogging, joint-position or -torque controllers, flexible drivetrain, and reduced order models for flexible links. The results are verified using measurements from a UR10 robot. A similar methodology was used by my student ZIMMERMANN for a Dymola model in her master's thesis [312], which I supervised in cooperation with *ABB Robotics*. The results are partially published in our paper [313].

- The first experimental modal analysis of a biped walking robot. We were able to showcase the influence of the dynamics of the mechanical structure of our biped robot LOLA on her control system, and also use the results to later improve her mechanical design. The results are published in our papers [50, 52, 240].

- Investigation of the feasibility of using proof-mass actuators and active vibration damping techniques with acceleration feedback to damp the structural dynamics of a moving robot manipulators and subsequently improve their path accuracy. The approach is tested in simulation and an actuator prototype is developed to perform experiments on our CROPS harvesting robot. Preliminary simulation results using an intermediate version of our robot simulation model are published in our papers [48, 49]. I also comment on the performance of modern control methods for this application based on the results of the master's thesis of my student HARDER [125] and the semester thesis of my student BODEIT [54].

- The development of a stabilization unit for high precision applications of robot manipulators. The approach is again first tested in simulation and two actuator prototypes are developed and tested on a UR10 robot. The second version of the stabilization unit improves the path tracking performance of the robot from a maximum error of 1 mm to below 15 μm. The results are also partially published in our paper [51].

During my time at the Chair of Applied Mechanics, I published 7 papers as the main-author and 4 papers as a co-author that are relevant to this thesis. I also co-authored 9 further unrelated publications[7]. My full publication list can be found in Appendix E.

I also had the pleasure to supervise 15 student theses and 16 student assistants for various research and industry projects. Some of them also produced results that I reuse or reference in this thesis. A full list of my students and their contributions can be found in Appendix D.

[6] For the sake of simplicity, I will always refer to the students I had the pleasure to work with as 'my students', without wanting to sound possessive. The various student theses I refer to during this work were of course always co-supervised together with Prof. Rixen.

[7] These are mainly resulting from my preceding time as a student assistant in the rotordynamics group of the chair.

Chapter 2

State of the Art

In this chapter, I will summarize the state of the art of the relatively broad fields that will be addressed during this thesis.

In section 2.1, I will talk more deeply about the accuracy of current robot manipulator systems and absolute calibration methods in subsection 2.1.1. Subsection 2.1.2 will be about the modeling of robot manipulators with regards to the joint motor, drivetrain and joint- / link flexibilities. I will also shortly introduce a full flexible robot manipulator model developed by my student ZIMMERMANN during her master's thesis in cooperation with *ABB*. Subsection 2.1.3 summarizes the current state of the art of control concepts for high precision robotics and will touch on the topics of position- and torque-controlled robots, as well as robots with micro / macro redundancy and other approaches.

Section 2.2 will be about inertially stabilized platforms like image stabilization systems or gimbals, since these type of systems are quite comparable to the external stabilization approach for robot manipulators investigated in this thesis.

Finally, section 2.3 will give an overview of the capabilities and applications of current active vibration damping techniques.

Since these are three quite different and extremely broad fields, I will mainly focus on the summary of publications that are also concerned with the development of real prototype systems or the application of methods to real systems. While a deeper exploration of more theoretical work might also be interesting and of value, it would simply go way beyond the scope of this thesis.

2.1 High Precision Robot Manipulators

As we have already seen in the introduction, small commercially available robot manipulators can reach a claimed pose repeatability of up to 10 μm [3, 94, 162]. Unfortunately, the actual pose accuracy as well as the path repeatability and path accuracy according to ISO 9284 are not disclosed by most manufacturers. The main reason for this is that for most industrial applications, the other accuracy measures are just not as important. Most processes automated with robot manipulators are variations of point-to-point applications, which do not need high accuracy while moving between the planned points and mostly care about time efficiency and collision avoidance while actually moving the robot. Most industrial processes that actually benefit from the large workspace of robot manipulators are also comparatively slow and do not need micrometer precision [117]. This means that achieving a high pose repeatability is usually good enough, since a worker has to teach the program for the robot anyway and can just adapt the planned end points of the robot's trajectory for the process until they achieve satisfactory results.

For high-speed pick-and-place applications like the mass assembly of circuits boards, parallel kinematics robots can be designed much stiffer and can therefore move a lot faster at

	ABB IRB 360 (Parallel kin.)	*ABB* IRB 120 (Small size)	*ABB* IRB 4600 (Medium size)	*ABB* IRB 6700 (Large size)
Max. reach [mm]	400	580	2050	3200
Max. load [kg]	1	3	40	150
Pose repeatability [mm]	0.04	0.01	0.06	0.05
Pose accuracy [mm]	0.09	0.02	0.02	0.06
Path repeatability [mm]	0.52	0.07-0.16	0.28	1.6
Path accuracy [mm]	0.21	0.21-0.38	0.57	0.14
Source	[5]	[3]	[6]	[7]

Table 2.1: Accuracy of differently sized robot manipulators from *ABB* according to ISO 9283.

the cost of available workspace. For example, *ABB*'s FlexPicker robot can achieve a maximum acceleration of its TCP of $150\,\mathrm{m/s^2}$ and maximum velocity of $10\,\mathrm{m/s}$ [5]. However, these types of robots are of course also limited by their structural dynamics, which will cause large oscillation amplitudes at their TCP when moved too quickly [88]. While parallel kinematics or SCARA robots (Selective Compliance Assembly Robot Arm) are an interesting alternative, their workspace is also very limited. For this reason, I will concentrate on classic serial robot manipulators in this work.

Tab. 2.1 compares the accuracy of a selection of ABB robots[1]. All of these robots achieve a quite impressive pose repeatability in the $10-50\,\mu$m range. However, the path repeatability gets worse the larger the robot is and none of these robot would achieve our accuracy requirement, which would demand both the path accuracy and repeatability to be below $20\,\mu$m. Unfortunately, the path accuracy also does not allow us to determine how much of the path error can be attributed to the quasi-static and dynamic error amplitudes, since the path repeatability is just the average radius of a tube containing all test trajectories. The path accuracy only tells us how close the TCP is on average to the desired path. It is probably a reasonable assumption that larger robots will experience more sag and larger vibration amplitudes while moving, which both contribute to a worse path repeatability.

This reveals a quite significant weakness of the current way of determining the accuracy of robot manipulators according to ISO 9283: there is no way to differentiate between quasi-static and dynamic error. The quasi-static error profile is usually well repeatable, since it is mostly caused by geometric errors due to manufacturing tolerances, as well as the static sag of the robot caused by the bending of its flexible components due to its own weight (see Fig. 1.2 and Fig. 1.3). This type of error can therefore often reliably be reduced by using calibration methods. If we were able to potentially reduce the quasi-static error to zero using a calibration procedure, we would still be left with the dynamic error. This would cause the path accuracy to be 0.0 mm while the path repeatability would be equal to the largest amplitude of the dynamic error (see Fig. 1.3), which would be quite a misleading way to specify 'accuracy'.

Nevertheless, the first commonly taken step to further improve the accuracy of robot manipulators are absolute calibration methods, which are already offered by some manufacturers (e.g. the 'absolute accuracy option' offered by *ABB* [2]).

[1] I am at the risk of being suspect of advertising for *ABB* here. However, they just publish the most comprehensive product specifications compared to other large robot manufactures like *KUKA*, *Fanuc* or *Stäubli*.

2.1.1 Absolute Calibration Methods

Robot calibration methods have been studied since the 1980s [34] and are categorized into three different levels [248]:

- **Level 1** calibration is only applied on the joint level and tries to compensate the difference between actual and measured joint angles. This only compensates the flexibility of the individual joint's gears and drivetrains.
- **Level 2** calibration tries to compensate the error between the actual and planned TCP position and therefore also includes geometric errors of the entire robot structure, as well as static sag caused by the robot's flexible components. The calibration is usually performed by updating the robots Denavit-Hartenberg (DH) parameters, which results in a more accurately planned TCP trajectory.
- **Level 3** calibration also includes non-geometric parameters like stiffness, joint compliance and friction. This kind of calibration not only creates a compensation map for multiple measured points in the workspace, but also tries to fit model parameters like a stiffness model in certain positions that are then expected to be valid for every pose of the robot.

Level 2 calibrations are the most common ones and are usually performed by measuring the actual TCP position using a laser tracker, laser interferometry, camera systems, string pull devices, or any other kind of distance sensors. Earlier calibration efforts sometimes also just touched reference parts [117]. Level 3 calibrations are much more involved, since they try to derive a parametric model using for example measured transfer functions [290]. I will go into more detail about the modeling of robot manipulators in the next section.

A quite comprehensive compilation of recent calibration efforts for robot manipulators can be found in [206]. A Motoman P-8 robot is calibrated in [202] using an SMX laser tracker by measuring 367 robot configurations and identifying 27 kinematic error parameters. The RMS error at the TCP is reduced from 3.595 mm to 2.524 mm, which is validated at 21 TCP positions. In [299], an *ABB* IRB 2400/L industrial robot is calibrated using a Faro laser tracker. The mean position errors at the TCP are improved from 0.963 mm to 0.470 mm and the maximum errors from 1.764 mm to 0.64 mm. The results are verified at 20 robot positions. An *ABB* IRB 2000 robot arm is calibrated in [113] using a *ROMER* measurement arm. The mean error at the TCP is reduced from 1.25 mm to 0.3 mm and the maximum error from 2.2 mm to 1.4 mm. Finally, an *ABB* IRB 1600 robot is calibrated in [206] using a laser tracker and 1,000 measurement points. The mean error at the TCP is reduced from 0.968 mm to 0.364 mm and the maximum error from 2.158 mm to 0.696 mm. The results are verified using 8 robot configurations.

The above mentioned examples are all level 2 calibrations. An example for a level 3 calibration that actually provides verified experimental results is [172], where the authors load a *Mitsubishi* PA10-6C robot with a 44 N weight and determine the parameters for a simple flexible model using torsional springs for the joint stiffnesses. The calibration using the flexible model improves the mean error at the TCP from 1.8 mm to 0.33 mm and the maximum error from 2.45 mm to 0.71 mm. The results are verified using a coordinate measurement machine with 10 measurement points.

The shown calibration results are summarized in Tab. 2.2. The 'mean' value here is determined by moving the robot into multiple poses and determining the absolute positioning error at the TCP. The mean is then taken over all measurement points. This makes the mean value shown in Tab. 2.2 quite comparable to the pose accuracy of ISO 9283 shown in Tab. 2.1. It is immediately apparent that the accuracies determined by the independent sources

		Moto. P-8	*ABB* IRB 2400	*ABB* IRB 2000	*ABB* IRB 1600	*Mits*. PA10-6C
Before	mean [mm]	3.595	0.963	1.25	0.968	1.8
	max [mm]	–	1.764	2.2	2.158	2.45
After	mean [mm]	2.524	0.47	0.3	0.464	0.33
	max [mm]	–	0.64	1.4	0.696	0.71
Red.	mean [%]	29.79	51.24	76	52.07	81.67
	max [%]	–	63.72	36.36	67.75	71.02
Level		2	2	2	2	3
Source		[202]	[299]	[113]	[206]	[172]

Table 2.2: Static accuracy of a selection of robots after a calibration procedure.

in Tab. 2.2 are in general quite a lot worse than the values provided by *ABB* in Tab. 2.1. Admittedly, the robot models on which the calibration methods were performed are quite a bit older. However, *ABB* still offers the IRB 1600 and specifies a pose repeatability of 0.02 mm, pose accuracy of 0.04 mm, path repeatability of 0.19 mm and path accuracy of 1.03 mm according to ISO 9283 [4]. This would indicate that the static accuracy of this robot should be much better than it was determined by [206].

The reason for this is most likely different applied testing procedures. For example, ISO 9283 uses a tilted test plane that fits into the largest possible cube inside of the robot's workspace, while the sources cited above use somewhat arbitrary pose configurations for the calibration procedures[2]. Interestingly, the tests that were performed by us on different types of robots (see Fig. 1.2) all showed the error to be within the margin specified by the manufacturers. The large differences here are definitely notable and show how important it is to use standardized testing procedures to determine the 'accuracy' of a robot in a meaningful and comparable manner.

Nevertheless, all the calibration methods prove to be quite powerful tools to improve their specifics robot's static accuracy. However, the static accuracies reached by all of these examples are lower than the specified pose accuracies of modern *ABB* robots (see 2.1) and definitely lower than our requirements. While the amount of improvement reached by all of these examples is quite impressive, they will most likely never be able to fully compensate the static error, especially not over the entire workspace. They also do not give any indications regarding how the path accuracy is affected by these methods. It is reasonable to assume that the path accuracy will somewhat improve. However, because of the residual quasi-static error and the still unaffected dynamic error, absolute calibration methods will by themselves never be enough to reach a path accuracy in the micrometer range with robot manipulators.

To further improve the accuracy of robot manipulators, most approaches try to acquire a more complete model of the robot that also includes parameters like joint-/link flexibilities and drivetrain effects like backlash, friction or hysteresis. This was already summarized as a level 3 calibration in this subsection. However, in order to also reduce the dynamic error of the robot, these high-fidelity models also need to be combined with active control approaches. I will give an overview of both of these topics in the following two subsections.

[2]The accuracy values cited in Tab. 2.1 also probably only represent a 'best case' scenario and are not necessarily representative for the performance of the robot for real applications.

2.1.2 Modeling of Robot Manipulators

Regarding the modeling of robot manipulators, my student ZIMMERMANN already gave a very thorough overview of the entire field in her master's thesis [312], which I co-supervised in cooperation with *ABB*. The results of her thesis are summarized in our paper [313]. Popular books like [248] and [249] also give a very comprehensive summary of a lot of relevant topics for the modeling of robot manipulators. This subsection will therefore be partially based on the above mentioned sources. However, written in a more concise manner and with several more recent additions by me. I will go into more detail about our work [313] at the appropriate places.

Since robot manipulators usually have a tree-like structure, most modeling challenges can be described by looking at a single link. If we are able to perfectly model one link, we can then chain together multiple links using a flexible multi body simulation to model an entire robot. Fig. 2.1 gives an overview of the main topics that might be relevant to create a high-fidelity robot model. A robot link can be divided into three subsystems:

- **The motor**, including the power electronics and joint control system, which will receive a desired position / torque from the robot's higher-level planning system.
- **The drivetrain**, which receives the motor torque and has the main purpose of amplifying the motor torque via its gear ratio. As we will see, the drivetrain is probably the main source of error for robot manipulators and also receives the most attention from the research community.
- **The link** itself, which is moved by the drivetrain. While the errors introduced by the link flexibilities are probably smaller compared to the drivetrain, they can still be quite significant for high-precision tasks.

Modeling of the Motor

Most robots are driven by brushless DC (BLDC) motors. This type of electrical machine is fairly well understood and can be modeled quite well, see e.g. [28, 195, 284]. I will show a simple model and a few control approaches for position- and torque-controlled joints in the Fundamental Theory section 3.4, since this is going to be important to get a good understanding of the influence of a robot's structural dynamics on its control system.

A significant source of error that I want to mention here is *torque-ripple*, which describes the variation of the motor-torque during operation [263]. This effect is probably the main excitation source that causes the dynamic error at the TCP of the robot by exciting the structural dynamics of the mechanical system. Unfortunately, there are quite a lot of effects that can contribute to torque-ripple [127, 160]:

- For trapezoidal electromotive force (EMF) machines, the ideal EMF waveform gets disturbed by fringing fields at the pole edges of the rotor. The torque magnitude can also change significantly because of the finite time intervals required by the commutation between the stator phase windings [138]. Furthermore, the currents applied to the motor are not perfectly rectangular. The variation in the motor torque can reach up to 25 % of the rated torque and happen periodically with the revolution of the rotor [78].
- Sinusoidal EMF machines experience much less torque ripple. However, they are still affected by residual non-sinusoidal flux linkages and current waveform distortion, which cause additional harmonic torque components.

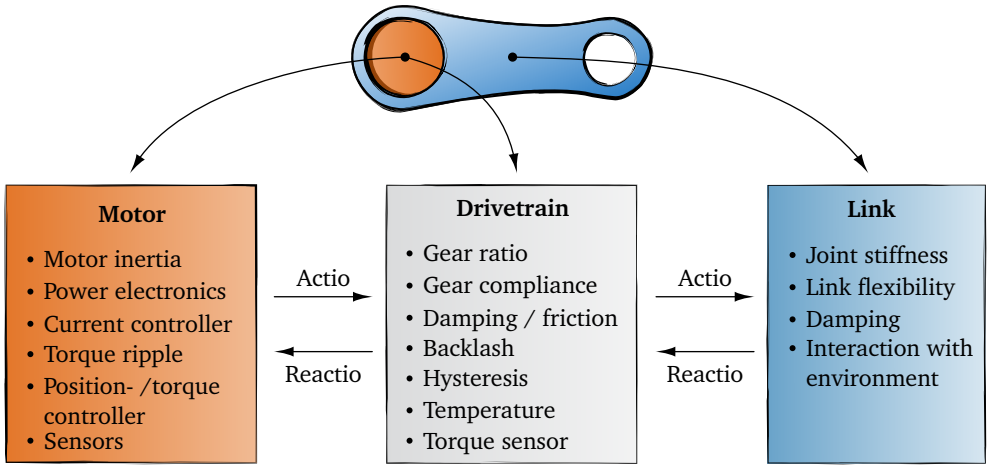

Figure 2.1: Overview of subsystems and effects relevant for the modeling of a single robot link.

- Stator slot harmonics are caused by variable magnetic reluctance in the air gaps and show up as a multiple of the rotational speed and number of slots. Lower frequency torque harmonics result from the interaction between unbalanced magnetization of the poles with rotor eccentricity.

- Strain wave gears like Harmonic Drives introduce a kinematic error, which shows up as an additional disturbance mainly proportional to the second harmonics of the motor rotation. The actual cause of this error is still not clearly identified, but is most likely linked to the deformation of the flexspline while the wave generator is being pressed into it under different loading conditions [111, 140, 180].

While these are quite a lot of effects that add up to the total torque-ripple and are naturally difficult to differentiate by looking at a torque measurement, the disturbance caused by the torque-ripple is usually well controllable on sinusoidal EMF machines by the motor controller in the lower frequency range. Torque-ripple effects therefore usually show up in the 100 Hz - 2 kHz range, with higher frequency disturbances being mechanically filtered by the motor inertia [127]. Lower frequency torque-ripple, which can cause quite large displacement amplitudes at the TCP of the robot and is still present in most industrial robots, is therefore usually a sign of insufficient tuning of the joint-controller or too much flexibility in the drivetrain[3].

Since excitation frequencies above 100 Hz are negligible because of their very low displacement amplitudes, these effects are usually omitted when modeling a robot manipulator. Lower frequency torque-ripple caused by the electrical machine itself can be considered as an unknown disturbance on the motor axis and can theoretically be controlled quite well by having a robust current control loop.

In order to still have a somewhat realistic excitation source, I will use a harmonic disturbance with additional higher harmonics proportional to the motor speed in my models. This assumptions matches quite well with measurements we made on different robots, which I will show in section 4.1.

[3]When we did our measurements with the RWTH Aachen on an *ABB* IRB 4600 robot, the low frequency motor cogging was actually so large that we could use the motor angle measurements and forward kinematics to quite accurately predict the dynamic error at the TCP for very slow trajectories. Unfortunately, for faster motions the motor cogging frequencies are high enough to excite the structural dynamics of the robot, which causes much larger amplitudes at the TCP. This behavior can no longer be predicted by only using the measured motor angles without a high fidelity model that includes joint and link flexibilities.

Modeling of the Drivetrain

Most publications concerning the flexibility of robot manipulators will assume a flexible drivetrain. The most simple, and also most common, approach is to assume a torsional spring between the motor angle θ_m and the actual joint angle θ_j (Fig. 2.2), see e.g. [164, 259, 264, 272]. Since most of these publications are concerned with the derivation of a control law that includes joint flexibility, they often only assume viscous damping between the motor and joint axis for simplicity. This is of course a quite gross oversimplification of the friction inside of a typical robot drive. Additionally, most publications ignore the typically large gear ratios, which basically completely eliminate the influence of external disturbances on the control of the motor axis. The main disturbance on the motor side is therefore mainly friction caused by the gearbox.

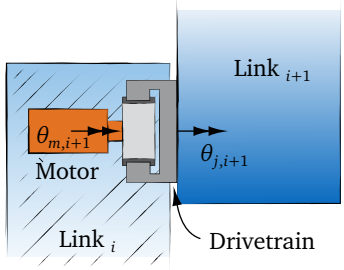

Figure 2.2: Drivetrain of a robot.

The friction inside of robotic gears can induce large positioning errors, stick-slip and limit cycles [55] and is quite difficult to model [242]. The most common friction model combines viscous damping with Coulomb friction [90] and is for examples also used in [115] for a more accurate model of a robot drivetrain. A more detailed model is *Stribeck friction*, which includes a continuous function between the stiction pre-sliding regime and the friction during sliding [23]. In [37], the friction of harmonic drive gears is parameterized using a Stribeck model with good results. It is notable that the measurements and identified model vary quite a lot from the data provided by the manufacturer. For our work [313] we achieved the best results using the *LuGre* model [62], which is a dynamic friction model. A large amount of further friction models and compensation methods are summarized in [24].

According to [233], the transmission stiffness curve of typical robot gearboxes like harmonic drive gears include non-linear effects like backlash, hysteresis, soft- and windup zones, which are quite difficult to model and to parameterize using experiments. A more detailed model is for example used in [115], which uses a stiffening spring characteristic for the gear, viscous damping with additional Coulomb friction and current limiters for the motor.

The complexity of the drivetrain dynamics is probably the main reason why control methods that just use the position of the motor axis could never significantly improve a robot's performance outside of simulation models[4]. As we will see later, using additional position feedback from the joint side with an absolute encoder will also limit the achievable control bandwidth significantly without the use of accurate models [47]. All of these problems have caused a significant amount of research effort to shift towards torque-controlled robots over the last decades, which I will discuss in the following section 2.1.3.

Modeling of the Links

While the most common approach to model the structural dynamics of a robot manipulator is to just model the flexibility of the drivetrain as mentioned above, the obvious deficiency of these kinds of models is that they can only represent torsional flexibilities around the motor axes. Such a robot model would therefore behave completely rigid for any disturbance acting orthogonally to the robot's joint space. In some poses, the real dynamic behavior can also

[4] In my experience, the limit of the actuators, sensor noise and controller clock-rate are often the most significant effects that limit controller performance when trying to apply control methods to real systems. Unfortunately, these effects are often completely ignored by most publications, which is why I supervised a bachelor's theses by my student MAICHNER to investigate exactly these effects on a simple harmonic oscillator test rig. The results can be found in Appendix B.

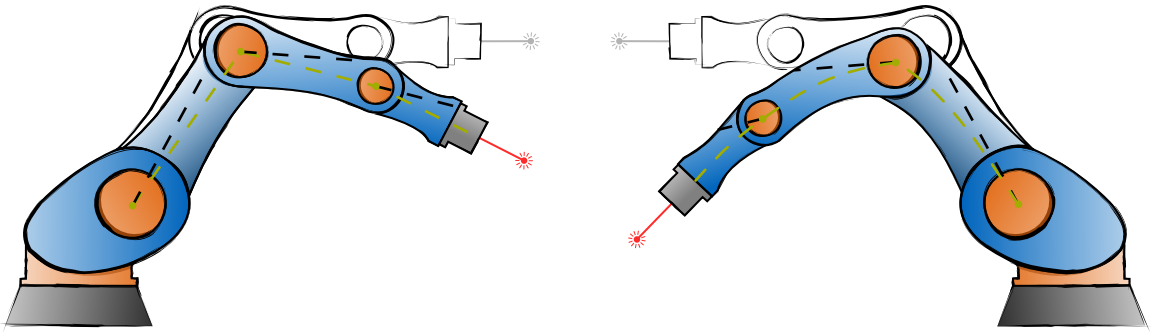

(a) Model with flexible joints and rigid links.

(b) Model with flexible joints and links.

Figure 2.3: Static deformation due to gravity of models using either only flexible joints/drivetrains or flexible joints and links. Motor angles are indicated with black dotted lines and joint angles and actual deformation of the links with green dotted lines. A completely rigid model with the same motor angles is sketched in the background.

often not be modeled precisely enough by just using torsional springs around the motor axes [193].

In [207], it is therefore proposed to use three dimensional spring damper pairs at the joints of the robot, Fig. 2.4.a., in addition to drivetrain flexibilities. The links are still assumed to be stiff, however, the model is parameterized using real measurements. The contribution of the flexible links is therefore lumped together with the joint stiffnesses. A similar approach is done in [8] for a milling robot. The authors also combine a flexible drivetrain model including backlash with a lumped parameters model for the three main axes of the robot. In both works, the simulation is capable of predicting the quasi-static error, which is good enough for their specific applications, however, fail to predict the dynamic error.

A lumped parameter model that concentrates the compliance of the robot in its joints has its charm in terms of simplicity and might be good enough in some cases. However, for high-accuracy applications we would need models of much higher quality. My student ZIMMERMANN did a sensitivity analysis for her master's thesis that suggested that the total compliance of a modern robot manipulator is distributed rather evenly among its joints and links. The real situation for modern large industrial robots is therefore probably more closely represented in Fig. 2.3b.

There has been a significant amount of research effort in the field of modeling robot manipulators with flexible links [89]. Most modeling attempts can be categorized as

- **lumped parameter models** that add additional spring-damper pairs at the links to model the link flexibilities (Fig. 2.4.b), e.g. [148, 188, 309],
- **assumed mode models** where the link flexibility is modeled by a truncated finite modal series, e.g. [146, 226, 314],
- or full **finite element models** that investigate the dynamic behavior of robot manipulators in specific poses, e.g. [87, 198, 200].

Most published research is concentrated on deriving mathematical models for flexible link manipulators without verifying their results on real systems. The sources mentioned in the items above even only concentrate on single link systems. Sources that focus on two-link system are for example [102, 103, 197].

It was recognized quite early that for larger multi-link robot models, the system dynamics can be linearized in a fixed pose, however, the mode shapes and dynamic behavior of the system are dependent on the current pose and will therefore change with the configuration

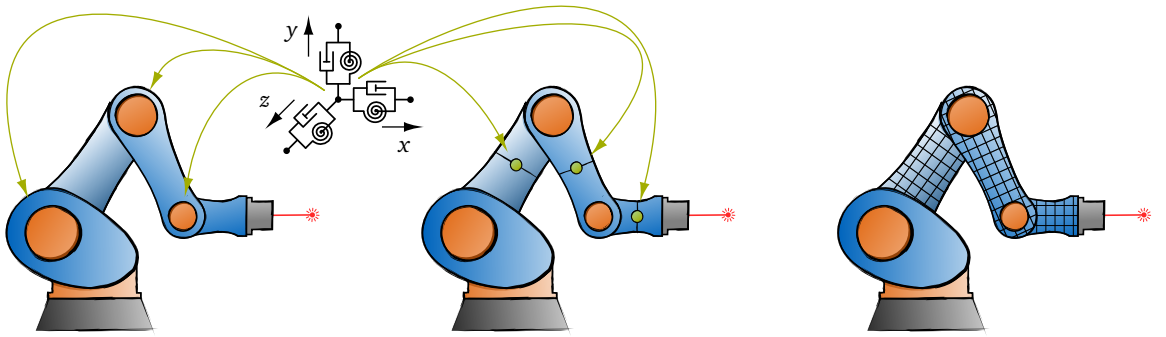

(a) Lumped paramter model with three dimensional spring-damper pairs at the joints.

(b) Lumped paramter model with three dimensional spring-damper pairs at the links.

(c) Flexible multi-body simulation with reduced FE models for the links.

Figure 2.4: Common approaches to model flexibilities in robot manipulators.

of the overall non-linear multi-body system [226]. There is still quite a large amount of publications that try to tackle this modeling problem and can again mostly be categorized in the three above mentioned approaches, e.g. [10, 56, 158, 178, 262]. A very good literature overview for specific modeling approaches can be found in [89]. I will go into more detail regarding how to use a lumped parameter and reduced FE model for a flexible multi-body simulation in the Fundamental Theory section 3.2.

Unfortunately, most research is only concerned with deriving mathematical models and investigating quite specific theoretical effects using these models. There are some publications that manage to verify their models on academic test benches with one joint and a large flexible beam with somewhat accurate results [199, 298, 305]. However, there are no publications that can use their models to actually predict the dynamic error of a full industrial robot manipulator, especially not in the 10 μm range as is needed for this work. As already mentioned, there are a few lumped parameter models that could later be tuned with real measurement data that can achieve a quite accurate prediction of the quasi-static error [8, 207], however, these tuned models also fail to give an accurate prediction of the dynamic error at the robot's TCP.

A Full Robot Manipulator Model

In order to show the capabilities of current modeling techniques, I want to showcase the work of my student ZIMMERMANN here, who developed a full robot manipulator model in cooperation with *ABB* in her master's thesis [312]. The results are also published in our paper [313].

ZIMMERMANN built two robot models of a six-axes *ABB* robot in Dymola:

- The *Flex-Model* uses data sheet parameters to estimate models for drivetrain components like the gear box and bearings. A LuGre friction model is identified for the gear box using measurement data available from *ABB*. The joint and link flexibilites are modeled using reduced FE models. The link substructures are first meshed in a FEM software and then reduced using the *Craig-Bampton* method[5]. The reduced models for the substructures are then imported into Dymola using the *Standard Input Data* (SID) format. Finally, the model is coupled to a real *ABB* robot controller using a software-in-the-loop approach.

[5] I will go into more detail about model order reduction techniques in the Fundamentel Theory section 3.2

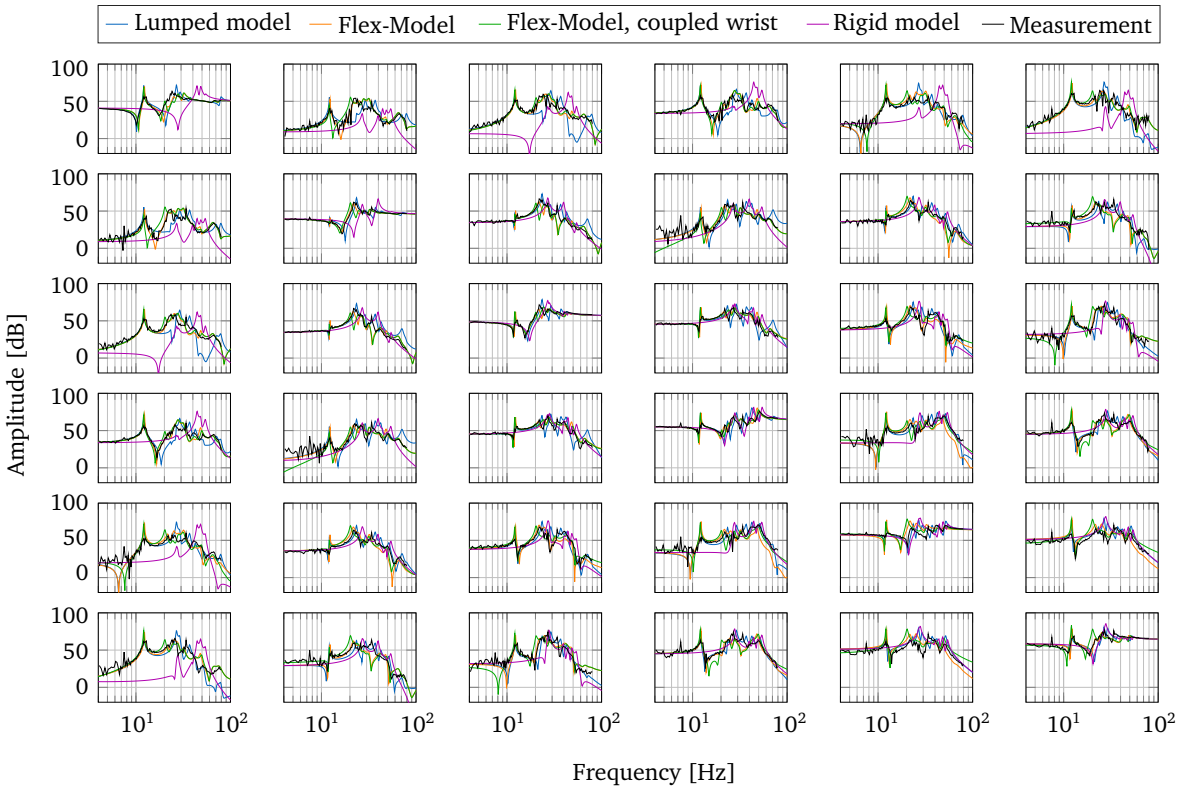

Figure 2.5: Matrix of FRFs from motor torque (columns) to motor acceleration (rows) for one robot pose. Adapted from our paper [313].

- The *Flex-Model, coupled wrist* is the same as the *Flex Model*, however, also considers the kinematic couplings of the final three joints of the robot.

The performance of these models is compared to the following data:

- The *Lumped-Model* is based on seven rigid bodies and flexible joints with three-dimensional pairs (see Fig. 2.4.b). The parameters are then tuned using measurement data from the real robot as described in [194, 290]. The main difference here is that the models developed by ZIMMERMANN are entirely based on manufacturer data sheets and CAD data, which is already available in early development stages. The Lumped-Model, however, can only reach a good predictive quality after it is tuned with real measurement data of the already existing robot.
- The *Rigid-Model* is based on the Flex-Model, but only uses the drivetrain models with rigid links, which is more similar to the common modeling approach for robot manipulators.
- Finally, the data is compared to real frequency and time domain measurement data taken on the real robot.

Fig. 2.5 shows the frequency response functions (FRF) from the motor torque to the motor axis acceleration. The measurements are organized in a matrix showing the FRFs of e.g. the input torque of the first joint with the output acceleration of the third joint axis in the first column and third row. An enlarged view of one measurement is shown in Fig. 2.6.

The Flex-Models predict the dynamic behavior very well across all of these transfer functions. This is remarkable, especially since these models are only based on data sheet and CAD data, without any additional model tuning. The tuned Lumped-Model also does a good

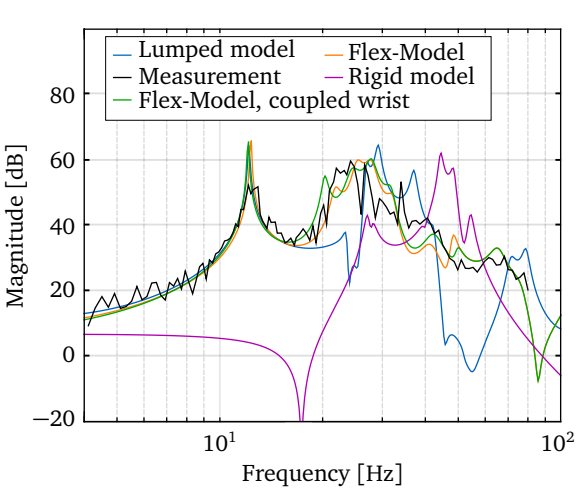

Figure 2.6: FRF from motor torque of axis 1 to acceleration of motor 3 for one robot pose. Adapted from our paper [313].

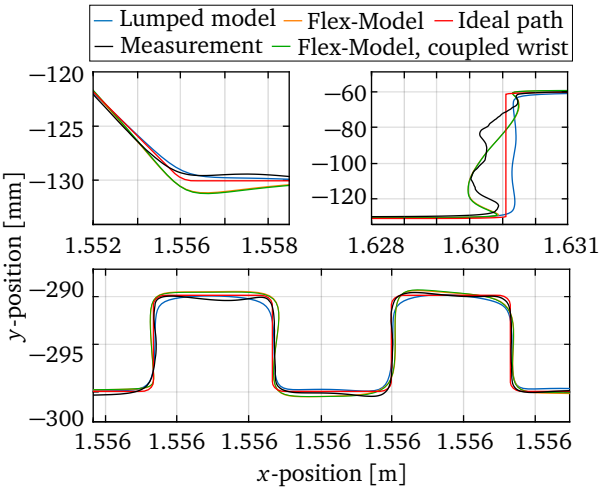

Figure 2.7: Three sections of the test trajectory to test the the different simulation approaches. Adapted from our paper [313].

job for the first mode of most FRFs, however, often fails to give an accurate prediction of the higher frequency behavior. The Rigid-Model almost always shows a significant mismatch between the model and the measurements. This again underlines the importance of including flexible links in the model to achieve a high fidelity dynamic model. Link flexibilites can be somewhat neglected, however, the model then needs to be tuned later with the real measurement data to lump the link flexibilities onto the joints as it was done here for the Lumped-Model.

Fig. 2.7 shows three sections of a test trajectory performed by the robot with a constant speed of 500 mm/s. The real TCP position is measured using a laser tracker. The Lumped- and Flex-Model perform roughly the same on average, however, depending on the specific trajectory sections one of the models will shortly perform significantly better, e.g. at the top right Fig. 2.7. The average model deviation over the entire test trajectory is 0.367 mm for the Flex-Model, which is again very impressive for an entirely un-tuned predictive model, however, still one order of magnitude worse than the 20 μm accuracy requirement for this work.

These results make it quite clear that even with very sophisticated modeling approaches, the current state of the art is not capable of making predictions for the real TCP path of a large robot manipulator in the 20 μm range. The main reason for this is that while we are able to achieve quite a good model fit for the overall dynamic behavior as can be seen in Fig. 2.5 and Fig. 2.6, we still have no good way of estimating the actual excitation sources of the real system. The main driving forces of the dynamic error are probably torque-ripple at the motors, grinding and stick-slip effects at the gears, as well as additional external excitation sources like running factory equipment. In order to achieve a perfect prediction of the actual TCP path, we not only need a high quality model of the pose depend system dynamics of the robot, but also a good estimation of all of these excitation sources, which are transferred through different paths of the system and finally add up to the total response at the TCP .

This currently makes it unfeasible to use models to predict the actual TCP position in high enough accuracy for this work, by just using measurement data available to the typical robot manipulator like the motor angles. However, an accurate models of the robot's structural dynamics could still be used for active vibration damping approaches that aim to dampen the system's dynamic response by reducing resonance peaks in the transfer path of

the control plant. I will present a few common control approaches for high-precision robotics applications in the following section.

2.1.3 Control Concepts for High Precision Robotics

Over the past decades, there has been a very large research effort to find suitable control strategies to precisely control the TCP of a flexible robot using its joint torques. The main challenge here is the non-collocated nature of the control problem that makes it quite difficult to achieve a stable closed-loop system [219], especially with high enough bandwidth to control multiple modes of the structural dynamics of the system to achieve a tracking performance in the 10 μm range. A lot of common control approaches are already well summarized in the books [248, 249] and overview papers [44, 89]. Most methods can be categorized as follows:

- Feedforward based approaches:
  These methods usually assume that the joint torque is an available control variable and will then try to use an inverse model of the link flexibilities of the system to predict the robots structural dynamics in order to steer the joint torques in a predictive way to reduce the tracking error at the robot's TCP.
- Methods using additional feedback:
  For these approaches, most authors still use the joint torques of the robot as the control input, however, they try to augment the control system with additional feedback sensors. These are usually either strain gauges or acceleration sensors attached to the links of the robot, or a measured distance between the robot's TCP and the process surface using e.g. laser sensors. While this will simplify the control problem, the inputs and outputs of the system are still non-collocated and also require high quality models to function. The applied approaches vary widely, from just passivity based approaches that try to introduce more damping into the system to full tracking controllers.
- Passivity based methods:
  Some methods just try to introduce more damping at the joint controllers to reduce the dynamic error by increasing the dissipation of energy in the system. These methods can work quite well without additional knowledge about the exact system behavior. However, they will not improve the overall tracking performance of the system, since the controllers can not influence the quasi-static error, which cause the robot's TCP to sag down due to gravity.

Most literature concentrates on simplified single link (e.g. [80, 141, 166, 177]) or two link systems (e.g. [22, 39, 147, 192]), which I will not discuss here because of their lack of practical relevance. In the following, I will shortly describe some approaches used by authors that at least tried to tackle a flexible multi-link problem for completeness' sake. However, since most of the proposed control methods share the same issues, when trying to apply them to the control system of a real robot manipulator, I will not go into too much detail here.

In [173], a controller for a model with joint and link flexibilities is designed by using non-linear feedforward and PID state feedback controllers. The controllers are designed by converting the manipulator dynamics into error driven system dynamic equations, which are then stabilized using the second method of Lyapunov. The controller shows good results, however, is only implemented on a numerical model.

The authors of [85] combine a closed-loop shaped-input filter with a conventional PD controller. The control approach is tested on an academic manipulator test rig with five DOFs,

however, with the main portion of the robot being a stiff parallel kinematic and only the final link being a large flexible beam. The controller is capable of significantly reducing the vibration amplitudes of the large flexible beam from 20 mm to 2 mm. However, it is questionable how much these results could be transferred to a more typical industrial robot manipulator that consists of more than just one artificially imposed flexible component. [228] developed a passive control design that uses a passive D part that directly acts on the measured joint angle instead of the error. The controller is tested on the same academic test bench as [85] and achieves a similar reduction of the vibrations, however, with quite bad tracking performance.

A computed torque control law for flexible manipulators is derived in [147] using generalized Newton-Euler models. The work is more focused on the efficiency of the implementation in Mathematica and does not show any performance results for the derived controller. [106] introduces a non-linear vibration feedback term into a traditional PD controller to control a flexible SCARA robot. The controller can perfectly control the simulation model, however, there are no experiments shown.

A purely feedforward computed torque based approach is shown in [25] using an analytical model for flexible beams. The results are also only tested in simulation on a simple flexible multi-link model. [128] also uses a computed torque approach based on the iterative inversion of a non-linear non-minimum phase model. Tests are also only performed on a simple simulation model.

The authors of [44] utilize a backwards integration scheme of the elastic dynamics along the desired joint trajectories. Additionally, a feedback controller is implemented that only requires measurable joint states. The method is shown to be stable on an academic test bench with two flexible links. However, the experiments still show quite large tracking errors of over 10 mm and settling times of over 15 seconds. The authors then propose an optimal trajectory planning algorithm to reduce jerk in the planned trajectory.

The authors of [232, 297, 304] derive mathematical flexible link models in order to compensate the TCP error with measured position feedback using a laser. The models and control methods are again only tested in simulation.

A neural network based adaptive controller to damp the vibration of a flexible multi-link system is developed in [135], resulting in a slight reduction of residual vibrations in their simulation model. [167] investigates an adaptive energy-based robust control scheme, which shows some improvement in their simulation model.

A model using non-linear generalization of the standard Euler-Bernoulli kinematics is shown in [43]. They then propose a feedforward approach using causal stable inversion over a bounded time domain of non-linear non-minimum phase systems. The method is again only tested numerically, showing good results.

A more robust approach is investigated in [308]. The authors enhance the standard PD joint controllers with another dissipative term to derive a control scheme that does not require exact model knowledge to function. However, the authors can not give any tuning guidelines for their control parameters and also only test their method in a simple simulation. A similar approach is used in [105]. [67] also investigates a passivity based approach using modal feedback vibration control on the joint level. The method is tested on an academic test bench resembling a large flexible double pendulum. The authors are capable of significantly reducing the vibrations caused by a step response. However, with the settling time still being over two seconds and without performing additional tracking experiments. In [271], it is shown that the over-estimation of natural frequencies can lead to an unstable closed-loop response when using a model based inversion controller. The authors also propose a robust control design based on the second method of Lyapunov. The control design is only tested on a simple numerical model.

[149] investigates the possibility of using additional piezo electric sensors and actuators

across the flexible links. Input/output linearization and adaptive feedback linearization is used to design a control scheme for a multi-link model where only one final link is flexible. The controller is capable of reducing vibrations in their simulation model by about 50 %.

While there is quite a large amount of publications available that try to solve the underlying control problem, almost none of these are even tested on academic test benches. There seems to be no published work available that managed to adapt the control system of a real industrial manipulator in a way to improve its dynamic error below the 20 μm range required for this work. The main reasons for this are probably:

- Most approaches assume that the joint torques are just readily available as the control input. The motor current, and therefore torque on the motor side, can indeed be measured. However, industrial robots usually utilize gear boxes with a quite large gear ratio of $N \geq 100$, which are also not perfectly stiff. As already mentioned in the previous subsection, this means that the torque on the motor side and joint side are not equal, because of the large effects of friction and compliance inside of the drivetrain of the robot joint. Consequentially, for torque-controlled robots there is an additional torque-controller needed that just tries to enforce the desired torque on the joint side. However, the bandwidth of these controllers is usually severely limited by sensor noise and modeling errors. E.g. the Franka Panda robot claims a bandwidth of 10 Hz, which would already be quite low in order to control multiple structural modes for effective vibration damping. I will go into more detail into the limitations of torque-controlled robots in section 4.3.2.

- Because of the non-collocated nature of the control problem, most proposed approaches require very precise models in order to be stable. I already elaborated on the large challenges to get a good dynamic model of a real industrial manipulator in the previous subsection: Because of the large amount of components, bolted connections and non-linear effects like friction, backlash and stick slip in the drivetrain, it is still quite unfeasible to acquire a good enough model of the entire global dynamic behavior of an industrial robot manipulator.

- As it is unfortunately still common practice in the control community, almost all proposed approaches are not tested while also considering effects like sensor noise, signal delay, actuator dynamics/limits and discrete controller clock rates. However, these kind of effects are very relevant for the performance, robustness and stability of a real mechatronic system and a newly developed control approach should always be tested with these in mind to give them more practical relevance[6].

Force controlled robots that use position controlled joints with a force/torque sensor at the robot's end effector to apply a desired contact force also have similar stability issues, when their structural dynamics are not considered in the control scheme, see e.g. [142, 159, 163, 169, 186, 295]. However, since this work is only concerned with high-accuracy path tracking for non-contact processes, I will not go into more detail here.

Collaborative Robots

Over the past two decades, a new class of collaborative robots has started to emerge. The main purpose of these types of robot manipulators is to be light weight, easy to handle and

[6] I am aware of the importance of doing fundamental research on simplified simulation models to keep the field moving and potentially discover new powerful control methods. However, this thesis is mainly concerned with the development of working mechatronic prototypes, which is why I am a bit harsh here on purely theoretical publications.

to safely operate in cooperation with human workers. These robots often utilize torque-controlled joints in order to enable them to sense any kind of unforeseen contact and operate safely in the proximity of human workers.

One of the early origins of torque-controlled robot is for example the German Aerospace Center of DLR [84]. The main challenge of building a collaborative robot is actually controlling the joint torque, which is a requirement for most methods described in the above section. In order to achieve this, most collaborative robots utilize a torque sensor on the joint side and a simple model for the drivetrain flexibilities [12, 260, 272]. When the joint torque is then available as a control variable, one common strategy is to use an impedance controller to enforce a desired stiffness and damping for the respective joints, or globally in the task space. This enables the control system to let the robot behave quite softly against external disturbances, which has advantages for the safe operation with humans and certain assembly tasks [182]. In order to still achieve an accurate tracking performance, an additional gravity compensation scheme is usually applied that uses a model of the robot's rigid body dynamics to compensate for the quasi-static gravity loads on the joints. A lot of incremental improvements to these types of control schemes can for example be found in [13–17], which also led to the development of commercial collaborative robots like the *Kuka* iiwa [161] or *Franka* Panda [98].

While these robots can achieve new applications in the field of collaborative robotics like human robot interaction and assembly tasks, they are still not suitable for high-precision path tracking yet. The main issue for torque-controlled robots is that they rely on an accurate model of the robot's rigid body dynamics for quasi-static accuracy. As I have already shown in the Fig. 1.2b in the introduction of this theses, the *Franka* Panda actually shows significantly worse tracking performance than the position controlled UR10, which is comparable in size, weight and cost. This is most likely because of the imperfect gravity compensation. However, this is mostly a tuning issue that might be improved using similar absolute calibration methods as mentioned in section 2.1.1. Torque-controlled robots should be also better suited for individual calibration, since their control system is inherently designed with a gravitation compensation. In contrast, traditional position-controlled robots are usually calibrated by modifying their DH parameters, which is not necessarily easy to do for most commercially available robot manipulators.

The second issue is the bandwidth of the joint torque-controller. While development of new and better torque-controlled robots continues to move forward, their control bandwidth is probably still not sufficient to apply most methods described in the above section.

One of newest torque controlled robots is the SARA IV by the German Aerospace Center. This robot uses improved hardware that enables it to incorporate direct position feedback from the joint side into the control system. This simplifies its control scheme, since a lot of previous methods needed to estimate the actual joint angle for their gravity compensation [18, 210]. The current control scheme of the robot is published in [134]. The authors show that they are able to significantly reduce the quasi-static and dynamic errors on the joint side position below 0.2 mrad using the additional joint side feedback. Unfortunately, measurements on the tracking performance at the TCP of the robot are not provided. However, assuming two *rigid* main links with 0.5 m lengths each, this would still result in a tracking error at the TCP of the robot in the range of 100 μm. The authors also show a validation measurement for their torque controller, which shows good tracking of the desired torque with some residual vibrations. However, the torque-controller is only verified up to a bandwidth of 0.3 Hz.

Micro / Macro Redundancy and Other Approaches

In the previous sections we have seen that the current state of the art is not capable of reaching a path tracking accuracy below 20 μm using the control system of an industrial robot manipulator. In this section, I want to briefly discuss other methods that are also somewhat similar to our completely external approach.

An idea that is closely related to this work, and has already been explored in the literature, is the utilization of micro/macro redundancy: A first set of actuated macro DOFs provide a large range of motion, but without the required accuracy. The second set of micro DOFs utilize smaller sized actuators, which only have to carry the robot's tool or payload and provide the required high precision over a larger bandwidth. In [58], the authors try to suppress unwanted vibrations of a large flexible manipulator through the inertial forces induced by the joint torques of a small robot arm located at the TCP of the large robot. The concept is further explored in [57] by using the small arm as a two DOFs vibration absorber with acceleration feedback. Similarly, the vibrations of the mounting base of a manipulator are compensated by acceleration feedback in [170]. In [246], a small reach manipulator is also used to damp the vibrations of a long reaching one. Simulation and experimental results of a similar approach are shown in [107].

The main difference to the external approaches investigated in this work is that these methods are implemented within the control structure of the robot system, while the following concept is supposed to work independently of the base robot. The project that produced most of the works cited above was only focused on very large manipulators with over 10 m reach for disaster sites. They were therefore more concerned with just keeping the oscillations at the TCP of the large robot in some manageable region, than high-precision tracking of a desired trajectory.

The most closely related work is probably [82], where the author developed a 6-DOF Lorentz actuator with gravity compensation for vibration isolation in in-line surface metrology. The actuator is supposed to stabilize a camera system carried by a robot to perform high precision measurements on nano-scale production lines of e.g. wafers or solar panel cells. However, only the gravity compensation is controlled actively, while the vibration isolation is implemented using a passive design. The actuator achieves up to 35 Hz bandwidth in 6 DOFs for its closed-loop tracking performance with a 2 kg payload. The controller achieves 5 μm tracking precision on a step response, however, only within a movement range of 100 μm. Unfortunately, the system is only tested on an isolated test bench and never used on a moving robot.

Conclusions

The literature research for this section made it quite clear that there is currently no robot manipulator system available that can achieve the accuracy requirements specific to this work. Since we are are convinced that there is no way to achieve the required path accuracy using the robot's own control system with the current state of the art, we decided to investigate external stabilization approaches in this thesis.

A similar concept to the micro/macro approach for robots are inertially stabilized platforms, which I will discuss in the coming section.

2.2 Inertially Stabilized Platforms

The concept of inertially stabilized platforms (ISP) is already well explored and has multiple applications, such as stabilizing the imaging sensor inside of a camera [69], precise pointing

of space telescopes [130] or inter-satellite laser communications [119]. While these devices mainly share the same goal of controlling the line of sight (LOS) of one object relative to another object or inertial space, the requirements and implementation for their specific application can be considerably different [86, 95, 187]. A comprehensive overview of the main concepts and challenges of building an ISP can be found in [126].

Image Stabilization Systems

The general idea of an ISP is to stabilize a mass against external disturbances. For example, the imaging sensor of a camera system has to be held as stable as possible to produce sharp images. In order to isolate the sensor against the natural hand shake of the human operator, a lot of camera manufacturers started to employ optical image stabilization- (OIS) and in body image stabilization (IBIS) systems over the past decade. An OIS system stabilizes a lens of the optical system [196, 256, 303], while an IBIS system stabilizes the sensor itself inside of the camera [212]. A typical IBIS system is shown in Fig. 2.8.a. The sensor is usually embedded on a stabilized platform, which is passively held in place by a set of springs (not depicted). The platform is then actuated by a set of Lorentz-actuators. Feedback is usually provided by a MEMS acceleration sensor placed on either the stabilized platform or in the camera body, or even by using the image data from the sensor itself. Unfortunately, since IBIS systems are part of the quite competitive commercial camera market, there is not much information available about the exact workings of the control systems. Control algorithms are usually a lot harder to reverse engineer than mechanical designs and are therefore well protected by the individual companies.

Typically, the performance of IBIS systems is specified by camera manufactures using 'stops of light', meaning the ability of the system to reduce disturbances at the camera sensor to allow for a lower shutter speed while still being able to produce a sharp image. The testing procedure is very specific to imaging systems and is described in the CIPA standard [71]. One of the most modern professional cameras is the *Sony* Alpha 1, which claims an improvement of 5.5 'stops of light' from their IBIS system [257]. Since one 'stop of light' is equal to one halving of the possible shutter speed. This could, somewhat naively, be equated to a reduction of vibrations of about 45-fold. For comparison, for this work we need a 50-fold improvement of the tracking performance of the UR10 robot.

Of course it is difficult to directly compare these two quite different applications. IBIS systems do not have to actually track a target and only have to decouple the vibrations from the sensor, while they can still allow a slow drift. The stabilized load is also significantly smaller and the typical disturbance frequencies produced by human hand shake is only around 5 Hz. A human operator also usually tries to stay as still as possible and is not moving while they are taking pictures. The testing procedure applied to camera systems is also quite hard to compare to the application investigated in this work.

There are significantly more scientific publications available that investigate the performance of digital image stabilization algorithms for video [203]. For example, [120] compares the performance of various digital image stabilization methods on a series of video tests. The most modern algorithm [154] is capable of reducing the average acceleration of feature points in the video by around a factor of 7. From experience, digital image stabilization algorithms, which can be applied in post processing, usually perform much better for video than the physically actuated IBIS systems in the camera. This is therefore probably a much more reasonable metric to evaluate the performance of modern camera stabilization systems. For comparison, the stabilization unit developed in this work is capable of reducing the average position tracking error of an UR10 robot by a factor of c.a. 140, while attenuating the average accelerations below 5 Hz by a factor of 100 and below 50 Hz by a factor of 20.

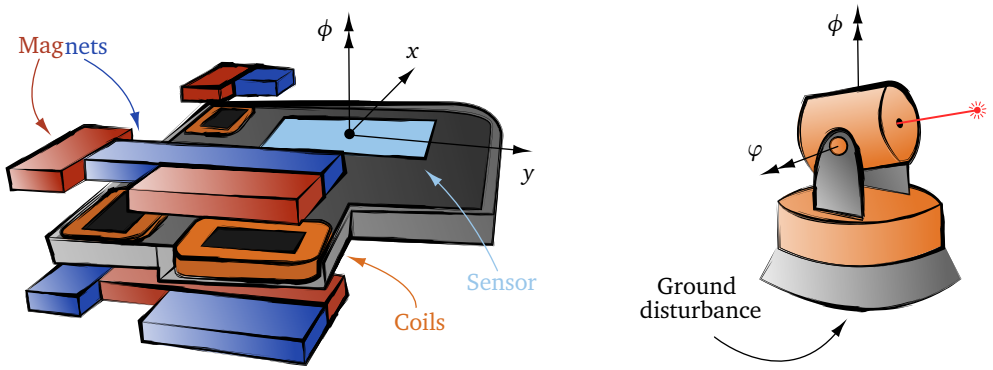

(a) 3 DOF stabilization system for camera sensors.

(b) 2 DOF laser pointing gimbal.

Figure 2.8: Examples for ISP systems.

While we drew quite a bit of inspiration from typical IBIS systems, the stabilization unit that we developed in this work for robot manipulators is capable of reducing vibrations by a significantly larger amount with higher bandwidth, while also being able to precisely track a desired trajectory in the 10 μm range with a higher payload. Additionally, our system also had to deal with the interaction between actuation forces and the structural dynamics of the robot and typical implementation challenges like sensor noise which get significantly more difficult to handle as the system becomes more precise.

Gimbal Systems

Another example for ISPs are gimbal systems, which are usually actuated by two to three rotary DOFs, Fig. 2.8.b. They are for example used for laser pointing devices or stabilization systems for cameras [185]. Gimbals are mostly actuated by BLDC or stepper motors and sometimes utilize gears if higher accuracy is needed. They are usually used to track or stabilize larger motions and can be quite effective in reducing the quasi-static error, however, are often less suited for high precision applications where high bandwidth control is needed [110].

In practice, most gimbals can be controlled using simple PID control strategies, depending on the application. In [171], a cascaded extended state observer is investigated for the precise control of a control moment gyroscope (GCO), which are commonly used in spacecraft for attitude control. Using a desired harmonic speed profile with an amplitude of 5 deg/s at 3 Hz, the system can achieve an angular speed error of 0.5 deg/s , which correspond to a 0.4 mrad angular position error. For comparison, a gimbal with the same performance mounted on a robot and assuming a distance of 10 cm to the process surface would result in a 40 μm tracking error at 3 Hz. The authors of [176] also investigate a GCO system and achieve a similar angular speed error of 0.6 deg/s at 3.8 Hz. This seems like a good enough performance to consider these systems also for this work. However, GCOs are generally not intended for pointing applications, which allows them to be build in a very compact way, which partially explains there good performance. It would therefore be quite challenging to transfer the typical GCO design to a pointing device, while still maintaining the same performance. The above mentioned systems are also only tested at relatively low bandwidth and at a very low speed of 5 deg/s. As of the time of writing, there seems to be no commercial gimbal system that would be suitable to our applications, since most systems are designed to stabilize comparatively large disturbances for camera systems and do not require high speed or μm precision.

As with IBIS systems, it is difficult to find accurate information about the exact control architecture and possible precision with these kinds of systems, since the majority of them are used in commercial or military applications. The French manufacturer of UAC payload systems *Merio* claims a precision of 150 μrad for their gyro-stabilized camera gimbal systems [280], with a usable bandwidth of $\sim$ 10 Hz for our specific requirements[7]. In 2016 the US Air Force published a Small Business Innovation Research (SIBR) project about a multi-axis precision seeker-laser pointing gimbal [281]. The claimed goal of this project is a precision of 100 μrad with no specified bandwidth. Using the same 10 cm distance, this new military grade gimbal system would result in a 10 μm tracking error.

One of the main reasons why the gimbal systems quoted above can be this precise is that they usually do not have to consider the dynamic interaction between the actuated gimbal and the system carrying the gimbal. For example, a laser pointing gimbal attached to a ship is negligibly lighter than its host system and does not have to worry about the reaction forces from its motions effecting the ship, if it is rigidly mounted. The same is true for gimbals that are carried by humans to stabilize camera footage. In this case, the gimbal is used to stabilize larger quasi-static disturbances caused by for example walking and the IBIS system of the camera to attenuate higher frequency jitter introduced by hand shake. On the other hand, a gimbal mounted to a UAV might by limited in its dynamics because of the effects of its own motion on the flight controller.

The Effects of Structural Dynamics on Gimbal Systems

Structural dynamics can also have a quite significant influence on the performance of gimbal systems. For example, the effect of bending of the gimbal structure itself is investigated in [190, 224]. In [79], a lead compensator is used to attenuate jitter by 20 dB up to 100 Hz. An interesting application is shown in [270], where the authors use GPS data to control the structural modes of a large academic gimbal structure using a LQR control scheme, with the closed-loop system achieving a precision of 0.1 rad. The control for the gimbal system inside of the Hubble telescope is investigated in [291]. A standard PID controller is extended with two dipoles to reject disturbances coming from two structural modes of the system. The controller is able to attenuate the the two resonance peaks by up to -40 dB and achieves an overall control bandwidth of 1.5 Hz.

Similar to the drivetrain flexibilities of robots, the torsional flexibilities of the servo motors can severely limit the performance of gimbal systems. Typically, the important transfer function is from the servo motor torque to the gyro feedback at the gimbal, which can experience an amplification of up to a factor of 15-25 at the resonance peaks, which usually limits the closed-loop bandwidth to 1/10 of the first resonance frequency [126]. The most common control approach to improve the performance of the system regarding torsional structural modes are notch filters. However, because of the additional phase lag introduced by these filters, the final closed-loop control bandwidth is often limited to 1/3 of the first resonance peak [175]. For example, a controller for a gimbal moving a panel for the Orbiting Solar Observatory-8 is investigated in [300], which employs a compensation filter to cancel structural modes of the system.

A third effect that will effect the performance of gimbal systems is flexibilities in the

[7] *Merio* does not specify the bandwidth of their gimbals. However, I got a confirmation from their engineering team that they achieved a closed-loop transfer function for one of their military projects that could be fitted with a second order system with $\omega_n = 122.23$ rad/s and $\zeta = 0.3$. This would result in a control bandwidth of about $\sim$ 30 Hz if the bandwidth is defined at -3 dB. Using the same 10 cm distance as before, we would need 200 μrad precision. Starting from 150 μrad precision, we can define the 'usable bandwidth' at the frequency at which the closed-loop transfer function has a larger error than 200 μrad, which would happen here at $\pm$2.5 dB magnitude or more than 30 deg phase delay, which both happens at about 10 Hz in the transfer function given to me by *Merio*.

mounting structure. Especially if relative feedback between the gimbal and the ground is needed, which is a similar situation to a the stabilization of a flexible robot that is investigated in this work. The most common approach here is to stiffen the mounting structure. Effective control methods again mostly include the employment of notch filters to attenuate resonance frequencies in the closed-loop transfer function [60, 118].

As we have seen in this subsection, the performance of gimbal systems can be severely limited by the structural dynamics of the gimbal itself or its mounting structure. Systems that have to deal with structural dynamics can still be quite precise, however, can often only operate with rather limited bandwidth. Some commercial systems like the gimbal systems available from *Merio* come close to our required specifications at first glance, however, these systems are probably tested on fixed rigid mounting structures.

Conclusions

As this short overview has shown, there is probably no commercial product available that we could just mount on our robot as an 'of-the-shelf' solution to meet our accuracy requirements. Especially, since the dynamic interaction between the pose dependent structural dynamics of a lightweight robot arm and a high-precision stabilization unit is a rather untouched field as of right now. The overview papers [126, 185] also recommend that every gimbal solution should be developed specifically for the desired application, since the requirements and possible approaches can vary widely. For these reasons, we decided to develop our own stabilization unit for our specific application.

2.3 Active Vibration Damping Approaches

The other approach we want to investigate in this work is the employment of active vibration damping techniques using additional proof-mass-actuators at the robots TCP. In this section, I will give a short overview of the field of active vibration control, with focus on the application and capabilities for real world systems. A more detailed overview about the theory of vibration control that is necessary for this work will be given in the Fundamental Theory chapter 3.3

Active vibration control has a very long history with already a lot of good books summarizing the most common control approaches [77, 219, 282]. Good overview papers are for example [20, 168, 190]. A typical active vibration damping problem is shown in Fig. 2.9. A flexible structure is excited by a disturbance force f_{dist}, causing the structure to react with high vibration amplitudes depending on its system dynamics. The general goal of active vibration control is to reduce any residual vibrations at one or multiple points of interest on the structure. In order to do this, one or multiple actuator forces f_{act} are applied to the structure following a control law. Feedback might also be provided by one or multiple sensors placed on the structure.

The most commonly used actuators to produce a control force on the structure are shakers, which are directly connected to the structure via a stinger and are usually actuated using a piezoelectric, elctrodynamic or hydraulic design. Another possibility are proof-mass-actuators, which create a control force using the inertia of a moving mass without needing to be attached to another structure. A less common approach is also to use actuators that are attached at two points of the same structure and can exert a force by contracting or extending themselves. Typical sensors for feedback are piezo accelerometers, MEMS, strain-gauges, or

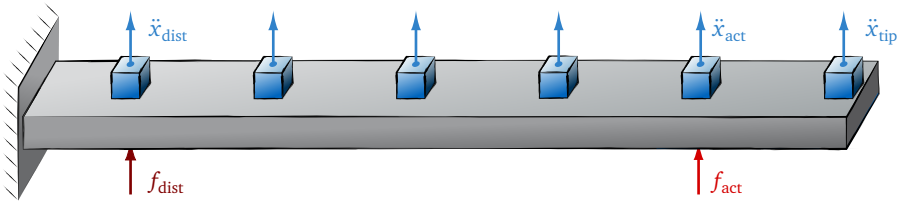

Figure 2.9: A flexible beam as a typical active vibration damping problem.

any kind of position sensors like lasers or eddy-current sensors [139].

The most common control approaches can be structured as follows:

- Classical active vibration damping feedback based approaches like *Positive Position Feedback* [114], *Direct Velocity Feedback* [219], lead compensators, or notch filters.
  These methods usually aim to reduce resonance peaks in the closed-loop transfer function and are therefore also only effective at those frequencies. Their big advantage, however, is their simplicity and guaranteed stability if sensors and actuators are collocated. They also do not require accurate models and are quite robust against spillover due to unmodeled system dynamics [93].

- Model based approaches with sensors feedback like *Pole Placement*, *Linear Quadratic Regulators*, H_∞ *Control*, or *Receptance Based Eigenstructure Assignment* [222].
  Modern control methods can seem quite powerful, since they are theoretically able to completely reshape the entire closed-loop transfer function and therefore the dynamic behavior of the controlled system. However, they require very accurate models and often even full state feedback to work properly. This makes them very sensitive to typical implementation problems like modeling errors, sensors noise, or time delay [219].

- Pure feedforward approaches like LMS or fxLMS based noise canceling methods [11].
  The basic idea of these methods is to produce a 180 degree phase shifted copy of the vibration signal at the point of interest to cancel out any disturbance. These methods can work quite well if the disturbance is stationary and does not change rapidly. They require no system models, however, are mostly effective against narrow-band disturbances. Unfortunately, these methods need a good measurement of the disturbance signal to function properly. This works quite well in for example noise canceling headphones, since the disturbing sound vibrations can be measured with a microphone outside of the headphones to produce a 180 degree phase shifted signal at the ears. However, the measurement of the underlying excitation signal of the system becomes much more difficult for mechanical systems like our robot manipulators that are mainly excited by a combination of torque ripple and gearbox stutter. These methods also often work very well at reducing the vibrations at the point of interest, however, might produce a large amplifications of vibrations at other points of the structure.

Active vibration damping has found a lot of use in any form of application that has to deal with harmful vibrations like the reduction of gearbox vibrations [27], vibration control in helicopters [155] and the suppression of vibrations in rotating machines [307]. Active vibration damping techniques are also often employed in civil engineering for structural control against earthquakes [1, 250], floor vibration control [241], or vibration control for telescopes [150].

Most relevant for this work are active vibration control applications in the field of high-precision machines and processes, which I will elaborate in a bit more detail in the following.

Active Vibration Control for High-Precision Applications

An H_∞ controller is designed in [306] for the active suspension of hard drive disks. The system dynamics are described by a simple model with two states, with the controller managing a reduction of the RMS of the residual motion at the hard drive of 42 %. Another H_∞ controller is used in [66] for the control of the pick up head of a disk drive, achieving an improvement of 43 % in tracking precision. For the same application, a sliding mode controller is designed in [293], reducing the tracking error by 50 %. All of these publications have in common that they only have to control the first dominant mode of the system and can use very simplified models to design their controllers. It is rather questionable if the same or better results could not also have been achieved with much simpler classical controllers.

In [201], a positioning system of a space borne interferometer mounted on a 10 m long flexible structure is described, which requires 10 nm precision. The system consists of three actuated stages: a stepper motor for low frequency, long travel reach (1 m); an intermediate voice-coil actuator for medium-frequency (< 10 Hz); and an actuated piezoelectric device (PZT) for high-bandwidth control ($10 - 1,000$ Hz). Classical control design methods were used to design the control-loops of the each subsystem using measured transfer functions of the control plants. All three stages managed to reduce the tracking error of the telescope by 98.6 % from 735 nm to 10.1 nm, which is a similar ratio of improvement needed for this work[8].

A 6-DOF vibration isolation platform is shown in [152]. The concept is similar to the stabilization unit developed in this work. The platform is held by four parallel springs and actuated by Lorentz actuators. In order to deal with the coupled dynamics of the 6 DOFs of the system, the authors used a modal PI controller with the control goal to set all modal accelerations to zero. The platform is tested for one DOF and achieves a vibration attenuation of up to -24 dB at the first 10 Hz resonance frequency of the system. The system is, however, not designed to also perform a tracking task.

In [136], a survey is performed for high-precision control of 2-DOF lightweight galvano scanners. Classical control strategies for these kinds of systems are shown for example in [26, 189]. The design of disturbance observers are investigated in e.g. [33, 151]. Feedforward approaches are for example discussed in [61, 205, 230]. However, the authors of [136] recommend to always use feedforward approaches in combination of feedback methods to compensate for modeling errors.

As an example for the performance of 2-DOF galvano scanners, I want to discuss the system shown in [136]: Two lightweight galvano mirrors are mounted on one BLDC motor each in order to reflect a laser beam on printed circuit boards. The authors use a linear matrix inequality (LMI)-based robust feedforward compensator design as the bases of the positioning system. In order to attenuate any residual vibrations, the control scheme is complemented with a feedback compensator consisting of a lead-lag phase filter and two notch filters. The system achieves a pointing accuracy of 5 μm on the circuit boards. The bandwidth of the system is not shown, however, the settling time of a step response is below 1 ms. Compared to the application investigated in this work, the overall challenge of designing 2-DOF galvano scanners is a bit simpler. For example, the two mirrors of the system can be actuated completely independently, meaning one does not have to worry about the coupled DOFs in the control system. The mirrors are also very lightweight and probably do not cause any dynamic interaction with the mounting structure, with the main dynamics visible in the control-loop probably coming from the structural dynamics of the actuated mirrors

[8] This is a nice example of using clever system design in combination with properly applied classical control methods to achieve very impressive results on a real system. The key for this application were the three different actuator stages, which are each suitable for a specific region of the desired control bandwidth. This is a similar approach that we tried with our first stabilization unit prototype, see Appendix C.

themselves. The system can also be mounted on a fixed rigid structure, instead of a moving, flexible robot manipulator. However, the accuracy that can be achieved with these systems is certainly impressive and we used some lessons learned from the above sources in the design of our stabilization unit, like ensuring a mechanical design with decoupled DOFs.

Even more accurate scanner systems are usually actuated using piezos and are for example discussed in [165, 294], however, at the cost of way lower actuation range. In both cases, a high-gain PD feedback controller is accommodated with notch-filters at the resonance peaks of the close-loop systems to achieve better system performance. Additionally, creep and hysteresis compensation schemes are employed. The system shown in [165] achieves a maximum error of 1 μm at 200 Hz scanning rate with a maximum motion range of 50 μm, which corresponds to a 2 % accuracy relative to the maximum motion range of the system. Unfortunately, piezo actuators were not suitable for our application because of their very limited possible range. For comparison, the stabilization unit developed in this work achieves 15 μm tracking precision on a moving robot with a maximum motion range of 5 mm, which corresponds to a relative accuracy of 0.3 %.

More similar to the topic of this thesis is the system shown in [245], which uses PZTs on an academic test bench with one flexible beam actuated by one joint. The PZTs are mounted on different positions across the beam and position feedback at the tip of the beam is measured using a laser diode mounted near the joint of the system. The authors use a Positive Position Feedback controller and achieve an attenuation of about −20 dB at the first two resonance frequencies of the system, which is tested using the step response of the joint.

Active Vibration Damping with Proof-Mass-Actuators

For our second external stabilization approach, we will use proof-mass-actuators (PMA) to change the closed-loop structural dynamics of the robot manipulator in order to damp undesired vibrations. This concept has of course already been explored in quite a bit of detail in the literature, however, mainly for stationary systems that do not change their dynamic properties over time.

In [83, 213], a small scale PMA is built using a voice coil and three spring rings. The actuator is used to damp the frequency response of a plate. The authors note that even the uncontrolled actuator already adds a significant amount of damping to this system by just acting like a passive spring-mass vibration absorber. A standard Velocity Feedback Controller adds another −10 dB of attenuation to the closed-loop system response over a broad frequency range of $1 - 1.000$ Hz.

Another standard PMA consisting of a voice-coil and two springs is used in [42] to actively damp a plate. The authors first modify the actuator dynamics of the PMA by using a position PID controller as an inner-loop. This is a similar approach as we used for this work, except that we completely removed the physical spring from the PMA to give us more flexibility in the actuator control design. The authors then use an outer-loop Velocity Feedback Controller to attenuate the plates structural dynamics. The system is capable of attenuating the first resonance peak by −20 dB, however, it worsens the frequency response below the first resonance peak by +15 dB, which might be undesirable depending on the application[9].

In [63], a PMA is used to damp the structural dynamics of an entire bridge. A single large PMA of typical design is placed in the middle of the bridge using a H_∞ controller to damp the first mode of the bridge. The controller achieves an attenuation of −20 dB at the first resonance peak, however, also worsens the frequency response of the bridge in the lower frequency region by up to +10 dB. The system is tested by measuring the decay of the impulse response of the bridge using people jumping as the excitation force, resulting in an increase

[9] This is a typical behavior of these type of controllers that I will explain in more detail in section 3.3.

of modal damping from 0.91 % to 3.53 %.

Another PMA is used in [132] to damp the vibrations of an academic test structure. The authors test a skyhook control scheme, a virtual passive absorber, virtual passive-active absorber and multi-mode virtual passive absorber. All control methods achieve a similar performance of −30 dB attenuation at the first resonance peak. In [30], a Positive Position Feedback controller is used to damp the structural resonances of an academic cantilever beam using two piezo shear actuators. The PPF controller is designed for the first four structural modes of the system and manage to damp all resonance peak by about −10 dB to −30 dB. A portable PMA is shown in [53] using an automatic tuning procedure for standard loop shaping control design. The device is tested on multiple pieces of factory equipment, achieving an attenuation of up to −40 dB.

Conclusions

PMA's seem to be a rather accepted approach to deal with vibration issues in various applications. They are mostly employed using classical control strategies like Positive Position Feedback or Direct Velocity Feedback. There are some applications that utilize modern control techniques, however, they are often still limited to only damp the first few modes and seldom achieve a complete reshaping of the closed-loop system dynamics on a real system. The reasons for this are probably that for modern control design, effects like actuator dynamics, sensor noise and signal delay are often still ignored. Especially for PMA's it is important to consider the dynamics of the actuator in the control design as shown in e.g. [42, 70]. Most applied approaches achieved an attenuation of −20 dB to −30 dB at the resonance frequencies of the controlled structures. However, most systems are not able to also effect broad band disturbances outside of the natural frequencies of the closed-loop system and often even slightly worsen the response near the resonance peaks.

I was not able to find any publications that applied PMA's to damp the structural dynamics of robot manipulators, or any other real system with time variant structural dynamics in general. Another difference from this work to most publications is that we used a PMA design without a mechanical spring, completely relying on the controller to design the desired actuator dynamics. The approach is similar to [42], however, the authors modified the actuator dynamics of a PMA that still used a mechanical spring.

Chapter 3

Fundamental Theory

In this chapter, I will go over the fundamental theory for the concepts applied in the following chapters. My assumption about the prior knowledge of the typical reader of this thesis is that they have a strong background in robotics topics like inverse kinematics and trajectory planning, however, a probably less strongly developed understanding of structural dynamics and active vibration damping.

For this reason, I will begin with a more comprehensive introduction to structural dynamics in section 3.1, starting with the basics of the mechanical single harmonic oscillator[1], followed by the dynamic description of multi-degree-of-freedom systems and modal analysis.

Section 3.2 will go into detail about flexible multibody simulations and model order reduction techniques. However, without going into too much detail, since we are going to mainly apply these concepts using Simulink/SimMechanics models and not do research about these specific methods themselves.

In section 3.3, I will give an overview of classical active vibration damping methods that will be applied throughout this thesis. Finally, section 3.4 will introduce typical joint control methods for position- and torque-controlled robot joints, which will be important to understand the possible dynamic interaction between the robot's control system and external stabilization devices.

3.1 Structural Dynamics

This section will introduce a selection of concepts from the field of structural dynamics, which are necessary for the understanding of this thesis. There is already a number of good books available that do a great job of summarizing the field from the view of a structural engineer [72, 76, 91]. In this section, I will try to also incorporate the view of a controls engineer, since both fields can be quite similar, however, are not perfectly unified. Another book that is following the same approach is [219], which I can also greatly recommend.

3.1.1 The Basics: Single Harmonic Oscillator

The mechanical single harmonic oscillator (MSHO) is the most simple dynamic structure we can design that is able to vibrate. Despite its simplicity, it is a great tool to analyze basic structural dynamics phenomena. Sometimes, it is even good enough as a simple approximation

[1] That might seem like an unnecessary low starting point for a theory chapter in a Ph.D. thesis. However, most problems that we will face in the following chapters can be broken down to the control of a single harmonic oscillator. For this reason, it is quite important to me that there is a strong understanding of the dynamics of these types of systems. The educated reader is of course invited to just skim through the first subsection.

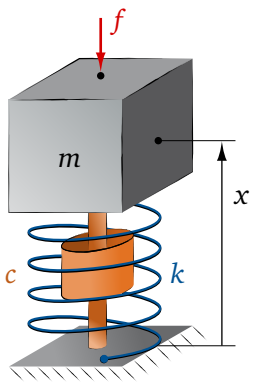

Figure 3.1: A mechanical spring-damper-mass system.

of the real system dynamics to design machines such as a Laval rotor or washing machines [68].

The MSHO consists of a mass m that is connected to a fixed point via a linear spring k and a viscous damper c, Fig. 3.1. By summing up the forces created by the spring and damper, as well as an external force f acting on the mass, we can use Newton's second law of motion to derive the ordinary differential equation (ODE) governing the dynamic behavior of the system:

$$m\ddot{x} + c\dot{x} + kx = f \ , \tag{3.1}$$

with x being the displacement of the mass relative to the point of equilibrium. Using the substitutions

$$\omega_0^2 = \frac{k}{m} \qquad \text{and} \qquad \zeta = \frac{c}{2m\omega_0} \ , \tag{3.2}$$

we can rearrange this equation to the more general form of a second order system:

$$\ddot{x} + 2\zeta\omega_0\dot{x} + \omega_0^2 x = \frac{1}{m}f \ , \tag{3.3}$$

with ω_0 being the undamped eigenfrequency[2] and ζ the damping ratio of the system. The general dynamic behavior of the MSHO is therefore equal to an electrical harmonic oscillator consisting of an inductance, capacitance and resistance, which can also be described as a second order system.

Solution in the Time Domain

We can analyze the dynamic behavior of the system by calculating its step response, which is the response of the system to a constant applied force f_c. We start by deriving the homogeneous solution of the system by plugging the ansatz function

$$x_h = \phi e^{\lambda t} \qquad \rightarrow \qquad \dot{x}_h = \lambda\phi e^{\lambda t} \qquad \rightarrow \qquad \ddot{x}_h = \lambda^2\phi e^{\lambda t} \tag{3.4}$$

[2]Note that ω_0 is the angular undamped eigenfrequency in radians with the unit $[\omega_0] = 1/s$. It relates to the undamped eigenfrequncy f_n with the unit $[f_n] = \text{Hz}$ with the equation $\omega_0 = 2\pi f_n$. For simplicity, I will just call both "frequency" in the following, assuming that the reader knows the difference.

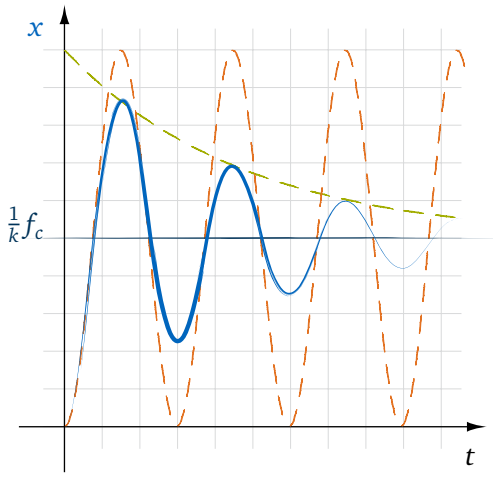

Figure 3.2: Step response (blue) to a constant force f_c with the oscillating (orange) and damping (green) part of the solution.

into the ODE (3.3) while setting the input force f_c to zero which gives:

$$\left(\lambda^2 + 2\zeta\omega_0\lambda + \omega_0^2\right)\ \phi e^{\lambda t} = 0\,, \tag{3.5}$$

with ϕ being a yet unknown constant and λ the eigenvalue of the system. We can calculate the eigenvalues of the system by computing the roots of the above characteristic polynomial:

$$\begin{aligned}\lambda_{1/2} &= -\zeta j\omega_0 \pm \omega_0\sqrt{\zeta^2 - 1} \\ &= -\zeta\omega_0 \pm j\omega_0\sqrt{1-\zeta^2}\end{aligned} \tag{3.6}$$

We therefore get an eigenvalue pair, which is complex for damping ratios between $-1 < \zeta < 1$.

The harmonic solution describes the inherent eigendynamics of the system. In order to get the total solution for our step response, we also have to derive the response of the system to the particular input force f_c, which is called the particular solution x_p. We can calculate this by using the Method of Undetermined Coefficents, which assumes an ansatz function for the particular solution x_p that is from the same type as the input function. In this case, we have a constant input force. Consequently, we also assume the particular solution to be constant:

$$x_p = \text{const.} \tag{3.7}$$

Plugging this into the ODE (3.3) with the constant input force yields:

$$\begin{aligned}\omega_0^2 x_p &= \frac{1}{m} f_c \\ \rightarrow \quad x_p &= \frac{1}{k} f_c\end{aligned} \tag{3.8}$$

Finally, we can derive the total solution for the step response by superimposing all fundamental solutions of the harmonic solution x_h and the particular solution x_p:

$$\begin{aligned}x &= x_h + x_p \\ &= \phi_1 e^{(-\zeta\omega_0 + j\omega_0\sqrt{1-\zeta^2})t} \ + \ \phi_2 e^{(-\zeta\omega_0 - j\omega_0\sqrt{1-\zeta^2})t} \ + \ \frac{f_c}{k}\end{aligned} \tag{3.9}$$

In order to determine ϕ_1 and ϕ_2 we can evaluate the above equation for the two boundary conditions

$$x(0) = 0 \qquad \text{and} \qquad \dot{x}(0) = 0\,, \tag{3.10}$$

which yields for the constants

$$\phi_1 = \frac{f_c}{k} \cdot \frac{-\zeta - j\sqrt{1-\zeta^2}}{2j\sqrt{1-\zeta^2}} \qquad \text{and} \qquad \phi_2 = -\frac{f_c}{k} \cdot \frac{-\zeta + j\sqrt{1-\zeta^2}}{2j\sqrt{1-\zeta^2}}\,. \tag{3.11}$$

Plugging these into the total solution (3.9) and then slightly rearranging it we finally get:

$$x = \frac{f_c}{k}\left(\frac{-\zeta - j\sqrt{1-\zeta^2}}{2j\sqrt{1-\zeta^2}} e^{j\omega_0\sqrt{1-\zeta^2}t} - \frac{-\zeta + j\sqrt{1-\zeta^2}}{2j\sqrt{1-\zeta^2}} e^{-j\omega_0\sqrt{1-\zeta^2}t}\right) \cdot e^{-\zeta\omega_0 t} + \frac{f_c}{k} \tag{3.12}$$

The resulting step response is plotted in blue in Fig. 3.2. There are three parts to this solution:

- The large portion between the brackets includes two exponential functions with complex conjugate arguments for damping ratios between $-1 < \zeta < 1$. This can be interpreted as two complex pointers rotating in opposite directions. The summation of both results in a cancellation of their imaginary parts and a purely real oscillation.
  We can prove this mathematically by rearranging (3.12) using Euler's formula

  $$e^{jx} = \cos(x) + j\sin(x) \tag{3.13}$$

  which after some additional mathematical operations results in

  $$x = -\frac{f_c}{k}\left(\frac{\zeta}{\sqrt{1-\zeta^2}} \sin(\omega_0\sqrt{1-\zeta^2}t) + \cos(\omega_0\sqrt{1-\zeta^2}t)\right) \cdot e^{-\zeta\omega_0 t} + \frac{f_c}{k}\,. \tag{3.14}$$

  The resulting motion of the part between the brackets is therefore a single harmonic oscillation with the frequency $\omega_d = \omega_0\sqrt{1-\zeta^2}$, which is also called the damped eigenfrequency of the system[3]. It becomes apparent from equation (3.14) that increasing the damping ratio in the interval $0 < \zeta < 1$ not only decreases the vibration frequenecy of the step response ω_d, but also causes a phase shift. However, this only really becomes noticeable for higher damping ratios $\zeta \to 1$. The oscillating part of the solution is marked in orange in Fig. 3.2.

- The oscillating part of the solution is then multiplied by another exponential function with a purely real argument. For positive damping ratios $\zeta > 0$, this exponential function causes the oscillating part of the solution to ring down with the decay constant $\delta = \zeta\omega_0$. This represents the damping portion of the response, which is caused by the dissipation of energy by the viscous damper. The damping part of the solution is marked in green in Fig. 3.2.

- While the first two parts represent the harmonic part of the solution that will always ring down after a certain amount of time depending on the damping ratio ζ, the last part of the solution represents the particular solution that is imposed on the system by the external force. In this case, the steady state solution that is left over after the harmonic part has rung down is just a static deflection, which is caused by the spring being displaced by the applied constant force f_c. The steady state solution is marked in dark blue in Fig. 3.2.

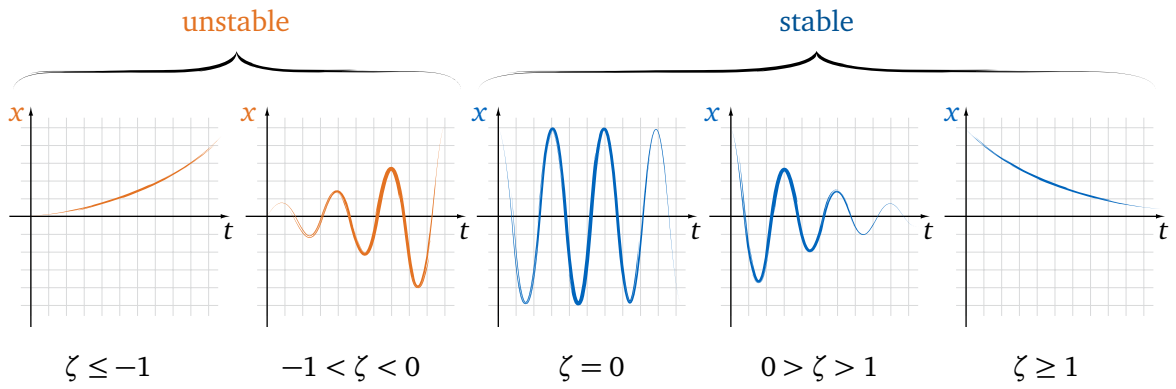

Figure 3.3: Step response of a MSHO for different damping ratios ζ.

The step response is therefore a very good way to test a system. In this case, we can fully parameterize a MSHO by just applying a known constant force f_c to the system. We can get the damped eigenfrequency ω_d by looking at the oscillation frequency of the response and the damping ratio ζ by identifying the decay constant δ from the peaks ringing down. We can get the stiffness k of the system by measuring the steady state solution, after the harmonic oscillation has died down, and the mass m and viscous damping coefficient c using equations (3.2).

While the step response shown in Fig. 3.2 is the most common one for real oscillating systems, there are also different types of responses possible depending on the damping ratio ζ, which are shown in Fig. 3.3:

- For no damping $\zeta = 0$, the system oscillates forever and never rings down. This can be seen in equation (3.12) by the argument of the exponential function causing the damping to become zero.
- For damping ratios between $0 > \zeta > 1$ we get the already discussed behavior.
- A damping ratio larger then $\zeta \geq 1$ causes the system to be over-damped and suppresses all vibrations. This can bee seen in equation (3.12) by the arguments of the exponential functions between the brackets becoming real, meaning the solution does not oscillate anymore.
- Negative damping ratios generally show the same behavior regarding oscillations, however, the system is unstable. A negative damping ratio can be interpreted as instead of dissipating energy from the system, we continuously pump more energy into the system. This can also be seen in equation (3.12) by the argument of the exponential function causing the damping to become positive, and therefore exponentially increasing the envelope of the solution instead of ringing it down.

All of these properties are already included in the eigenvalues (3.6) of the system, which fully characterize its dynamics. The real part of the eigenvalue pair is equal to the argument of the exponential function causing the damping in (3.12), while the imaginary part is equal to the argument of the two exponential functions between the brackets governing the oscillation behavior.

A good way to analyze the dynamics of a system is therefore to plot its eigenvalue pairs in the complex plane, Fig. 3.4. The real part gives information about the amount of damping

[3] Equation (3.12) can also be rearranged into a single cosine function with a phase delay. However, in order to calculate the phase delay the inverse of the tangent function is needed, which is why I prefer the version with the separated sine and cosine as shown here.

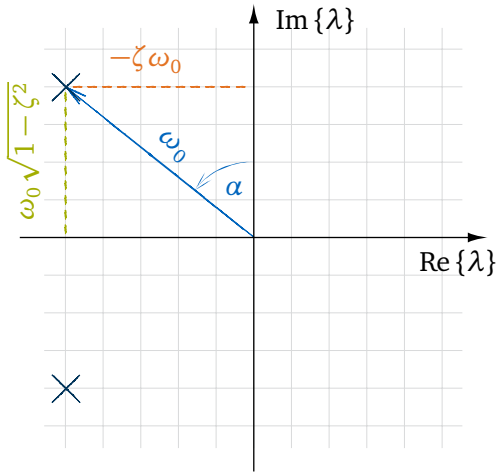

Figure 3.4: Complex eigenvalue pair with the real (orange) and imaginary part (green) highlighted.

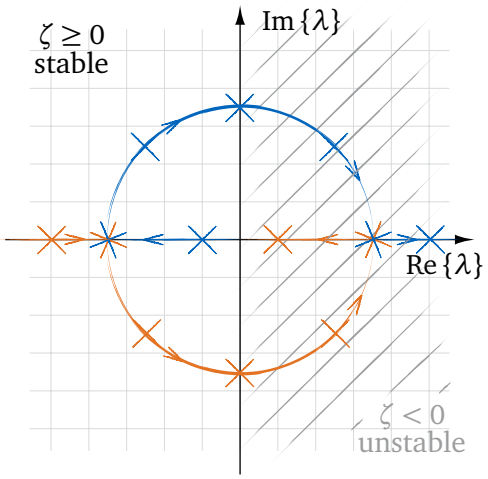

Figure 3.5: Movement of the eigenvalue pairs λ_1 (blue) and λ_2 (orange) when decreasing the damping ratio from $\zeta > 1$ to $\zeta < -1$.

in the system, as well as stability, making all systems with positive eigenvalues unstable. The imaginary part is equal to the damped eigenfrequency ω_d, giving information about the oscillating behavior of the system, where systems with purely real eigenvalue pairs are overdamped. The movement of the eigenvalue pairs depending on the damping ratio ζ is shown in Fig. 3.5.

Two other important properties of the eigenvalues in the complex plane are that the length of the corresponding complex pointer is equal to the undamped eigenfrequency for $\zeta \leq |1|$:

$$|\lambda|_2 = \sqrt{(-\zeta\omega_0)^2 + \left(\omega_0\sqrt{1-\zeta^2}\right)^2} = \omega_0 \,, \tag{3.15}$$

and that systems with the same damping ratio ζ always have the same angle between the imaginary axis and their corresponding complex pointer:

$$\sin(\alpha) = \frac{-\zeta\omega_0}{\omega_0} = -\zeta \,. \tag{3.16}$$

Solution in the Frequency Domain

Instead of analyzing a system in the time domain by measuring its response to test inputs like the step or impulse function, we can also characterize its dynamics by looking at the steady state response of the system to any harmonic excitation

$$f(t) = F(s)e^{st} \,, \tag{3.17}$$

with s being the Laplace variable $s = \sigma + j\omega$ and $F(s)$ the excitation amplitude at the frequency ω. For the subjects discussed in this thesis, the damping portion σ of the Laplace variable is not needed and we can set

$$s \mathrel{\hat{=}} j\omega \tag{3.18}$$

for the remainder of this thesis[4].

[4]This basically makes the Laplace transform equal to the Fourier transform and is a little sloppy use of the Laplace variable s. However, as long as we are only interested in the steady state response it is fine to replace

Since we are interested in the steady state solution, we only need the particular solution that according to the Method of Undetermined Coefficients again has to be of the same type as the input:

$$x(t) = X(s)e^{st} \ . \tag{3.19}$$

Plugging input and output into the ODE (3.3) of the MSHO yields:

$$\underbrace{\left(ms^2 + cs + k\right)}_{G_Z(s)} X(s) = F(s) \tag{3.20}$$

The transfer function between the brackets is called the impedance $G_z(s)$ of the system. In the case of displacements as the output quantity, it is also called the dynamics stiffness. It can be used to calculate the specific harmonic input $F(s)$ needed to cause the harmonic output $X(s)$:

$$G_Z(s) = \frac{F(s)}{X(s)} = ms^2 + cs + k \qquad \text{(dynamic stiffness)} \tag{3.21}$$

A more intuitive transfer function to describe the system behavior can be found by solving for the output in (3.20):

$$X(s) = \underbrace{\frac{1}{ms^2 + cs + k}}_{G_Y(s)} F(s) \tag{3.22}$$

The quotient that relates the harmonic input force $F(s)$ to the harmonic output $X(s)$ is called the admittance $G_Y(s)$ and is the inverse of the impedance $G_Z(s)$. In the case of displacements as the output, it can also be called the receptance:

$$G_Y(s) = \frac{X(s)}{F(s)} = \frac{1}{ms^2 + cs + k} = G_Z^{-1}(s) \qquad \text{(receptance)} \tag{3.23}$$

This is often also just called 'the transfer function of the system', since it can be used to calculate output of the system to any harmonic input.

We can again transform the transfer function $G_Y(s)$ of the MSHO into a more general form of a second order system by using the same substitutions as in (3.2):

$$G_Y(s) = \frac{\frac{1}{m}}{s^2 + 2\zeta\omega_0 s + \omega_0^2} \tag{3.24}$$

Note that the roots of the numerator of $G_Y(s)$ are equal to the eigenvalues (3.6) of the system, which are also called the poles of the transfer function.

The receptance $G_Y(s)$ of the MSHO is plotted in Fig. 3.6 for different damping ratios ζ. For low excitation frequencies $\omega \ll \omega_0$ we can ignore the dynamics of the system, since the system approximately behaves like a spring in static equilibrium with a displacing force at every point in time:

$$X(\omega \ll \omega_0) \approx \frac{1}{k} F(\omega \ll \omega_0) \tag{3.25}$$

$s \to j\omega$. This seems to be common practice in control theory literature, without really being specifically mentioned a lot. Structural dynamics and signal analysis literature more often uses $j\omega$ of the Fourier transform. For sake of consistency and not having to switch around between the two when switching topics, I will stick to s with $s = j\omega$ in this thesis.

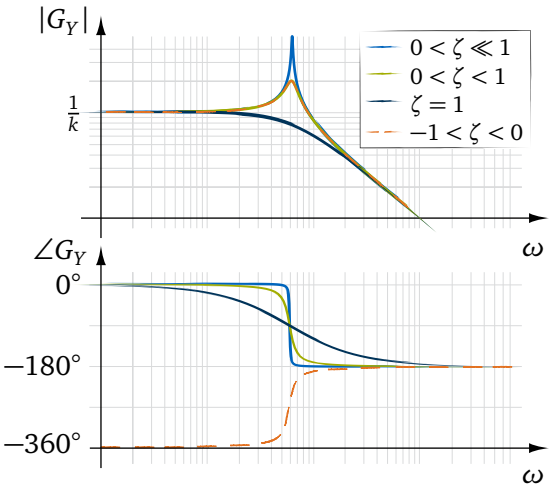

Figure 3.6: The receptance $G_Y(s)$ of the MSHO with different damping ratios ζ.

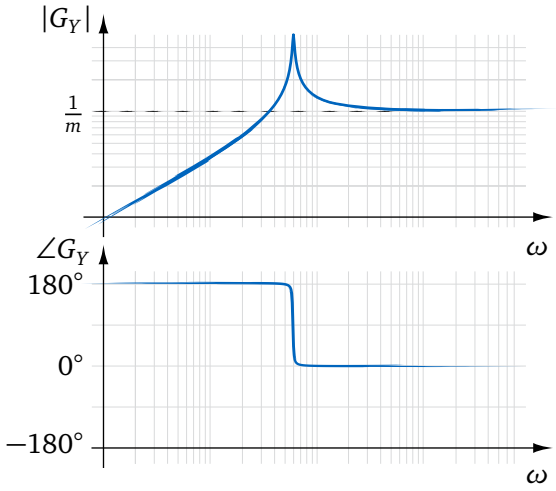

Figure 3.7: The accelerance $G_A(s)$ of the MSHO.

Remark
This is a similar assumption as when we assume rigid bodies for the analysis of the dynamics of robot manipulators. It is important to realise that *there is no such thing as a rigid mechanical structure*.

Every structure will start to behave like a flexible body as soon as the excitation frequencies approach the eigenfrequencies of the structure. The structural dynamics of mechanical components inside the control loop can be safely ignored as long as the bandwidth of the controller is much lower than the first eigenfrequency of the mechanical structures.

As soon as we need high control bandwidth for high-performance systems that either need to be very quick or very precise, we either have to be careful that the mechanical structures are still stiff enough to ignore their dynamics, or we have to consider their strucutral dynamics in the control design.

Increasing the input frequency initially causes a phase delay, depending on the damping ratio ζ, and then a large amplification of the output around the damped resonance frequency ω_d. The response reaches exactly 90° phase delay at the undamped eigenfrequency ω_0 and then approaches 180° phase delay for higher frequencies, while the amplitude response approaches zero. This is caused by the system being dominated by its inertia for higher frequencies $\omega \gg \omega_0$:

$$X(\omega \gg \omega_0) \approx \frac{1}{ms^2} F(\omega \gg \omega_0) \,. \tag{3.26}$$

The damping ratio ζ influences the height of the resonance peak and also moves the peak slightly to lower frequencies for higher damping ratios. A high damping ratio might be beneficial because of the lower amplitude response at the resonance. However, it also causes the phase delay to affect lower frequencies, which might be unacceptable if we want to design a high bandwidth system that follows the input as exactly as possible. Unstable systems with negative damping ratios can easily be spotted by the phase delay decreasing over the resonance frequency.

For this work, we will often design controllers using acceleration feedback. The admittance for the acceleration response is called the accelerance $G_A(s)$ and can be obtained by differentiating the receptance $G_Y(s)$ twice:

Response quantity	Impedance		Admittance	
Displacement	Dynamic stiffness	$G_Z = F/X$	Receptance	$G_Y = X/F$
Velocity	(mechanical) Impedance	F/Xs	Mobility	Xs/F
Acceleration	Apparent mass	F/Xs^2	Accelerance	$G_A = Xs^2/F$

Table 3.1: Common denotations in literature for impedance and admittance transfer functions, adapted from [238].

$$G_A(s) = G_Y(s)s^2 = \frac{X(s)s^2}{F(s)} = \frac{\frac{1}{m}s^2}{s^2 + 2\zeta\omega_0 s + \omega_0^2} \qquad \text{(accelerance)} \tag{3.27}$$

An overview for common denotations for impedance and admittance transfer functions is shown in Tab. 3.1. The accelerance $G_A(s)$ for the MSHO is plotted in Fig. 3.7. For low excitation frequencies we start off with zero amplitude and positive 180° phase shift. After the resonance, the system is again dominated by its mass and follows the input force with 0° phase delay. This is a nice property, since we can make the MSHO perfectly follow a desired acceleration for frequencies $\omega \gg \omega_0$, only requiring knowledge of the mass m. We will partly use this in the following chapters for the control design of the voice coil actuator.

3.1.2 Multi Degree of Freedom Systems

We can create a multi degree of freedom (MDOF) system by just stacking multiple MSHOs on top of each other. Fig. 3.8 shows an MDOF system with three MSHOs. We can model this system by applying Newton's second law of motion to each mass separately, resulting in a system of three coupled ODEs:

$$\begin{aligned} &\underbrace{\begin{bmatrix} m_1 & 0 & 0 \\ 0 & m_2 & 0 \\ 0 & 0 & m_3 \end{bmatrix}}_{\boldsymbol{M}} \underbrace{\begin{bmatrix} \ddot{x}_1 \\ \ddot{x}_2 \\ \ddot{x}_3 \end{bmatrix}}_{\ddot{\boldsymbol{x}}} + \underbrace{\begin{bmatrix} c_1 + c_2 & -c_2 & 0 \\ -c_2 & c_2 + c_3 & -c_3 \\ 0 & -c_3 & c_3 \end{bmatrix}}_{\boldsymbol{C}} \underbrace{\begin{bmatrix} \dot{x}_1 \\ \dot{x}_2 \\ \dot{x}_3 \end{bmatrix}}_{\dot{\boldsymbol{x}}} \\ &+ \underbrace{\begin{bmatrix} k_1 + k_2 & -k_2 & 0 \\ -k_2 & k_2 + k_3 & -k_3 \\ 0 & -k_3 & k_3 \end{bmatrix}}_{\boldsymbol{K}} \underbrace{\begin{bmatrix} x_1 \\ x_2 \\ x_3 \end{bmatrix}}_{\boldsymbol{x}} = \underbrace{\begin{bmatrix} f_1 \\ f_2 \\ f_3 \end{bmatrix}}_{\boldsymbol{f}}, \end{aligned} \tag{3.28}$$

with $\boldsymbol{M}$ being the mass matrix, $\boldsymbol{C}$ the damping matrix, $\boldsymbol{K}$ the stiffness matrix, $\boldsymbol{x}$ the vector of the respective positions of the masses and $\boldsymbol{f}$ the vector of the input forces acting on each mass. The resulting system of coupled ODEs has generally the same structure as the ODE of the MSHO (3.1):

$$\boldsymbol{M}\ddot{\boldsymbol{x}} + \boldsymbol{C}\dot{\boldsymbol{x}} + \boldsymbol{K}\boldsymbol{x} = \boldsymbol{f} \ . \tag{3.29}$$

We can analyze this system by generating the transfer functions resulting from a single input force at the third mass f_3 to the displacements at the three masses $\boldsymbol{x} = [x_1 \ , \ x_2 \ , \ x_3]^T$. One way to do this is by first computing the dynamic stiffness matrix $\boldsymbol{G}_Z(s)$ using (3.21) for each frequency of interest and then inverting each of these dynamic stiffness matrices to get the receptance matrix $\boldsymbol{G}_Y(s)$ at each frequency, Alg. 1. However, this will only generate the data points to plot the transfer functions, without a full mathematical relation between the inputs and outputs. It is still a useful algorithm to keep in mind when working with data points acquired from measured transfer functions instead of parameterized models.

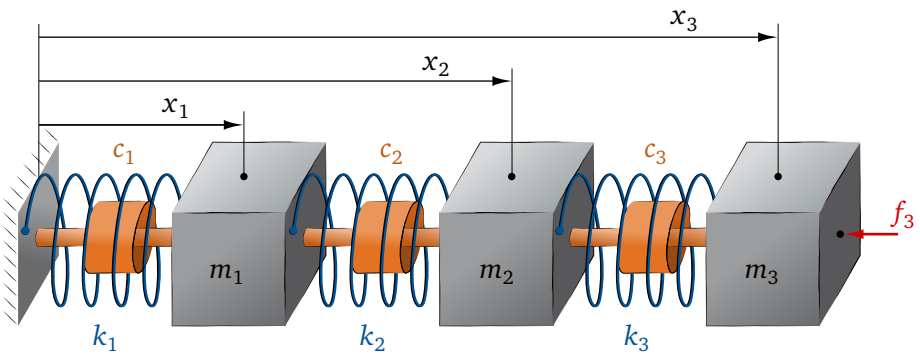

Figure 3.8: Three MSHO stacked on top of each other to create a 3 DOF mechanical oscillator.

Algorithm 1 Calculate $\boldsymbol{G}_Y(s)$

$\omega = [\text{frequencies of interest}]$

for $i \leq$ number of frequencies **do**
$\boldsymbol{G}_Z(:,:,i) = -\omega(i)^2\boldsymbol{M} + j\omega(i)\boldsymbol{C} + \boldsymbol{K}$
$\boldsymbol{G}_Y(:,:,i) = \boldsymbol{G}_Z(:,:,i)^{-1}$
end for

A way to generate the transfer functions as parameterized mathematical functions from a $\boldsymbol{MCK}$ model (3.29) is by first transforming it into a state space model:

$$\begin{aligned} \dot{\boldsymbol{x}}_s &= \boldsymbol{A}_s\boldsymbol{x}_s + \boldsymbol{B}_s\boldsymbol{u}_s \\ \boldsymbol{y}_s &= \boldsymbol{C}_s\boldsymbol{x}_s + \boldsymbol{C}_s\boldsymbol{u}_s \end{aligned} \tag{3.30}$$

with

$$\begin{aligned} \underbrace{\begin{bmatrix}\dot{\boldsymbol{x}}\\ \ddot{\boldsymbol{x}}\end{bmatrix}}_{\dot{\boldsymbol{x}}_s} &= \underbrace{\begin{bmatrix}\boldsymbol{0} & \boldsymbol{I}\\ -\boldsymbol{M}^{-1}\boldsymbol{K} & -\boldsymbol{M}^{-1}\boldsymbol{C}\end{bmatrix}}_{\boldsymbol{A}_s}\underbrace{\begin{bmatrix}\boldsymbol{x}\\ \dot{\boldsymbol{x}}\end{bmatrix}}_{\boldsymbol{x}_s} + \underbrace{\begin{bmatrix}\boldsymbol{0}\\ \boldsymbol{M}^{-1}\end{bmatrix}}_{\boldsymbol{B}_s}\underbrace{[\boldsymbol{f}]}_{\boldsymbol{u}_s} \\ \underbrace{[\boldsymbol{x}]}_{\boldsymbol{y}_s} &= \underbrace{[\boldsymbol{I}\quad \boldsymbol{0}]}_{\boldsymbol{C}_s}\underbrace{\begin{bmatrix}\boldsymbol{x}\\ \dot{\boldsymbol{x}}\end{bmatrix}}_{\boldsymbol{x}_s} + \underbrace{[\boldsymbol{0}]}_{\boldsymbol{C}_s}\underbrace{[\boldsymbol{f}]}_{\boldsymbol{u}_s} \end{aligned} \tag{3.31}$$

and $\boldsymbol{x}_s = [x_1\ ,\ x_2\ ,\ x_3\ ,\ \dot{x}_1\ ,\ \dot{x}_2\ ,\ \dot{x}_3]$ being the states, $\boldsymbol{u}_s$ the inputs, $\boldsymbol{A}_s$ the system matrix, $\boldsymbol{B}_s$ the input matrix, $\boldsymbol{C}_s$ the output matrix and $\boldsymbol{C}_s$ the feedthrough matrix of the system.

We can then transform the state space model (3.30) into the frequency domain:

$$\begin{aligned} \boldsymbol{x}_s(s)\,s &= \boldsymbol{A}_s\boldsymbol{x}_s(s) + \boldsymbol{B}_s\boldsymbol{u}_s(s) \\ \boldsymbol{y}_s(s) &= \boldsymbol{C}_s\boldsymbol{x}_s(s) + \boldsymbol{C}_s\boldsymbol{u}_s(s) \end{aligned} \tag{3.32}$$

with $\boldsymbol{x}_s(s)$ being the vector containing the Laplace transforms of the states $\boldsymbol{x}_s(s) = [X_{s1}(s)\ ,\ \ldots,\ X_{s6}(s)]^T$, $\boldsymbol{y}_s(s)$ the vector containing the Laplace transforms of the outputs which in this case are the displacements of the three masses $\boldsymbol{y}_s(s) = [X_1(s)\ ,\ X_2(s),\ X_3(s)]^T$ and $\boldsymbol{u}_s(s)$ the vector containing the Laplace transforms of the inputs which are the forces acting on the masses $\boldsymbol{u}_s(s) = [F_1(s)\ ,\ F_2(s),\ F_3(s)]^T$. Rearranging the first line of (3.32) to

$$(\boldsymbol{I}s - \boldsymbol{A}_s)\,\boldsymbol{x}_s(s) = \boldsymbol{B}_s\boldsymbol{u}_s(s) \tag{3.33}$$

and multiplying with $(\boldsymbol{I}s-\boldsymbol{A}_s)^{-1}$ from the left hand side yields:

$$\boldsymbol{x}_s(s) = (\boldsymbol{I}s-\boldsymbol{A}_s)^{-1}\boldsymbol{B}_s\boldsymbol{u}_s(s)\ . \tag{3.34}$$

Finally, we can insert the above equation into the second equation of (3.32):

$$\boldsymbol{y}_s(s) = \underbrace{\left[(\boldsymbol{I}s-\boldsymbol{A}_s)^{-1}\boldsymbol{B}_s+\boldsymbol{C}_s\right]}_{\boldsymbol{G}_Y(s)}\boldsymbol{u}_s(s)\ , \tag{3.35}$$

which gives us the receptance matrix $\boldsymbol{G}_Z(s)$ which relates all harmonic inputs $\boldsymbol{u}_s(s)$ to all outputs $\boldsymbol{y}_s(s)$:

$$\boldsymbol{G}_Y(s) = (\boldsymbol{I}s-\boldsymbol{A}_s)^{-1}\boldsymbol{B}_s+\boldsymbol{C}_s\ , \qquad \text{(receptance matrix)} \tag{3.36}$$

Each entry $\boldsymbol{G}_{Y,i,j}(s)$ of the receptance matrix is a linear transfer function of the form:

$$\boldsymbol{G}_{Y,i,j}(s) = \frac{b_{0,i,j}s^n\ +\ b_{1,i,j}s^{n-1}\ +\cdots+\ b_{n-1,i,j}s\ +\ b_{n,i,j}}{a_0s^m\ +\ b_1s^{m-1}\ +\cdots+\ a_{m-1}s\ +\ a_m}\ , \qquad \text{(general form)} \tag{3.37}$$

with b / a being the coefficients of the polynomials of the numerator / denominator respectively, and n / m being the order of these polynomials.

Note that the denominator of all entries of $\boldsymbol{G}_{Y,i,j}(s)$ is always the same, because it is determined by the characteristic equation $(\boldsymbol{I}s-\boldsymbol{A}_s)^{-1}$. The only difference between the transfer functions of a multi-input-multi-output (MIMO) system is therefore their numerator.

We can calculate the roots of the numerator and denominator of the general transfer function (3.37) and rearrange it to

$$\boldsymbol{G}_{Y,i,j}(s) = K_{zp}\frac{(s-z_{1,i,j})(s-z_{2,i,j})\dots(s-z_{n,i,j})}{(s-p_1)(s-p_2)\dots(s-p_m)}\ , \qquad \text{(zero-pole form)} \tag{3.38}$$

with p being the roots of the denominator which are equal to the poles (and eigenvalues) of the system, z being the roots of the numerator which are also called the zeros of the system, and K_{zp} being a gain factor.

Using f_3 as our only input, we are only interested in the third column of the receptance matrix $\boldsymbol{G}_{Y,1-3,3}(s)$. The resulting transfer functions of the 3DOF harmonic oscillator are plotted in Fig. 3.9a - 3.9c for a generic set of m_i, c_i, k_i parameters of equation (3.28). As with the MSHO, we can identify each stable pole by a resonance peak with a 180° negative phase shift. The frequency at half of the 180° gives us the undamped eigenfrequency $\omega_{0,i}$ of this particular pole, while the broadness of the peak gives us information of the damping associated with this pole. The zeros of the transfer function show up as anti-resonances with a positive 180° shift. We can associate a frequency $\omega_{z,i}$ and damping ratio $\zeta_{z,i}$ to each zero the same way we have already done with the poles.

The only difference between the three shown transfer functions are the total gain and placement of the zeros. Of note is the transfer function $\boldsymbol{G}_{Y,3,3}(s)$, which describes the dynamic behavior between an input force and output measurement at the same DOF. In Experimental Dynamics this transfer function is often called the driving point measurement. A special property of these transfer functions is that their poles and zeros always alternate, causing their phase to always stay between 0° and −180°. As we will see later, this property simplifies a lot of control problems by placing our feedback sensor (output) and actuator (input) in the same collocated manner.

The general trend of the receptance transfer functions is also similar to that of the MSHO: The amplitude starts of at a static gain and then begins to role off following a trend proportional to $\sim 1/\omega^2$. This general trend will continue to 'drag down" all resonance peaks caused

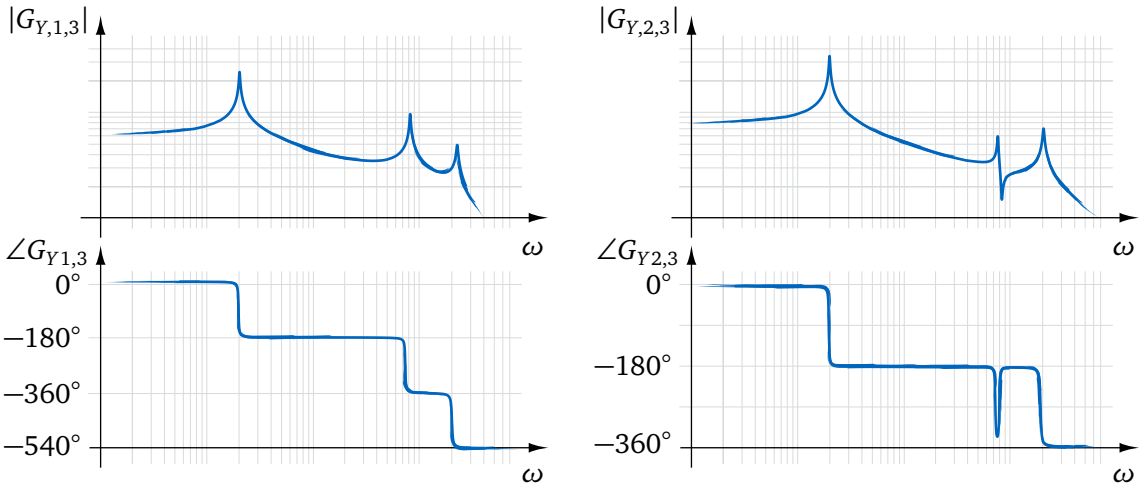

(a) $G_{Y,1,3}(s)$ receptance transfer function.

(b) $G_{Y,2,3}(s)$ receptance transfer function.

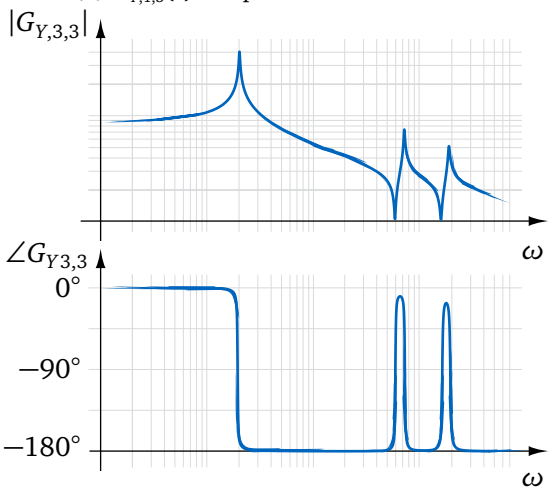

(c) $G_{Y,3,3}(s)$ receptance transfer function.

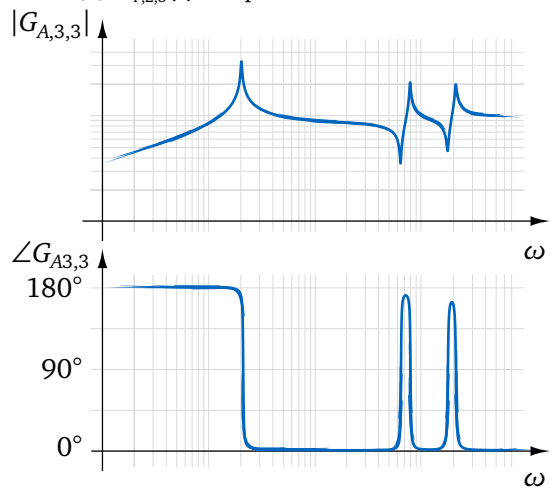

(d) $G_{A,3,3}(s)$ accelerance transfer function.

Figure 3.9: A selection of receptance and accelerance matrix entries of a generically parameterized 3DOF mechanical oscillator.

by higher eigenfrequencies. Similarly, the acclerance transfer functions (Fig. 3.9d) also follow the same trend as the MSHO: The amplitude starts of at zero and then stays on the same level after the first resonance peak. This can easily cause all following resonance peaks to stay within the same order of magnitude as the first one, even for real mechanical systems.

Remark
This already has some important consequences for the goal of this thesis:

- Since we want to improve the accuracy of robot manipulators by reducing their mechanical vibrations, it is important, and probably sufficient, to focus on the control of the first few structural modes of the system. The contribution of higher frequency modes scale down proportional to $\sim 1/\omega^2$ and often do not contribute much to the overall dynamic displacement error at the robots TCP.
  This may of course still vary slightly depending on the real mechanical structure and the excitation source causing the disturbance. However, for robot manipulators, the main disturbance sources are torque-ripple and high jerk caused by their own motion. Both of these disturbance sources excite the mechanical structure across a broad frequency range.

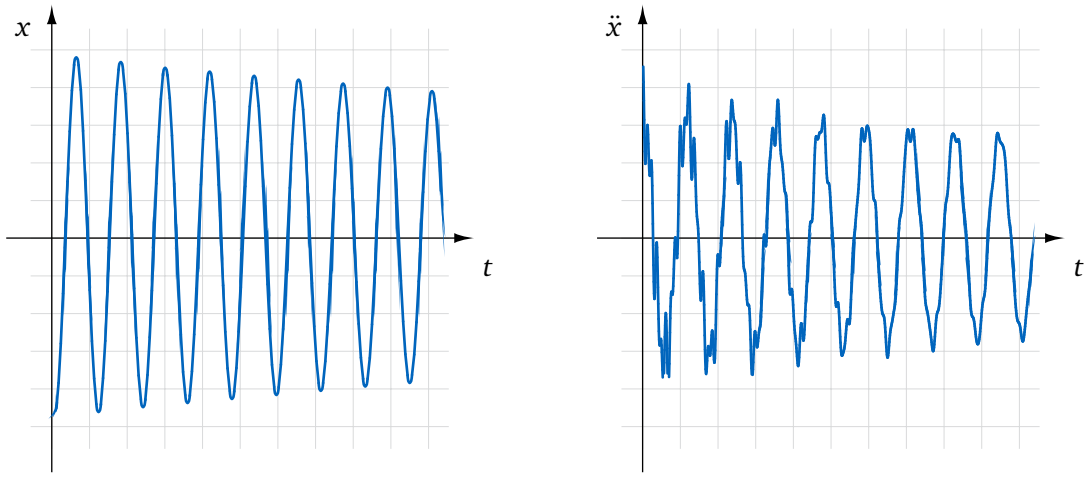

(a) Step response of $G_{Y,3,3}(s)$.

(b) Step response of $G_{A,3,3}(s)$.

Figure 3.10: Step response of the 3DOF mechanical oscillator with displacements or accelerations as the output.

Factory equipment running at fixed rotational speeds or other external disturbance sources that excite specific high frequencies might still cause vibration problems at the TCP of the robot when they are close to higher eigenfrequencies of the system. This unfortunately has to be investigated on a case by case bases to decide if specific higher frequency modes need to be considered in the control system.
However, from my personal experience when investigating different types of robot manipulators, it has always been enough to focus on the first few modes to already achieve a considerable accuracy improvement.

- This also simplifies our control problem a bit, since we only have to consider the dynamics of the first few modes in our controller. In practice, there is the problem of control- and observer spillover which might cause the control system to become unstable, because of unmodeled system dynamics interacting with the controller. However, this problem becomes way more manageable when using position feedback, since the contribution of higher frequency modes to the measured displacement feedback scales down so quickly. So even when we are not considering higher frequency dynamics, which in theory might cause problems for our control system, their contribution often quickly falls below the noise and resolution limit of the position sensors, making them essentially unobservable for the control system.

- However, for the external active vibration damping approach we want to use acceleration feedback. Here, we are not so lucky, since the higher frequency modes are usually well visible within the spectrum of the acceleration senors and are therefore always present in the control loop. This caused quite a lot of trouble to keep the control system stable, since in practice we can not accurately model the entire system dynamics. This will be discussed in more detail in section 5.1.5.

The difference between using a position or acceleration based output can be made more clear by computing the corresponding impulse response, which are plotted in Fig. 3.10 for the same set of generic parameters as before. The impulse response with displacements as output is completely dominated by the first mode of the system (Fig. 3.10a), while the signal clearly shows higher modes contributing to the overall response when using accelerations as an output (Fig. 3.10b).

3.1.3 Modal Analysis

To gain even further insight into the dynamics of mechanical structures, we can use a well established tool called Modal Analysis. We begin by again trying to solve the eigenvalue problem for a MDOF system described by a $\boldsymbol{MCK}$ model (3.29). For now, we ignore the damping matrix $\boldsymbol{C}$ and want to analyze a dynamic system described by the system of ODEs:

$$\boldsymbol{M}\ddot{\boldsymbol{q}} + \boldsymbol{K}\boldsymbol{q} = \boldsymbol{f} \ . \tag{3.39}$$

with $\boldsymbol{q}$ being a generalized vector containing all DOFs of the system (for the 3DOF mechanical oscillator $\boldsymbol{q} = [x_1 \ , \ x_2 \ , \ x_3]^T$).

The ansatz function to solve the system is again

$$\boldsymbol{q} = \boldsymbol{\phi} e^{\lambda t} \tag{3.40}$$

with $\boldsymbol{\phi}$ being a vector containing one constant for each DOF, which we will call the eigenvector from now on. Plugging the ansatz function above in the system of ODE's (3.39) and looking for the homogeneous solution results in the eigenvalue problem

$$\left(\lambda_i^2 \boldsymbol{M} + \boldsymbol{K}\right)\boldsymbol{\phi}_i = \boldsymbol{0} \ , \qquad \text{with} \quad i = 1, \ \ldots, n \tag{3.41}$$

and n being the number of DOFs. Solving this eigenvalue problem yields n complex conjugated eigenvalue pairs $\lambda_i = \pm j\omega_{0,i}$ that are associated with one eigenvector $\boldsymbol{\phi}_i$ each. Similarly to before, we can reconstruct the total solution by superimposing all eigensolutions:

$$\boldsymbol{q} = \boldsymbol{\phi}_1\eta_1 + \boldsymbol{\phi}_2\eta_2 + \cdots + \boldsymbol{\phi}_n\eta_n \tag{3.42}$$

$$= \sum_{n}^{i=1} \boldsymbol{\phi}_i \eta_i \tag{3.43}$$

with $\boldsymbol{\Phi} = [\boldsymbol{\phi}_1, \ \boldsymbol{\phi}_2, \ldots, \ \boldsymbol{\phi}_n]$ being the modal matrix including all eigenvectors and η_i being the modal coordinates. We can write the above equation in short as

$$\boldsymbol{q} = \boldsymbol{\Phi}\boldsymbol{\eta} \qquad \text{(modal transformation)} \tag{3.44}$$

which is a spacial transformation from the modal domain defined by the modal coordinates $\boldsymbol{\eta}$ into our original spacial domain defined by the initial set of DOFs in $\boldsymbol{q}$.

We can use this transformation to decouple the system of ODEs (3.29), by plugging in (3.44) and multiplying with $\boldsymbol{\Phi}^T$ from the left-hand side:

$$\underbrace{\boldsymbol{\Phi}^T\boldsymbol{M}\boldsymbol{\Phi}}_{\boldsymbol{M}_M}\ \ddot{\boldsymbol{\eta}} \ + \ \underbrace{\boldsymbol{\Phi}^T\boldsymbol{C}\boldsymbol{\Phi}}_{\boldsymbol{C}_M}\ \dot{\boldsymbol{\eta}} \ + \ \underbrace{\boldsymbol{\Phi}^T\boldsymbol{K}\boldsymbol{\Phi}}_{\boldsymbol{K}_M}\ \boldsymbol{\eta} = \boldsymbol{\Phi}^T\boldsymbol{f} \tag{3.45}$$

This can be further simplified by using the modal mass matrix $\boldsymbol{M}_M$, modal damping matrix $\boldsymbol{C}_M$ and modal stiffness matrix $\boldsymbol{K}_M$:

$$\boldsymbol{M}_M = \boldsymbol{\Phi}^T\boldsymbol{M}\boldsymbol{\Phi} = \operatorname{diag}\left\{\boldsymbol{M}_{M,i,i}\right\} \tag{3.46}$$

$$\boldsymbol{C}_M = \boldsymbol{\Phi}^T\boldsymbol{C}\boldsymbol{\Phi} = \operatorname{diag}\left\{\boldsymbol{C}_{M,i,i}\right\} \tag{3.47}$$

$$\boldsymbol{K}_M = \boldsymbol{\Phi}^T\boldsymbol{K}\boldsymbol{\Phi} = \operatorname{diag}\left\{\boldsymbol{K}_{M,i,i}\right\} \tag{3.48}$$

which are all diagonal matrices[5]. This means that we transformed our system of coupled ODE's (3.29) into a system of decoupled ODE's (3.45) where each line can be solved independently.

[5] A word on the validity of using the eigenvectors derived from a system without damping to transform a $\boldsymbol{MCK}$ system with damping follows later.

Note that this transformation depends on the eigenvectors $\boldsymbol{\phi}_i$, which can be scaled arbitrarily. A common way to deal with this is to scale the eigenvectors $\boldsymbol{\phi}_i$ such that the modal mass matrix $\boldsymbol{M}_M$ is equal to the identity matrix $\boldsymbol{I}$:

$$\boldsymbol{M}_M = \boldsymbol{\Phi}^T \boldsymbol{M} \boldsymbol{\Phi} = \boldsymbol{I} \tag{3.49}$$

$$\boldsymbol{C}_M = \boldsymbol{\Phi}^T \boldsymbol{C} \boldsymbol{\Phi} = \operatorname{diag}\left\{2\zeta_i \omega_{0,i}\right\} \tag{3.50}$$

$$\boldsymbol{K}_M = \boldsymbol{\Phi}^T \boldsymbol{K} \boldsymbol{\Phi} = \operatorname{diag}\left\{\omega_{0,i}^2\right\} \tag{3.51}$$

Transforming the system using these so called mass normalized eigenvectors causes each line of (3.45) to become

$$\ddot{\eta}_i + 2\zeta_i \omega_{0,i} \dot{\eta}_i + \omega_{0,i}^2 \eta_i = \boldsymbol{\phi}_i^T \boldsymbol{f} \ , \tag{3.52}$$

which is the same as the ODE of the MSHO (3.3). This means that the dynamics of any complex structure, that can be modeled using a linear $\boldsymbol{MCK}$ model, can be described by a superposition of MSHOs. Each MSHO is thereby associated with one eigenfrequency $\omega_{0,i}$, damping ratio ζ_i and eigenvector $\boldsymbol{\phi}_i$ of the system, and are often just called the *modes* of the system. Calculating the response of any $\boldsymbol{MCK}$ system to any dynamic load $\boldsymbol{f}$ can therefore easily be done by first transforming the model into modal coordinates using (3.45), then calculating the response η_i of each mode using (3.52)[6] and then calculating the response of the system in our coordinate system of interest using (3.44). This is often much more efficient than calculating the response just using the initial $\boldsymbol{MCK}$ model, since the diagonalized model (3.45) can be solved quite quickly.

A Word on Damping

Above, we used the eigenvectors of an undamped $\boldsymbol{MK}$ system to transform an $\boldsymbol{MCK}$ system with damping. This is valid as long as the resulting modal damping matrix $\boldsymbol{C}_M$ is still diagonal. Systems for which this is possible are called *triple diagonalizable*, meaning that one can neglect the damping coupling between the modes at first order. This is true for systems with small damping and when the eigenfrequencies are well separated [108]. Their eigenvectors are independent of the amount of damping $\boldsymbol{C}$ and are always equal to the eigenvectors of the undamped $\boldsymbol{MK}$ system [64].

When generating a $\boldsymbol{MCK}$ system numerically using for example a FE method, we can usually generate the $\boldsymbol{M}$ and $\boldsymbol{K}$ matrices quite accurately. The accurate modeling of damping, however, is still a matter of research and quite involved. In practice, there are two common ways to model damping that still ensure that the resulting system is triple diagonalizable:

1. Designing the damping matrix $\boldsymbol{C}$ as a linear combination of the mass $\boldsymbol{M}$ and stiffness matrix $\boldsymbol{K}$:

   $$\boldsymbol{C} = \alpha \boldsymbol{M} + \beta \boldsymbol{K} \qquad (\textit{Rayleigh damping}) \tag{3.53}$$

   results in a diagonalizable damping matrix and is called *Rayleigh damping* [223]. α and β are thereby weighting coefficients. Giving more weight to the mass matrix increases the damping for lower frequency modes, while giving more weight to the stiffness matrix will increase the damping of higher frequency modes.

[6] Note that the initial dynamic load is distributed to each MSHO/mode using the right-hand side term $\boldsymbol{\phi}_i^T \boldsymbol{f}$. Depending on how the load $\boldsymbol{f}$ is acting on the system, there might be cases where the vector $\boldsymbol{f}$ is orthogonal to one or more eigenvectors $\boldsymbol{\phi}_i$. This results in $\boldsymbol{\phi}_i^T \boldsymbol{f} = 0$, meaning that this specific mode does not get excited by this load case. This ties into the concept of controllability and will be discussed together with mode shapes in the following.

2. Directly designing the modal damping matrix $\boldsymbol{C}_M$ by first getting the $\boldsymbol{MK}$ matrices from the FE model, calculating the eigenvectors $\boldsymbol{\phi}_i$, setting the damping ratios ζ_i of each mode to a desired value and then transforming the desired modal damping matrix $\boldsymbol{C}_M$ back to the desired damping matrix $\boldsymbol{C}$:

$$\boldsymbol{C} = \boldsymbol{\Phi}\ \mathrm{diag}\left\{2\zeta_i\omega_{0,i}\right\}\boldsymbol{\Phi}^T \tag{3.54}$$

This approach has the advantage of being able to specifically set the damping ratio of each mode.

There are also more possible ways to model damping, like *Caughey damping* [72] or a lot of non-linear approaches. However, for this work we will always operate within the linear realm when applying Modal Analysis using the methods described above.

When measuring real systems using Experimental Modal Analysis, the above assumption of triple diagonalizable systems is often still good enough. As we will see later, even for a quite complex and highly damped structure like our walking robot LOLA, we still achieved quite good results by just applying these linear methods.

Deriving the Receptance Matrix Using Modal Parameters

In section 3.1.2, we already derived the receptance matrix $\boldsymbol{G}_Y(s)$ in a more general way by starting from the state space form. We can derive a physically more interpretable version of it by transforming the diagonalized system (3.52) into the frequency domain:

$$H(s)_i s^2 + 2\zeta_i\omega_{0,i}H(s)_i s + \omega_{0,i}^2 H(s)a_i = \boldsymbol{\phi}_i^T \boldsymbol{f}(s)\ , \qquad \text{with} \quad i = 1,\ \ldots, n \tag{3.55}$$

$H(s)_i$ being the Laplace transform of η_i, and the vector $\boldsymbol{f}(s)$ containing the Laplace transforms of each force input $\boldsymbol{f}(s) = [F(s)_1,\ F(s)_2\ ,\ldots,\ F(s)_n]$. Writing the resulting n equations in matrix form and solving for $\boldsymbol{\eta}_i(s)$ gets us:

$$\boldsymbol{\eta}(s) = \mathrm{diag}\left\{\frac{1}{s^2 + 2\zeta_i\omega_{0,i}s + \omega_{0,i}^2}\right\}\boldsymbol{\Phi}^T\boldsymbol{f}(s)\ , \tag{3.56}$$

with the vector $\boldsymbol{\eta}(s) = [H(s)_1,\ H(s)_2\ ,\ldots,\ H(s)_n]$ containing the Laplace transforms of η_i. Transforming this equation back into our original coordinates using the modal transformation (3.44) yields

$$\boldsymbol{q}(s) = \underbrace{\boldsymbol{\Phi}\ \mathrm{diag}\left\{\frac{1}{s^2 + 2\zeta_i\omega_{0,i}s + \omega_{0,i}^2}\right\}\boldsymbol{\Phi}^T}_{\boldsymbol{G}_Y(s)}\boldsymbol{f}(s)\ , \tag{3.57}$$

which gets us the receptance matrix:

$$\boldsymbol{G}_Y(s) = \boldsymbol{\Phi}\ \mathrm{diag}\left\{\frac{1}{s^2 + 2\zeta_i\omega_{0,i}s + \omega_{0,i}^2}\right\}\boldsymbol{\Phi}^T\ . \tag{3.58}$$

We can also compute every entry of the recaptance matrix $\boldsymbol{G}_{Y,i,j}(s)$ by using the sum

$$\boldsymbol{G}_{Y,i,j}(s) = \sum_{k=1}^{n}\frac{\boldsymbol{\Phi}_{i,k}\boldsymbol{\Phi}_{j,k}}{s^2 + 2\zeta_k\omega_{0,k}s + \omega_{0,k}^2}\ . \tag{3.59}$$

While equation (3.37) is a bit more general formulation of the receptance matrix that basically works for any kind of linear system, the above equation is based on the knowledge that

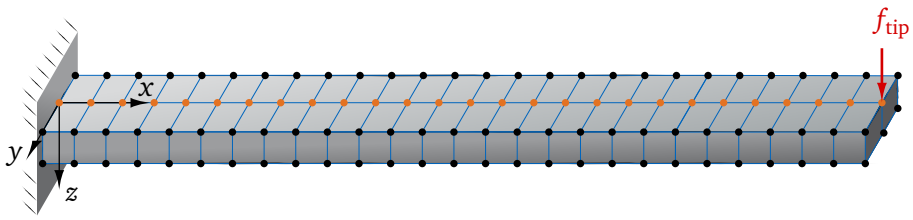

Figure 3.11: A cantilever beam discretized by a mesh in order to create a $\boldsymbol{MCK}$ model.

we are modeling a mechanical structure that can be described by a $\boldsymbol{MCK}$ model. This gives us a bit more insight into the mathematical structure of the transfer functions contained in the recaptance matrix, since the nominator and denominator are not just polynomials with a generic set of parameters a_i and b_i, but are based on a sum of weighted MSHO transfer functions that are described by the modal parameters $\omega_{0,i}$, ζ_i and $\boldsymbol{\Phi}$.

The above equation is also a much more effective way to compute the receptance matrix $\boldsymbol{G}_Y(s)$ than Alg. 1, since only one trivial inversion of a diagonal matrix is needed to compute the modal parameters. We also do not need to include every single mode in the computation of (3.59) and can decide to only include for example the first ten modes, if that results in a sufficient accuracy of the computed receptance matrix. This idea will also be used for model order reduction techniques shown in section 3.2.

Mode Shapes

The weighting factors of each term in the sum of equation (3.59) are determined by the entries of the modal matrix $\boldsymbol{\Phi}$, which contains the eigenvectors $\boldsymbol{\phi}_i$. We can get a deeper look into the physical meaning of the eigenvectors by looking at the change of a transfer function described by (3.59), while changing the output DOF.

In order to visualize this better, we move on from the 3 DOF mechanical oscillator to a generic cantilever beam, Fig. 3.11. The dynamics of such a mechanical beam structure can be modeled by describing the continuous system using a set of nodes. In this case, each node has three translational DOFs and the dynamic relationship between each DOF can again be described using a $\boldsymbol{MCK}$ model, which can be derived using a FE model[7].

Using this model and equation (3.59), we can now generate a set of transfer functions that always have the same input force in z direction at the tip of the beam f_{tip}, while moving the displacement output $z(x)$ of the transfer function along the middle line of the beam (orange nodes in Fig. 3.11). The amplitudes of the resulting set of transfer functions $Z(s,x)/F_{\text{tip}}(s)$ are plotted as a heat map on the left in Fig. 3.12.

We can see how the the poles of each transfer function always stay at the same frequency while shifting the output DOF along the orange middle line of the beam. The frequencies of the zeros depend on the position of the input / output DOF and start to move between the poles while moving the output DOF towards the input DOF. Directly at the input DOF, we again have a driving point transfer function with alternating zero pole pairs.

Every time a zero matches a pole it is canceled out, which creates geometrical shapes of the amplitudes along the eigenfrequencies of the transfer functions. Since the frequency of the zeros are determined by the entries of the modal matrix $\boldsymbol{\Phi}$, these shapes correspond to the eigenvectors $\boldsymbol{\phi}_i$, Fig. 3.12 right side. The eigenvectors are therefore also often called *mode shapes* and can not only be used as mathematical basic building blocks to recreate the real

[7] I will not go into detail here how a FEM formulation works, since it is not necessary for a proper understanding of the results of this work. There is a lot of very good and detailed literature available, e.g. [292, 311]. In this case, I used the *AMfe* code of the Chair of Applied Mechanics to generate the $\boldsymbol{MCK}$ matrices of a generic cantilever beam (thanks to Christian Meyer for helping me with *AMfe*).

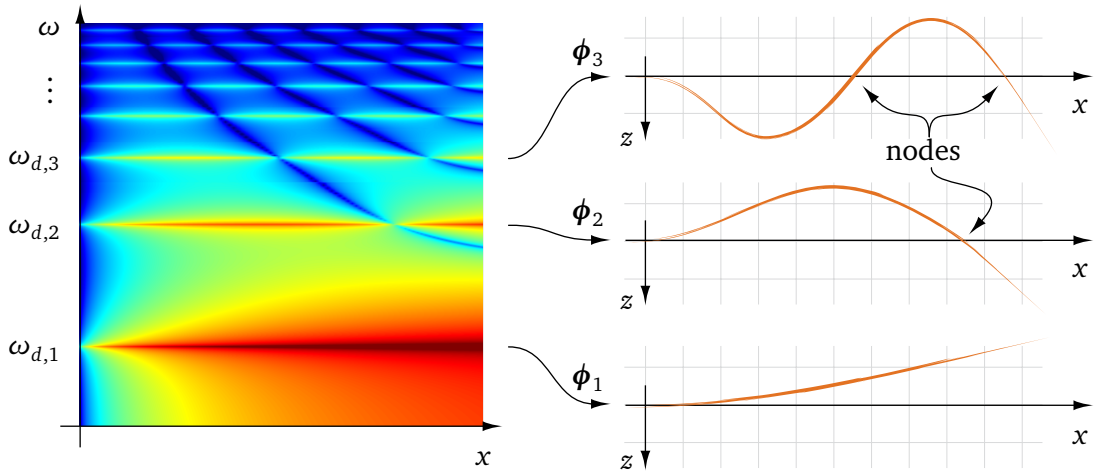

Figure 3.12: Visualizing the connection between the frequency and modal domain. Left: A set of transfer functions with the input being fixed at the end of a generic beam (Fig. 3.11) and the output being moved along the length of the beam x. The amplitudes are color coded. Right: Corresponding mode shapes of the first three modes.

dynamic response of the system using (3.44), but also to interpret important properties of the underlying system dynamics. For example, if we move the output (e.g. a sensor of a control system) of a transfer function into the node of a specific mode shape, a zero will cancel out the corresponding pole in the transfer function, causing the mode to be *unobservable*. In a similar way, if we place an input (e.g. an actuator of a control system) in a node of a mode shape, we are not going to be able to control this specific mode, making it *uncontrollable*. Mathematically, this can also be expressed using the equation

$$\boldsymbol{\phi}_i^T \boldsymbol{f} = 0 \tag{3.60}$$

meaning that the load vector $\boldsymbol{f}$ is orthogonal to a specific mode shape $\boldsymbol{\phi}_i$. This can also be interpreted as the right-hand side of equation (3.52) being zero, meaning the corresponding MSHO of this mode can not be excited by this load case[8].

Mode shapes can also be useful to identify weaknesses in a structure and develop simple improvements to a mechanical design to avoid vibration problems. In the case of this cantilever beam example, we could easily increase the stiffness of the entire system by just fixing the other end of the beam as well, since this will have a large restrictive impact on every single mode shape of the system. This knowledge will also be of use for the vibration analyses of our CROPS harvesting robot in section 4.2.1 and our walking robot LOLA in section 4.4.

State Space Modal Canonical Form

To conclude this subsection, let us have a look at the connection between the modal analysis of a $\boldsymbol{MCK}$ model as shown above and the state space formulation. We have already seen that

[8]Note that in Fig. 3.12 we are only looking at transfer functions on the orange middle line of the beam pointing into the z-direction. Since we modeled the beam as a three dimensional structure this also means we can not observe the bending modes bending around the z axis, or torsional modes. Mathematically, the corresponding modes will still show up in the receptance using (3.59), however, the poles will always stay canceled out by their respective zeros at any point of the heat map in Fig. 3.12. When measuring the same system, we might still see these modes in the measurement because of small sensor misalignments. This will show up as unexpected spurious peaks consisting of a resonance followed very closely by an antiresonance in the transfer function, caused by the corresponding zero / pole pair only almost canceling each other out. This might even happen in simulation models when no damping is used due to numerical errors.

we can transform a $\boldsymbol{MCK}$ model into the state space domain using (3.31). We can also do an eigenanalysis starting from the eigenvalue problem

$$\boldsymbol{A}_s \boldsymbol{\phi}_{s,i} = \lambda_i \boldsymbol{\phi}_{s,i} \ . \tag{3.61}$$

Note that because of the transformation (3.31), this eigenvalue problem has twice the size than when we analyzed the $\boldsymbol{MCK}$ model using (3.41). After solving the eigenvalue problem we can again use the resulting modal matrix $\boldsymbol{\Phi}_s$ to transform the states of the system $\boldsymbol{x}_s$ into modal states $\boldsymbol{\eta}_s$:

$$\boldsymbol{x}_s = \boldsymbol{\Phi}_s \boldsymbol{\eta}_s \ . \tag{3.62}$$

This transformation can be applied to (3.31) to gain the *modal canonical form* (MCF) of the state space model:

$$\begin{aligned} \dot{\boldsymbol{\eta}}_s &= \tilde{\boldsymbol{A}}_s \boldsymbol{\eta}_s + \tilde{\boldsymbol{B}}_s \boldsymbol{u}_s \\ \boldsymbol{y}_s &= \tilde{\boldsymbol{C}}_s \boldsymbol{\eta}_s + \tilde{\boldsymbol{C}}_s \boldsymbol{u}_s \end{aligned} \qquad \text{(modal canonical form)} \tag{3.63}$$

with

$$\begin{aligned} \tilde{\boldsymbol{A}}_s &= \boldsymbol{\Phi}_s^{-1} \boldsymbol{A}_s \boldsymbol{\Phi}_s \\ \tilde{\boldsymbol{B}}_s &= \boldsymbol{\Phi}_s^{-1} \boldsymbol{B}_s \\ \tilde{\boldsymbol{C}}_s &= \boldsymbol{A}_s \boldsymbol{\Phi}_s \\ \tilde{\boldsymbol{C}}_s &= \boldsymbol{C}_s \ . \end{aligned} \tag{3.64}$$

Conveniently, the original inputs $\boldsymbol{u}_s$ and outputs $\boldsymbol{y}_s$ stay unchanged under this transformation and will still produce the same transfer functions. However, the internal states have changed and the new system matrix $\tilde{\boldsymbol{A}}_s$ is now diagonal and contains the eigenvalues λ_i of the system. This is particularity useful for this work, since our main goal will be to increase the damping of the robots structural dynamics. We can therefore just identify a state space model of the original dynamics of the system, transform it into the MCF and then design the new closed-loop dynamics by increasing the damping of the desired modes.

Provided that the original $\boldsymbol{MCK}$ model was triple diagonalizable, the resulting diagonal system matrix will contain the eigenvalues as complex pairs $\lambda_{j/j+1} = -\zeta_i \omega_{0,i} \pm j\omega_{0,i}\sqrt{1-\zeta_i^2}$:

$$\tilde{\boldsymbol{A}}_s = \begin{bmatrix} -\zeta_1\omega_{0,1} + j\omega_{0,1}\sqrt{1-\zeta_1^2} & 0 & 0 & 0 & \dots \\ 0 & -\zeta_1\omega_{0,1} - j\omega_{0,1}\sqrt{1-\zeta_1^2} & 0 & 0 & \dots \\ 0 & 0 & -\zeta_2\omega_{0,2} + j\omega_{0,2}\sqrt{1-\zeta_2^2} & 0 & \dots \\ 0 & 0 & 0 & -\zeta_2\omega_{0,2} - j\omega_{0,2}\sqrt{1-\zeta_2^2} & \dots \\ \vdots & \vdots & \vdots & \vdots & \ddots \end{bmatrix} \tag{3.65}$$

As already mentioned, this makes the MCF quite useful since every system state has a physically interpretable meaning. Under the same condition, the eigenvectors $\boldsymbol{\phi}_{s,i}$ resulting from (3.61) contain the eigenvectors $\boldsymbol{\phi}_i$ from the original $\boldsymbol{MCK}$ model:

$$\boldsymbol{\phi}_{s,i} = \begin{bmatrix} \frac{1}{\lambda_i}\boldsymbol{\phi}_i \\ \boldsymbol{\phi}_i \end{bmatrix} \tag{3.66}$$

With the upper half of $\boldsymbol{\phi}_{s,i}$ corresponding to the same eigenvector $\boldsymbol{\phi}_i$ of the original $\boldsymbol{MCK}$ model, however, scaled with the corresponding eigenvalue λ_i.

Note that when we were solving the eigenvalue problem (3.41) for the $\boldsymbol{MCK}$ model, we solved for the square of the eigenvalues λ_i^2. With n DOF, we therefore got n eigenvectors and corresponding squared eigenvalues λ_i^2. When taking the root of each eigenvalue we consequently can only get complex conjugated eigenvalue pairs that each correspond to one eigenvector. This has the consequence that we can only solve problems with a damping matrix D that leads to a triple diagonalizable system and therefore complex conjugate eigenvalue pairs.

When solving the eigenvalue problem (3.61) of the state space formulation, we can directly solve for each eigenvalue λ_i which will correspond to twice the amount of eigenvectors of the original $\boldsymbol{MCK}$ model. For triple diagonalizable systems we will again get complex eigenvalue pairs as shown in (3.65), however, this time with twice the amount of eigenvectors of which two $\boldsymbol{\phi}_{s,i}$ are always the same and correspond to one complex conjugate eigenvalue pair. Additionally, since we can now solve for the eigenvalues λ_i directly, we are not limited to just triple diagonalizable systems. This makes the transformation of a $\boldsymbol{MCK}$ model into the state space domain particularly useful to solve eigenvalue problems for system with a non-proportional damping matrix D. The resulting eigenvalues λ_i then do not have to be complex conjugated pairs anymore and the eigenvectors $\boldsymbol{\phi}_{s,i}$ can be complex[9]. While this is a very useful property of the state space domain, the assumption of a proportional damping matrix D was always good enough for the topics covered in this thesis.

3.2 Flexible Multibody Simulation and Model Order Reduction

In order to create a model of a robot manipulator with flexible joints and links, we need to build a flexible multibody simulation. As already described in the State of the Art section 2.1.2, there are two main approaches to do this.

Lumped Parameter Approach

The first one is a lumped parameter approach (see e.g. [191]), which just splits up each structure in multiple rigid bodies that are also connected by flexible joints, Fig. 3.13a. The needed spring stiffnesses can then simply be computed using classical beam theory

$$k_R = \frac{EJ_A}{l} \qquad \text{(rotational stiffness)} \tag{3.67}$$

$$k_T = \frac{GJ_T}{l} \qquad \text{(torsional stiffness)} \tag{3.68}$$

$$k_A = \frac{EA}{l}\,, \qquad \text{(axial stiffness)} \tag{3.69}$$

with J_A and J_B being the area- / torsional moment of inertia, E and G Young's and shear modulus, and A and l the area and length of one beam segment. The total length of the beam is $L = Nl$, with N being number of segments.

The easiest way to introduce damping is by making it proportional to the stiffness of each segment:

$$c_R = \alpha k_R\,, \tag{3.70}$$

with α being a tuning factor.

[9] This basically means that the entries of $\boldsymbol{\phi}_{s,i}$ do not have to be either positive or negative, which correspond to a phase of either 0° or 180° in the complex plane, but can also be complex and can therefore have an arbitrary phase shift in respect to each other. The effect on the mode shape can be visualized by not letting each DOF start at zero, but by animating them using their respective phase shift on their periodic path.

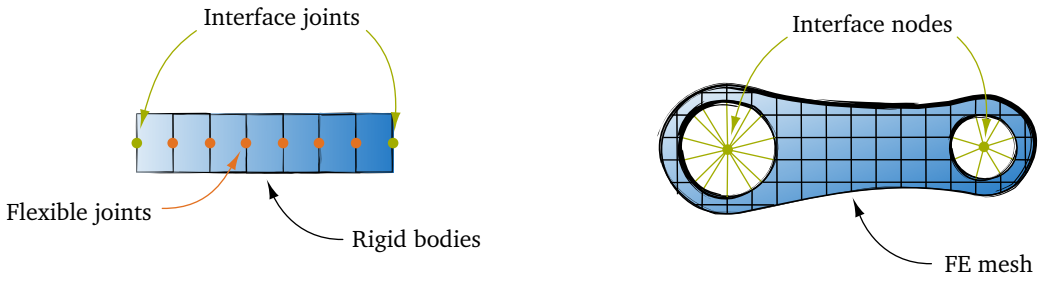

(a) Approximation of a link structure using a series of simple rigid bodies and flexible joints.

(b) FE model of a link structure with interface nodes.

Figure 3.13: Two approaches for the modeling of flexible links structures in multibody simulations.

The biggest advantage of this approach is its simplicity, since it can be easily implemented in most rigid MBS frameworks that allow flexible joints. The flexible beam is then just another series of small rigid bodies with flexible joints, with only the real robot joints at the beginning and the end being actuated. The accuracy of this kind of model is acceptable when using a large number of elements. The main disadvantage is that only simple beam geometries can be modeled. The model will also loose accuracy for modes higher than about half of the number of segments, while also significantly losing damping for the highest mode[10].

Floating Frame of Reference and Model Order Reduction

A more sophisticated approach to model flexible links in a multi-body simulation framework is called *Floating Frame of Reference* (FFR) [35, 243]. This method assumes large rigid body transformations with small local deformations in the bodies. This is a reasonable assumption for our problem, since the robot will undergo large motions when moving its links, while the dynamic error caused by the dynamic deformation of the robot's joints and links will be relatively small[11].

Since I will use this method mainly as a tool to investigate the effectiveness of external stabilization approaches for robots, I will not go into too much detail here. The method is already described very well in e.g. [35, 243] and a full understanding of its implementation is not necessary to understand the results of this work.

The general idea of the FFR approach is to use an FE formulation to derive a $\boldsymbol{MCK}$ model of all bodies, which is then added to a rigid multibody formulation. However, depending on the mesh size, the FE model can be quite large, which can have a large impact on computation time. In order to reduce the size of the individual $\boldsymbol{MCK}$ models, one can apply model order reduction techniques. These methods aim to find a reduction basis $\boldsymbol{R}$ to reduce the system matrices and force vector

$$\underbrace{\boldsymbol{R}^T\boldsymbol{M}\boldsymbol{R}}_{M_R}\ddot{\boldsymbol{q}} + \underbrace{\boldsymbol{R}^T\boldsymbol{K}\boldsymbol{R}}_{K_R}\boldsymbol{q} = \underbrace{\boldsymbol{R}^T\boldsymbol{f}}_{f_R} \tag{3.71}$$

such that the dynamics at the interface nodes of interest are still replicated as accurately as possible. Damping is often added after the $\boldsymbol{MK}$ model is reduced, using for example Rayleigh

[10] This actually caused quite a lot of trouble for modern control methods with acceleration feedback, since these mostly could not handle an unmodeled high frequency mode with almost no damping. We were still stuck using this approach in Simulink for the majority of my time at the chair, since the floating frame of reference approach with reduced order models proposed by Matlab itself in [191] was faulty and could basically only model the first mode of a beam correctly. This was fixed in the Matlab release 2020a.

[11] If one also wants to analyze large body deformations, then methods like *Non-Linear Finite Elements for Multibodies* [109] or *Absolute Nodal Coordinates* [243] should be considered.

damping (3.53).

In order to derive a suitable reduction basis $\boldsymbol{R}$, the $\boldsymbol{MK}$ model is split up into remaining *master* DOFs (index m) and condensed *slave* DOFs (index s):

$$\begin{bmatrix} \boldsymbol{M}_{mm} & \boldsymbol{M}_{ms} \\ \boldsymbol{M}_{sm} & \boldsymbol{M}_{ss} \end{bmatrix} \begin{bmatrix} \ddot{\boldsymbol{q}}_m \\ \ddot{\boldsymbol{q}}_s \end{bmatrix} + \begin{bmatrix} \boldsymbol{K}_{mm} & \boldsymbol{K}_{ms} \\ \boldsymbol{K}_{sm} & \boldsymbol{K}_{ss} \end{bmatrix} \begin{bmatrix} \boldsymbol{q}_m \\ \boldsymbol{q}_s \end{bmatrix} = \begin{bmatrix} \boldsymbol{f}_m \\ \boldsymbol{f}_s \end{bmatrix} \tag{3.72}$$

In order to couple the FE model with an MBS, the master nodes should be chosen where boundary conditions and forces are defined in the MBS or any other node that might be of interest, e.g. a node at a location with a sensor to create feedback for our external vibration damping approaches. Sometimes, it its also beneficial to include nodes in the set of master DOFs that experience large deformations, or are areas with concentrated mass and small local stiffness [312].

There are multiple model order reduction techniques. The most simple one is the *Guyan Reduction Method* [122, 133]: After choosing a suitable set of master DOFs, the reduction basis for the Guyan reduction is associated with the displacement patterns created by a unit displacement of the master coordinates. We first solve (3.72) for $\boldsymbol{q}_s$ with $\boldsymbol{f}_s = \boldsymbol{0}$:

$$\boldsymbol{q}_s = -\boldsymbol{K}_{ss}^{-1} \left(\boldsymbol{M}_{sm} \ddot{\boldsymbol{q}}_m + \boldsymbol{M}_{ss} \ddot{\boldsymbol{q}}_s + \boldsymbol{K}_{sm} \boldsymbol{q}_m \right) . \tag{3.73}$$

The Gyuan Reduction Method then assumes that the dynamics between the condensed and remaining DOFs can be correctly represented by only static modes. Meaning that all inertia terms are set to zero, resulting in the reduction basis $\boldsymbol{R}_{\mathrm{Gy}}$

$$\begin{bmatrix} \boldsymbol{q}_m \\ \boldsymbol{q}_s \end{bmatrix} = \begin{bmatrix} \boldsymbol{I} \\ -\boldsymbol{K}_{ss}^{-1} \boldsymbol{K}_{sm} \end{bmatrix} \boldsymbol{q}_m = \boldsymbol{R}_{\mathrm{Gy}} \boldsymbol{q}_m \, . \qquad \text{(Guyan reduction basis)} \tag{3.74}$$

This method will retain an accurate solution for static problems, however, might not be very accurate for dynamic solutions depending how much the dynamic modes of the substructures contribute to the global dynamic behavior of the system. The dynamic representation of the reduced model can be improved by retaining additional master nodes [59, 244]. The Guyan reduction will also destroy the sparseness of the mass and stiffness matrices, which might lead to a more expensive eigensolution [312].

Another reduction method that can retain a more accurate model of the dynamic behavior of the system is the *Hurty-Craig-Bampton Method* [75]. The method also includes a set of dynamic vibration modes in addition to the static modes. The transformation can be written as

$$\begin{bmatrix} \boldsymbol{q}_m \\ \boldsymbol{q}_s \end{bmatrix} = \begin{bmatrix} \boldsymbol{I} & \boldsymbol{0} \\ \boldsymbol{\psi} & \boldsymbol{\Phi} \end{bmatrix} \begin{bmatrix} \boldsymbol{q}_m \\ \boldsymbol{\eta} \end{bmatrix} = \boldsymbol{R}_{\mathrm{HCB}} \begin{bmatrix} \boldsymbol{q}_m \\ \boldsymbol{\eta} \end{bmatrix} , \qquad \text{(Hurty-Craig-Bampton reduction basis)} \tag{3.75}$$

with $\boldsymbol{\Phi}$ being the interior partition of the fixed-interface modal matrix, $\boldsymbol{\psi}$ the interior partition of the constraint-mode matrix, and $\boldsymbol{\eta}$ a set of generalized coordinates representing the fixed-interface normal modes [229]. The accuracy depends on the number of retained dynamics modes for the reduction basis. In practice, there are often just the first few modes included that are associated with natural frequencies below a certain frequency range of interest.

Since version 2020a, Matlab included a new usable flexible body block in their multibody Simscape library. The block is based on the FFR approach with reduced order models as described above. Matlab also recently added rudimentary FE modeling capabilities and the Craig-Bampton reduction to their tool set. This simplified the modeling process for this thesis significantly, since the entire modeling tool chain could be done within Matlab/Simulink. I will explain the modeling process in more detail in section 4.1.

3.3 Active Vibration Control

In this subsection, I want to give a brief overview of classical active vibration damping techniques. I will not go into detail about standard control methods like PID, or notch- and lead-lag filters. However, the following control methods are specific to active vibration control and might not be necessarily part of the standard repertoire of most readers. I will also use these methods frequently throughout this theses. All of these methods are already very well explained in more detail in for example [219]. I will only go into detail about the collocated control problem, since this was a core decision of this thesis.

As an example system, I want to use the 3 DOF mechanical oscillator from section 3.1.2 again, Fig. 3.8. The dynamics of the system can be described in state space form using:

$$\dot{\boldsymbol{x}}_{3DOF} = \boldsymbol{A}_{3DOF}\boldsymbol{x}_{3DOF} + \boldsymbol{B}_{3DOF}\boldsymbol{u}_{3DOF} \ , \tag{3.76}$$

with $\boldsymbol{A}_{3DOF}$ and $\boldsymbol{B}_{3DOF}$ being the system matrices as described in (3.30). The input of the system is only acting on the third DOF

$$\boldsymbol{u}_{3DOF} = \begin{bmatrix} 0 \\ 0 \\ f_c + f_d \end{bmatrix} \ , \tag{3.77}$$

with f_c being the control force provided by our controller and f_d an additional disturbance force that we can use to test the closed-loop response of our controlled system.

Positive Position Feedback (PPF)

The first control method I want to talk about is *Positive Position Feedback* (PPF), which was derived in [93] for the control of large space structures. As the name already suggests, the controller utilizes position feedback, which is the position of the third DOF in our example:

$$y_p = \begin{bmatrix} 0 & 0 & 1 & 0 & 0 & 0 \end{bmatrix} \boldsymbol{x}_{3DOF} = x_3 \tag{3.78}$$

The control law in the Laplace domain is equal to a second order system:

$$F_c(s) = \frac{g_{PPF}}{s^2 + 2\zeta_{c,PPF}\omega_{c,PPF}s + \omega_{c,PPF}^2} \cdot Y_p(s) \ . \qquad \text{(Positive Position Feedback)} \tag{3.79}$$

The natural frequency of the controller $\omega_{c,PPF}$ is set equal to the natural frequency of the system that is supposed to be damped. The damping ratio of the controller $\zeta_{c,PPF}$ can be set somewhat arbitrarily. With lower damping ratios the controller will work more aggressively in a narrower band, however, it also has to be placed more closely to the real natural frequency of the system to work properly. A good starting value is $\zeta_{c,PPF} = 0.5$ to get good performance on a broader frequency range. The concept is similar to attaching a tuned-mass damper to the structure to damp a specific mode. However, since the damper is implemented as a digital control law, we can increase the effectiveness of the damper by increasing the control gain g_{PPF}.

The effect on the disturbance transfer function $G_d(s) = X_3(s)/F_d(s)$ for different amounts of gain is shown in Fig. 3.14a. We can see that for a medium amount of gain (orange line), the effect on the system dynamics indeed looks like an increase in damping for the first mode of the system. Increasing the gain further reveals that the controller initially places a new zero-pole pair at the designed natural frequency $\omega_{c,PPF}$. Increasing the gain of the controller then

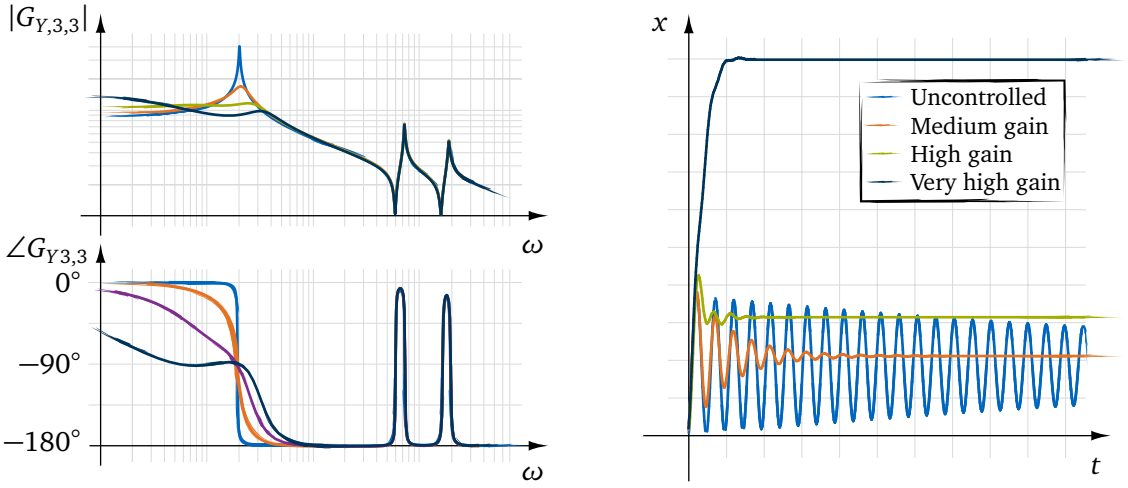

(a) Disturbance transfer function $G_d(s) = X_3(s)/F_d(s)$.

(b) Step response.

Figure 3.14: The effects of a PPF controller on the 3 DOF mechanical oscillator system for different amounts of control gain. $\omega_{c,PPF}$ is set to the first structural eigenfrequency $\omega_{0,1}$ and $\zeta_{c,PPF} = 0.5$, the controller gain g_{PPF} is increased.

causes the new pole pair to move to lower frequencies, while also pushing the original pole pair of the system to higher frequencies. The new zero pair remains at the design frequency $\omega_{c,PPF}$. For very high gains, the new pole pair becomes real and further gain very quickly pushes one of the poles into the unstable region (not depicted). One side effect of the new pole pair moving to lower frequencies is that the gain of the system gets increased, which is equal to a decrease in overall stiffness of the system. This is also visible in the step response, Fig. 3.14b, and might be undesirable behavior depending on the application.

The main advantage of PPF controllers is that they are simple to use and quite effective in attenuating specific resonance frequencies. The only real system knowledge needed is a good estimate of the frequencies of the system resonances that are supposed to be damped. While they have an inherent stability limit, real systems usually already become unstable with less gain anyway, because of issues like the amplification of sensor noise. Another advantage is that since the transfer function of the PPF controller is a simple second order system, the controller response naturally roles off for frequencies higher than the designed controller natural frequency $\omega_{c,PPF}$ and therefore can not interact with higher order dynamics of the real system. The controller is also quite robust against unmodeled system and actuator dynamics [93, 219, 245, 254].

Direct Velocity Feedback

While we will use a PPF controller as part of the control system of the stabilization unit, we need other control strategies that work better with acceleration feedback for our active vibration damping concept with proof-mass-actuators.

Let us first change the output of our 3 DOF mechanical oscillator to accelerations at the third DOF:

$$\boldsymbol{y}_{v,a} = \begin{bmatrix} \dot{\boldsymbol{x}} \\ \ddot{\boldsymbol{x}} \end{bmatrix} = \begin{bmatrix} \boldsymbol{0} & \boldsymbol{I} \\ -\boldsymbol{M}^{-1}\boldsymbol{K} & -\boldsymbol{M}^{-1}\boldsymbol{C} \end{bmatrix} \begin{bmatrix} \boldsymbol{x} \\ \dot{\boldsymbol{x}} \end{bmatrix} + \begin{bmatrix} \boldsymbol{0} \\ \boldsymbol{M}^{-1} \end{bmatrix} \boldsymbol{u}_{3DOF} \tag{3.80}$$

$$y_{a,3} = \begin{bmatrix} 0 & 0 & 0 & 0 & 0 & 1 \end{bmatrix} \boldsymbol{y}_{v,a} \tag{3.81}$$

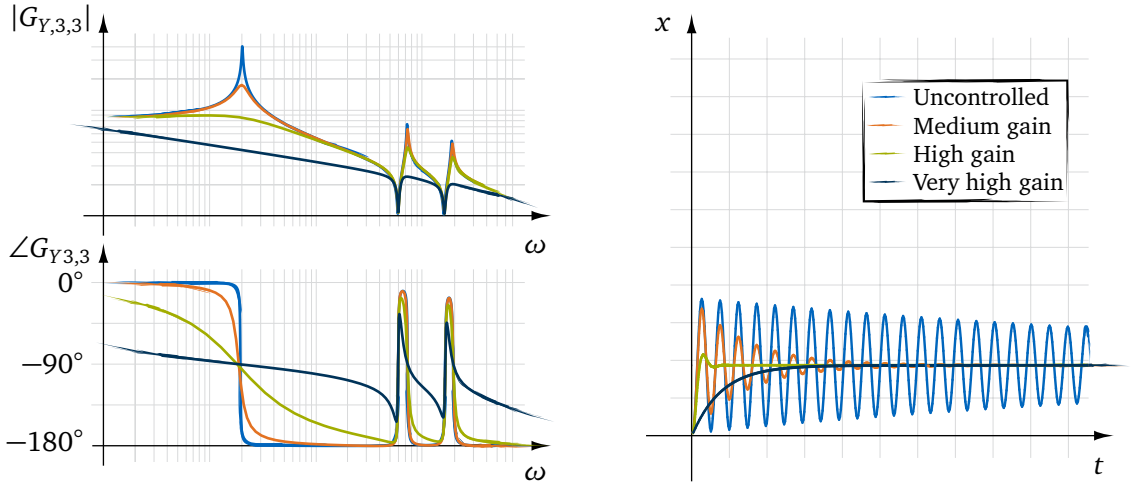

(a) Disturbance transfer function $G_d(s) = X_3(s)/F_d(s)$.

(b) Step response.

Figure 3.15: The effects of a DVF controller on the 3 DOF mechanical oscillator system for different amounts of control gain.

which represents the acceleration measurement we would get from our real sensor. As the name suggests, *Direct Velocity Feedback* (DVF), however, needs velocity feedback to work. Consequently, we need to integrate the measured accelerations once for our control law:

$$F_c(s) = -\frac{g_{DVF}}{s} \cdot y_{a,3} \ . \qquad \text{(Direct Velocity Feedback)} \tag{3.82}$$

The controller itself simply feeds the determined velocity back into the system with a negative controller gain g_{DVF}. This general control structure acts dissipatively and is similar to most passivity based control approaches. The effect of increasing the gain on the disturbance transfer function is shown in Fig. 3.15a. In theory, a DVF has no stability limit for a collocated system. The controller will increase the damping first on the lower modes of the system until these modes are over damped and become real. One of the real poles will than be pushed towards lower frequencies (without ever becoming unstable) and the other one to higher frequencies.

As we can see in Fig. 3.15b, the entire system can very effectively be damped with this very simple control strategy, without effecting the overall stiffness of the system. The big disadvantage of DVF is that one needs access to the velocity state of the system. This is often an issue, since there are few sensors that can really directly measure velocity besides a laser Doppler vibrometer. Usually, either a derivative filter has to be used on a position measurement, or an acceleration measurement has to be integrated. The additional dynamics introduced by the new filter then usually have a negative effect on the achievable system performance. Getting the velocity from a derived position signal usually requires quite aggressive filter coefficients to suppress the amplification of noise. Integrating an acceleration signal is a bit cleaner, however, still needs a high-pass filter to prevent signal drift, which might effect the control design and system performance [32, 40, 104, 219]. Additionally, while the damping performance of this very simple controller can be quite effective in a broad frequency range, it also slows down the entire system response. This might be an undesirable effect if one wants to only damp resonances, but still maintain a quick system response, which is usually the case.

Negative Acceleration Feedback

Another way to directly incorporate acceleration feedback into a simple control scheme for active vibration damping is *Negative Acceleration Feedback* (NAF) [36, 219, 269, 296]. Similar

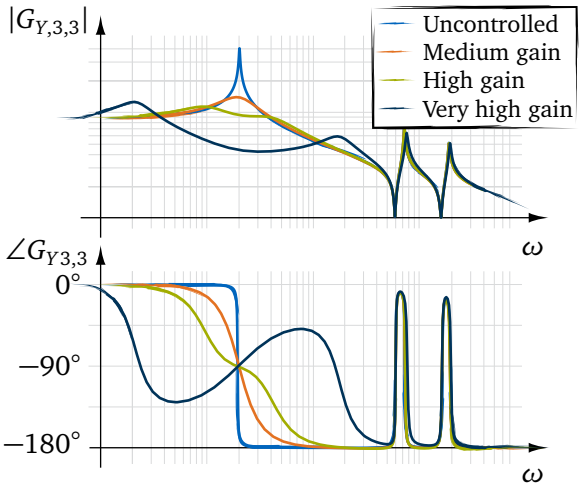

(a) Disturbance transfer function $G_d(s) = X_3(s)/F_d(s)$ when applying a NAF controller with different amounts of gain.

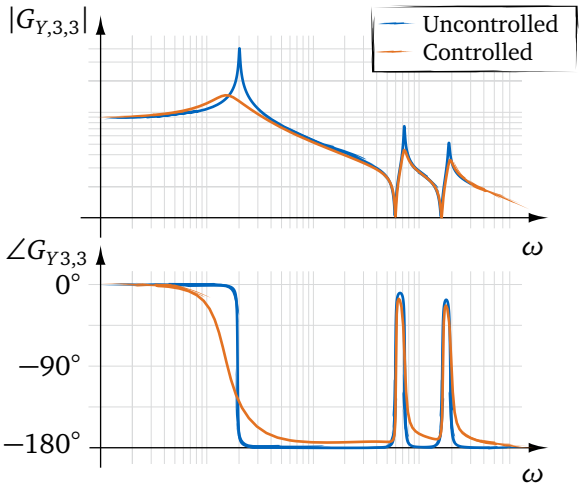

(b) Disturbance transfer function $G_d(s) = X_3(s)/F_d(s)$ when applying multiple NAF controllers to all three modes.

Figure 3.16: The effects of a NAF controller on the 3 DOF mechanical oscillator system.

to the PPF controller, the control law is just a second order system

$$F_c(s) = \frac{-g_{NAF}}{s^2 + 2\zeta_{c,NAF}\omega_{c,NAF}s + \omega_{c,NAF}^2} \cdot Y_a(s)\,, \qquad \text{(Negative Acceleration Feedback)} \quad (3.83)$$

however, with negative controller gain g_{NAF}. The controller is designed in a similar way to the PPF controller, by also setting the controller's natural frequency $\omega_{c,NAF}$ equal to the resonance frequency that is supposed to be damped.

The effect of increasingly larger controller gains is plotted in Fig. 3.16a. The controller behaves similar to the PPF controller. While the old and new pole pair are again pushed to higher and lower frequencies respectively, they do not become real at any point and even lose damping along the way. A collocated system with a NAF controller is theoretically stable for any gain and also does not change its gain/stiffness. The big advantage of this controller is that it directly uses acceleration feedback without the need of any additional filters. Of course, actuator dynamics still have an influence on the system design, as we will see later. In this case, the controller transfer function looks like the second derivative of a second order system, meaning that the transfer function starts at zero and then converges to a constant magnitude for frequencies higher than the controller natural frequency $\omega_{c,NAF}$. This controller has the advantage of not effecting the overall gain of the system, however, it will effect higher order dynamics.

The NAF controller can also easily be used to damp multiple modes by just adding together multiple NAF controllers tuned to the specific resonance frequencies:

$$F_c(s) = \left(\sum_{i=1}^{n} \frac{-g_{NAF,i}}{s^2 + 2\zeta_{c,NAF,i}\omega_{c,NAF,i}s + \omega_{c,NAF,i}^2} \right) \cdot Y_a(s) \quad (3.84)$$

with n being the number of damped resonance peaks. An example of this is shown in 3.4. 3.16b.

This generally also works with the PPF controller. However, for the PPF controller one should tune the controller chain by starting with the highest natural frequency, since the controller gain of the higher controller will influence the gain of the lower controllers, because

of the shape of the controller transfer function. The same is true for the NAF controller in reverse, meaning the controller chain should be tuned starting from the lowest resonance frequency [219].

3.4 Robot Joint Control

In this section, I will briefly go over the most common control concepts for robot joint position- and torque control.

3.4.1 Position Control

For joint position control, most robot manufactures implement a decentralized cascaded P-PI-PI motor controller [153, 248], Fig. 3.17. Each joint gets the desired planned joint angle θ_d, which is then independently controlled by each joint controller on the motor angle θ_m.

The control plant for the cascaded joint position controller is basically just the individual motor of the joint. The dynamics of the electrical system for most motors can be described as a first order system:

$$I(s) = \frac{\frac{1}{R}}{\frac{L}{R}s+1} \cdot (U_m(s) - \underbrace{\dot{\theta}_m(s) k_m}_{U_{\text{ind}}(s)}) \,, \qquad \text{(electrical system)} \tag{3.85}$$

with L and R being the inductance and resistance of the electrical system, U_m the voltage supplied to the motor, k_m the motor constant and U_{ind} the counter voltage caused by self-inductance[12].

The motor then drives the mechanical system following the dynamic equation

$$\ddot{\theta}_m(s) = \frac{1}{J_m} \cdot (\underbrace{I(s) k_m}_{\tau_m(s)} + \tau_{\text{dist}}(s)) \,, \qquad \text{(mechanical system)} \tag{3.86}$$

with J_m being the motors area moment of inertia and τ_m the motor torque. With this simple model, all other effects like friction/compliance in the drivetrain or gravity loads created by the links are included in the disturbance torque τ_{dist}. This is fine for the design of the controller, since all the control loops are essentially collocated on the motor DOF.

The first control loop is the current controller

$$U_m(s) = \left(g_{P,I} + \frac{g_{I,I}}{s}\right) \cdot (\underbrace{I_d(s) - I(s)}_{e_I} + I_{ff}(s)) \,, \qquad \text{(current controller)} \tag{3.87}$$

with the PI gains $g_{P,I}$ and $g_{I,I}$. The controller receives the desired current I_d from the preceding velocity controller and measures the motor current I. Additionally, we can utilize a feedforward term I_{ff}, which I will explain in more detail later.

The velocity controller works in the same way

$$I_d(s) = \left(g_{P,v} + \frac{g_{I,v}}{s}\right) \cdot (\underbrace{\dot{\theta}_d(s) - \dot{\theta}_m(s)}_{e_{\dot{\theta}}} + \dot{\theta}_{ff}(s)) \,. \qquad \text{(velocity controller)} \tag{3.88}$$

[12] This model always fitted quite well for multiple measurements that we did on the joint modules of our walking robot LOLA and harvesting robot CROPS. The self inductance U_{ind} is not depicted in Fig. 3.17 for clarity sake, since the effect is quite small and usually easily controllable

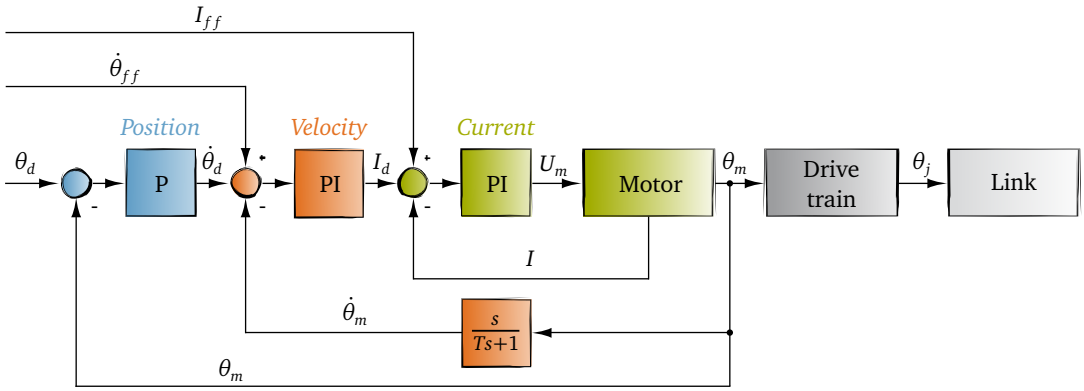

Figure 3.17: Signal flow chart for a cascaded joint position controller.

The velocity $\dot{\theta}_m$ usually has to be determined by using the derivative of the measured position θ_m. I indicated this in Fig. 3.17 with a simple derivative filter. However, in practice the position is often measured using an incremental encoder. With these types of encoders, the velocity can be determined by counting the number of encoder lines per seconds. This is a relatively robust process that just needs a high frequency glitch filter to avoid errors caused by skipped lines.

Finally, the position controller is usually just a proportional controller:

$$\dot{\theta}_d(s) = g_{P,p} \cdot \underbrace{(\theta_d(s) - \theta_m(s))}_{e_\theta} . \qquad \text{(position controller)} \tag{3.89}$$

The I part is omitted to avoid inducing additional oscillations caused by the integral action of the controller on the position level. The cascaded controller still manages to converge the steady state error to zero, because of the I part in the velocity controller. Since the position controller produces a desired velocity $\dot{\theta}_d$, the only state at which the position controller produces a desired velocity of $\dot{\theta}_d = 0$ is at a position error of $e_\theta = 0$. Because of the I part in the velocity controller, the controller is able to reduce the steady state error on the velocity level to zero and therefore also on the position level.

These types of cascaded controllers are very popular for motor control, because of their simplicity and very strong tracking performance. The controller can easily be tuned by just starting with the most inner loop, which then becomes the new control plant for the next outer control-loop. Since the outer controllers produce the desired values for the inner controllers, the dynamics of the inner closed-loops need to be fast enough to follow the dynamics of the outer loops. A good rule of thumb is to design the control loops in such a way that the closed-loop dynamics of the inner loop are about ten times faster than the dynamics of the outer loop. This is an important aspect for cascaded control loops, which also has a large influence of their ability to control robot joints with a flexible drivetrain and link, as I will discuss in section 4.3.1.

Influence of the Feedforward Terms

The performance of this motor controller can be improved even further by utilizing the feedforward terms $\dot{\theta}_{ff}$ and I_{ff}. Let us change the control plant to a general second order system, in order to investigate their influence:

$$x(s) = \frac{g}{s^2 + 2\zeta\omega_0 + \omega_0^2} \cdot f(s) \qquad \text{(second order system)} \tag{3.90}$$

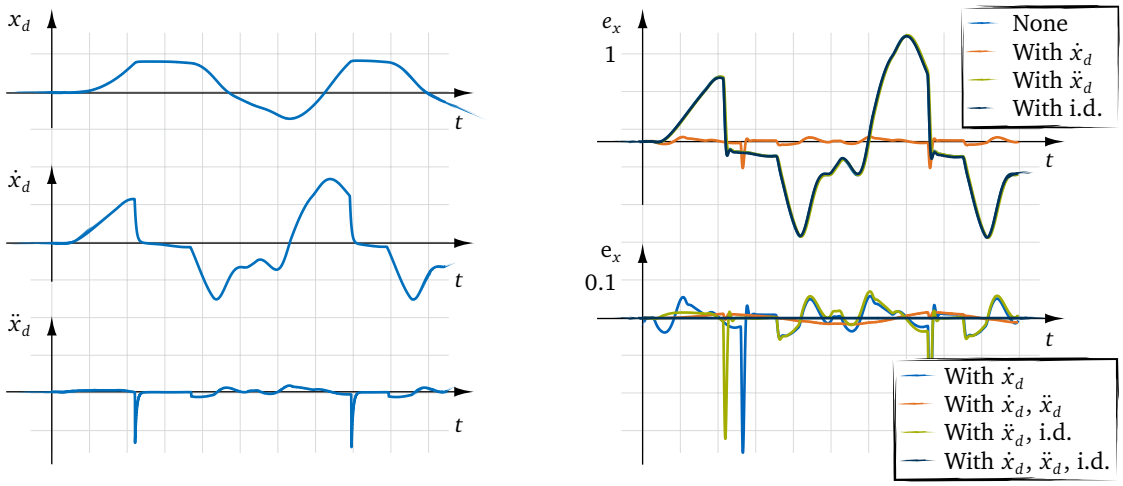

(a) Desired trajectory profile.

(b) Normalized position error e_x.

Figure 3.18: Influence of different feedforward terms on the cascaded control structure. Adapted from my master's thesis [45].

and use the controllers:

$$f(s) = \left(g_{P,a} + \frac{g_{I,a}}{s}\right) \cdot (\ddot{x}_d(s) - \ddot{x}(s) + \ddot{x}_{ff}(s)) \qquad \text{(acceleration controller)} \qquad (3.91)$$

$$\ddot{x}_d(s) = \left(g_{P,v} + \frac{g_{I,v}}{s}\right) \cdot (\dot{x}_d(s) - \dot{x}(s) + \dot{x}_{ff}(s)) \qquad \text{(velocity controller)} \qquad (3.92)$$

$$\dot{x}_d(s) = g_{P,p} \cdot (x_d(s) - x(s)) \qquad \text{(position controller)} \qquad (3.93)$$

which is the same structure as shown in Fig. 3.17, but with the motor replaced with a second order system and the current controller replaced with an acceleration controller.

Sticking to this structure, one might think that the best possible feedforward term for the acceleration would be

$$\ddot{x}_{ff}(s) = \frac{s^2 + 2\zeta\omega_0 + \omega_0^2}{g} \; \frac{s}{g_{P,a}s + g_{I,a}} \; \frac{1}{(Ts+1)^2} \cdot x_d(s) \qquad \text{(inverse dynamics)} \qquad (3.94)$$

with the first term being the inverse control plant, the second one the inverse acceleration controller and the last one a second order system with a very small time constant T to get the denominator to the same polynomial order as the numerator and make the system implementable. Ignoring the velocity and position control loop, this transfer function should compute the perfect input for the acceleration controller for the system to exactly follow the desired position x_d.

The position error for different combinations of feedforward terms for the cascaded controller is shown in Fig. 3.18b. We can see that just using the inverse dynamics (i.d.) feedforward term (3.94) will not effect the error at all (dark blue line, top graph), when all the other controllers are also active. The reason for this is that the most significant contribution to the error is already created earlier in the cascade: The position controller has to produce the desired velocity for the following velocity controller. The position controller will be delayed by its own dynamics to produce the desired velocity, which causes the velocity controller to follow a delayed velocity profile. We can see this by comparing the desired trajectory Fig. 3.18a to the error in the top graph of Fig. 3.18b, which shows an almost exact match between the desired velocity and the position error profile. This behavior is always the same and independent of the amount of control gain used. The only way to significantly reduce

this error is by first feeding the planned velocity $\dot{x}_p$ into the velocity feedforward term $\dot{x}_{ff}$ (orange line, top graph)[13].

This will usually reduce the error by one order of magnitude and make the new position error look like the acceleration profile for the same reasons as explained above (blue line, bottom graph). The only way to further reduce the error is now by also feeding the planned acceleration $\ddot{x}_p$ into the acceleration feedforward term $\ddot{x}_{ff}$ (orange line, bottom graph). Only then can we achieve a nearly perfect controller by also adding the inverse dynamic term to the feedforward term $\ddot{x}_{ff}$ (dark blue line, bottom graph).

In practice, we observed the exact same behavior for the robot joint modules of our walking robot LOLA and harvesting robot CROPS, which I investigated in much more detail in my master's thesis [45][14]. However, in order to correctly feed the planned velocity profile into the cascaded control structure, we also needed to account for delays in the EtherCAT bus communication. The procedure is described in more detail in our paper [268]. Unfortunately, for the real controller, we can not directly feed the planned acceleration into the system, since the real system uses a current controller. With the assumption that the motor acceleration is somewhat proportional to the motor current, one can try to still feed the acceleration into the current feedforward term using a gain factor $I_{ff} = g_{I,ff} \cdot \ddot{\theta}_p$. However, in practice, this never achieved any further improvements for us. This is probably because the torque on the motor is completely dominated by friction from the drivetrain, with only little contributions from the acceleration of the motor inertia. For the same reason, any form of inverse dynamics that does not include a very good friction model also has very little use for this type of robot joint position controller, when it is also operated with high gear ratios.

With our modified velocity feedforward, we achieved an average joint error in the 100 μrad range on the motor side, with a control bandwidth of 240 Hz [268]. Assuming a rigid drivetrain, this would result in joint position errors in the 1 μrad range for our humanoid robot LOLA. This would certainly be a very impressive result and underlines the very good possible tracking performance of these types of cascaded controllers. However, in reality the drivetrain and links of the robot are not perfectly rigid. I will discuss the influence of compliant gears and flexible links on cascaded joint position controllers in section 4.3.1.

3.4.2 Torque Control

There are many books [248, 249] and papers [12–17, 260, 272] that deal with the general structure of torque controlled joints and their various challenges in detail. A common problem in the past was for example that measured feedback from the joint position θ_j was either not available at all or only with poor quality absolute encoders. This led to various different approaches attempting to estimate the actual joint position θ_j using iterative methods to solve models fed by the measured motor position θ_m. For this overview, I will use the most recent publication of the DLR's SARA IV robot [134] as a basis. In this work, they could avoid this problem by just using high quality absolute encoders on the joint side, which allowed them to directly incorporate measured joint position feedback into their control law, which results in the most simple and intuitive version of a typical joint torque controller, Fig. 3.19.

Most publications will assume the control plant as a rigid multibody system described by the generic mathematical model:

$$\boldsymbol{M}(\boldsymbol{\theta}_j)\ddot{\boldsymbol{\theta}}_j + \boldsymbol{C}(\boldsymbol{\theta}_j, \dot{\boldsymbol{\theta}}_j)\dot{\boldsymbol{\theta}}_j + \boldsymbol{g}(\boldsymbol{\theta}_j) = \boldsymbol{\tau}_j + \boldsymbol{\tau}_{\text{dist}} \,, \tag{3.95}$$

with the inertia matrix $\boldsymbol{M}(\boldsymbol{\theta}_j)$, the damping matrix $\boldsymbol{C}(\boldsymbol{\theta}_j, \dot{\boldsymbol{\theta}}_j)$ consisting of Coriolis and cen-

[13] Joint trajectories are usually planned smoothly, with a known velocity and acceleration profile.
[14] The results are also partially published in our paper [268].

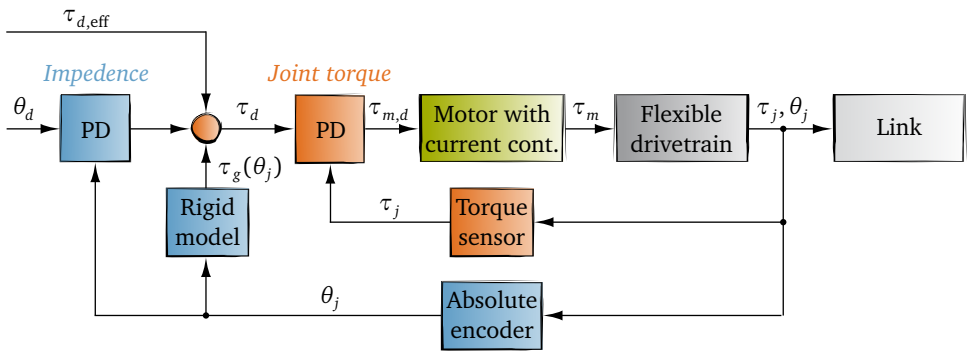

Figure 3.19: Flow chart for a typical joint torque controller.

trifugal torques, the vector $\boldsymbol{g}(\boldsymbol{\theta}_j)$ including gravitational loads, the joint torque $\boldsymbol{\tau}_j$ and additional disturbance torques $\boldsymbol{\tau}_{\text{dist}}$ including unmodeled effects like friction.

The joint torque of a single joint is then often modeled as a simple linear spring-damper pair, coming from the flexible drivetrain:

$$\tau_j = k_j(\theta_m - \theta_j) + c_j(\dot{\theta}_m - \dot{\theta}_j) \tag{3.96}$$

with k being the drivetrain stiffness and c the viscous damping coefficient. This joint torque τ_j is then assumed to be measurable with a torque sensor[15].

The drivetrain is then coupled to the mechanical system of the motor with the equation

$$J_m\ddot{\theta}_m + \tau_j = \tau_m \ . \tag{3.97}$$

The dynamics of the electrical system and its current controller are often just ignored. The reason for this is that the motor torque can be easily computed using the motor constant $\tau_m = Ik_m$ and that the achievable bandwidth of the current controller is a lot higher than the possible bandwidth of the torque controller. The motor torque is therefore equal to the desired motor torque $\tau_m \approx \tau_{m,d}$ in the frequency range of interest[16].

The most popular control laws for the torque controller are:

$$t_{m,d} = \tau_d + g_P \cdot (\tau_d - \tau_j) - g_D \cdot \dot{\tau}_j \qquad \text{(P with passive D controller)} \tag{3.98}$$

$$t_{m,d} = \tau_d + g_P \cdot (\tau_d - \tau_j) + g_D \cdot (\dot{\tau}_d - \dot{\tau}_j) \qquad \text{(PD controller)} \tag{3.99}$$

$$t_{m,d} = \tau_d + g_P \cdot (\tau_d - \tau_j) + g_D \cdot (\dot{\tau}_d - \dot{\tau}_j) + g_A \cdot (\ddot{\tau}_d - \ddot{\tau}_j) \qquad \text{(PDA controller)} \tag{3.100}$$

[15] This is done differently depending on the publication. A lot of papers also assume that the measurable joint torque is just the stiffness $\tau_j = k_j(\theta_m - \theta_j)$. The reasoning being that the torque sensor will mechanically measure the torque by measuring deformations on a purposefully flexible part of the drivetrain structure. This assumes that the main flexibility in the drivetrain actually comes from the torque sensor itself. Any friction or even viscous damping coming from the mechanical system is often completely ignored for the sake of getting a simpler derivation of stability proofs. All these assumptions are just equally wrong considering how much a typical robot joint is influenced by friction. However, for the sake of simplicity, I will also do the same here and just assume that the drivetrain can be modeled and measured as described in (3.96). We did some experiments in simulation on different possible combinations, e.g. using a measured torque $\tau_j = k_j(\theta_m - \theta_j)$ while there is still unmeasured viscous damping present in the mechanical system, and the influence was not that notable as long as friction is ignored.

[16] This is a reasonable assumption. We can achieve a bandwidth of 2500 Hz with the current controllers of LOLA's joint modules, while most published torque controllers of robot joints can achieve a bandwidth in the 10 Hz range. Meaning that the motor current and therefore the motor torque is basically perfectly controlled in the frequency range of interest.

All of these controllers first use a direct feedforward term of the desired joint torque τ_d with a proportional controller[17]. The main difference between most proposed control laws is how the D part is handled. In (3.98) a purely passive term is used, which is the easiest one to prove stability for [19, 209]. However, a large passive g_D gain will also slow down the controller and its tracking performance. Using a D part to track a desired first derivative of the joint torque $\dot{\tau}_j$ (3.99) will generally improve the tracking performance, however, also requires a smoothly planned desired torque τ_d and will be more sensitive to sensor noise.

In [134] it is even proposed to use a PDA controller (3.100) with the second derivative of the desired torque $\ddot{\tau}_d$. The second derivative of the measured torque is determined using the third derivative of the measured joint position $\ddot{\tau}_j = c_j \theta_j^{(3)}$ with a state observer. However, while the tracking performance of a PDA controller is of course always superior in theory, it is rather questionable if the controller can be tuned with any reasonable amount of g_A gain in the presence of modeling errors and noise.

Since the first controller (3.98) is probably the most relevant one in practice, I will use this torque controller for any future analyses.

The gains of the controller can be derived such that

$$g_P = J_m J_{m,d}^{-1} \tag{3.101}$$

$$g_D = c_j k_j^{-1} + c_{\tau,d} k_j^{-1} \ , \tag{3.102}$$

which shapes the closed-loop response of the system like a second order system with the inertia $J_{m,d}$, stiffness k_j and damping $c_{\tau,d}$. The bandwidth of the system can then be increased by decreasing the desired inertia $J_{m,d}$. The authors of [19] could tune their controller with $J_{m,d}$ being about 1/5 of the original motor inertia J_m, until the system became unstable because of the amplification of noise[18]. For our analysis in section 4.3.2, we used a factor 1/10 to account for improved hardware and sensors.

Impedance Control

A high bandwidth joint torque controller is one of the main assumptions of most control methods discussed in Section 2.1.3. As already discussed earlier, with the current hardware it is not really possible to achieve high enough bandwidth to implement complex modern control schemes for active vibration control using the robot joints. However, a reasonable control strategy that is already implemented on most collaborative robots is *Impedance Control* (see e.g. [134]), which uses another passive PD controller for the joint position:

$$\tau_d = k_{j,d}(\theta_{j,d} - \theta_j) - c_{j,d}\dot{\theta}_j + \tau_g(\theta_j) + \tau_{d,\text{eff}} \ . \tag{3.103}$$

The PD portion of the controller essentially acts like a desired joint stiffness $k_{j,d}$ and damping $c_{j,d}$, when interacting with the robot from the outside. This is one of the main advantages of such a controller, since the robot can be tuned to behave rather softly when interacting with its environment, which makes the robot safer for operation in close proximity to human workers. In order to compensate the potentially bad tracking performance of a very soft robot joint, the control scheme includes a gravity compensation term $\tau_g(\theta_j)$. The gravity compensation can for example be computed by feeding the current joint angles θ_j into a rigid body model of the robot, which predicts the expected gravity loads $\tau_g(\theta_j)$ on each joint.

[17] Depending on how the model is derived, some people also use τ_j as a feedback instead. We found very little difference between using τ_j or τ_d for the first feedback/-forward term in our simulations for any reasonable parameters.

[18] This is of course not really different to directly tuning the PD gains, however, this gives us a nice base line for our investigation in section 4.3.2

Finally, another desired torque term $\tau_{d,\text{eff}}$ can be included to perform any form of additional action, like pressing against a wall.

For high-precision tasks, the idea for this controller is to induce a sufficient amount of damping in the robot's joints through the passive $-c_{j,d}\dot{\theta}_j$ term, reducing the dynamic error of the robot. The quasi-static accuracy would rely on a high fidelity model of the rigid body dynamics for the gravity compensation. The effectiveness of this approach will be investigated in section 4.3.2.

Chapter 4

The Influence of Structural Dynamics on Robots

The main purpose of this chapter is to gain a better understanding of the influence of structural dynamics on the dynamics at the TCP of a robot. The knowledge gained in this chapter is then used in chapter 5 to develop prototypes for the external vibration damping and external stabilization approach for high-precision trajectory tracking.

Section 4.1 will show the development of a full simulation model of a robot manipulator that includes all relevant effects like flexible links / -joints and torque-ripple at the joint motors. The purpose of this model is not to exactly replicate the dynamic error of a real robot, since that would be a quite involved task as I have already discussed in the State of the Art section 2.1. However, the model is capable of reproducing the same type of errors that are observable on a UR10 robot and is therefore useful to develop external stabilization approaches by providing a realistic representation of the dynamic coupling between the stabilization devices and the robot's structural dynamics.

Section 4.2 investigates the influence of the pose dependent structural dynamics on the driving-point dynamics at the TCP of the robot using the previously developed model and experiments on our sweet pepper harvesting robot CROPS.

In section 4.3, I will discuss our results regarding the influence of structural dynamics on the joint position- and torque-controllers of a robot manipulator. This is important, since there might be undesirable interaction between the joint controller and driving-point dynamics at the TCP of the robot, which is also influenced by the external stabilization approaches developed in chapter 5. The second subsection is about the limitations of torque-controlled robots regarding high-precision trajectory tracking and serves as another motivation for the application of external stabilization devices.

The final section 4.4 is about the influence of structural dynamics on the control system of our humanoid walking robot LOLA. This section is not absolutely necessary for the understanding of the external stabilization prototypes developed in chapter 5, however, it is still another motivational example for the influence of structural dynamics on the performance of a complex mechatronic system.

4.1 Simulation of a Robot Manipulator

In order to develop the prototypes for the external stabilization approaches investigated in this thesis, a simulation environment was needed that is capable to model a fully flexible robot manipulator with all relevant effects as described in section 2.1. The model also needed to be easily modifiable in order to add new actuators at the end effector of the robot and to efficiently test new control approaches for external stabilization. Matlab/Simulink provides all of these features, while also having the great advantages of providing all the necessary tools in the same software environment.

Matlab's *Partial Differential Equation Toolbox* gives rudimentary FEM functionality to mesh and calculate $\boldsymbol{MCK}$ models for structures based on `.stp` files and simple material parameters. Reduction methods like Craig-Bampton are also implemented within this toolbox.

The *Simscape Multibody* environment for Simulink allows a straight-forward implementation of multi body systems. Since 2019, this toolbox also includes flexible bodies based on the lumped parameters approach described in section 3.2. In version 2020a, support for reduced order models was also added.

While the provided functions are not as powerful as established structural dynamics tools like *Ansys*, *Abaqus* or *Nastran*, they are sufficient enough to include the effects of flexible links in a full robot manipulator model. The true strength of Matlab/Simulink is the easy application of its powerful *Control-* and *Linearization Toolbox* on such a flexible multi body model to develop new control approaches.

I want to stress here that the goal of this model is not to exactly replicate the behavior of an existing robot manipulator like the UR10, *Franka* Panda, ABB IRB 4600 or our CROPS robot, which were all available for testing during my time at the chair. As we will see later, all of these robots show very different behaviors unique to their specific design, which would be quite hard to model exactly, especially at the accuracy needed for this thesis. Instead, the purpose of this model is to provide a simulation test bench of a generic robot manipulator that includes all relevant effects. Since the external stabilization approaches investigated in this thesis are supposed to work with as little prior knowledge about the underlying system dynamics as possible anyway, it is not important that the developed simulation model exactly matches the dynamic behavior of e.g. the UR10 robot.

In order to be useful as a test bench, the model has to be able to correctly depict the dynamic interaction between the joint controllers and structural dynamics of a robot manipulator, as well as the dynamic interaction with an additional actuator system at the end effector of the robot. This will be verified later by investigating if the model shows approximately the same effects as a real robot, like pose dependent structural dynamics. However, without trying to exactly match the measurement results.

The following model was developed and further improved by my students and me during most of my time at the Chair of Applied Mechanics. Most notably, my student assistant OCHSENIUS helped with numerous testing activities during the early stages of the model, especially since the support for flexible links in Simscape Multibody was not very good before 2019. He is also a co-author for our papers [47, 48], which both used an early version of the model to investigate the influence of structural dynamics on cascaded joint position control and external vibration damping approaches. Furthermore, my student PRAUTZSCH contributed to the model by implementing and testing torque control methods in his semester [216] and master's thesis [217]. He is also the main author of our paper [218].

The model is implemented as Simulink library blocks, which are shown in more detail in appendix F. The general structure of the model is shown in Fig. 4.1. The model consists of joint & flexible link pairs, which can be linked together to form any kind of robot with a tree-like structure using DH-parameters.

Flexible link models

The flexible links are implemented within Simscape Multibody. Historically, there are two versions that are used throughout this thesis. The first model version is the lumped parameter model as described in section 3.2. Matlab version 2019a also added the library blocks *Flexible Beams*, which are based on the same approach and simplified the implementation effort. As of the time of writing, there are a few blocks available based on the cross section of the

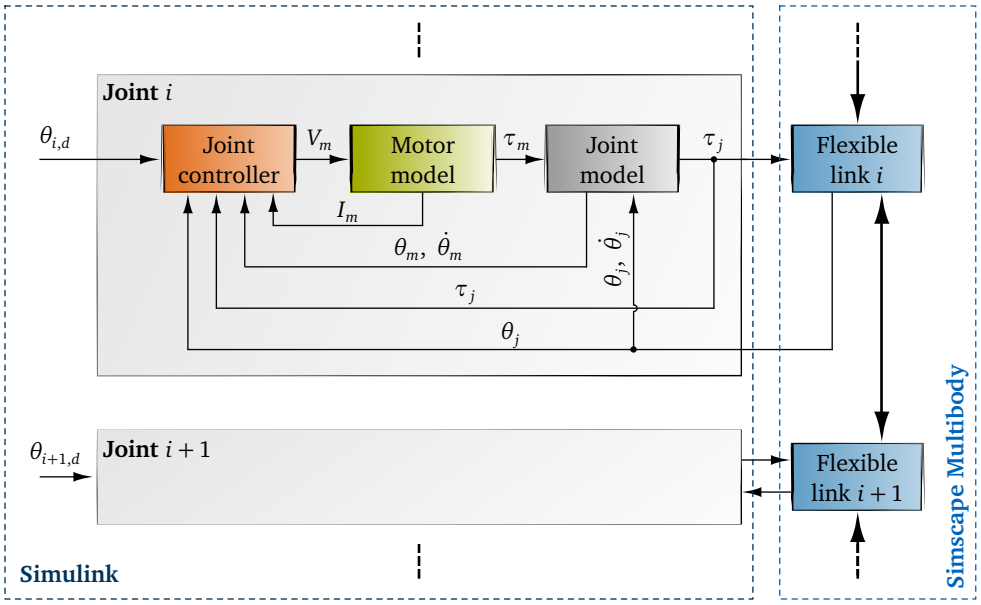

Figure 4.1: Structure of the flexible robot manipulator simulation model developed during this thesis.

flexible beam. The beam can then be parameterized by simply using the geometry, density, Young's modulus and Poisson's ratio. Damping can be specified using Rayleigh damping as described in 3.1.2, or with proportional modal damping. The main disadvantage of the lumped parameter model is that only very simple geometries are possible and that there is no coupling between external forces and orthogonal DOFs, which might exist in more complex structures.

The second method used in later versions of the model utilizes reduced order models as described in the second part of section 3.2. As of Matlab version 2020a, the workflow can be done completely in Matlab. First a $\boldsymbol{MK}$ model is created based on a `.stp` file and basic material and mesh parameters using the `createpde()` function. The interface nodes are then specified with the `structuralBC()` function. In this case, the interface nodes are always at the connection points of the joints. Finally, the $\boldsymbol{MK}$ model can then be reduced using the `reduce()` function by specifying a upper bound for the highest frequency mode in the reduction bases. The resulting reference frame location-, mass- and stiffness matrices can then be used in the Simscape Multibody block *Reduced Order Flexible Solid*. The damping can be specified in the same way as in the *Flexible Beams* blocks.

Both approaches were tested on a simple fixed-free beam problem by comparing the static solution to a constant force, as well as the driving-point transfer function at the tip of the beam to the results generated in *Ansys*. In general, both approaches perform quite similar if a high enough number of elements / large enough reduction basis is used. However, we found that the reduced order model is a bit more accurate, while also more computationally efficient when using more heavily reduced models [217]. More importantly, the reduced order model is also capable of modeling more complex structures, while also being able to correctly model the coupling of orthogonal DOFs. For these reasons, we always used the reduced order model for later publications[1].

Since most of the tests for the stabilization unit were done on the UR10, we also based the simulation model on the DH- and inertia parameters of this robot, which are published at

[1] I will specify which model was used at the appropriate places. Since we always used quite simple structures like the simple pipe shaped links of the UR10, there was no significant difference between the results of these two approaches for the topics of this thesis.

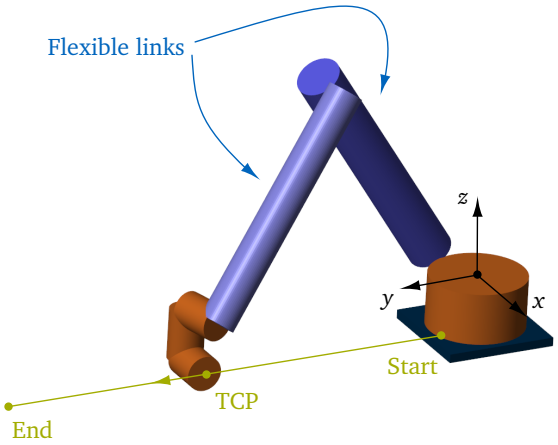

Figure 4.2: Robot model with flexible joints and links in Simulink/Simscape Multibody based on the UR10.

e.g. [277]. In order to save computational costs, we only modeled the first two main links as flexible bodies, since these have the largest contributions to the overall flexibility of the link structures, Fig. 4.2.

The flexible multi body system is then driven by joint torques τ_j produced by the joint model.

Joint Model

All further models are implemented in Simulink. The joint model is a simple spring-damper pair for each joint to model the drive train flexibility, as it is common practice in most publications concerned with the flexibility of robots. However, the model also considers the gear ratio N, which is important to correctly model the weak coupling between the motor axis and dynamics at the TCP of the robot, as we will see later:

$$\begin{bmatrix} J_m & 0 \\ 0 & 0 \end{bmatrix} \begin{bmatrix} \ddot{\theta}_m \\ \ddot{\theta}_j \end{bmatrix} + \begin{bmatrix} c_j & -c_j\,N \\ -c_j\,N & c_j\,N^2 \end{bmatrix} \begin{bmatrix} \dot{\theta}_m \\ \dot{\theta}_j \end{bmatrix} + \begin{bmatrix} k_j & -k_j\,N \\ -k_j\,N & k_j\,N^2 \end{bmatrix} \begin{bmatrix} \theta_m \\ \theta_j \end{bmatrix} = \begin{bmatrix} \tau_m \\ \tau_j \end{bmatrix}. \tag{4.1}$$

With J_m being the motor inertia, k_j the joint stiffness and c_j the viscous damping factor of the joint. The model sends the joint torque τ_j to the FMBS in Simscape and receives the current joint position / velocity θ_j, $\dot{\theta}_j$. The model is driven by the motor torque τ_m from the motor model.

The gear ratio is set to $N = 100$ for all joints. The damping c_j and stiffness k_j parameters are tuned by hand using torque measurements from the *Franka* Panda, which we acquired during our investigation of torque controlled robots as discussed in section 4.3.2. The main reason for this is that the Panda was the only robot available to us with a torque sensor, which is the most sensible output to use for tuning such a model.

I already commented in section 2.1 that just using viscous damping is a gross oversimplification of the complex friction, stick-slip and backlash effects in a robot joint drivetrain. For example my student *Zimmermann* tested multiple friction models for *ABB* in her master's thesis [312] and achieved the best results with the more complex LuGre model. However, this was still with the goal in mind to achieve the best possible modeling result for a robot control system using the motors of the robot. The external stabilization approaches investigated in this thesis have the great advantage that they are barely influenced by the complex dynamic

behavior inside of the joint, which is one of the great strengths of this concept. Since the use of any more complex friction models did not effect the development or end result of the stabilization unit in section 5, I decided to refrain from using more complex friction models in this thesis[2].

Motor Model

The motor model is the basic BLDC motor model described in section 3.4 and uses identified inductance and resistance parameters from the joint modules of our walking robot LOLA[3]. During our measurements with an *ABB* IRB 4600 robot we also noticed that one of the most significant excitation sources for robot joints is torque ripple / motor cogging. This is also considered in this model as a rough approximation by adding an harmonic disturbance torque to the motor torque τ_m:

$$\tau_{i,\text{cog}} = \sum_{n=1}^{3} A_{c,n} \sin\left(\dot{\theta}_m n t\right), \tag{4.2}$$

with $\tau_{i,\text{cog}}$ being the cogging torque from the i-th joint and $A_{c,n}$ the amplitude of the n-th cogging harmonics. The cogging frequency is proportional to the motor velocity $\dot{\theta}_m$ with n higher harmonics. For this model, only three harmonics are considered. The amplitudes $A_{c,n}$ are tuned by hand to get similar relative error amplitudes at the TCP as in the measurements performed on the UR10.

As discussed in section 2.1.2, the real disturbances acting on the drivetrain of the joint are of course a lot more complex. However, since we only want to test the robustness and performance of the external stabilization approaches developed in section 5 against any form of disturbance acting on the motor side of the drivetrain, we do not need a more complex model of these effects.

Joint Controller

The joint controller for most parts of this work is the industry standard cascaded P-PI-PI motor position controller described in section 3.4. For our investigation of the influence of structural dynamics on torque-controlled robots, we used the most recent torque-controller published by [134] and described in section 3.4.2.

4.1.1 Verification Experiments

In order to verify that the model produces reasonable results, we let the model perform a 1 m long horizontal trajectory from a completely retracted pose to a stretched out pose, Fig. 4.2. The trajectory is planned with constant velocity in order to produce a high jerk motion at the beginning and the end of the trajectory. While not very practically relevant, this is done to

[2] However, I would still strongly advise to consider better friction models, if one is truly interested in improving the general performance of joint position or torque controllers.

[3] With the motor model tuned using measurements from our walking robot LOLA, the joint model tuned with data from the *Franka* Panda and the DH- and inertia parameters taken from the UR10 robot, this is starting to look like Frankenstein's robot model. However, I want to reiterate here again that the goal is to have a generic robot model that is only able to represent the behavior of a robot realistically enough to develop external stabilization methods. The goal is not to exactly model the behavior of a specific robot model. The most sensible approach to me was therefore to use the best possible measurement data available to us to tune and verify subcomponents. The reasoning being that a robot created from verified subsystems will show a realistic enough global dynamic behavior to be useful.

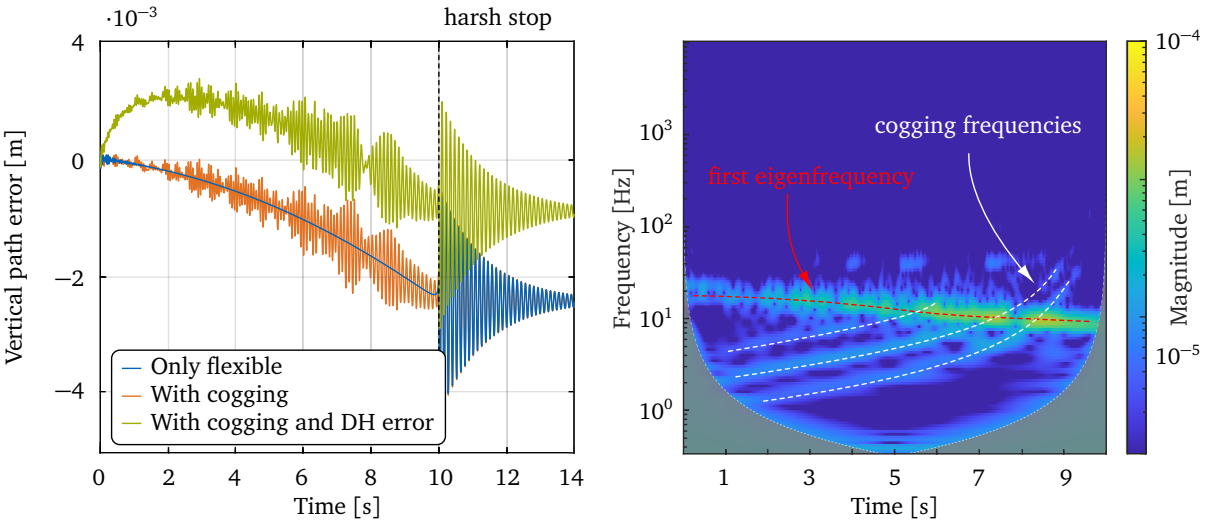

(a) Simulated vertical path error at the TCP of the robot with different error sources.

(b) CWT of the simulated vertical path error with cogging and DH error.

Figure 4.3: Simulation of a 1 m long horizontal trajectory at 100 mm/s speed.

provoke high excitation forces at the beginning and the end to test the effectiveness of the stabilization approaches under extreme conditions.

The simulated vertical path error at the TCP of the robot during this motion is shown in Fig. 4.3. The blue line shows the result of the model without any additional error sources like motor cogging. The model shows a short vibration response at the start due to the high jerk at the beginning of the trajectory. The TCP then continuously sags downwards due to the flexibilities in the system. At the end, the robot shows a large vibration response due to the sudden stop at the end of the trajectory.

Comparing this to the actual measurements at the UR10 robot performing a similar trajectory (Fig. 4.4a), we find that the model response is missing a lot of vibrations during motion[4]. The real robot also does not continuously sag downwards.

Adding motor cogging to the robot model results in more similar behavior of the simulated robot to the measurement (Fig. 4.3a orange line). We can also produce a similar raising motion at the beginning of the trajectory by adding a random 2 % error to the DH parameters of the robot during trajectory planning (Fig. 4.3a green line). The sagging of the real robot is still a bit more complex, showing multiple short plateaus during the trajectory. This is probably a combination of multiple small manufacturing errors as well as effects like backlash in the robot joints, which would be quite hard to model. However, the model now shows a more similar error behavior at the TCP to the measurements from the real robot, which was the goal of this model.

We can also analyse the error in a bit more detail by performing a continuous wavelet transform (CWT) on the error data[5]. Fig. 4.3b shows the CWT of the simulated robot before the harsh stop at 10 s. We can see how the vibration response is a superposition of the particular response of the system to the excitation caused by motor cogging, and the har-

[4]The measurements are performed using highly precise eddy-current sensors measuring against a reference surface. The procedure is explained in more detail in section 5.2. We do not perform a trajectory with constant velocity to protect the robot, meaning that the measurement is missing the sudden stop at the end.

[5]A CWT is an advanced short time Fourier transformation (STFT), which gives information about the frequency content in a signal over time. The problem with a normal STFT is that there is always a compromise between time and frequency resolution, which is often particularly inconvenient for low frequency content. The CWT offers a better compromise by having a frequency dependent time resolution. For more information see e.g. [9, 225].

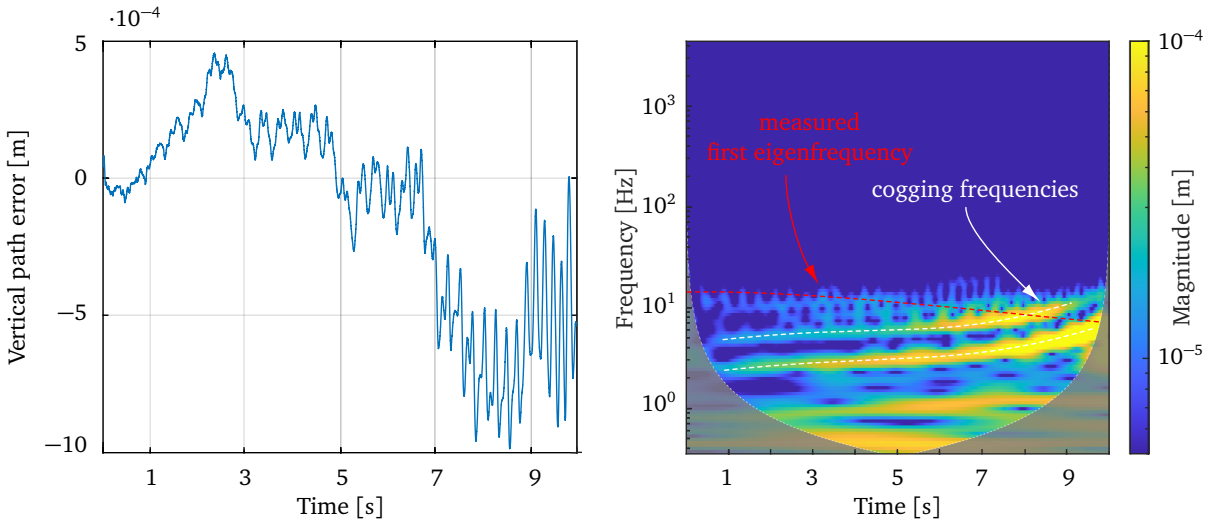

(a) Measured vertical path error at the TCP.

(b) CWT of the measured vertical path error.

Figure 4.4: Measurement of a 1 m long horizontal trajectory at 100 mm/s speed using the UR 10 robot with eddy-current sensors at the TCP.

monic response from the first structural eigenfrequency. We can already see here that the first eigenfrequency depends on the pose of the robot and starts at around 20 Hz and then continuously lowers to 10 Hz (we will analyse this in more detail in the following section). The robot shows a particularly large response when one of the cogging frequencies hits the first eigenfrqeuency. The response to higher eigenfrequencies is not visible in this diagram, since we are looking at position data that only shows very low vibration amplitudes for high frequency content.

The CWT of the measurement of the same trajectory on the real robot is shown in Fig. 4.4b. We can see that the real response is mostly dominated by the particular response of the robot to the excitation of the cogging frequencies. This is probably because of the UR10 robot having more damping than our model, keeping the harmonic response well suppressed during most of the motion. However, after second 6 of the motion, the second cogging frequency comes close to the first eigenfrequency, causing a larger vibration response in that particular part of the CWT. The change of the cogging frequencies is a bit different than in our model, which is probably because of the UR10 robot having lower gear ratios than $N = 100$. The cogging frequencies also do not have the same steep raise at the end of the trajectory, since the UR10 trajectory was planned with significantly less jerk in the end.

For even lower speeds of the UR10 robot (e.g. 30 mm/s shown in Fig. 4.5) all cogging frequencies are well below the first eigenfrequency of the system up to 30 s. In this case, a prediction of the error at the TCP using the motor angles of the robot with pure forward kinematics could probably work quite well, since the system responds quite rigidly to the low excitation frequencies[6]. For lower speeds, the dynamic accuracy of the robot could probably significantly be improved by reducing motor cogging by e.g. using a better drive system.

The first eigenfrequency of the UR10 robot was determined by measuring the driving-point transfer function at the TCP of the robot using impact measurements[7]. The pose of the robot is gradually changed along the planned trajectory and the measurement is performed at 30 different poses. The resulting transfer functions are shown in the Campbell-like diagram

[6]We noticed something similar for the *ABB* IRB 4600 robot, which also showed a quite rigid response for low speeds. However, this robot has a lower eigenfrequency due to its weight, which causes its structural dynamics to be excited by the cogging frequencies at any reasonable speed.

[7]The procedure is explained in more detail in section 4.2.1.

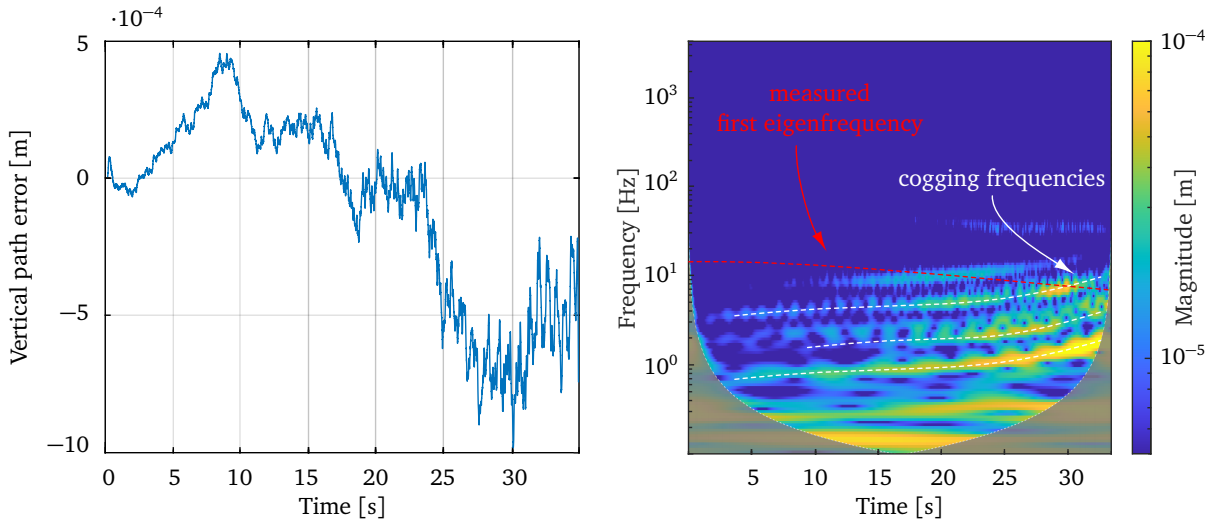

(a) Measured vertical path error at the TCP.

(b) CWT of the measured vertical path error.

Figure 4.5: Measurement of a 1 m long horizontal trajectory at 30 mm/s speed using the UR 10 robot with eddy-current sensors at the TCP.

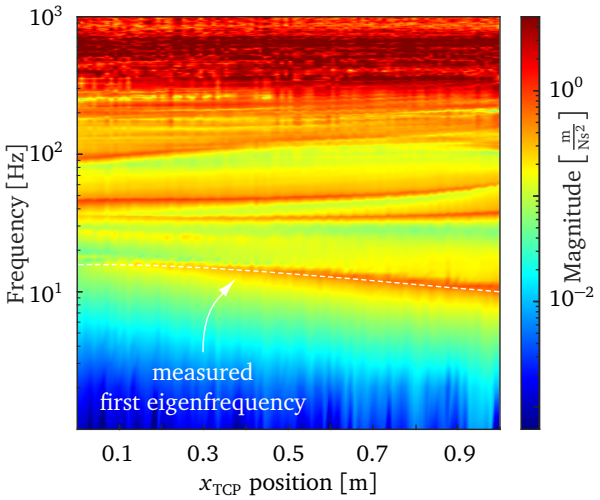

Figure 4.6: Campbell diagram of the driving-point measurement at the TCP of the UR 10 robot in z direction while moving the robot along a 1 m horizontal trajectory.

Fig. 4.6, which plots a heat map of these transfer functions depending on the current TCP position of the robot. The first measured eigenfrequency shows quite similar behavior to the simulation results. However, we will see in the following section that the higher-order dynamics do not match as well. This is most likely because the measurements were performed with the stabilization unit prototype attached to the robot, while the following simulation results were generated with just the unloaded robot.

Although the model is not capable of perfectly reproducing the exact measured error profile of the UR10 robot, it still clearly shows very similar behavior. As we will see later, the model was very useful in the development of the stabilization unit, since we could test the dynamic interaction between the additional actuator system and its controller with a generic flexible robot.

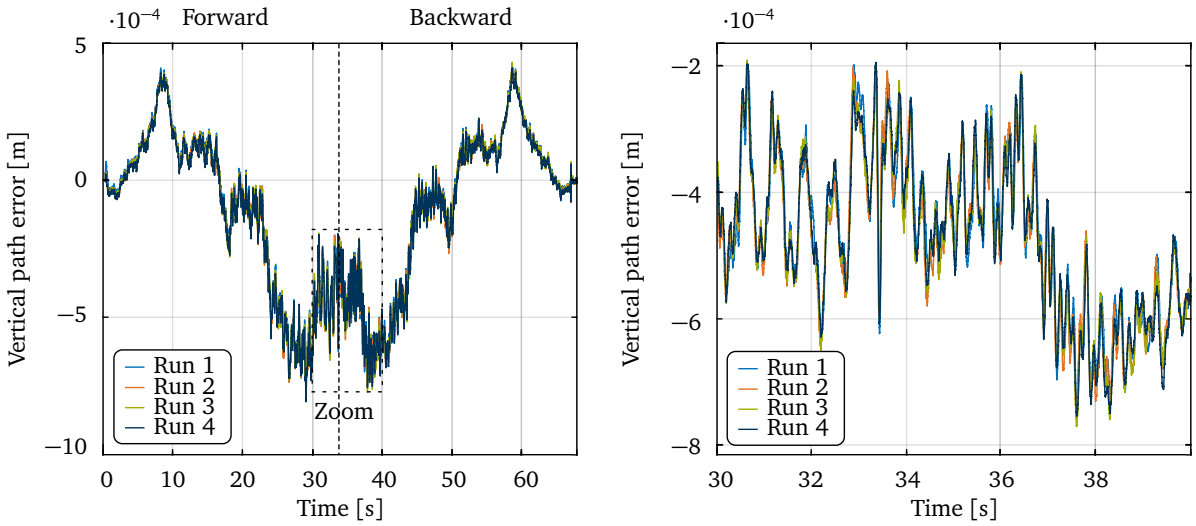

(a) Horizontal path error.

(b) Zoom at the turning point from forwards to backwards motion.

Figure 4.7: Repeated measurements of a 1 m long horizontal trajectory at 30 mm/s speed using the UR 10 robot with eddy-current sensors at the TCP.

Repeatability

Let us finally also have a look at the repeatability of the UR10's behavior. Fig. 4.7a shows again the measured vertical path error during a 1 m long horizontal trajectory at 100 mms^{-1} speed. This time, we also measure the robot moving backwards with the same settings. Fig. 4.7b shows a zoom at the middle portion of the measurement, where the robot stops the forward motion and starts to move backwards.

The test is repeated four times with the same starting conditions and settings. We can see that even the dynamic behavior of the robot is very well reproducible up to about 50 μm. This is somewhat reassuring, since we are not dealing with chaotic phenomena, but clearly systematic behavior. This indicates that, given a better understanding of the effects in the drivetrain and other subcomponents, we might be able to reproduce this behavior using sophisticated simulation models.

I want to stress here that it would not be enough to just measure this error profile to apply a calibration method as described in section 2.1.1. This might reduce the quasi-static error, as we have already seen before. However, there are still multiple problems regarding the dynamic error: First of all, a pure feedforward approach based on a measured error profile does not take the dynamic interactions within the system into account. This means, if we would use this error profile to compensate the error with the robot's motors, we would change the input of the system. Therefore, the dynamic error of the robot would respond differently to the error profile measured before, which would probably strongly reduce the effectiveness of this approach. In order to properly apply a feedforward based method, we would need a model that is also capable of reproducing the correct response for all other possible inputs, which is a much more involved task than just measuring the error profile once. More importantly, most robot joints would not be capable to follow such highly dynamic desired motions anyway, since the control bandwidth of the joint controllers on the joint side is quite limited (see section 4.3).

4.2 Pose Dependent Structural Dynamics of Robot Manipulators

Apart from the very complex joint dynamics of a real robot, the pose dependent structural dynamics is another challenging problem for high-precision robot control. We have already seen this in the previous section in the CWT of the simulated horizontal trajectory Fig. 4.3b, or the measured Campbell diagram of the UR10 robot Fig. 4.6. In this section, I want to give a bit more detailed look at the pose dependent structural dynamics of the simulated model. In subsection 4.2.1, I will show measurements of the structural dynamics of our CROPS robot to verify that we can also find similar effects on a different type of robot manipulator.

Let us first have a look at a few Campbell diagrams for different trajectories of the simulated model Fig. 4.8. The robot performs a horizontal, diagonal and vertical trajectory (Fig. 4.8a), with all of them being in the same plane parallel to the y-z-inertial coordinate axes. Each trajectory is evenly split into 100 poses and the model is linearized at each pose to generate the driving-point transfer function $\ddot{z}_{\mathrm{TCP}}/f_{\mathrm{TCP,z}}$ at the TCP of the robot. The output acceleration $\ddot{z}_{\mathrm{TCP}}$ and input force $f_{\mathrm{TCP,z}}$ are measured in the inertial coordinate frame.

Fig. 4.8b shows the 100 linearized transfer functions for the horizontal trajectory in a Campbell-like diagram depending on the distance of the TCP to the starting point of the trajectory. We can see that the dynamics of the system significantly change depending on the pose. The most dominant one is the first eigenfrequency, which starts at around 18 Hz and then moves down to 8 Hz. In general, the frequency and change of the first eigenfrequency is in the same ball park as the measured one of the UR10 in Fig. 4.6. We can also see a few more changing eigenfrequencies between 10 Hz and 100 Hz, however, with significantly less amplitude than the first one. That is probably why there are no more eigenfrequencies visible in the measured Campbell diagram Fig. 4.6: With the real system having a bit more damping, these poles are probably too attenuated to show up in a simple impact measurement. The next mode with high amplitude shows up at around 100 Hz, which is also visible in both the measurement and simulation. Overall, the global dynamic behavior of the model matches quite well with the measurements. That is also thanks to the quite simple design of the UR10 robot, since structures with similar topologies will always also show a similar dynamic behavior. This is also why the structural dynamics of robots do not scale very well: Most robot structures have a first eigenfrequency around $7-15$ Hz regardless of their size. A larger robot might have more stiff components, however, it will also be heavier and still have a tree like topology, bringing its eigenfrequencies again in the same range as most other robot manipulators.

Since the desired control bandwidth of the stabilization system is around 50 Hz (see section 1.1), we probably only have to deal with the first eigenfrequency for the horizontal trajectory when using a robust control scheme. However, both the diagonal (Fig. 4.8c) and vertical (Fig. 4.8d) trajectory show additional changing eigenfrequencies with significantly higher amplitudes. This underlines the difficulty of the control problem: An additional stabilization system at the TCP of the robot has to be either very robust against those changing system dynamics, or somehow be able to adapt to them without requiring too precise knowledge about the underlying system dynamics. Remember that we are able to reproduce similar effects with our model, however, the exact dynamic behavior is still quite off (e.g. Fig. 4.4a compared to Fig. 4.3a or Fig. 4.6 compared to Fig. 4.8b). Any kind of control scheme that is based on precise system models is probably not very effective on the real robot, or will have significant robustness issues[8].

Control methods that rely on the control system of the robot itself will have to face even harder obstacles, since they also have to deal with the quite complex dynamics of the driv-

[8] I will summarize our efforts to make modern control methods work in section 5.1.5.

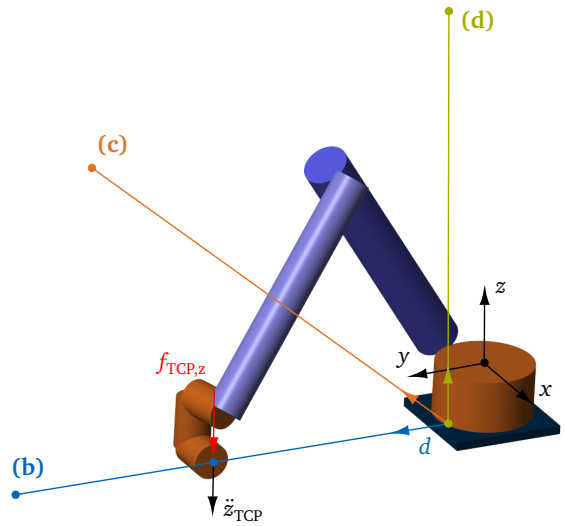

(a) UR10 model following three different straight trajectories.

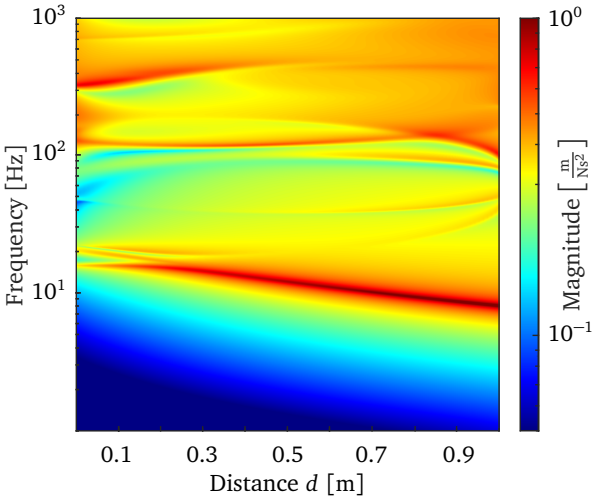

(b) Campbell diagram of the transfer function $\ddot{z}_{TCP}/f_{TCP,z}$ for the horizontal trajectory.

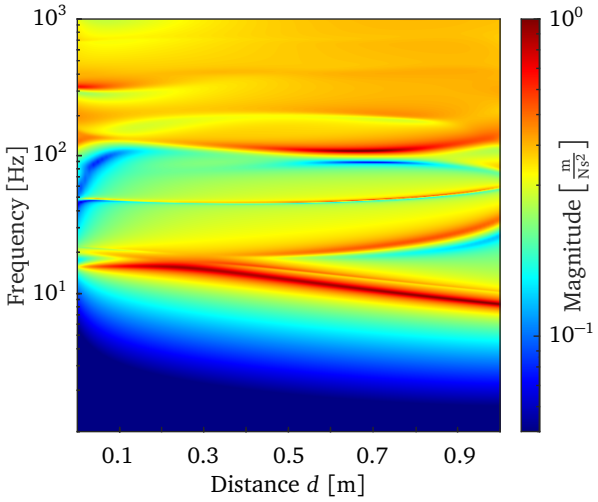

(c) Campbell diagram of the transfer function $\ddot{z}_{TCP}/f_{TCP,z}$ for the diagonal trajectory.

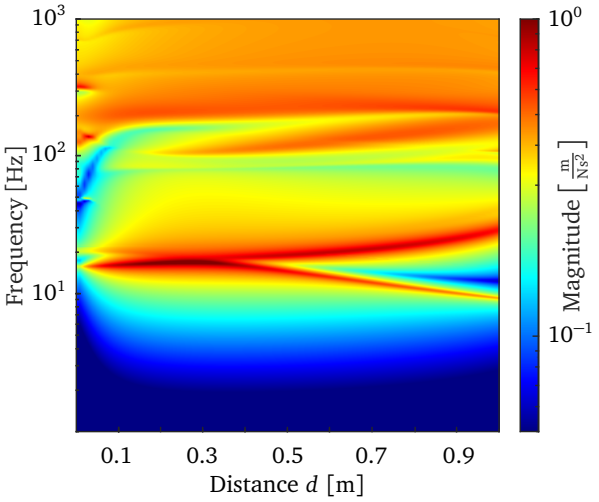

(d) Campbell diagram of the transfer function $\ddot{z}_{TCP}/f_{TCP,z}$ for the vertical trajectory.

Figure 4.8: Demonstrating the pose dependent structural dynamics of the robot model via the driving-point transfer function $\ddot{z}_{TCP}/f_{TCP,z}$ (measured in the inertial coordinate frame).

etrain and then additionally have to somehow properly control the structural dynamics of the robot. Additionally, because of the usually quite high gear ratios, the dynamics of the drivetrain and joint controllers have very little influence on the driving-point dynamics at the TCP (which are the control plants for any external stabilization approach). We will see this in the following experiments and also analyse the influence of the joint controllers in more detail in section 4.3.1.

4.2.1 Verification Experiments on the CROPS Robot

To verify this behavior, and also to get some hands-on experience with the structural dynamics of robot manipulators, my students and I did a series of experiments on our sweet pepper harvesting robot CROPS. This subsection is based on our paper [46]. My student FUDERER also did some preliminary work during his bachelor's thesis [99].

Figure 4.9: Our sweet pepper harvesting robot CROPS in 9 DOF configuration [215].

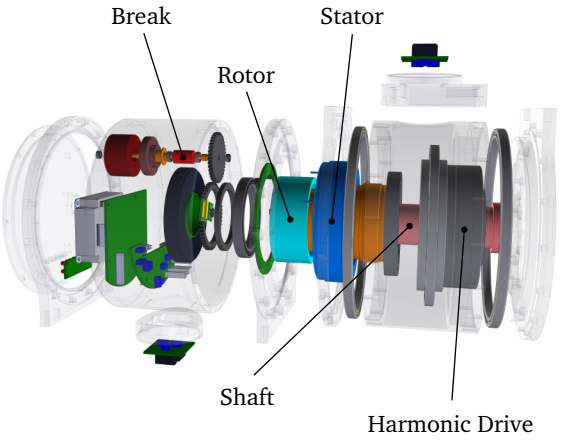

Figure 4.10: Assembly of one of the CROPS robot's joint modules. Adapted from [215].

The robot was initially developed at our Chair in 2012 during the European project *Clever Robots for Crops* for the purpose of automated sweet pepper harvesting [29]. Since then, the robot has further been utilized for the development of new methods for motion planning and adaptive motion control of redundant manipulators in uncertain environments based on tactile feedback [235, 267], estimation of joint torques [236] and teleoperation. In 2018 and 2019, we also did a new series of field tests to evaluate the harvesting performance of the robot [123] and built a new gripper prototype [144].

The robot's base is attached to one large prismatic joint for vertical movement and otherwise consists of rotary joints [276], Fig. 4.9. The design of the joint modules is similar to typical robot joints, utilizing harmonic drive gears and a breaks on the motor side [215], Fig. 4.10. The joints are controlled using a decentralized joint position control scheme as explained in section 3.4.1. The robot can be assembled in a 7 or 9 DOF configuration, thanks to its modular design.

Experimental Setup

The robot is used in its 7 DOF configuration for the following experiments, Fig. 4.11. In this configuration, the robot consists of three large rotatory joints for the positioning of the TCP and three small joints for its rotation, making it quite similar to most industrial robot manipulators. The base of the robot is attached to the first large linear joint.

To analyse the pose dependent dynamics of the robot, the poses are gradually changed from a fully stretched out position to a completely retracted pose while rotating around the z-axis of the inertial coordinate system, Fig 4.11. The vertical position of the first prismatic joint is kept the same for all tests. An Experimental Modal Analysis (EMA) will be performed at the three poses shown in Fig 4.11 with the specific joint angles:

Pose 1:	$\theta_2 = 0°$,	$\theta_3 = 0°$,	$\theta_4 = 0°$,	$\theta_6 = 0°$.
Pose 2:	$\theta_2 = 45°$,	$\theta_3 = -30°$,	$\theta_4 = -75°$,	$\theta_6 = -45°$.
Pose 3:	$\theta_2 = 90°$,	$\theta_3 = -60°$,	$\theta_4 = -150°$,	$\theta_6 = -90°$.

All tests are performed by measuring FRFs using a *PCB* impact hammer and *Kistler* triax acceleration sensors with 100 mV/g sensitivity and 6 g of weight. We could also have used sensors with higher sensitivity and less bandwidth, since we were mainly only interested in

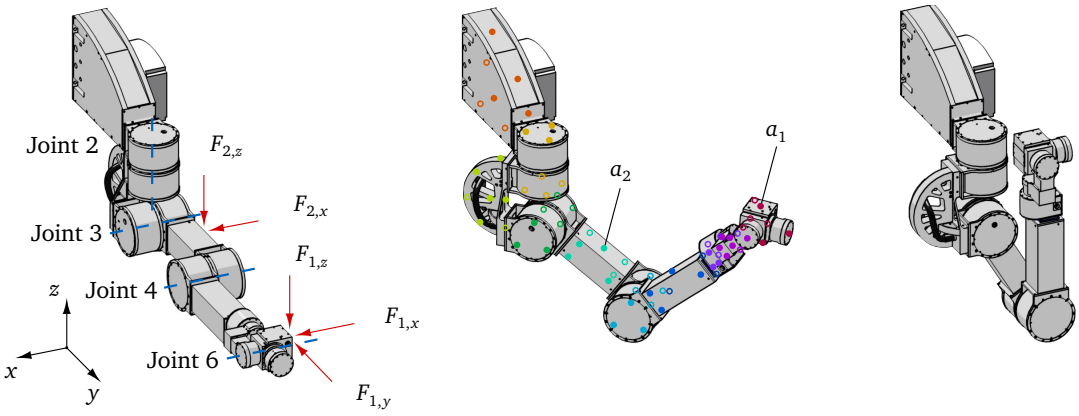

(a) First pose with joint numbers and excitation forces.

(b) Second pose with measurement points. One color per measurement run.

(c) Third pose.

Figure 4.11: Experimental setup with the CROPS robot in 7 DOF configuration. Adapted from our paper [46].

the frequency range of up to 100 Hz. However, sensors with higher sensitivity are usually also significantly heavier and might influence the system response due to the added mass effect [92]. The chosen sensors are a good compromise between weight and sensitivity for this application.

Impact locations for the input measurements are near the TCP and between the third and fourth joint of the robot, Fig. 4.11. Because of the high amount of measurements needed for the following experiments, we preferred an impact hammer with 0.3 kg mass as excitation source[9]. A *Siemens* LMS system with 24 channels is used for data acquisition, allowing seven triax sensors to be used per measurement run. For the EMA, one measurement run is performed per link and joint of the robot, resulting in overall 11 measurement runs with 77 measurement points for each pose, Fig. 4.11. The output acceleration sensors used for the other tests are located near the TCP (a_1) and between joint three and four (a_2), Fig. 4.11.b. The EMA is performed using the LMS Impact Testing sofware with the PolyMax algorithm [214]. All further post-processing is done in Matlab.

Preliminary Tests

To setup the measurements, we first performed the typical initial tests. For the impact hammer, we tested three different hammer tips, Fig. 4.12a. The metal tip will excite the highest frequency range, however, with the least amount of energy in the frequency range of interest below 100 Hz. It will also often cause nearby sensors to reach overload during the impact, making the ranging process between measurements quite cumbersome. The rubber tip is able to excite the targeted frequency range best, however, falls below −10 dB right after the 100 Hz mark. In order to still have some margin for higher frequencies, we chose the vinyl tip, giving the best compromise between bandwidth and input energy for the frequency range of interest.

The impulse response of sensor a_1 in the z direction after an impact at the TCP in the same direction is shown in Fig. 4.12.b. Using a measurement window of 2 seconds provides a good signal to noise-ratio, without having to apply any kind of extra windowing, which

[9]Such a light hammer will usually not be able to introduce enough energy for a reasonable response of a larger industrial robot manipulator. These larger structures usually have to be excited using a much heavier impact hammer or a shaker, which is more inconvenient to use. As we will see shortly, the small weight hammer used for these experiments was good enough in this case.

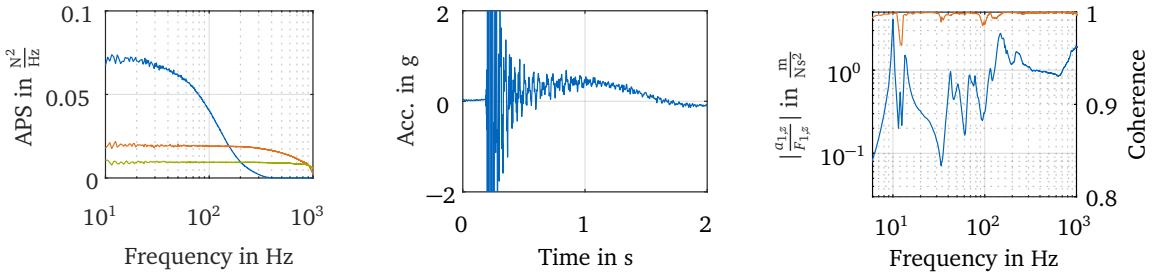

(a) Auto power spectrum of the hammer tip force measurement with rubber (orange) vinyl (orange) and metal (green).

(b) Time signal of sensor a_{1z}.

(c) Driving point FRF at the TCP (blue) and coherence (orange).

Figure 4.12: Initial test measurements after an $F_{1,z}$-impact to setup the EMA. Adapted from our paper [46].

results in an acceptable frequency resolution of 0.5 Hz for the FRF measurements[10].

A test driving-point measurement at the TCP in z-direction is shown in Fig. 4.12.c. The measured FRF shows very good coherence after five averages, never dropping below 0.95 over the entire frequency range. The first mode appears to be around 10 Hz, making the used frequency resolution of 0.5 Hz just about sufficient. We maintained the bandwidth for all following measurements at 1024 Hz, however, all following FRF's will be zoomed in on the 200 Hz range, since we are mainly interested in this frequency range.

Repeatability and Influence of Temperature

Considering the complexity of the mechanical structure of a typical robot manipulator, the first area of interest for us was the repeatability of FRF measurements using impact testing. We tested this by taking a reference driving-point measurement at the TCP of the robot in all directions for the three main poses. We then repeated the measurements after moving the robot into a different pose and back into the reference pose using its control system. We did another test measurement in the same poses, after leaving the robot turned off for a day in a different pose. Fig. 4.13 shows a comparison of the three measured FRFs in z - direction at the stretched out pose, showing a good agreement of the measurements between the pose changes, indicating a very good repeatability of the measurements. This is also the case for the other poses that we measured.

Since the robot joints of the CROPS robot significantly heat up during longer operation, we also tested the influence of the temperature on the FRF measurements. We again compared a reference measurement in multiple poses with cold robot joints to a second set of measurements taken after the robot was in operation for 30 minutes. A selected result is again shown Fig. 4.14. There is some visible change to the measured FRF, however, the influence is overall not very significant over all test measurements.

Non-Linearity and Influence of the Joint Controller

Another issue I was concerned about is the possibility of non-linear behavior of the force to acceleration transfer function at the TCP of the robot, which is the control plant for both

[10]The slow 'drift' visible in the impulse response is caused by the robot being mounted on a very heavy damped experimental table. The table is isolated from the building using four highly damped pneumatic springs. However, the system still shows a slow reaction to an impact, basically reacting like a very heavy single harmonic oscillator. The resonance frequency of the table's suspension is low enough (< 0.5 Hz) that it does not interfere with the measurements performed here, with the first frequency of interest being the first resonance of the robot at 10 Hz.

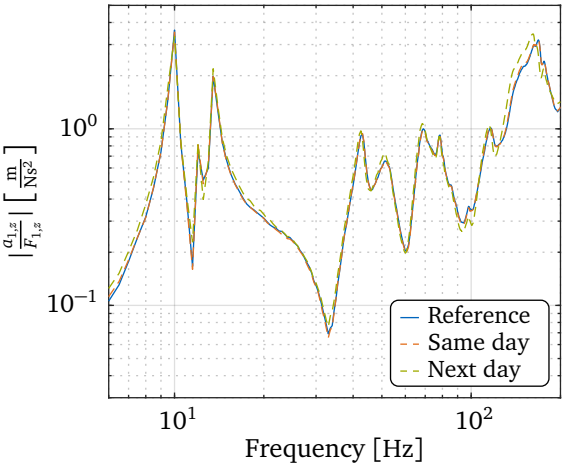

Figure 4.13: Comparison between a reference measurement, after a significant pose change on the same day and a pose change after one day. Adapted from our paper [46].

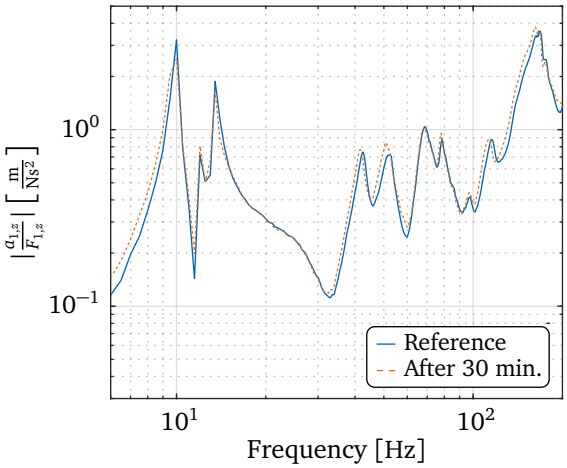

Figure 4.14: Comparison between a reference measurement and after 30 minutes of operation. Adapted from our paper [46].

stabilization approaches investigated in this thesis. To do simple test, we compared the same FRFs as before, measured with a large and low amount of impact force, Fig. 4.15. We can see that there is some non-linear behavior depending on the amount of input force, however, mostly for higher frequency modes above 40 Hz. The first two resonance peaks are mainly unaffected. The reason for this will become more clear, when I discuss the mode shapes of the system in the EMA section.

There are definitely some visible non-linearities for large differences in input forces, however, the pose dependent structural dynamics of the robot ultimately proved to be the much larger challenge for any potential control approach. For all further measurements, we made sure to check that the spectrum of the impact force was always similar.

Finally, we also tested the influence of the joint controller on the driving-point FRF at the TCP of the robot by measuring again the same FRFs in the same poses, once with the breaks engaged and once with the joint angles held by the joint controllers, Fig. 4.16. The controller only seems to have an effect on the damping of the mode around 40 Hz, which also seems to be consistent with the mode shapes acquired with the following EMA. This behavior can also only be observed for the completely stretched out pose.

Influence of the Pose on the TCP Dynamics

One of the main interests for these experiments was to measure the pose depended structural dynamics of the robot at its TCP. In order to test this, we measured the driving-point measurement at the TCP of the robot for all three directions for 60 poses in total, while gradually changing the pose of the robot starting from pose 1 through pose 2 till pose 3. We started with pose 1 and then increased the joint angles in the following increments:

$$\Delta\theta_2 = 1.5°, \quad \Delta\theta_3 = -1.0°, \quad \Delta\theta_4 = -2.5°, \quad \Delta\theta_6 = -1.5°.$$

The breaks were engaged for all measurements. The results are plotted in a Campbell-like diagram by plotting the measured FRFs on a heat map depending on the current pose, Fig. 4.17.

It is quite obvious that the structural dynamics of the robot are significantly dependent on its current pose. The first mode at 10 Hz barely changes its frequency, however, it loses a lot

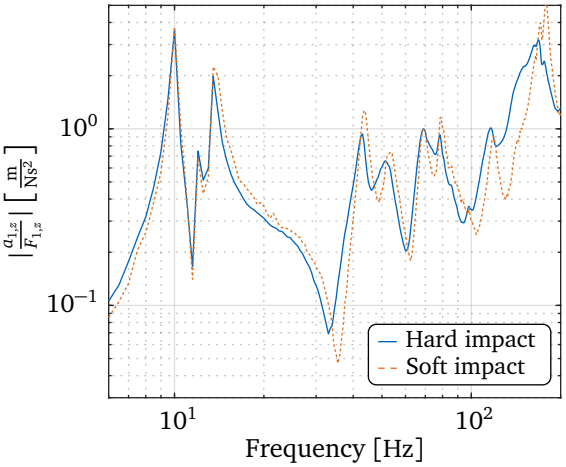

Figure 4.15: Comparison between a FRF obtained after a hard and a soft impact. Adapted from our paper [46].

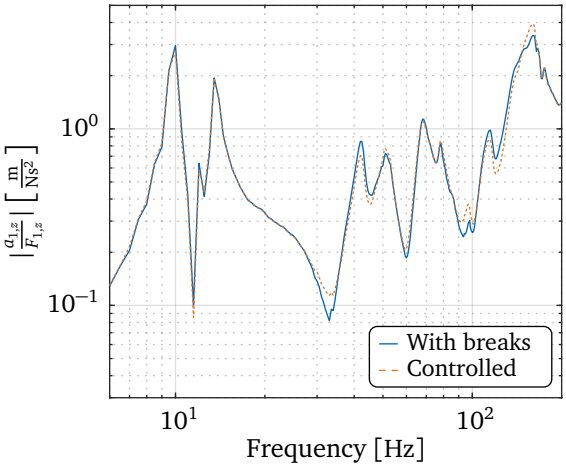

Figure 4.16: Comparison between a FRF obtained with engaged breaks and with activated joint controller. Adapted from our paper [46].

of amplitude after passing the second main pose. The second mode starts around 13 Hz and then gradually increases to 20 Hz. The third mode starts at 40 Hz and changes the most in frequency. This mode also has two short nodes in the amplitude before the second and right between the second and third main pose. The EMA revealed that these nodes also mark a significant change in the corresponding mode shape. E.g. the mode shape of the third mode starts as a bending mode in the y-z-plane mainly and then abruptly changes to a torsion mode around the axis of the second joint right before the second main pose.

These measurements also highlight the complexity of the structural dynamics of a robot manipulator. This poses a particular challenge for modern control methods, which often depend on accurate models for robust performance.

Experimental Modal Analysis

Finally, the EMA is performed for the three main poses shown in Fig. 4.11. A good way to check the quality of the identified model is by examining the synthesized FRFs produced by the PolyMax algorithm, Fig. 4.18. The plot shows two FRF measured by an impact in z-direction at the TCP to the a_2 sensor in x- and z-direction, respectively. The synthesized FRFs are plotted as dotted lines in the same color. Both FRFs show a very good agreement with the measurement in amplitude and phase, which is also the case for all other transfer functions measured for the EMA, indicating a good result of the EMA.

The acquired mode shapes are shown in Fig. 4.19. The first mode at 8.6 Hz is a horizontal bending mode in the x-y-plane caused by torsion of the "C"-shaped link between joints 2 and 3. This mode does not show up in the Campbell diagram (Fig. 4.17), since it can not be excited by an impact in z-direction, making it uncontrollable for these kind of inputs. The mode is mainly caused by the bending of the link between the first and second joint of the robot and the "C"-shaped link between joint 2 and 3. The rest of the arm stays almost completely rigid for this particular mode shape, and no bending of the joints is observed.

The second mode at 10 Hz is the first bending mode in the y-z-plane. This mode is mainly caused by bending of the large prismatic joint 1, with no actual deformation of the robot arm itself. This is also why this mode does not change its frequency, but only loses amplitude in the Campbell-diagramm Fig. 4.17: By gradually retracting the robot arm, the lever of the impact excitation at the TCP with respect to the large linear joint is reduced. The joint itself

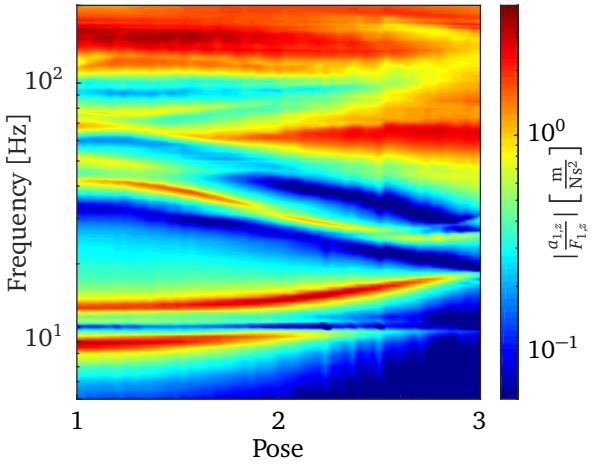

Figure 4.17: Campbell diagram of the TCP in z-direction for different poses. Adapted from our paper [46].

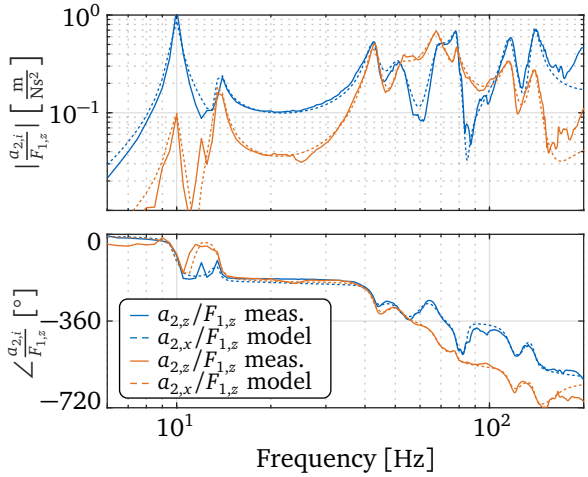

Figure 4.18: FRF synthetisation using PolyMax for two measured FRFs. Adapted from our paper [46].

is by far the heaviest part of the robot and basically behaves like a large beam that is excited by a decreasing moment during the pose change of the robot arm. This causes the measured mode to lose amplitude, but not frequency, since the mode is completely dominated by the bending of the large prismatic joint.

The third mode at 13.6 Hz looks quite similar to the second mode and also yields a quite high modal assurance criterion (MAC) of 91 %. However, this mode also involves a significant amount of bending at the "C"-shaped link between joints 2 and 3, which moves out of phase with the bending motion of the linear joint 1. The rest of the arm also stays rigid for this mode.

Mode 5 and 6 are both bending modes in the x-y-plane and both have a node between the small joints 5 and 6. The difference between these modes is again the additional bending of the "C"-shaped link of mode 5.

Mode 6 at 42 Hz is the second bending mode in the vertical direction and is the first mode that actually involves bending of some of the robot's joints around their motor axes. Consequently, this is the first mode that can actually be influenced by the joint controller of the robot, as we already observed in the test measurement shown in Fig. 4.16.

Modes 7 and 8 look like the third bending modes in the vertical and horizontal direction respectively, with both having a vibration mode at the link between joints 3/4 and the link between joints 5/6. Mode 9 is the first torsional mode around the y-axis.

The mode shapes of pose 2 and 3 are considerably harder to depict on paper, which is why I will omit showing these. However, looking at these modes also does not really add anything to the understanding of the underlying system behavior besides confirming the same conclusions.

Discussion of Results

There are a few key takeaway points that can be made from the results of these experiments, both for the goal of this thesis and for robot manipulators in general:

- *Experimental Modal Analysis can be a very powerful tool to analyse the dynamic behavior of a robot manipulator.*
  This is nothing new, similar works have for example been done in [41, 101, 137, 221, 283] for different types of robot manipulators. However, these works all have been

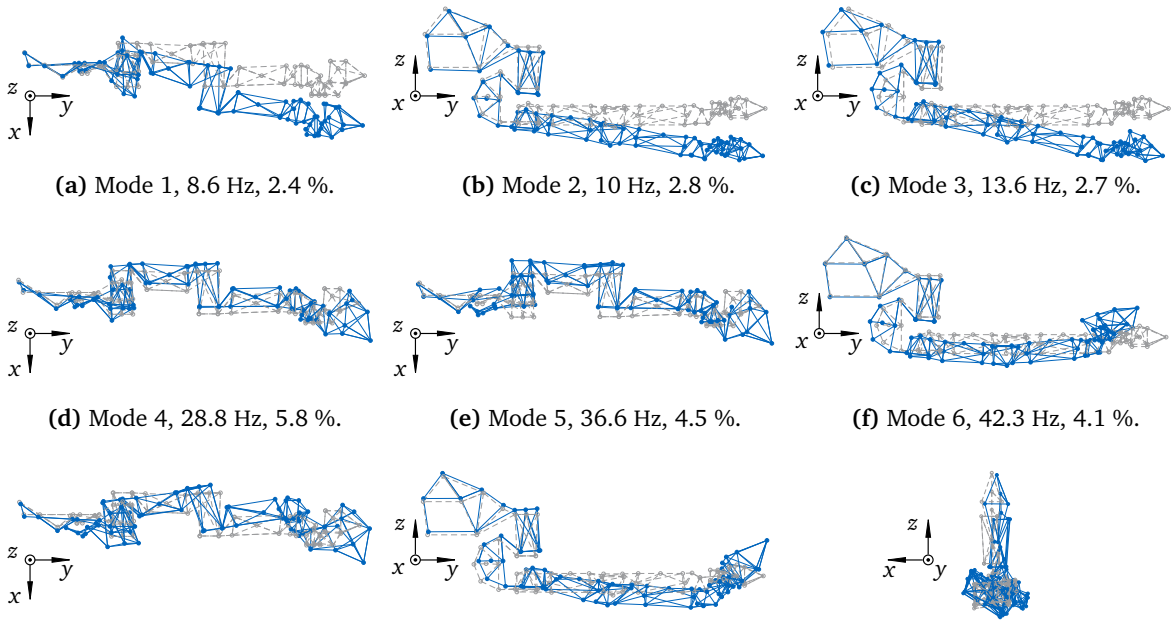

(a) Mode 1, 8.6 Hz, 2.4 %. **(b)** Mode 2, 10 Hz, 2.8 %. **(c)** Mode 3, 13.6 Hz, 2.7 %.

(d) Mode 4, 28.8 Hz, 5.8 %. **(e)** Mode 5, 36.6 Hz, 4.5 %. **(f)** Mode 6, 42.3 Hz, 4.1 %.

(g) Mode 7, 51 Hz, 6.7 %. **(h)** Mode 8, 68 Hz, 6.4 %. **(i)** Mode 9, 78.2 Hz, 2.7 %.

Figure 4.19: Mode shapes, eigenfrequencies and modal damping for pose 1. Adapted from our paper [46].

done in a lot less detail, often only using one sensor per robot joint. This is good enough if one is only interested in the eigenfrequencies and damping of the first few modes. However, in order to derive sensible conclusions using the modes shapes, an EMA should be performed with a lot more measurement points, as done here.
For the CROPS robot, we can clearly determine that the weakest component is the "C"-shaped link between joints 2 and 3, which should be redesigned to improve the dynamic behavior of the robot. The other main issue is the large linear joint 1, which could be improved by also fixing the top or even middle portion of the beam to the environment.

- *The entire mechanical structure influences the dynamic behavior of the robot*.
  In this specific case, the 6th mode is the first one that actually involves torsion around the joint axes. All earlier modes are basically completely dominated by deformation of the link components. This would cause any model that only uses torsional springs in the joints, which is still the most popular modeling approach for most robots, to not be able to accurately model the structural dynamics of this robot.

- *Every robot is different*.
  While the CROPS robot is completely dominated by deformations of its link components, other robots will behave differently depending on their design. For example, a sensitivity analyses of the *ABB* industrial robot that we investigated in [312, 313] showed equal contributions of the links and joint components to the overall dynamic behavior. Meaning that general statements such that 'only the drive train flexibilities matter' should be avoided. The structural dynamics of robot manipulators should always be investigated with as much detail as possible using high fidelity measurements and models that include link and joint flexibilities. These models can then be reduced if the analysis shows that only certain components are influencing the behavior of interest.

- *Certain structural modes of the robot might be uncontrollable for its control system.*
  In the case of the CROPS robot this is actually rather extreme, since the first five modes of the robot are basically uncontrollable by the robots own joints. We can also see this in the controller test measurement of Fig. 4.16, where the controller only effects the 6th mode at 42 Hz. For example the second mode (Fig. 4.19.b) is caused completely by the bending of the beam like structure of the first joint, with all other joints remaining rigid. Inducing additional damping into the system via the joint controllers using for example an impedance controller would not effect this mode at all.
  If one is only interested in the position of the TCP, one could think of a control design that moves the joint angles in such a way that the TCP is kept more stable. However, that would require a very accurate model of the entire structural dynamics of the system, including the dynamics of each joint with its drivetrain. As already discussed in the State of the Art section 2.1, this is unfortunately still quite unfeasible with current methods, especially because the control system would need to be able to precisely move the entire robot with over 10 Hz bandwidth. This is again one of the main motivations for the investigation of external robot stabilization approaches in this thesis.
  Of course, this problem will not be as extreme for other industrial robots, however, we found similar issues of uncontrollable modes with our UR10 and *Franka* Panda models, as discussed in section 4.3.2.

4.3 Influence of Structural Dynamics on Robot Joint Control

After analyzing the structural dynamics of a robot manipulator more globally using an Experimental Modal Analysis in the previous section, I want to go into a bit more detail on the influence of structural dynamics on robot joint control in this section. The main purpose of the research shown in the following subsections was foremost to gain a more detailed understanding of the interactions between the joint control system, the flexible drivetrain and flexible links of a robot manipulator. The second reason was to examine if there could be any important interactions between external stabilization approaches applied at the TCP of the robot and the robot's own control system.

I will first summarize our research for position controlled robots in section 4.3.1, which is more relevant to the development for external stabilization approaches, since most industrial robot manipulators are still position controlled. For the sake of completeness, we also performed some tests on torque-controlled robots, which I will summarize in section 4.3.2.

4.3.1 Joint Position Controllers

This subsection is based on our paper [47]. My student HUANG also did some preliminary measurements in her semester thesis [129].

In order to gain a better understanding of the interactions between a position controlled robot and its mechanical structures, I reduced the problem to a single position controlled joint with a flexible joint and flexible link. The analysed model used a single link module as described in section 4.1, however, the flexible beam was still based on the lumped parameter approach. The results should be the same as using a reduced order model, since we used 20 elements to descretize the beam. The beam has a length of 1 m, a cross section of $5 \times 5\,\mathrm{cm}^2$ and the density of aluminum $\rho = 2.7\,\mathrm{g/cm}^3$.

A common P-PI-PI cascade is used for the joint position controller. However, the *ELMO* motor drivers that we use in most of our robots also offer different setups for this control

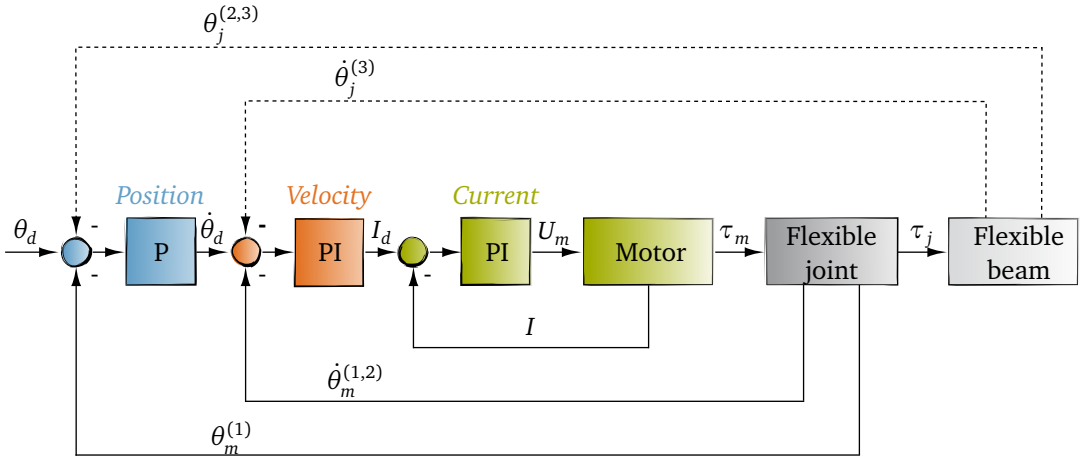

Figure 4.20: Flow chart for cascaded joint control of a flexible beam with a flexible joint. (1) Motor feedback, (2) dual feedback, (3) joint feedback. Adapted from our paper [47].

structure, Fig. 4.20. Since we can also measure the feedback on the joint side of our joint test rig (Fig. 4.28) with absolute encoders, there are different possible combinations for the feedback measurements:

(1) *Motor feedback*, which uses the motor angle θ_m as position and the motor angular velocity $\dot{\theta}_m$ as velocity feedback. This is the most commonly used set up in practice.

(2) *Dual feedback*, which uses the joint angle θ_j as position and the motor angular velocity $\dot{\theta}_m$ as velocity feedback. The idea here is to bypass the compliance in the gear and directly control the joint angle θ_j.

(3) *Joint feedback*, which uses joint angle θ_j and joint angular velocity $\dot{\theta}_j$ as feedback.

We will see in the following why (2) dual feedback might be preferred over (3) joint feedback.

Fixed Motor Axis

Let us first gain a better understanding of the dynamics of the mechanical portion of the system, without the joint controller interfering, by fixing the motor axis. The resulting system is a flexible beam connected to a flexible gear, which is fixed to the environment.

The most important transfer function for the external stabilization approaches investigated in this thesis is the driving-point measurement at the tip of the beam. In this case, the input is a force at the tip (point A in Fig. 4.22) acting perpendicular to the beam and the output are the accelerations at the same point in the same direction.

The driving-point transfer function is plotted in Fig. 4.21 with the same beam, but varying gear stiffnesses. We start with very low gear stiffness (blue line) and then increase the stiffness by one order of magnitude per step. The increase of gear stiffness raises the stiffness of all modes in the system, with the first mode being affected the most. The modal damping of the system decreases in each step, since the viscous damping factor for the damping in the joint and beam stays unchanged. The dynamics of the system converge to the dark blue line in Fig. 4.21, after which a further increase of the gear stiffness does not visibly change the system anymore.

This behavior can be explained by looking at the mode shapes of the system. The first mode of the system with low gear stiffness is shown in Fig. 4.22a. The mode shape is dominated by the deformation of the gear, since the beam is much stiffer than the joint and

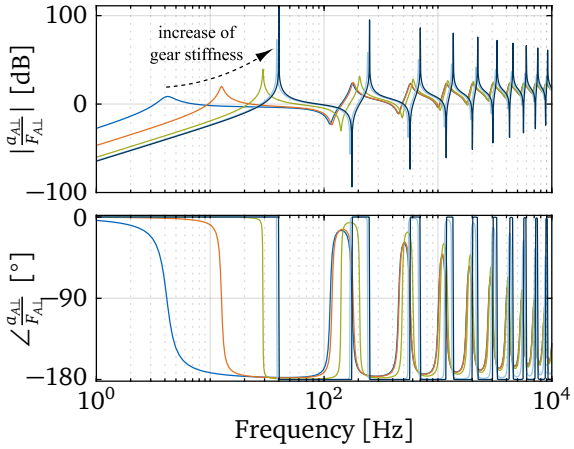

Figure 4.21: Driving-point measurement in vertical direction (force to acceleration) at the tip of the beam with a fixed motor axes. The gear stiffness is increased stepwise by one order of magnitude. Adapted from our paper [47].

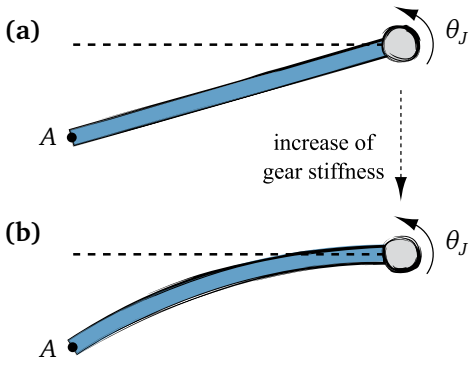

Figure 4.22: First mode of a flexible beam coupled to a flexible joint. (a) Low gear stiffness, (b) high gear stiffness. Adapted from our paper [47].

basically behaves like a rigid body[11]. The mode shape corresponding to a very high gear stiffness is shown Fig. 4.22.b. The system now behaves like a fixed flexible beam that shows no movement at the joint $\theta_j = 0$. A further increase in stiffness will not effect the system dynamics anymore, since the beam will just be pinned more rigidly to the joint, which is why the dynamics converge in Fig. 4.21. This is also why the first eigenfrequency raises so much when changing the gear stiffness: The first mode shape changes very significantly from no deformations to only deformations at the beam.

For the following analysis, we chose a relatively low gear stiffness (orange line in Fig. 4.21), causing the first mode shape to look like Fig. 4.22.a. Although it seems like that the beam flexibility could be neglected in this case, since it is much stiffer than the joint compliance, we will see in the following that there are still quite significant effects on the closed loop system dynamics.

Motor Feedback

The motor axis is now no longer fixed, but controlled by a P-PI-PI cascaded joint position controller with motor feedback, Fig. 4.20 (1). The resulting closed-loop transfer function from desired motor angle θ_d to motor angle θ_m is shown in Fig. 4.23. Let us vary the P-gain of the first P position controller in the cascade in order to analyse the influence of the control system. We start off again with very low P-gain (Fig. 4.23, blue line) and increase the gain by one order of magnitude per step. The pole caused by the velocity PI-controller stays at 5 kHz. The pole of the position controller[12] moves to higher frequencies as its gain is increased, causing the dynamics of the position control loop to be faster, improving the overall bandwidth of the closed-loop system on the motor angle θ_m. As the pole of the position controller approaches the velocity controller's pole, the pole looses damping, develops a resonance peak and eventually becomes unstable.

This can be explained by looking again at the structure of a cascaded controller, Fig. 4.20. Increasing the P-gain of the position controller causes the outer position control loop to react

[11] Note that this is only true for the first mode, all higher modes show deformations of both the beam and the joint.

[12] The pole only has 90° phase delay, since it is only a P-controller on the position level.

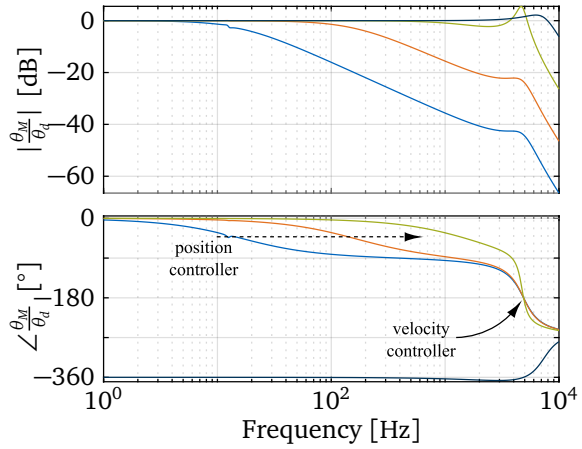

Figure 4.23: Closed-loop transfer function for motor feedback. Desired angle θ_d to motor angle θ_M. The position controller gain is increased by one order of magnitude per step. Adapted from our paper [47].

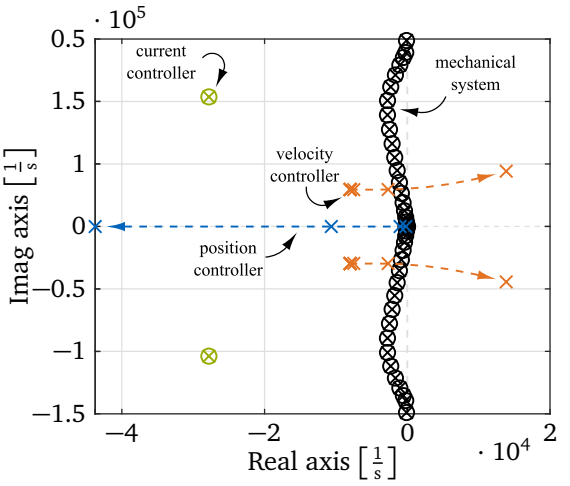

Figure 4.24: Root-locus plot of the closed loop transfer function for motor feedback with increasing position controller gain. Adapted from our paper [47].

faster, improving the overall bandwidth of the motor axes control. However, the position controller produces the desired velocity $\dot{\theta}_d$ for the following velocity controller. Consequently, as soon as the dynamics of the position controller are faster than the dynamics of the velocity control loop, the latter can not keep up anymore and the system becomes unstable.

This is already a well known fact for cascaded control structures that are applied to a collocated control problem: The time constant of the position control loop T_{pos} has to be larger than the time constant of the velocity control loop T_{vel}, which also has to be larger than the time constant of the current control loop T_{cur} in order for the system to be stable:

$$T_{\text{pos}} > T_{\text{vel}} > T_{\text{cur}} \,. \tag{4.3}$$

The structural dynamics of the mechanical system basically do not influence the closed-loop dynamics at all, which can be explained by looking at the root-locus plot, Fig. 4.24. The dynamics of the mechanical system are shown in black[13]. The large gear ratio of $N = 100$ causes the mechanical system to only be very weakly coupled to the motor axes. Thanks to the collocated nature of the control problem, a very low amount of gain is already enough to push all poles of the mechanical system to their corresponding zeros, canceling each other out in the closed-loop transfer function Fig. 4.23 [14].

A cascaded joint position controller can therefore easily be tuned to achieve a well behaved, first order system-like behavior with high bandwidth for the controlled motor axis θ_m (see e.g. the orange line in Fig. 4.23), without the dynamics of the mechanical system being any concern for stability or performance. However, although the motor angle θ_m can be controlled very precisely, the actual variable of interest is the joint angle θ_j after the flexible gear, since this variable gives a better description of the behavior of the whole robot.

The transfer function from the desired angle θ_d to the joint angle θ_j is shown in Fig. 4.25. We again increase the position controller's P-gain in the same way as before. The transfer function shows resonances at the same frequencies as the eigenfrequencies of the chosen

[13] Note that the poles should all follow a straight line, since the beam has the same amount of modal damping for all poles. The 'bend' above $1.5 \cdot 10^5$ 1/s is an approximation error caused by the discretization of the lumped parameter method. This will only effect very high frequency behavior above 10 kHz, which is not shown in the other plots and not relevant to the effects discussed in this subsection.

[14] See also Appendix A for a bit more general discussion about collocated and non-collocated control.

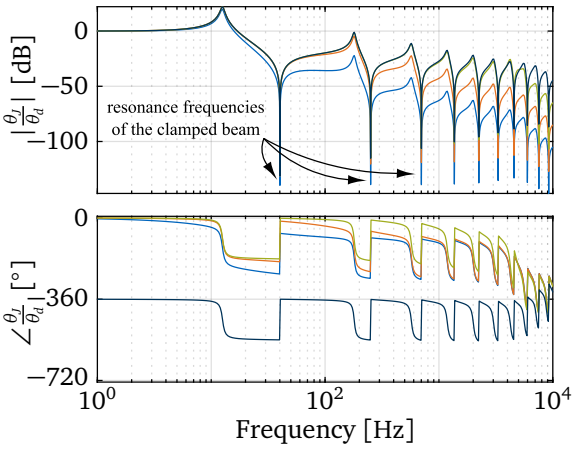

Figure 4.25: Transfer function from desired angle θ_d to joint angle θ_J for motor feedback. The position controller gain is increased by one order of magnitude per step. Adapted from our paper [47].

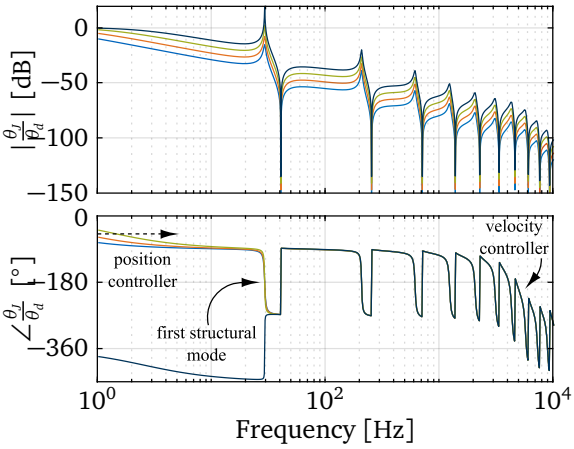

Figure 4.26: Closed-loop transfer function from desired angle θ_d to joint angle θ_J for dual feedback. The position controller gain is increased by small steps. Adapted from our paper [47].

mechanical system (orange line in Fig. 4.21). The first mode is almost unaffected by any reasonable amount of gain for the position controller. In practice, while very large bandwidth is possible for the controlled motor axis, this basically reduces the usable bandwidth to below 10 Hz, if one does want to avoid exciting unnecessary vibrations of the beam structure. The overall bandwidth at the joint angle θ_j is also limited by antiresonances, which correspond to the resonance frequencies of the fixed beam (dark blue line in Fig. 4.21).

For example, a desired joint angle θ_d at 12 Hz can easily be controlled on the motor axis (e.g. with a tuning like the orange line in Fig. 4.23), but will also excite the first mode of the mechanical system. The mode shape looks like in Fig. 4.22a, since we have chosen a relatively low gear stiffness. This causes the system to respond with large vibration amplitudes at the TCP of the beam, deteriorating the precision of the system without being noticed at the measured motor angle θ_m. A desired angle θ_d at 40 Hz will still be very well controlled on the same system, however, the joint angle will show no movement $\theta_j = 0$. The beam will again vibrate with large amplitudes, this time following the mode shape of the fixed beam Fig. 4.22.b. The control system will be unaware of both of these effects, since it only measures the motor angle θ_m.

Note that increasing the gear stiffness will push the resonance peaks in Fig. 4.25 towards their corresponding antiresonances. However, the antiresonances themselves will stay unchanged, since the modes of the fixed beam are uncontrollable for a position based controller acting on the motor axis. The structural dynamics of the mechanical system will therefore barely be influenced by the controller. This means that the driving-point transfer function at the tip of the beam (Fig. 4.21) will always look the same, regardless of the motor axis being fixed or controlled by a cascaded controller with any reasonable amount of gain.

Dual Feedback

Let us next have a look at the dual feedback variation, which closes the position loop with feedback from the joint axis θ_j instead. For this analysis, we increased the stiffness of the gear such that the system corresponds to the green line in Fig. 4.21 with the first eigenfrequency at 30 Hz. The resulting closed-loop transfer function from the desired angle θ_d to the joint angle θ_j is shown in Fig. 4.26.

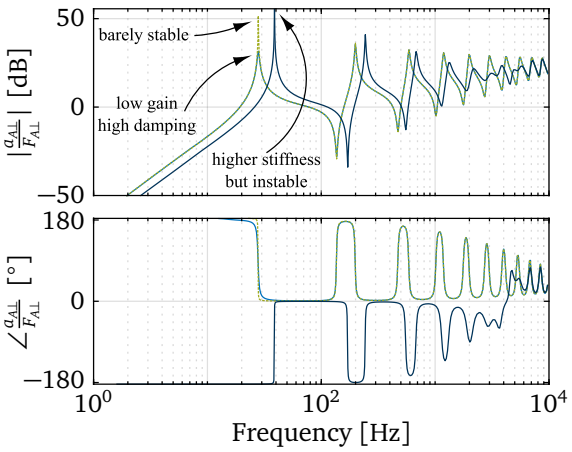

Figure 4.27: Driving-point measurement in vertical direction (force to acceleration) at the tip of the beam with dual feedback. Low (blue), medium (green), high (dark blue) position controller gain. Adapted from our paper [47].

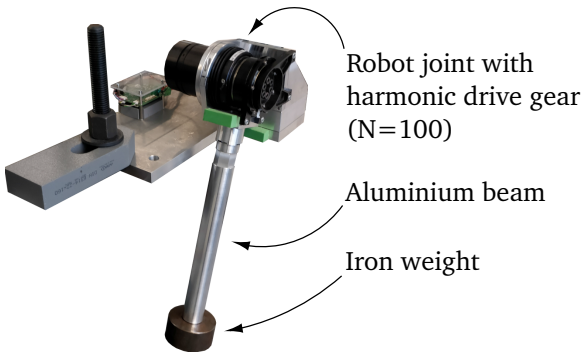

Figure 4.28: Joint test rig. Adapted from our paper [47].

The poles and zeros from the mechanical system now show up in the position control loop, since the loop has been closed behind the flexibility of the gear, making the control problem non-collocated. We start with very low amounts of P-gain for the position controller and only raise it slowly. The bandwidth improves slightly, however, higher P-gains also cause the resonance of the first mode of the mechanical system to raise and ultimately become unstable as soon as the pole is affected by the phase lag of the position controller.

This means that the time constant of the position control loop T_{pos} now also has to be larger than the time constant of the mechanical system T_{mech}, which is set by the eigenfrequency of the first structural mode of the system:

$$T_{\text{pos}} > T_{\text{vel}} \qquad \text{and} \qquad T_{\text{pos}} > T_{\text{mech}} \,. \tag{4.4}$$

Since the position loop is closed behind the compliance of the gear, we try to enforce a higher joint stiffness by raising the P-gain of the position controller. This will only work as long as the enforced stiffness is lower than the actual stiffness of the gear. As soon as the dynamics of the mechanical system are no longer able to follow the enforced dynamic of the closed joint position loop, the system becomes unstable. This can also be seen in the driving-point transfer function at the tip of the beam, Fig. 4.27. For low gain of the position controller the system behaves exactly the same as with a fixed motor axis (see Fig. 4.21 green line). By further increasing the gain of the position controller, the system loses damping without changing its stiffness. The system becomes unstable, as soon as we are theoretically enforcing a higher stiffness on the global dynamics.

The achievable bandwidth (e.g. 1 Hz for the green line in Fig. 4.26) on the joint side is actually worse than for pure motor feedback, even though we are now directly controlling the joint angle θ_j and using a gear with higher stiffness. Dual position feedback might still be useful, when a slow moving system with low control bandwidth is acceptable. The positive trade off would be higher steady state precision, since the controller is now able to directly control the joint angle and compensate for static sag of the robot caused by gravity loads on the joints[15].

[15] This controller would, however, still not be able to compensate for sag caused by the flexibilities of the links, since the controller has no way to measure the state of the links themselves.

This was also one of the main motivations for torque controlled joints, since these types of controllers can enforce stability by measuring the torque on the motor side (using the current measurement) and the torque on the joint side with a torque sensor.

Joint Feedback

For a joint position feedback controller, the velocity loop is now also closed behind the compliance of the gear by using the joint velocity $\dot{\theta}_j$ as feedback. Consequently, the dynamics of the velocity loop now also have to be slower than the dynamics of the mechanical system in order to be stable. The position loop again also has to be slower than the velocity loop:

$$T_{\text{pos}} > T_{\text{vel}} > T_{\text{mech}} \,. \tag{4.5}$$

In practice, this setup is basically unusable, since the the poles of the cascaded controller should also be well separated to ensure stability. The achievable closed-loop bandwidth would therefore be even lower than with dual feedback, which is already questionably low even for a system with high gear stiffnesses.

Test Rig Measurements

In order to verify the above findings, we performed the same tests on our joint test rig Fig. 4.28. The test rig consists of an elbow joint of our humanoid robot LOLA, using a custom BLDC motor with a harmonic drive gear (gear ratio $N = 100$). The joint is connected to an aluminum beam with length of 0.5 m and a 1 kg steel weight attached to its end.

In practice, the real system is far more limited than in simulation, where we could use quite extreme tunings to make the interconnections within the system more obvious. On the test rig, we can achieve a bandwidth of 2 kHz for the current controller and 80 Hz for the velocity controller. The achievable bandwidth of the velocity controller is mainly limited by noise, since the velocity has to be generated by counting the lines per second of the incremental encoder. This is still more robust than differentiating a measured position signal, however, it is also quite sensitive to miscounts caused by skipped lines. Nevertheless, we can still observe the same type of effects as in the simulation.

The beam is moved into a horizontal position for all tests to keep the joint loaded and minimize the influence of backlash in the gear on the measurements. The transfer functions are measured using multi-sine excitation signals [16]. The superimposed sine waves use Schroeder phases to minimize their crest factor. Meaning that the maximum peak of the signal is kept as low as possible, while maximizing the amplitude of each contributing sine wave [234].

Fig. 4.29 shows the closed-loop transfer function from the desired angle θ_d to the motor angle θ_m for motor feedback. In general, we can observe the same behavior as simulated in Fig. 4.23: When increasing the position gain in small steps, the pole of the position controller moves to higher frequencies, improving the control bandwidth. However, this also causes the resonance at the pole of the velocity controller to loose damping and consequently raise. Increasing the position gain further will again provoke instability of the velocity controller. On the real system this is visible by the joint performing limit cycle vibrations with large amplitudes, which is probably because of the backlash in the gear.

[16] We favor multi-sine excitations for complex mechatronic systems. Measuring a step response is out of the question, since it will put unnecessarily high stress on the system. Sweep excitations distribute the excitation energy too broadly in the frequency domain and will produce unusable signal-to-noise ratios, since the input signal has to go through the entire electrical system, the drivetrains with a lot of friction, the mechanical structures and back through the noisy sensors. Multi-sine can improve the signal-to-noise ratio by only using e.g. 5 discrete excitation frequencies for each measurement run, concentrating the input energy on those frequencies. This procedure is a good compromise between using a faster sweep excitation and going through each excitation frequency one by one.

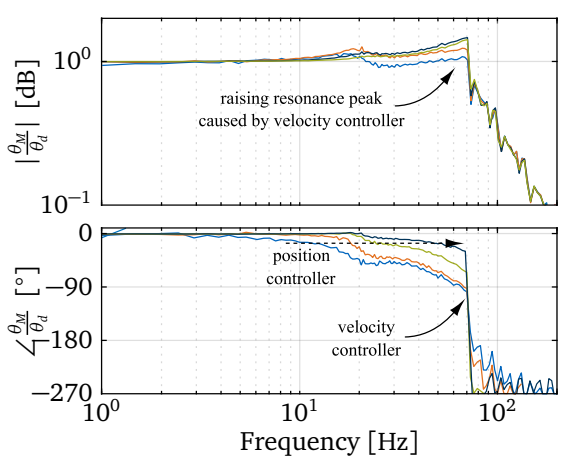

Figure 4.29: Closed-loop transfer function for motor feedback on the test rig while slowly increasing the position controller gain step wise. Adapted from our paper [47].

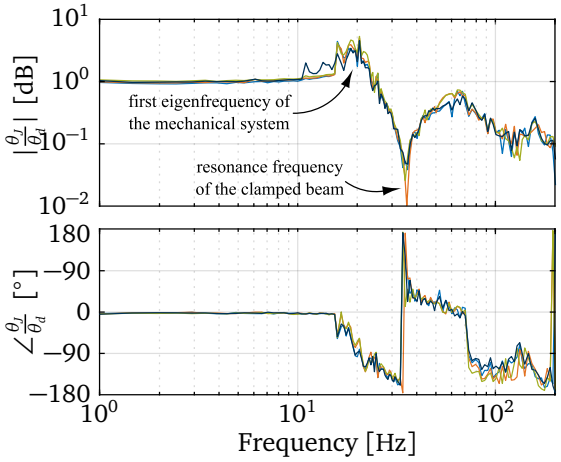

Figure 4.30: Transfer function from desired angle θ_d to joint angle θ_j for motor feedback on the test rig while slowly increasing the position controller gain step wise. Adapted from our paper [47].

The transfer function from the desired angle θ_d to the joint angle θ_j with the same position P-gains is shown in Fig. 4.30. Similar to the simulation results in Fig. 4.25, there is basically no difference on the joint side between the amounts of gains used for the controller with motor feedback. We can see the first eigenfrequency of the mechanical system at 20 Hz and an antiresonance at 37 Hz, which was confirmed to be the eigenfrequency of the fixed beam in Ansys by my student HUANG in her semester thesis [129].

We also tested dual feedback on the test rig, which we could tune to a usable bandwidth of about 1 Hz. For higher gains, the system was a lot less robust and could be made unstable by impacting the beam with an external disturbance. With a bandwidth below 1 Hz we could reduce the error on the joint side to about $e_{\theta,j} = 0.5$ mrad for slow trajectories. Which is quite impressive for a joint side controller, however, the low reaction time of the controller due to the low control bandwidth necessary to remain stable made this type of controller basically unusable for our humanoid walking robot LOLA[17].

Conclusions

The main takeaway points of the above investigations can be summarized as follows:

- There is barely any coupling between a joint controller with motor feedback and the structural dynamics of the mechanical system. This is mainly due to the high possible bandwidth of a collocated controller applied to the motor axis and the typically high gear ratios ($N \leq 100$) common in robotics applications. Since most industrial robots are still position controlled on the motor axis, we do not have to worry about any bad interactions between the robot's control system and an external stabilization approach, which will apply a reaction force to the TCP of the robot in order to reduce the error at the tool.

[17] I will refrain from showing error plots here, since this is only anecdotal evidence anyway. The amount of error for dual feedback, and also the stability limit, depends heavily on the structure attached to the joint. We had much trouble tuning a stable dual feedback controller for the 26 joints of LOLA during my master's thesis [45], since the load on the gears is much larger and the structure is also significantly more complex. We were able to tune a dual feedback controller such that the robot was able to walk. However, all limbs showed very large vibration amplitudes during walking, such that we deemed this type of controller unsafe for our walking robot.

- The structural dynamics of the joint and the substructure of the fixed beam are also very clearly visible in the transfer function from the desired angle θ_d to the joint angle θ_j (Fig. 4.25 and Fig. 4.30). This might make it viable to use the popular *Transmission Simulator* technique from the field of frequency based substructuring [21, 238] to identify robot joint dynamics: An easily predictable structure like a simple beam could be attached to a robot joint test rig with an acceleration sensor at the tip. Then, the transfer function from the motor angle to the joint angle and accelerations at the tip of the beam are measured. The dynamics of the easily predictable beam structure can then be removed from the measured system dynamics in postprocessing, only leaving the dynamics of the joint including the dynamics at the interface between the beam and the joint structure. These kind of models could then be used to enhance a flexible multi body simulation of a robot.

- While direct joint position feedback is possible using the common cascaded control structure with an absolute encoder on the joint side, it is only really usable using dual feedback. The possible bandwidth is also significantly lower than using a motor side feedback controller. However, the system might be a bit more precise. The tuning of these controllers is also quite involved, since now the dynamics of the entire structure of the robot contributes to the control plant.

4.3.2 Joint Torque Controllers

As described in the State of the Art section 2.1.3, the most common approach for higher precision robotics is to use quite involved model based methods using torque controlled robot joints. The external stabilization approaches investigated in this thesis are designed for motor position controlled robots. The main reason for this is that the vast majority of industrial robots still work this way. Furthermore, as we have seen in the previous subsection, a motor position controlled robot is actually beneficial to an external stabilization approach, since there is very weak coupling between the structural dynamics of the robot at its TCP and the motor controller. This reduces the complexity of the problem, since we do not also have to consider the control system of the robot itself.

Since external stabilization approaches are kind of an antithesis to using the robot's own motors and control structure for high-precision applications, I still wanted to have a little bit deeper look at the capabilities and limitations of torque controlled robots. Although this subsection is not needed to understand the development of the external stabilization prototypes in the following chapters, it is still beneficial for the motivation of the topic of this thesis.

The content of this subsection is based on our paper [218] with my student PRAUTZSCH as the main author. PRAUTZSCH also did some preliminary work for our results in his semester [216] and master's thesis [217].

For the following analysis, we exchanged the joint controller of our robot model to the first torque controller (3.98) discussed in 3.4.2.

Torque Measurements and Model Tuning

Since we had the *Franka* Panda available for measurements, we used the possibility of measuring the desired torque τ_d to actual joint torque τ_j transfer function to tune our model with data from a real torque controlled robot. Unfortunately, *Franka* does not disclose how their torque controller works with only the input & output data being available. For the measurements, we put the Panda robot in a simple pose shown in Fig. 4.31. A desired harmonic

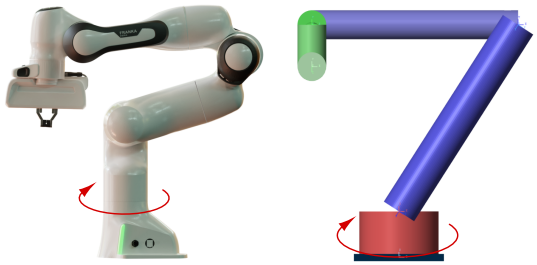

Figure 4.31: UR10 in a singular pose. Adapted from our paper [217].

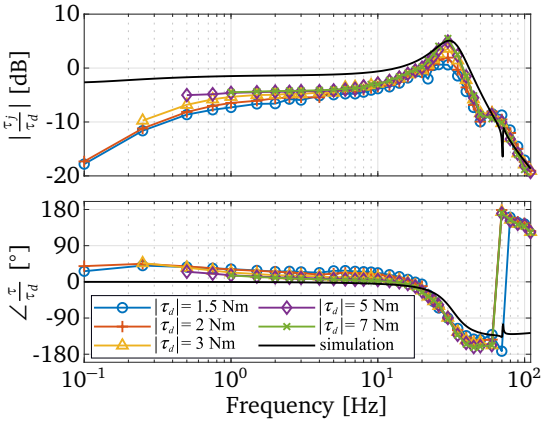

Figure 4.32: Frequency response of desired to measured torque at joint 1. Comparison of experimental data to tuned simulation result. Adapted from our paper [217].

torque is then applied to the base joint 1 of the robot in discrete frequency steps. The resulting transfer function to the actual joint torque τ_j is shown in Fig. 4.32. In order to test for non-linearities we repeated the measurement for different desired amplitudes. We can see that there is non-linear behavior visible in the transfer function, which is probably due to friction effects in the gear. With low desired torque amplitudes, the controller probably has to deal with significant stick slip effects in the gear. For desired amplitudes higher than 5 Nm, the controller shows a nice constant amplitude in the closed-loop transfer function for frequencies below 10 Hz and a resonance peak at 30 Hz. This gives the system a usable bandwidth of around 10 Hz, which is also indicated in the manual data published by *Franka* [98]. While the controller shows a flat amplitude and zero phase delay below 10 Hz, it only achieves up to 80 % of the desired torque amplitude. This is probably due to the rather cheap hardware used in the *Franka* Panda, which will not support very high torque controller gains for better performance. Fortunately, this is rather easily corrected by using a feedforward factor of 1.25 for the desired torques τ_d.

This directly shows one of the biggest weaknesses of torque controlled robots, when they are used with complex control schemes for high precision control which also have to consider the structural dynamics of the links. We found in the introduction chapter 1 that we roughly need a control bandwidth of about 50 Hz for our application. This would just not be possible with the torque controller of the Panda robot, since it is limited bandwidth would bottleneck any kind of higher-level control system for high precision control.

As mentioned in section 4.1, we also used this opportunity to tune the joint model of our robot simulation. For this we placed our UR10 model in the same pose (Fig. 4.31) and linearized the same transfer function, Fig. 4.32 black line. The joint stiffness k_j, -damping c_j, as well as the torque controller gains g_P and g_D were simply tuned by hand until we achieved the best match with the data. The model matches quite well with the measured transfer function and is even able to predict the close pole zero pair at 50 Hz and 70 Hz, which belongs to the first structural mode of the simulation model with dominant contributions by the flexible links.

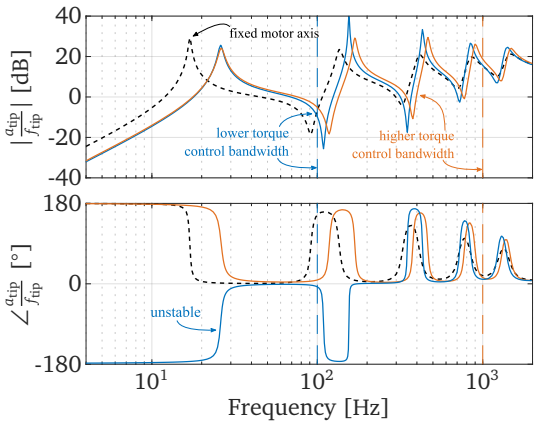

Figure 4.33: Simulated driving-point dynamics (force to acceleration) at the tip of the beam in direction of the joint rotation for different inner-loop torque controller bandwidths.

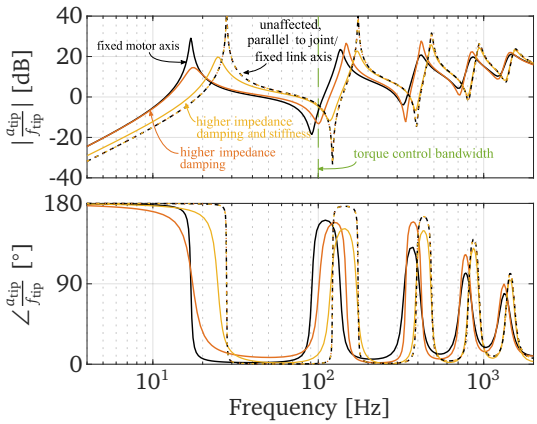

Figure 4.34: Simulated driving-point dynamics (force to acceleration) at the tip of the beam for an input force orthogonal to the joint axis (full lines) and parallel to the joint axis (dotted lines).

Flexible Joint with Flexible Beam Model

Let us next analyse the influence of the torque controller on the driving-point dynamics at the tip of the same simple beam model. Fig. 4.34 again shows the driving-point transfer function at the tip of the beam, with the input force f_{tip} acting orthogonally to the motor axis. The response of the system with a fixed motor axis is plotted with a black dotted line as a reference. In theory, one of the great advantages of the torque controller is that we can enforce any kind of joint stiffness and damping on the robot joint via the stiffness $k_{j,d}$ and damping $c_{j,d}$ as gains of an impedance controller. While the cascaded position controller with joint position feedback (Fig. 4.27) becomes unstable as soon as we enforced a higher stiffness on the joint than the mechanical system itself, we can easily increase the stiffness and damping of the system beyond that limit using a torque controlled impedance scheme (Fig. 4.33 orange line). However, the impedance controller still has to go through the lower-level torque controller, which needs to provide sufficient enough bandwidth for this to work. The orange and blue line in Fig. 4.33 both use the same impedance gains. The torque controller of the orange line has a bandwidth of 1 kHz ($J_{m,d} = 0.001 \cdot J_m$) and is stable, while the torque controller of the blue line has a bandwidth 100 Hz ($J_{m,d} = 0.1 \cdot J_m$) and is unstable.

In section 3.4.2, I mentioned an inertia ratio of $J_{m,d} = 0.1 \cdot J_m$ already being a very optimistic upper estimate of the capabilities of modern torque controllers. For our model, this results in a bandwidth of 100 Hz, which already makes it quite difficult to enforce any beneficial effect on the structural dynamics of the robot model using an impedance controller. We have seen in Fig. 4.32 that the usable bandwidth of the torque controller of the *Franka* Panda is even lower at 10 Hz.

Another problem for the single joint / -beam system is that the joint controller can only influence structural modes of the beam which produce torques around the joint axis. We can test this by again applying different impedance controllers to the single joint system and linearizing the transfer function at the tip of the beam for two different input force directions. Fig. 4.34 shows the effect on the driving-point transfer function for an input force orthogonal to the joint axis in full lines. The system behaves as expected and we can increase the damping and stiffness of the modes for this transfer function. However, the transfer function produced by an input force parallel to the joint axis (dotted lines) is not affected at all by any setting of the controller. This is because this transfer function only includes modes that do not produce torques around the joint axis, and are therefore uncontrollable by any kind of

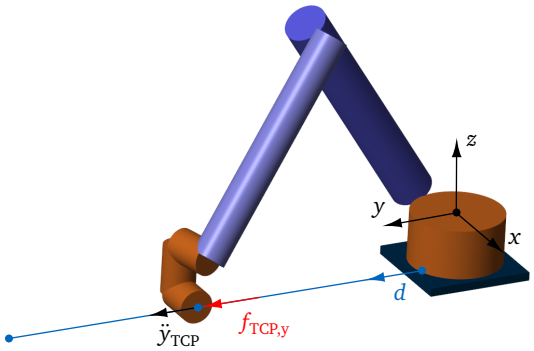

Figure 4.35: The torque controlled UR10 model moving along a horizontal trajectory.

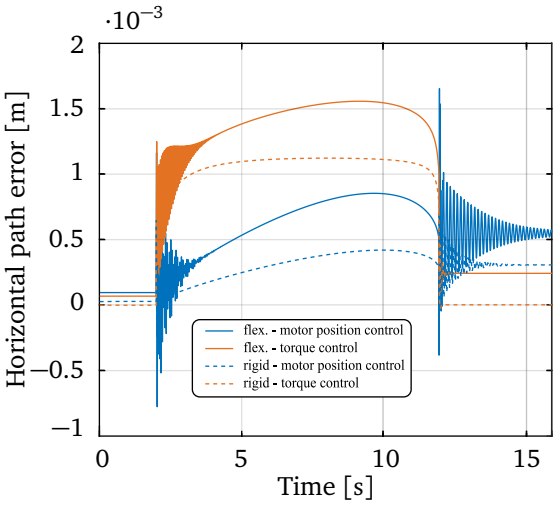

Figure 4.36: Horizontal path error in the y-direction at the TCP of the simulated robot. Adapted from our paper [217].

joint torque. We will later see that this can also affect a larger robot with 6+ DOFs.

Flexible Robot Model

Let us move on to the more complex robot simulation model, which is the same as described in section 4.1, only with torque controlled joints. To also have a look at other directions, we will this time concentrate on the horizontal path error (y-direction) of the robot, Fig. 4.35. The robot again moves along the same 1 m long horizontal test trajectory with constant velocity and high jerk at the beginning and at the end.

The horizontal path error for different model types are shown in Fig. 4.36. The errors for a model with flexible joints, but rigid links are plotted with dotted lines. We can see that the motor controlled robot (blue dotted lines) shows a static error at the end due to sag coming from the flexible links and large vibration amplitudes from the high jerk at the end of the motion. The torque controlled robot (orange dotted lines) compensates the static error with its gravity compensation and does not show any vibrations, since the joint flexibilities are included in the torque-controller.

The motor controlled model with flexible links (Fig. 4.36 blue full line) shows larger vibration amplitudes at the beginning and the end, as well as a larger static error due to the additional flexibility from the flexible links. The torque controlled model (Fig. 4.36 orange full line) also shows large vibration amplitudes at the beginning and a non-zero static error at the end. The static error is now larger, since the rigid model for the gravity compensation does not include the sag caused by the flexibilities of the links. The additional vibration issues of the torque controlled robot can be understood better by again taking a look at the Campbell diagram plotting the driving-point transfer functions dependent on the current pose, Fig. 4.37.

The left Campbell diagram shows the motor position controlled robot as a reference. We can see that there are two low frequency modes for the driving-point transfer function in y-direction of the TCP. The first one starts at 17 Hz and then moves down to 8 Hz. The second one starts at 22 Hz and then moves up to 40 Hz towards the end. The middle Campbell diagram shows the same transfer function with a torque controller and high stiffness impedance. We can see that the controller is able to increase the overall stiffness of the system, however, with still quite high vibration amplitudes.

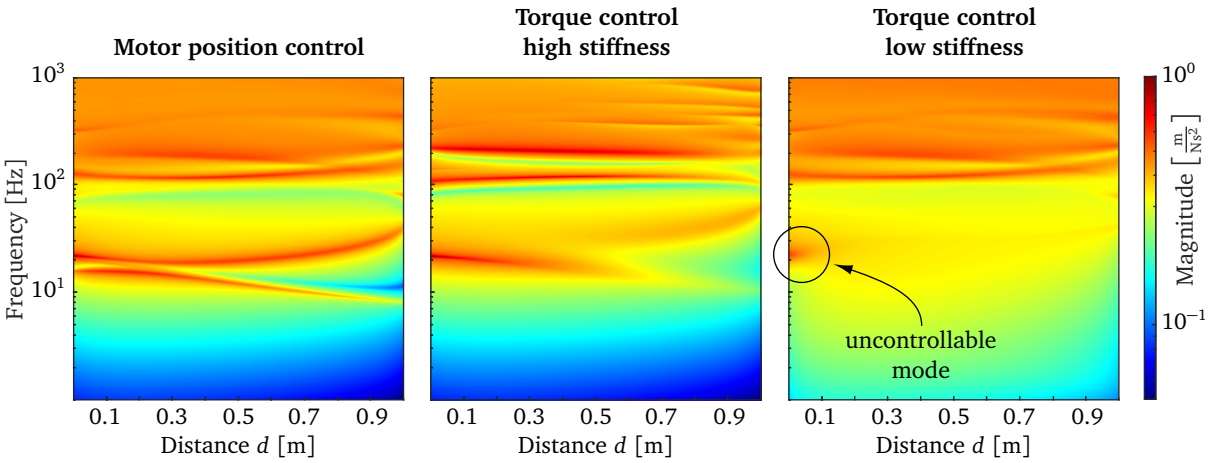

Figure 4.37: Campbell diagrams for an input force and output accelerations in the y-direction at the TCP a long a horizontal trajectory. Adapted from our paper [217].

A better idea to reduce unwanted structural vibrations is actually to reduce the stiffness of the impedance. This way, the mechanical damping of the robot becomes more dominant and less damping is also required from the impedance controller to achieve a high modal damping, and therefore lower vibration amplitudes. The performance of such a controller is shown in the right diagram of Fig. Fig. 4.37. This time, the first mode is basically completely attenuated. However, the second mode is not effected at the beginning at 22 Hz and then only becomes effectively damped after about 10 cm of traveled distance. This is also the reason why the horizontal path error of the torque controlled robot with flexible links (Fig. 4.36 orange full line) still shows large vibration amplitudes at the beginning of the trajectory.

This is happening for the same reason as for the simple flexible beam model (see Fig. 4.34). Fig. 4.38 shows the UR10e robot in a singular position with the first and fifth joint axis being in parallel. In this position, the robot is not able to exert a force at its TCP in the y-direction and therefore influence its structural dynamics. Fig. 4.39 shows the driving-point transfer function in x- and y-direction for fixed motor axis (full lines) as a reference and with an applied impedance controller with a large amount of desired joint damping (dotted lines). For the transfer function in the y- direction, the impedance controller is able to very effectively damp the first mode of the system. However, for the x-direction there is no effect of the controller on the structural dynamics of the robot, since this is the direction causing the singularity of this particular pose.

In practice, a robot will always avoid passing through singular poses. However, as shown in the Campbell diagram Fig. 4.37, it is already problematic when the robot moves close to a singular position, since the robot would still need very high joints torques to effect the almost singular direction at the TCP. This is why the robot is not able to properly reduce the vibrations caused by the second mode at the beginning of the trajectory, regardless of the applied control scheme.

In section 4.2.1, we have also already seen with the analyses of the CROPS robot that a robot does not necessarily need to be near a singular pose to experience uncontrollable structural mode shapes. Every structural mode that does not create a torque around the joint axes of the robot will be uncontrollable. For the CROPS robot this is actually the case for the first five modes, because of its unique mechanical design.

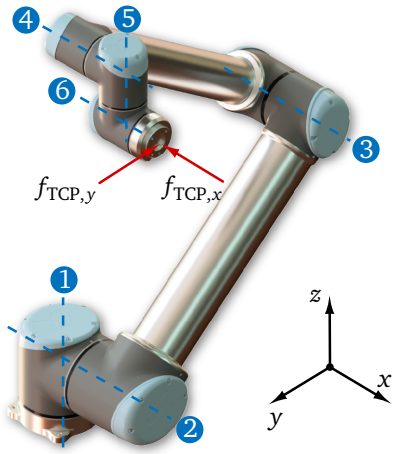

Figure 4.38: UR10e in a singular pose. Adapted from our paper [217].

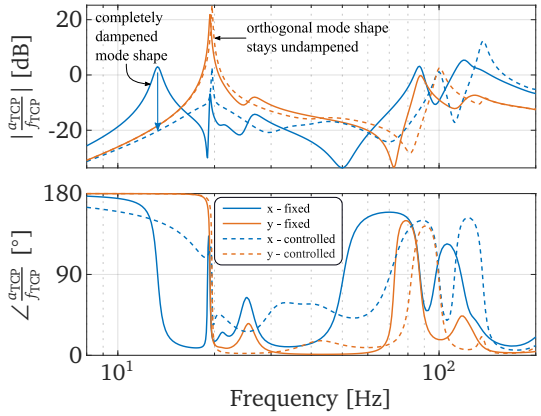

Figure 4.39: Simulated driving-points (force to acceleration) at the TCP for the fixed-motor and torque controlled case at the singularity pose of Fig. 4.38. Adapted from our paper [217].

Franka Panda Experiments

For the last part of this of this section about torque controlled robots, let us have a short look at a few measurements regarding the path accuracy of the *Franka* Panda robot.

The first important fact to note here is that the Panda specifies a maximum desired impedance joint stiffness of the three main joints of $k_{j,d,\max} = 600\,\mathrm{Nm\,rad^{-1}}$. The GUI of the robot actually only allows half of this, which is a quite low joint stiffness compared to the typical stiffness of a harmonic drive gear[18]. The usual strategy for high-precision tracking with torque controlled robots is to use a very high desired impedance stiffness to compensate for any error in the gravitation compensation. This is clearly not possible with the Panda robot. Additionally to the torque controller bandwidth of 10 Hz, the impedance gains are probably also limited by the usual implementation issues like sensor noise. This means that the Panda relies entirely on the accuracy of its gravity compensation for its tracking performance, because of the quite low possible impedance stiffness. On the other hand, the robot should be able to suppress the structural vibrations of the robot quite well using a low impedance stiffness and a high impedance damping[19].

Fig. 4.40a shows the measured vertical path error of the *Franka* Panda robot along a 80 cm horizontal trajectory moving at $42\,\mathrm{mms^{-1}}$. The error is again measured using highly precise eddy-current sensors. The trajectory is measured three times with different desired impedance stiffnesses. We can see that the robot is actually able to suppress any form of higher frequency vibrations quite effectively for the first half of the trajectory. However, vibrations appear in the second half of the trajectory for all stiffnesses. The CWTs of the measured error data show, that the frequencies of these vibrations are all almost the same with the same amplitude for all cases. The base frequency starts at about 1 Hz and then follows an almost perfect exponential rise up to 5 Hz. There is also a clear second order excitation visible. These are probably also torque ripple issues that can have many causes[20].

[18] E.g. a small sized harmonic drive gear of size 20 with a gear ratio over $N \geq 80$ typically has a stiffness in the region of $2 \cdot 10^4\,\mathrm{Nm\,rad^{-1}}$ [278]. For comparison, the maximum load of the Panda is 3 kg, which would cause a sag of 10 cm with a single joint with $300\,\mathrm{Nm\,rad^{-1}}$ stiffness and the load at 1 m distance.

[19] The maximum possible impedance damping is specified with $c_{j,d,\max} = 50\,\mathrm{Nms\,rad^{-1}}$, which is quite large compared to the maximum possible impedance stiffness.

[20] Unfortunately, without knowing the exact working of the Panda's torque controller, there is little point in trying to interpret these issues.

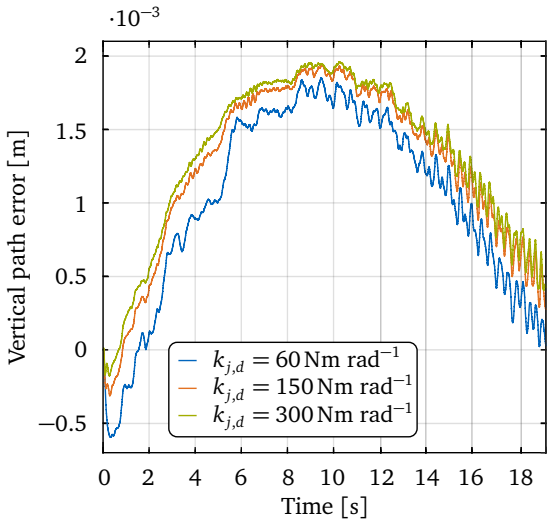

(a) Measured vertical path error at the TCP of the *Franka* Panda robot along an 80 cm horizontal trajectory with $42\,\mathrm{mms^{-1}}$.

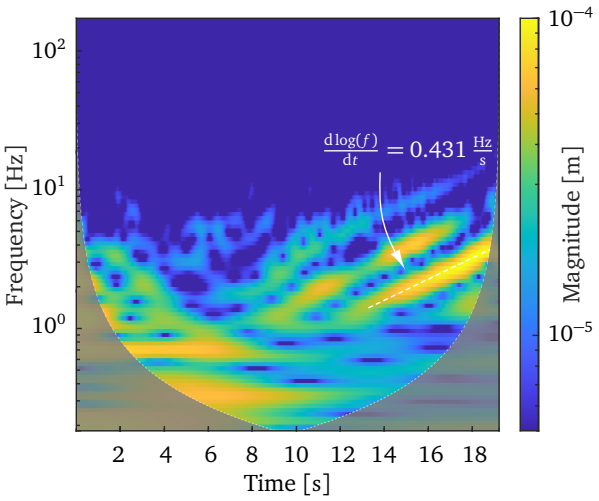

(b) CWT of the vertical path error at $k_{j,d} = 60\,\mathrm{Nm\,rad^{-1}}$.

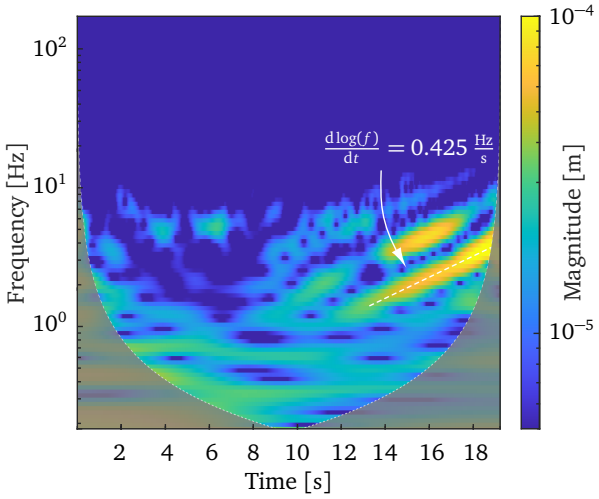

(c) CWT of the vertical path error at $k_{j,d} = 150\,\mathrm{Nm\,rad^{-1}}$.

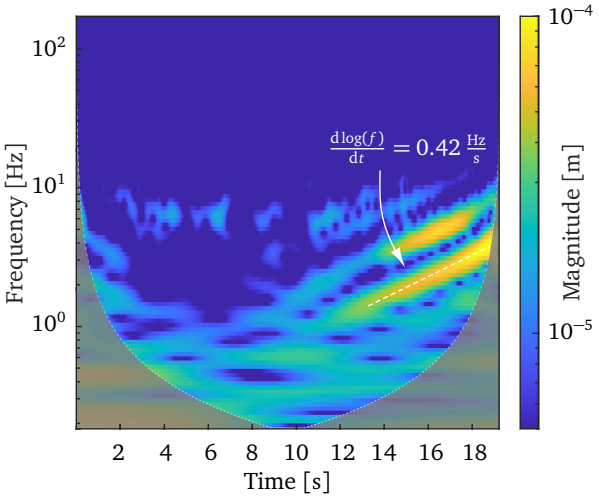

(d) CWT of the vertical path error at $k_{j,d} = 300\,\mathrm{Nm\,rad^{-1}}$.

Figure 4.40: Vertical path error of *Franka* Panda robot with different desired impedance stiffnesses. Measured at the TCP with eddy-current sensors.

The quasi-static error is, as expected, quite a bit higher than that of the UR10. The main issues here is probably that the gravity compensation would need to be better calibrated for the load on the robot (in this case a 500 g gripper). We can also see that the vertical path error rises upwards for higher desired impedance stiffnesses $k_{j,d}$. This is expected behavior, since higher impedance stiffnesses should cause less sag. Unfortunately, the robot seems to try to follow a wrong trajectory. This is again probably because of using slightly wrong DH parameters due to manufacturing tolerances, which effects trajectory planning as well as the gravity compensation scheme.

Discussion of Results

The *Franka* Panda is a bit of an unfair example, since the robot is not designed for high precision applications, but for a low-cost entrance into the field of collaborative robotics (and

it does a good job for that purpose). However, it nevertheless showcases the general problems that torque controlled robots still face when they are applied to high-precision applications:

- Any kind of control system that tries to incorporate the flexibilities of the links will be bottlenecked by the low-level torque-controllers bandwidth. In the case of the Panda robot 10 Hz is way too low for any higher-level control system to actively damp the structural dynamics of the robot[21]. Similar findings have also been reported in [183, 184], where the authors failed to apply a LQR controller tuned in simulation to a humanoid walking robot without considering the bandwidth of the torque controllers.
- The achievable gains for a higher-level impedance controller will also be further limited by the typical implementation issue like sensor noise and signal delay from the required absolute encoders on the joint side. This is probably why the *Franka* Panda can only achieve quite low desired impedance stiffnesses. In [97] and [116] it is argued that the bandwidth of the low-level controller inversely relates to the achievable impedance of the high-level controller.
- The comparatively low achievable impedance stiffnesses mean that the robot has to rely completely on its gravity compensation for accurate tracking. However, the underlying model usually only includes rigid links and can be quite unreliable for multiple reasons, as we have seen above.
- It still can be a quite effective strategy to use a low impedance stiffness combined with high impedance damping to achieve higher modal damping to reduce the dynamic tracking error due to structural vibrations. However, this approach, as any other control strategy using the robots joint motors, will only be able to affect structural modes that actually create torques around the motor axis of the robot. Any other structural mode will be uncontrollable, as we have seen with the CROPS robot in section 4.2.1. This might be somewhat circumvented with good mechanical design of the robot by making sure that there are no dominant structural modes that are uncontrollable. However, the robot will still have trouble to control the dynamics at the TCP of the robot close to a singular position, because of the very high joint torques needed.

While the control strategies developed for high-precision control with torque-controlled robots are certainly promising, the current hardware limitations do not allow for their implementation on real robots at the time of writing. Especially with 20 μm TCP tracking precision at 50 Hz bandwidth as required for this thesis.

As we will see in the next chapters, external stabilization approaches avoid most of the above issues and also do not need very precise models of the robot's structural dynamics to achieve very high tracking accuracy.

[21] The highest closed-loop bandwidth of joint torque-controllers known to me are achieved by the quadrupedal robot ANYmal from *ANYbotics*. The torque controllers can achieve a bandwidth of up to 70 Hz, however, only for a small desired torque amplitude of 1 Nm. For a desired amplitude of 10 Nm the bandwidth reduces to 20 Hz [131]. This is also probably due to only having to move the relatively small and lightweight legs of the quarduped.

4.4 Excursus: The Influence of Structural Dynamics on Biped Walking Robots

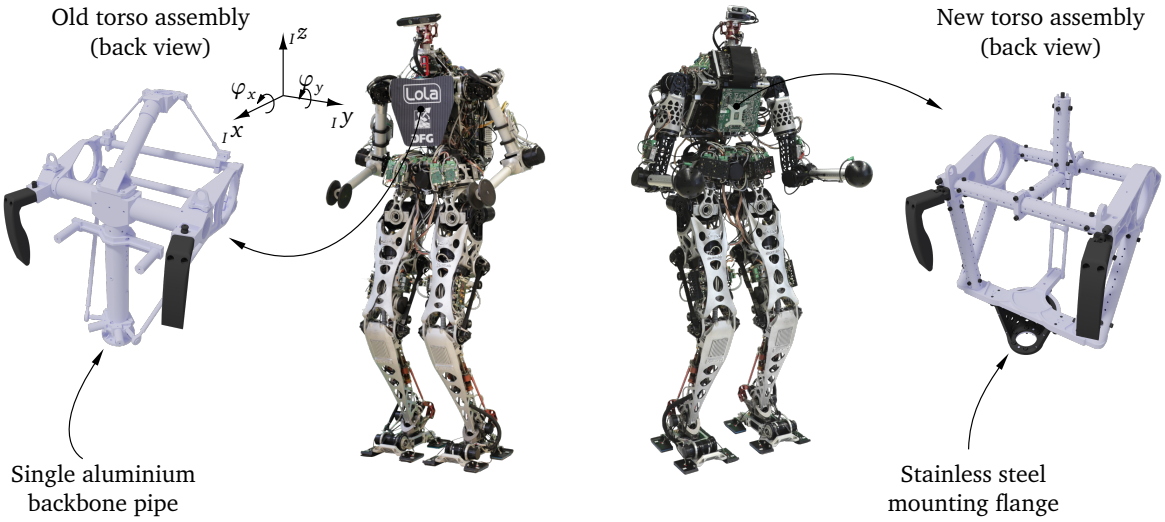

Figure 4.41: Old (left) and new (right) mechanical design of LOLA with the old and new torso assembly. Adapted from our paper [240].

During my time at the chair, we also noticed a significant influence of structural dynamics on the control system of our biped walking robot LOLA. While this thesis is mainly concerned with robot manipulators, I still want to include our findings in the main body of my thesis, since they can further improve the understanding of the influence of structural dynamics on the performance of complex mechatronic systems. It was also the first time that such experiments were published for biped walking robots, which also makes it worthwhile to showcase these results again here.

This section is based on the experimental results that we performed on the old version of LOLA in [52] and on the new version in [50]. I also did some preliminary works regarding LOLA's decentralized joint position control system in my master's thesis [45].

System Overview

LOLA is a humanoid biped walking robot that is actuated by 26 position controlled brushless DC motors. The goal for the mechanical design was to keep the structures of the robot as stiff and lightweight as possible. Most components are cast out of aluminum, resulting in an overall weight of 60 Kg for the robot at a height of 176 cm.

Both the hands and feet of the robot include a six-axis force/torque sensor each to measure the ground reaction forces. An inertial measurement unit (IMU) is installed at the middle of the torso to measure the upper body inclinations $\varphi_m = \left[\varphi_x, \varphi_y\right]^T$. The old version of the robot included a single aluminium backbone pipe in the upper body (Fig. 4.41, left), which also mounted the IMU. As we will see later, this component was especially critical for the robot vibration problems.

The robot recently got upgraded for multi-contact applications [240], which significantly improved the upper body mechanical design based on our findings of our first EMA performed in [52], Fig. 4.41. This upgrade also added two DOFs and two force/torque sensors to the arm extremities, which were already included in the initial description of the robot above.

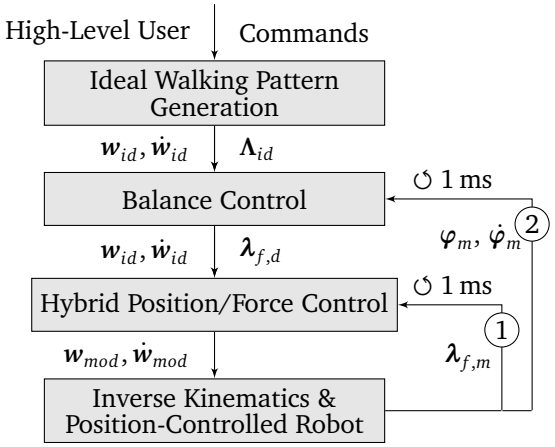

Figure 4.42: The control structure of LOLA with the two main feedback loops. Adapted from our paper [52].

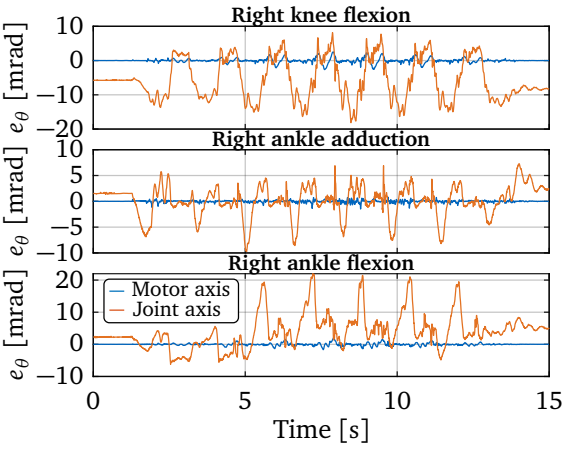

Figure 4.43: Angular position error e_θ at three different joints while walking in a straight line with 0.75 m/s. Adapted from our paper [52].

The hierarchical control structure of the robot is shown in Fig. 4.42. A *Walking Pattern Generator* first calculates trajectories $\boldsymbol{\omega}_{id}$, $\dot{\boldsymbol{\omega}}_{id}$ for the feet and center of mass (COM) based on simple dynamic models under the assumption of an ideal world. The ideal contact wrench $\boldsymbol{\Lambda}_{id}$ is then calculated using the trajectory of the COM [239]. Inaccuracies of the planning models and unexpected disturbances from the environment are then compensated by two subsequent control loops that adapt the ideal trajectories.

The *Balance Controller* uses measured IMU inclination data to modify the planned contact wrench $\boldsymbol{\Lambda}_{id}$ in order to keep the upper body upright. The total wrench is then distributed to the feet, which results in separate desired wrenches $\boldsymbol{\lambda}_{f,d}$ for both feet.

Afterwords, the *Hybrid Position/Force Controller* uses the measured wrench at each foot $\boldsymbol{\lambda}_{f,m}$ to control the desired wrenches $\boldsymbol{\lambda}_{f,d}$ by further adapting the desired pose of the robot [265]. The final modified trajectories $\boldsymbol{\omega}_{mod}$, $\dot{\boldsymbol{\omega}}_{mod}$ are then sent to the decentralized joint position controllers via inverse kinematics [268].

The joint position controllers are the same cascaded P-PI-PI controllers described in section 3.4.1. The motor angles θ_m are measured using incremental encoders. The motor torques are transmitted the robot joint with harmonic drive gears with high gear ratios of $N \leq 100$. The joint angles can also be measured using absolute encoders on the other side of the gears.

Structural Vibrations on the Joint Level

We first noticed the influence of LOLA's structural dynamics on her performance when we optimized her joint controllers and real-time communication architecture to achieve a better bandwidth for her low-level control hardware [268].

When directly controlling the motor axis of her joints, we were able to achieve a relatively high control bandwidth of 240 Hz. A walking test showed that, when we scale the errors measured at the motor axis up to the joint side after the gear, we should expect joint positioning errors in the μrad range (Fig 4.43, blue line). However, when measuring the actual errors at the joints using our additional absolute encoders, we found a significantly larger error at the joints (Fig. 4.43, red line). This is mainly due to the flexibility of the harmonic drive gears used in the joint modules of LOLA which deform under load.

We first see a static deflection of the gears when the robot is standing on the ground, which

is caused by initializing the robot after hanging on a rope without touching the ground. While walking, we can see different vibration frequencies depending on whether the corresponding leg is in contact with the ground. This is caused by a change of boundary conditions on her mechanical structure during the contact/non-contact phase of the legs, which consequently causes the structural dynamics of the robot to respond with different vibration frequencies while operating in a closed loop with the joint and walking/balancing controllers of LOLA. This already indicates relatively complex interactions between the robots structural dynamics, its control system and the environment. As already described in section 3.4.1, we tried to incorporate the absolute position feedback from the joint side into the cascaded joint position control scheme. However, these efforts only proved to be stable up to $1-2\,\text{Hz}$ bandwidth, which made it unusable for robust walking during more extreme balancing scenarios.

We ended up staying with a well tuned motor position controller that guarantees fast and robust control of the motor angles θ_m, accepting that the joint angles are not exactly correct.

Influence on the Balancing Controller

We noticed another issue related to the structural dynamics of the robot when tuning the balancing controller. The two main feedback loops for LOLA's balancing controller rely on sensor feedback of the force/torque sensors and IMU data, Fig. 4.42. However, these control loops are significantly influenced by the structural dynamics of the robot, since both loops are non-collocated. E.g. the balancing controller (2) measures the current inclination φ_m, $\dot{\varphi}_m$ using the IMU at the torso and controls the desired contact forces at the feet. This control loop includes the dynamics of the entire mechanical structure of LOLA between input and output, which is not yet considered in the control design.

For example, let us assume that the current vertical force at the foot is too low. This will cause the force control loop (1) to increase the vertical velocity of this foot, which then increases the contact force. However, this motions also excites the structural resonances of the robot, which causes vibrations at the IMU and consequently undesired feedback of structural dynamics through the inclination feedback (2). In practice, this means that the bandwidth of the current cascaded balancing controller needs to be lower than the first structural eigenfrequency of the robot in order to guarantee robust and stable operation of the control system.

In order to verify these assumptions, we performed a closed-loop identification of LOLA's feedback loop plants using the robot's own sensors and actuators. For the identification, both feedback loops are active to prevent the robot from tilting over. We then added a multi-sine excitation to the desired vertical foot velocities in LOLA's control software, for the same reasons as already explained in section 4.3.1. The measurements were performed in a range from $1-100\,\text{Hz}$ in 4 second runs with 20 sine waves each, resulting in a frequency resolution of $0.25\,\text{Hz}$ for the identified transfer function.

The measured open-loop transfer functions between the vertical velocities at the feet and the measured inclination rate at the IMU are shown in Fig. 4.45. As expected, there are several high resonance peaks in the measured plant. With this knowledge, the controller could be improved by placing notch filters near these resonances [22].

However, since the structural dynamics of the robot also change during motion, we found that the most reliable way to improve the performance of the balancing controller was by upgrading the mechanical design of the robot. We therefore performed an EMA on the old design of the robot to find weaknesses in the structure, as well as to confirm our findings of the open-loop transfer function in Fig. 4.45.

[22] The controllers and tuning procedures are explained in much more detail in the dissertation of my colleague SYGULLA [266].

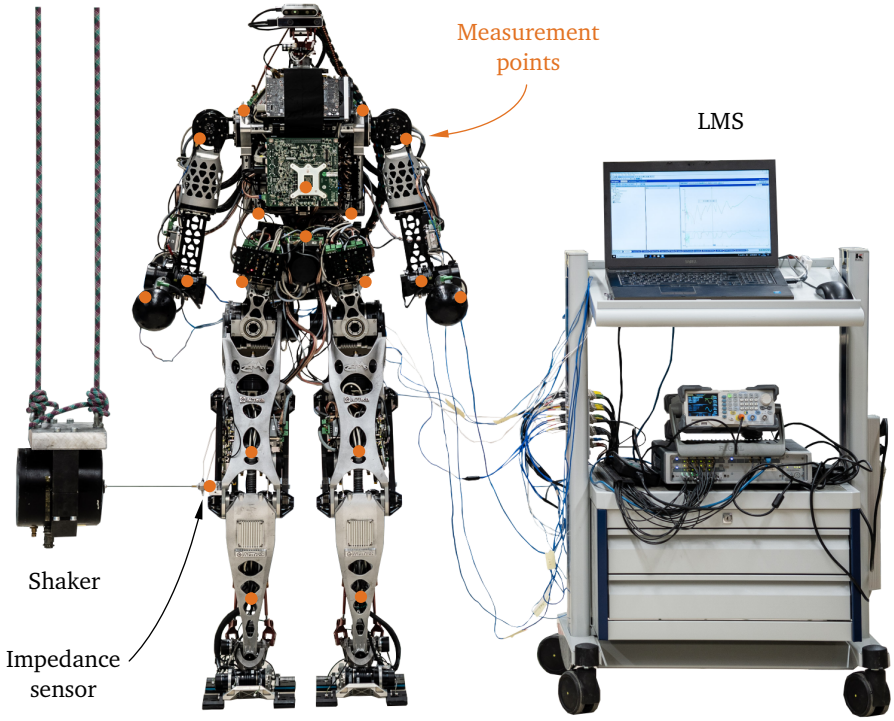

Figure 4.44: New mechanical design of LOLA with the measurement setup.

Experimental Modal Analysis of the Old Design

The experimental setup for the EMA is shown in Fig. 4.44. The setups were the same for the measurements on the old and new design. In both cases, we hung a shaker from the ceiling and excited the robot at the knee from the side and the front. The input signal was a logarithmic sweep for 20 seconds up to 30 Hz, which puts more energy in the lower frequency range of interest. The input force was measured using an impedance sensor.

For the response measurements we again used the same triax acceleration sensors with dimensions of $12.5 \times 12.5 \times 12.5$ mm, 6.7 grams of weight and a sensitivity of 100 mV/g. These sensors are again a compromise between measurement range, size and weight, since we needed to be able to place the sensors inside of the structure of the robot.

The measurement points for the measurements on the old design can be seen in Fig. 4.48a (blue points). Since, at the time, we suspected the main weakness to be the upper body, we placed most sensors in that region. We placed two sensors on each arm, one on each shoulder, one on the upper part of the backbone pipe (close to the IMU), one on the lower part of the backbone pipe and four sensors around the pelvis. One pelvis-sensor was placed next to the pelvis rotation motor, one near the pelvis adduction motor and two next to the left and right hip rotation motors each. The purpose of these pelvis sensors was to determine the influence of the deformation of the joints in this region on the overall dynamic behavior of the structure. This overall makes 14 measurement points with 3 measurement directions each. The data was again acquired using the *Siemens* LMS system.

During the measurements, LOLA stands on the ground in her typical starting position. The motor angles are actively held in place by the joint controllers, however, the balancing controllers (1) and (2) are turned off. For the measurement, we used as much force as possible at the shaker, without risking any damage to the components. The excitation caused large vibration amplitudes of over a centimeter at the arms. This is necessary to obtain clean results, since low vibration amplitudes would be quite dominated by non-linear friction

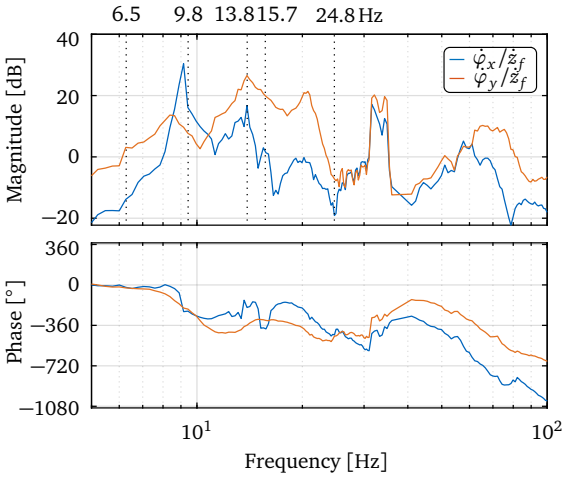

Figure 4.45: Measured open-loop transfer function from desired velocities at the feet $\dot{z}_f$ to the inclinations $\dot{\varphi}_{x/y}$ measured at the IMU. Adapted from our paper [52].

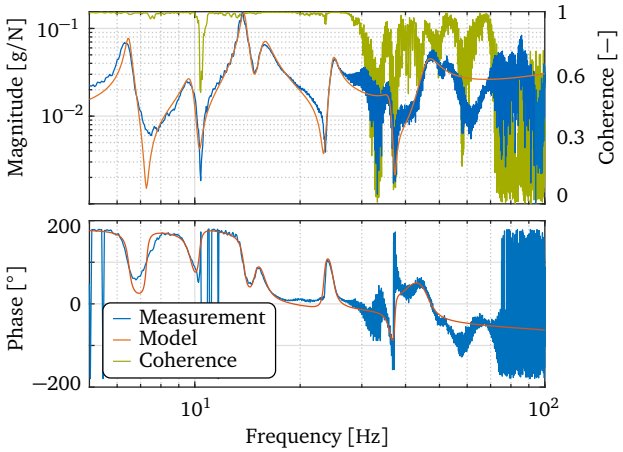

Figure 4.46: Measured FRF from the excitation force in I_y-direction at the knee to the acceleration measured in I_x-direction at the upper backbone pipe. Adapted from our paper [52].

effects in the high number of joints of the robot.

An exemplary FRF is shown in Fig. 4.46 (blue line), which is the most important transfer function for us from the shaker input to the spine of the robot. The measurement shows very good coherence up to 30 Hz, capturing the first few resonances very well. The synthetization result from the PolyMax algorithm also shows a very good match to the measured data. This good result also shows that, while the structure is highly damped, it still behaves like a linear mechanical structure.

The identified mode shapes are shown in Fig. 4.48a. The first mode at 6.5 Hz is mainly a rotation around the ${}_I z$-axis, which is also why it does not show up in the measured open-loop transfer function Fig. 4.45. The control loops of the balancing controller only use the IMU inclinations around the ${}_I x$- and ${}_I y$-axis, which makes this mode unobservable[23].

The second mode at 9.7 Hz is a motion in the ${}_I y$-${}_I z$-plane. The shoulders rotate to the right, while the hip rotates to the left, bending the backbone pipe in the process. All other structures stay rigid in respect to each other. This confirms our previous assumption that the weakest point of the structure is located in the upper body and is most likely the backbone pipe itself. This mode also matches the first resonance peak in the measured open-loop transfer function Fig. 4.46.

The third mode at 13.8 Hz can also clearly be seen in both open-loop transfer functions. The hips rotate around the ${}_I z$-axis, while the shoulders rock to the left and right with the arms staying rigid in respect to them.

Mode four at 15.7 Hz is dominated by torsion of the hip around the ${}_I z$-axis and is the first mode that also includes bending of the arms. The shoulders and hip stay parallel to each other, which means that the backbone mounting the IMU does not get deformed. For this reason, this mode is also only barely visible in Fig. 4.45.

The fifth mode at 24.8 Hz again mainly involves torsion of the backbone pipe, while it now also includes bending at the arms. The sensor near the IMU at the backbone pipe also barely moves during this mode. This indicates that the IMU is quite close to a node of this mode shapes, which is the reason for the antiresonance at this frequency in Fig. 4.45.

The sensors placed around the pelvis always stay rigid with respect to each other during all shown modes, which means that there is no deformation of these joints involved in those

[23] We were actually a bit lucky here, since otherwise this resonance would have limited the bandwidth of the balancing controller even sooner.

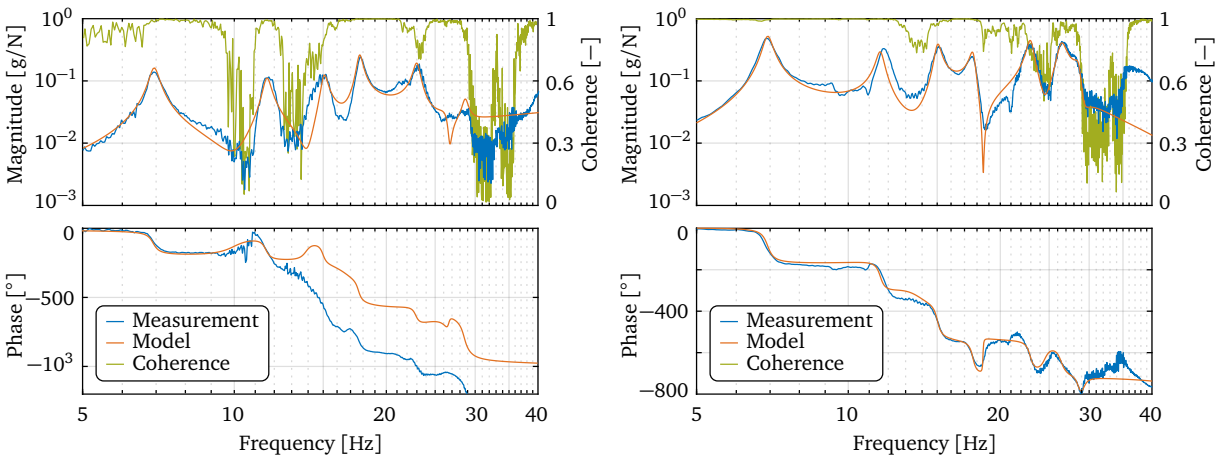

(a) FRF from the input at the shaker to the output acceleration at the lower right corner of the torso in vertical direction.

(b) FRF from the input at the shaker to the output acceleration at the left elbow in vertical direction.

Figure 4.47: Exemplary measured FRFs with the synthesized model and coherence (after upper-body redesign).

mode shapes.

Experimental Modal Analysis of the New Design

After LOLA's upper body was redesigned for multi-contact applications [240], we redid the same measurements to verify any improvements of the new design. The redesign completely replaced the old backbone pipe of the robot by a more rigid box-like assembly, which now houses the IMU. The torso is also now attached to the hip by a particularly stiff stainless steel mounting flange (Fig. 4.41, right). The arms of the robot were changed to add one additional DOF and one force/torque torque sensor at each of the hands. The rest of the robot remained unchanged. Overall, the robot's DOFs increased by 2 to 26, the height to 1.76 m (+1.21 %) and mass to 68.2 kg (+7.74 %). The redesign is explained in more detail in [240]. A video showcasing the new hardware upgrades is published at [301] and a video showcasing her multi-contact capabilities at [302].

The EMA was performed in exactly the same way as before, however, with a different placement of sensors. For these measurements we were also interested in the motion of the legs, using one more measurement run with a total of 18 sensors, Fig 4.48b.

The worst quality measurement is shown in Fig. 4.47a. The measurement still shows good coherence at the resonances peaks. However, the bad signal-to-noise ratio at around 13 Hz caused the PolyMax algorithm to miss-identify an antiresonance. Since we are only interested in the modal parameters of the system, this is not a concerning problem. The peaks are all well fitted and the phase after the miss-identified antiresonance still follows the correct path. Most other measurements are of higher quality, as depicted in Fig. 4.47b.

The resulting mode shapes of the EMA are shown in Fig. 4.48b. The first mode is basically unchanged and only slightly increased its eigenfrequency from 6.5 Hz to 6.9 Hz (+6.1 %). This is because the mode is almost completely caused by the twisting of the legs, with the upper body staying rigid and rotating around its yaw axis. The old design probably also contributed a bit more to this mode by torsion of the backbone pipe, which is why this mode is now slightly improved.

The more important second mode increased its eigenfrequency significantly from 9.7 Hz to 11.6 Hz by 19.6 %. The new mode now shows barely any movement in the torso and is only

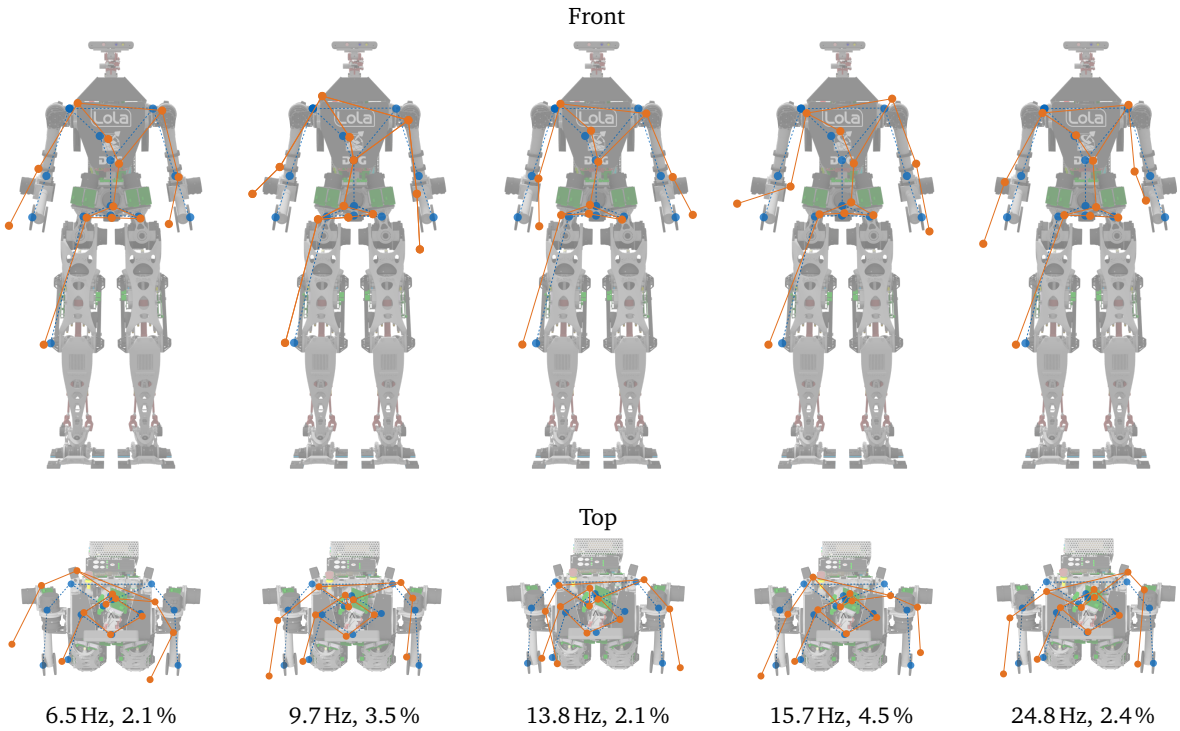

(a) Mode shapes before the redesign. Adapted from our paper [52].

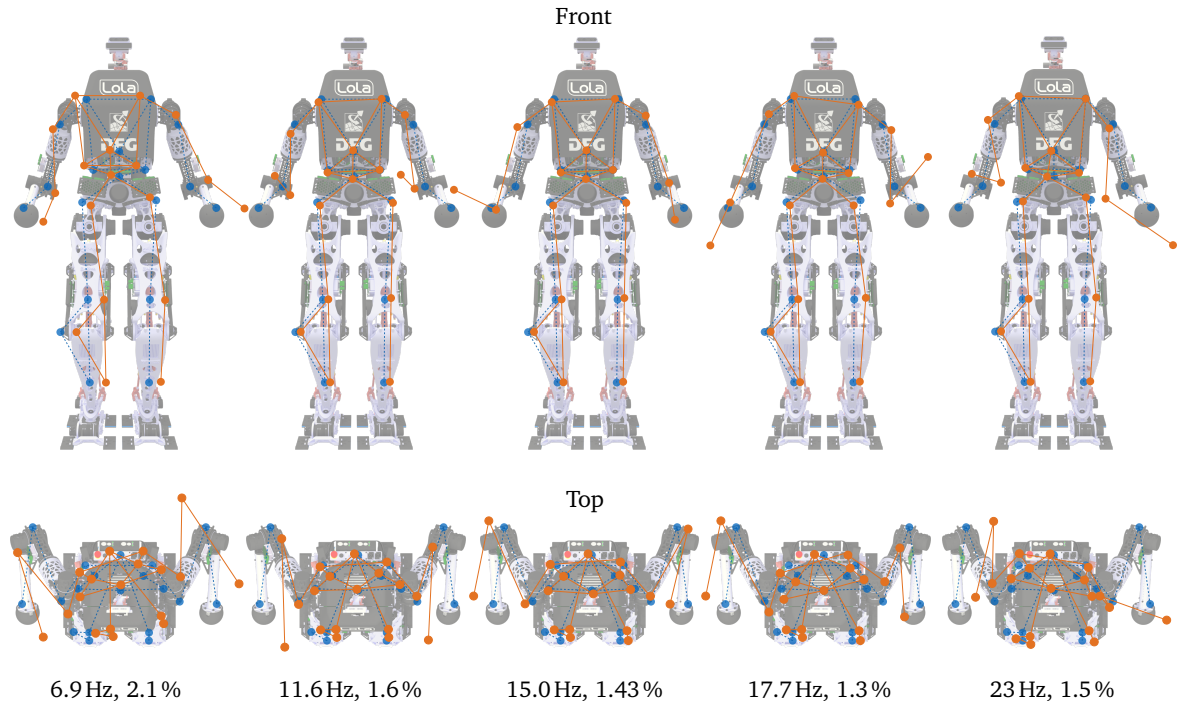

(b) Mode shapes after the redesign.

Figure 4.48: Front and top view of the first five mode shapes before and after the redesign with their respective eigenfrequency and damping ratio. Adapted from our paper [50].

dominated by large motion in the arms. This is exactly what we wanted to achieve, since the transfer paths from the IMU at the center of the torso to the force/torque sensors in the feet are now significantly more rigid.

The same is also true for the third and fourth mode, which are only different combinations

of arm and leg motions, while the torso and hip stay rigid relative to each. The first deformation in the upper-body can be seen in the fifth mode at 23 Hz. While the torso still behaves rigidly, there is now a relative motion between the torso and the hips caused by torsion of the hip joint. This is also why this mode is the only one that decreased in eigenfrequency: Since this mode was also dominated by the torsion of the hip joint in the old design, the additional torso weight reduced the natural frequency of this specific mode shape. This is comparable to adding weight to a single harmonic oscillator, with the hip joint being the spring and the torso being the mass.

The mechanical structure also lost a significant amount of damping due to the redesign, e.g. from 3.5 % to 1.6 % for the second mode. This is probably because of the new design being a new clean assembly that replaced a lot of old rivet connections which had started to deteriorate over the years.

Discussion of Results

Performing an EMA was again a very helpful tool to identify weaknesses in the structure. In this case, the main problem was the single backbone pipe of the old design that got replaced by a better torso assembly in the new one. This again showed that the flexibilities of the link structures can have a significant influence on the performance of a robot, even a biped walking machine. The state of the art for biped walking robots is still to model the robot as a rigid multi body system, which can cause significant vibration problems by ignoring the flexibilities of the system in the control design, as was shown here.

For example, by upgrading the torso assembly, we also lost a significant amount of damping in the mechanical structure. This caused the joint controllers of the robot to excite the first mode of the structure, causing very large vibration amplitudes in the arms and legs during operation. The PI-velocity portion of the cascaded joint position controllers had to be tuned more aggressively by my colleague SYGULLA in order to add more damping to the system, making it stable again. The effects on the control system are explained in much more detail in his dissertation [266].

While it was possible to improve the performance of the robot's balancing controller by placing notch filters near the resonances of the open-loop transfer function, we assume that we could reach an even better performance by also considering the changing structural dynamics of the robot during motion. While walking, LOLA's structural dynamics probably depend significantly on the current pose, which might have a large effect on the open-loop control plant Fig. 4.45. The effect is likely even more pronounced than on robot manipulators, since the robot is also constantly changing its boundary conditions with the environment during walking. This should be even more significant during multi-contact scenarios, where the robot can have any number of hands or feet in contact with the environment. Having a better understanding of how the structural dynamics of the robot behave during walking would definitely further improve our ability to design better control strategies with even higher bandwidths.

Chapter 5

Stabilization of Robot Manipulators

After gathering the necessary tools and insights about the influence of structural dynamics on the performance of robot manipulators in the previous chapter, I will describe our efforts to develop external stabilization devices for high-precision trajectory tracking in this chapter.

Section 5.1 will be about the external vibration damping approach using a proof-mass actuator near the TCP of the robot. After discussing the actuator and controller design, the system's performance is tested in simulation and on the CROPS robot's using experiments. At the end of this section I will also briefly discuss the potential of using modern control methods for this approach.

The external stabilization approach is discussed on section 5.2. With again the actuator and controller design being discussed first and the performance of the system being tested in simulation and experiments on the UR10 robot in the later subsections.

5.1 External Vibration Damping of Robot Manipulators

The idea of the external vibration damping approach is to use acceleration feedback at the TCP of the robot to employ active vibration damping techniques via a control force produced by a proof-mass actuator. The assumption being that actively damping the structural dynamics of the robot will reduce the dynamic error at the TCP while tracking a trajectory. This approach will of course not be able to also influence the quasi-static tracking error of the robot. However, the quasi-static error could also be improved by applying absolute calibration methods to the robot as described in section 2.1.1. The quasi-static error was also less of an issue for the manufacturing process of the industry project which motivated this thesis.

Some preliminary results of the topics discussed in this section are published in our papers [48] and [49].

5.1.1 Actuator and Controller Design

The actuator consists of a voice coil and a permanent magnet, Fig. 5.1. This is a common setup for force transmitters like shakers. However, usually the permanent magnet is also connected to leaf springs. The main function of the springs is to hold the permanent magnet in place, when the actuator is turned off and to prevent drift of the permanent magnet during operation, keeping it near the center of its motion range. The disadvantage of such springs is that the actuator acts like a single harmonic oscillator as described in section 3.1.1. The actuator will therefore have a resonance frequency determined by the mass of the permanent magnet and stiffness of the leaf springs.

We will see in the following that it is beneficial to tune the actuator eigenfrequency as low as possible to achieve the best force transmission behavior. However, this also means

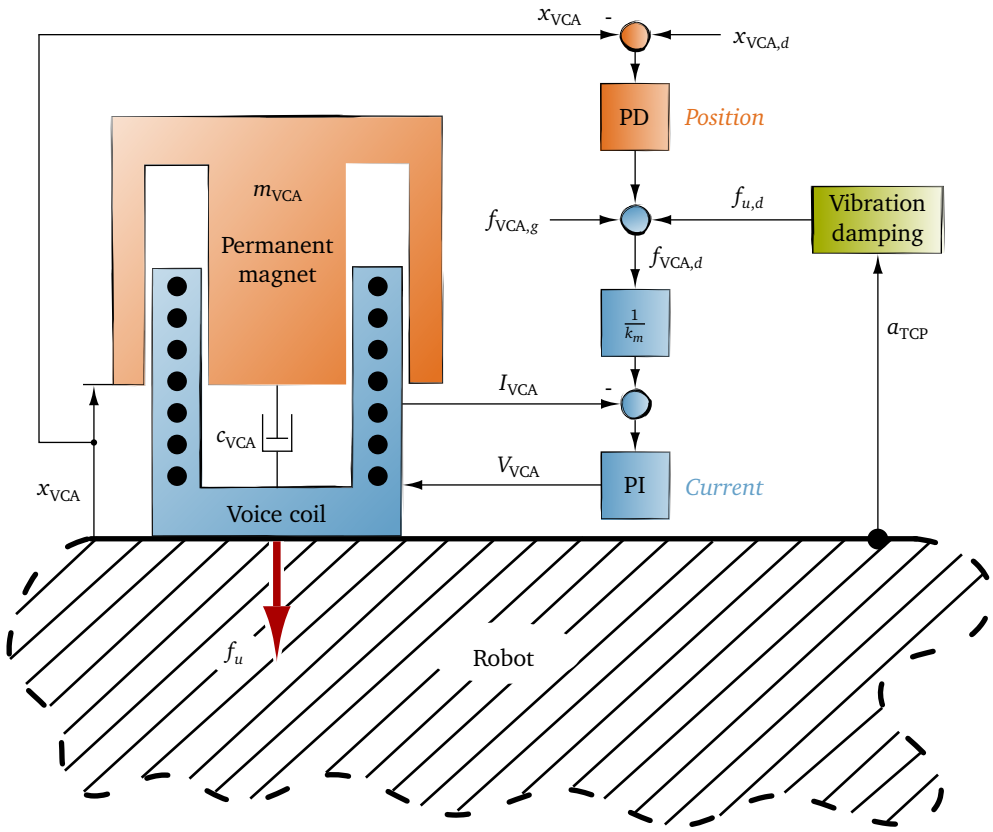

Figure 5.1: Proof-mass actuator attached near the end effector of a robot with control structure.

that the mechanical system has to be tuned and designed in advance and will not be easily changeable later, without exchanging mechanical components like the leaf springs. It is also quite hard to introduce a beneficial amount of viscous damping into the actuator dynamics by just using mechanical components, which usually means that the actuator resonance has quite a high peak.

I therefore wanted to retain some flexibility for the actuator design by omitting the mechanical springs and instead using a position controller for the permanent magnet position (Fig. 5.1). This has the advantage of being able to directly influence the actuator dynamics with the position controller. However, it also increases the systems complexity, since we now also need position feedback from the permanent magnet. Additionally, a secondary function of the usual leaf springs is to guide the permanent magnet within the voice coil. This function must now be realized with additional guide rails that glide on ball bearings in order to prevent the actuator from jamming, which has the disadvantage of introducing friction into the system.

The purpose of the actuator is to introduce a control force f_u near the TCP of the robot, which will be used by an higher-level vibration damping controller with acceleration feedback. The actuator is attached as close as possible to the TCP of the robot and will be able to transmit a force along the direction of motion of the permanent magnet. By applying a voltage to the voice coil, the resulting magnetic field will apply a force f_{VCA} to the magnet. The inertia force created by the acceleration of the magnets mass m_{VCA} will then be equal to the reaction force f_u at the robot.

Actuator Model and Controller

In order to model the system, let us start with the equilibrium of forces acting on the permanent magnet, which includes the inertia forces from its own mass m_{VCA}, viscous damping c_{VCA} coming from the contact with the guide rails[1] and the voice coil force f_{VCA}:

$$m_{\text{VCA}}\,\ddot{x}_{\text{VCA}} + c_{\text{VCA}}\,\dot{x}_{\text{VCA}} = f_{\text{VCA}}\,. \tag{5.1}$$

The control law for the actuator is a simple PD controller using the permanent magnets position x_{VCA} as feedback:

$$f_{\text{VCA}} = g_{P,x}(x_{\text{VCA},d} - x_{\text{VCA}}) + g_{D,x}(\dot{x}_{\text{VCA},d} - \dot{x}_{\text{VCA}}) + f_{u,d} + f_{\text{VCA},g}\,, \tag{5.2}$$

with $g_{P,x}$ and $g_{D,x}$ being the proportional and derivative gain of the PD position controller, respectively. $f_{u,d}$ is the desired force that the actuator is supposed to transfer to the robot and is generated by the higher level active vibration controller. $f_{\text{VCA},g}$ is a gravitation compensation term, which I will explain later.

Inserting the control law into equation of motion of the VCA (5.1), we get the closed-loop dynamics of the system:

$$m_{\text{VCA}}\ddot{x}_{\text{VCA}} + c_{\text{VCA}}\,\dot{x}_{\text{VCA}} = g_{P,x}(x_{\text{VCA},d} - x_{\text{VCA}}) + g_{D,x}(\dot{x}_{\text{VCA},d} - \dot{x}_{\text{VCA}}) + f_{u,d} + f_{\text{VCA},g}\,. \tag{5.3}$$

There are two transfer function of interest in the system. The first one is the position transfer function, which we can get by setting the other two inputs $f_{u,d}$ and $f_{\text{VCA},g}$ to zero

$$m_{\text{VCA}}\ddot{x}_{\text{VCA}} + (c_{\text{VCA}} + g_{D,x})\dot{x}_{\text{VCA}} + g_{P,x}x_{\text{VCA}} = g_{D,x}\dot{x}_{\text{VCA},d} + g_{P,x}x_{\text{VCA},d} \tag{5.4}$$

and then solve for the transfer function in the Laplace domain with the desired position $x_{\text{VCA},d}(s)$ as the input and the actual position $x_{\text{VCA}}(s)$ as the output:

$$\frac{x_{\text{VCA}}(s)}{x_{\text{VCA},d}(s)} = \frac{g_{D,x}s + g_{P,x}}{m_{\text{VCA}}s^2 + (c_{\text{VCA}} + g_{D,x})s + g_{P,x}} \qquad \text{(position transfer function)} \tag{5.5}$$

The other transfer function of interest is the force transfer function. We can again first set the other two inputs $x_{\text{VCA},d}$ and $f_{\text{VCA},g}$ to zero and rearrange to

$$m_{\text{VCA}}\ddot{x}_{\text{VCA}} + (c_{\text{VCA}} + g_{D,x})\dot{x}_{\text{VCA}} + g_{P,x}x_{\text{VCA}} = f_{u,d}\,, \tag{5.6}$$

which already looks like a mechanical single harmonic oscillator with stiffness $g_{P,x}$ and viscous damping $(c_{\text{VCA}} + g_{D,x})$.

The reaction force transferred to the robot can be approximated as the inertia force at the permanent magnet $f_u \approx m_{\text{VCA}}\ddot{x}_{\text{VCA}}$. Transforming the above equation into the Laplace domain with accelerations as the output gives

$$m_{\text{VCA}}\ddot{x}_{\text{VCA}}(s) + (g_{D,x} + c_{\text{VCA}})\ddot{x}_{\text{VCA}}(s)\frac{1}{s} + g_{P,x}\ddot{x}_{\text{VCA}}(s)\frac{1}{s^2} = f_{u,d}\,. \tag{5.7}$$

We can now solve for the product $m_{\text{VCA}}\ddot{x}_{\text{VCA}}(s)$, which is equal to the reaction force f_u applied to the robot. Finally, dividing by the desired force $f_{u,d}(s)$ gives us the force transfer function of the actuator:

$$\frac{m_{\text{VCA}}\ddot{x}_{\text{VCA}}(s)}{f_{u,d}(s)} = \frac{f_u(s)}{f_{u,d}(s)} = \frac{s^2}{1 + \frac{(c_{\text{VCA}}+g_{D,x})}{m_{\text{VCA}}}s + \frac{g_{P,x}}{m_{\text{VCA}}}} \qquad \text{(force transfer function)} \tag{5.8}$$

[1] We will see later that the friction at the guide rails is actually quite significant, despite using ball bearings. Modeling the friction at the ball bearings as viscous damping is again a substantial simplification. However, using ball bearings at least significantly reduces more complex effects like stick slip or surface friction.

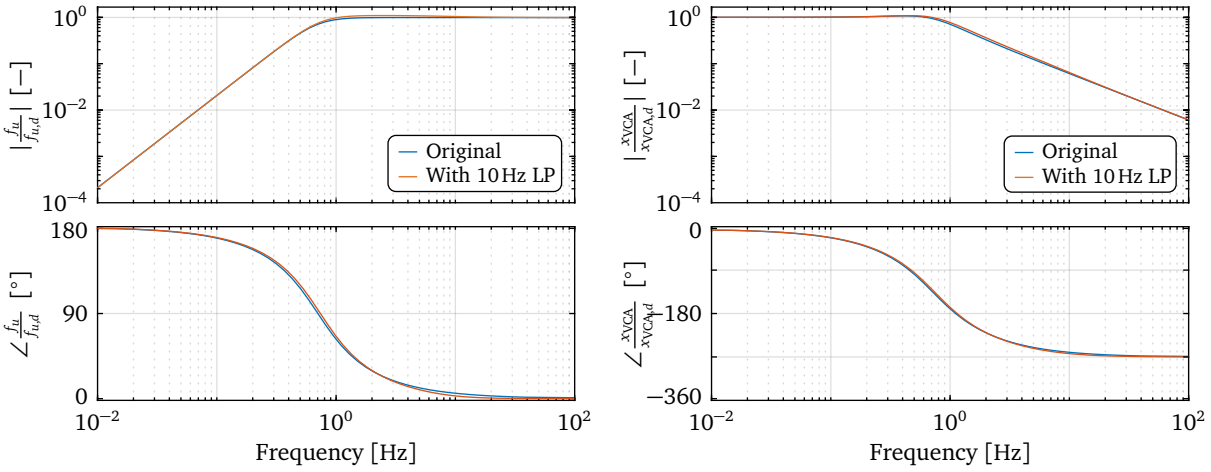

(a) Force transfer function.

(b) Position transfer function.

Figure 5.2: Transfer behavior of the position controlled voice coil actuator with $m_{\mathrm{VCA}} = 1\,\mathrm{kg}$, $c_{\mathrm{VCA}} = 10\,\mathrm{N/s}$, $\omega_{0,d} = 2\pi \cdot 0.7\,\mathrm{Hz}$ and $\zeta_d = 1$. With and without a lowpass filter at the measured position x_{VCA} with cutoff at $\omega_{\mathrm{LP}} = 2\pi \cdot 10\,\mathrm{Hz}$.

Controller Design

The force and position transfer functions of the position controlled voice coil actuator are plotted in Fig. 5.2 (blue lines). We can see that the force transfer function behaves like a mechanical single harmonic oscillator with

$$\omega_{0,d} = \sqrt{\frac{g_{P,x}}{m_{\mathrm{VCA}}}}\,, \tag{5.9}$$

$$\zeta_d = \frac{c_{\mathrm{VCA}} + g_{D,x}}{2 m_{\mathrm{VCA}} \omega_{0,d}}\,. \tag{5.10}$$

The PD position controller can therefore be tuned by choosing a desired lower bandwidth limit $\omega_{0,d}$ and damping ratio ζ_d and by then solving the above equations for the needed controller gains $g_{P,x}$ and $g_{D,x}$.

From the force transfer function Fig. 5.2a (blue line) it is obvious that we get the best force transfer behavior by choosing the desired actuator eigenfrequency $\omega_{0,d}$ as low as possible and a desired damping ratio of $\zeta_d = 1$ to prevent unnecessary oscillations. The actuator has infinite force bandwidth in theory. However, in practice, the bandwidth is limited by the lower level current controller, since the desired VCA force is scaled with the motor constant and then sent as a desired current to the current controller (see Fig. 5.1).

The desired actuator eigenfrequency $\omega_{0,d}$ also cannot be set arbitrarily low for two reasons: For one, by setting the $\omega_{0,d}$ very low, the virtual actuator stiffness $g_{P,x}$ also becomes very low. This might cause the static equilibrium with the gravity force acting on the mass to be below the physical range limit of the actuator. However, the static equilibrium should be in the middle of the displacement range of the actuator to guarantee the maximum possible range of motion for the permanent magnet. This can be done by compensating the gravitational pull with the feedforward term $f_{\mathrm{VCA,g}} = m_{\mathrm{VCA}} g$ in the control law (5.2) and setting the desired position $x_{\mathrm{VCA},d}$ to the middle of the actuator range[2].

[2] In practice, this still sets a lower limit for the possible desired actuator eigenfrequency $\omega_{0,d}$. By decreasing the virtual stiffnesses $g_{P,x}$, the control system needs a very accurate value for the gravitation compensation to keep the magnet in the middle of the actuator range.

The second limiting factor is the friction at the guiding rails of the actuator. As the virtual stiffness $g_{P,x}$ decreases, the inherent friction of the guiding rails (modeled as viscous damping c_{VCA} here) will become more dominant, increasing the overall damping ratio of the system. In practice, this effect can become so large that negative $g_{D,x}$ is needed to keep the desired damping ratio at $\zeta_d = 1$. This is in theory not an issue, however, as the friction becomes more dominant in its contribution to the overall system dynamics, the assumption of viscous damping c_{VCA} becomes even less valid. Although we are using ball bearings on the real system, very low virtual stiffnesses $g_{D,x}$ will cause the system dynamics to be significantly impacted by non-linear friction and stick-slip effects, degrading the actuator's force transfer performance.

The performance of the system is therefore dependent on how well friction can be avoided in the mechanical design of the actuator in order to achieve a low actuator eigenfrequency $\omega_{0,d}$. The system shown in Fig. 5.2a is already quite optimistic with an actuator eigenfrequency $\omega_{0,d}$ at 0.7 Hz. We can see that with a damping ratio at $\zeta_d = 1$, the phase only comes close to zero near 10 Hz, giving the actuator an effective lower bandwidth limit of also around 10 Hz for the higher level damping controller. This could be improved by reducing the damping ratio ζ_d, however, this will cause the actuator to develop a resonance peak in the position- and force transfer function, which might be excited by any form of jerk at the robot and again degrade system performance.

The main goal of the position controller is to keep the permanent magnet oscillation around the middle of the actuator range and to prevent drift of the actuator. We have already seen that we might need quite high $g_{D,x}$ gains to achieve a damping ratio of $\zeta_d = 1$, which might be problematic due to sensor noise. However, thanks to the low desired actuator eigenfrequency $\omega_{0,d}$, we can also apply a relatively aggressive lowpass filter to the position feedback. The red lines in Fig. 5.2 show the position- and force transfer functions with a lowpass filter cutoff frequency at 10 Hz, which barely effects the system performance and allows for much higher $g_{D,x}$ gains, even in the presence of noise.

For the following simulation results, the actuator dynamics will be considered by applying the force transfer function with the lowpass filter (Fig. 5.2a red line) after the vibration controller output.

5.1.2 Simulation Results

In this subsection, I will again use the position controlled UR10 based simulation model with two flexible links to investigate the effectiveness of the vibration damping controllers discussed in section 3.3. The model performs the same 1 m long horizontal benchmark trajectory as before with a speed of 100 mm/s at the TCP, Fig. 5.3. The trajectory is again planned with a constant velocity, causing high jerk in the beginning and the end, to test the robustness of the vibration damping controllers.

The transfer function of interest is the driving point transfer function in the y-direction at the TCP, since it shows two pose dependent modes in the frequency range below 50 Hz. We have seen in Fig. 4.8b that the second mode does not show up in the driving point transfer function in the z-direction. The reason for this is that the second mode is dominantly a bending motion around the inertial z-coordinate, which is therefore unobservable with this specific transfer function. In order to control this mode, we therefore need an actuator in the y-direction at the TCP. In theory, this actuator could also control the first mode, however, we would need unnecessarily high forces since the first mode is dominantly a bending mode around the inertial x-axis. The first mode is consequently much easier to control by using a second actuator in the z-direction at the TCP of the robot. For the following analysis, I will therefore apply one controller in the z-direction for the first mode and a second controller in

the y-direction for the second mode.

Vibration Controllers

The following active vibration controllers (Fig. 5.1 green box) will be applied at the TCP with the accelerations $\ddot{y}_{\mathrm{TCP}}$ / $\ddot{z}_{\mathrm{TCP}}$ as the feedback input and the force $f_{\mathrm{TCP},y}$ / $f_{\mathrm{TCP},z}$ as the controller output:

- The first one is the *direct velocity feedback controller* (3.82) with a gain factor of $g_{\mathrm{DVF},y/z} = 1 \cdot 10^3\,\mathrm{Nsm}^{-1}$ for both controllers acting in y- and z-direction at the TCP of the robot. To generate the needed velocity feedback, the acceleration measurements at the TCP of the robot are integrated and filtered with a high-pass filter with a corner frequency at 0.8 Hz to reduce drift from the integration of noise.
  The stability of the controller is limited by the bandwidth of the lower level current controller, sensor noise and maximum force of the actuator. In this case, the first bottle neck is the maximum actuator force, which is set to $f_{\max} = 80\,\mathrm{N}$ similar to the voice coil actuator used for the experiments. The gain is tuned such that the actuator force is only allowed to reach the maximum value for a short moment.

- The second controller is the *negative acceleration feedback controller* (3.83). The controller is tuned by looking at the closed-loop driving point transfer function $\frac{\ddot{y}_{\mathrm{TCP}}}{f_{\mathrm{TCP},y}}$, Fig. 5.4. The controller damping is set to $\zeta_{\mathrm{NAF},y/z} = 0.5$ for both controllers and the controller eigenfrequencies are set to $\omega_{\mathrm{NAF},y} = 2\pi \cdot 22\,\mathrm{Hz}$ and $\omega_{\mathrm{NAF},z} = 2\pi \cdot 18\,\mathrm{Hz}$ to damp the first and second mode at the initial starting pose of the robot. The controller eigenfrequencies are held constant during the test trajectory.
  As we have already seen in section 3.3, increasing the gain of both NAF controllers will decrease the magnitude at the targeted eigenfrequencies. However, after a certain amount of attenuation, the controller will push new resonance peaks to lower and higher frequencies (Fig. 5.4 dark blue line). Especially the lower resonance peak might become a problem, since lower frequency resonances will cause higher displacement amplitudes compared to higher frequency resonances. The controllers are therefore tuned such that there is only a small amount of side resonance created by the controller at $g_{\mathrm{NAF},y/z} = 5 \cdot 10^4\,\mathrm{Nm}^{-1}$ (Fig. 5.4 green line).

- The third controller is the same negative acceleration feedback controller as the second one. However, the controller eigenfrequencies $\omega_{\mathrm{NAF},y/z}$ now track the pose depended eigenfrequencies during motion of the robot[3].

Closed-Loop Dynamics at the TCP

The closed-loop dynamics of the controllers can again be analyzed by plotting the driving point transfer function $\ddot{y}_{\mathrm{TCP}}/f_{\mathrm{TCP},y}$ over the traveled distance of the TCP along the desired trajectory, Fig. 5.5.

We can see in Fig. 5.5b that the velocity feedback controller achieves the highest amount of attenuation, while also needing the least amount of tuning effort. The NAF controller with constant controller eigenfrequencies (Fig. 5.5c), performs a bit worse for the second structural eigenfrequency of the robot.

[3] In practice, the second controller could be tuned by measuring a single transfer function at an important point of the trajectory. The third controller would need to perform a test run over the desired trajectory in order to first identify the correct eigenfrequencies over the entire range of motion.

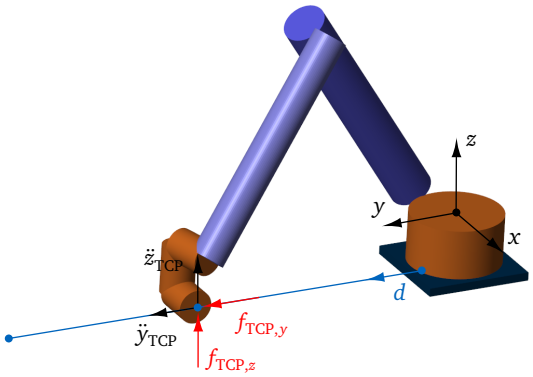

Figure 5.3: The UR10 model following a horizontal trajectory with two vibration controllers acting at the TCP in the y- and z-direction.

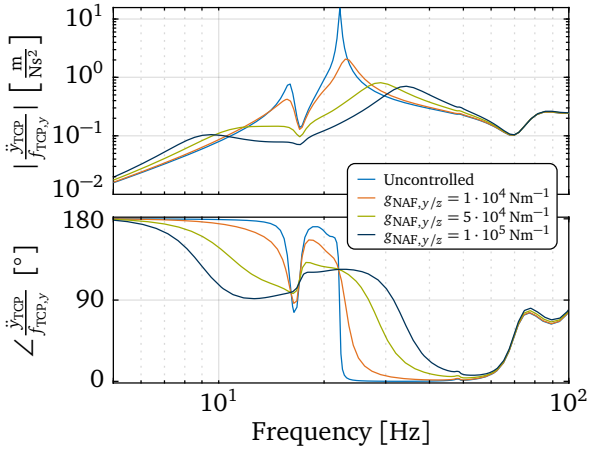

Figure 5.4: Influence of two NAF controllers on the driving point transfer function in the y-direction. The transfer function is linearized at the starting position.

The NAF controller with pose dependent controller eigenfrequencies (Fig. 5.5d) performs slightly better than the NAF controller with constant controller eigenfrequencies for the second structural mode of the robot. However, it actually performs slightly worse for the first one by creating a bit higher side resonance around 0.1 s. This is probably caused by the controller eigenfrequncies moving closer to each other during this part of the trajectory, effectively increasing the gain on for the lower frequency NAF controller and therefore also the peak for its side resonance.

Note that the important take-away from this is that all three of these controllers are able to effectively introduce damping into the TCP dynamics and therefore improve the system's behavior. The performance of all of these controllers could be arbitrarily improved in the simulation by performing a bit of parameter optimization for the gains, or even making the gain factors for the second NAF controller dependent on the current pose. However, these kind of exercises have little purpose without also precisely modeling the other bandwidth limiting effects like sensor noise, signal delay, or friction in the actuator. Nevertheless, it is still interesting to note that the DVF controllers seems to be the most effective ones, while also being the most simple controller to tune.

Effect on the Horizontal Path Accuracy

The horizontal path accuracy of the simulation model following the test trajectory without any external vibration damping controller is shown in Fig. 5.6a. We can see in the CWT of the horizontal error (Fig. 5.6b) that both structural eigenfrequencies of the robot are regularly excited by either the high jerk of the robot motion or torque-ripple frequencies crossing them.

The performance of the different external vibration damping controllers are shown in Fig. 5.7-5.9. We can see that all three of them are capable to basically completely attenuate the structural dynamics response of the robot on the position level, with the DFV controller again producing slightly better results. All controllers produce a relatively low control effort to achieve this, with only a short peak of high forces needed for the large stopping jerk at the end of the trajectory. We can also see that the NAF controller with variable control eigenfrequencies is slightly better in the end than the NAF controller with constant eigenfrequencies, since the former is tuned better to the changing system dynamics of the robot.

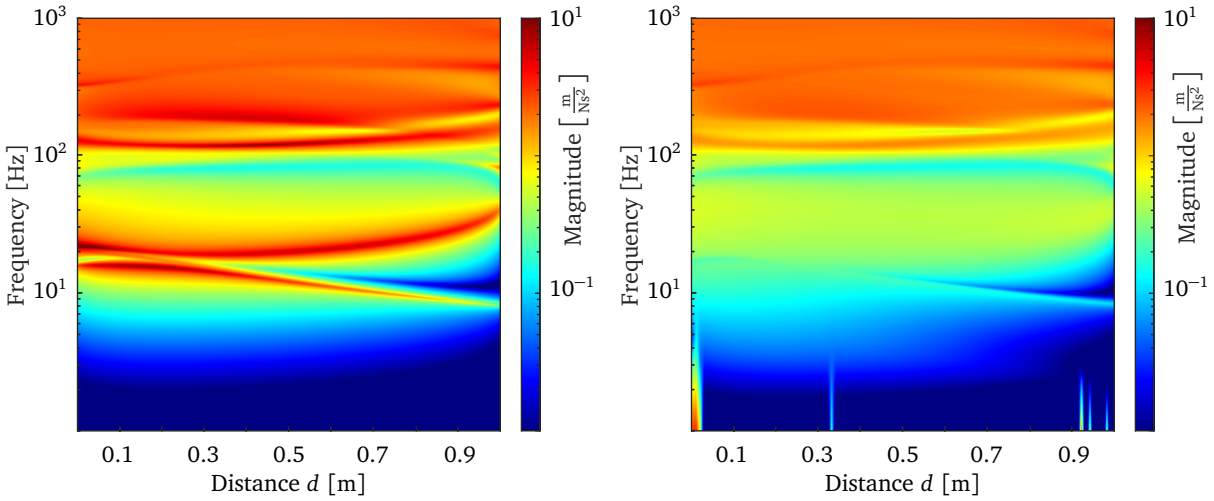

(a) Reference, without external vibration damping.

(b) With direct velocity feedback controller. $g_{\mathrm{DVF},y/z} = 1 \cdot 10^3\,\mathrm{Nsm}^{-1}$ and a high-pass filter at $\omega_{\mathrm{HP}} = 2\pi \cdot 0.8\,\mathrm{Hz}$.

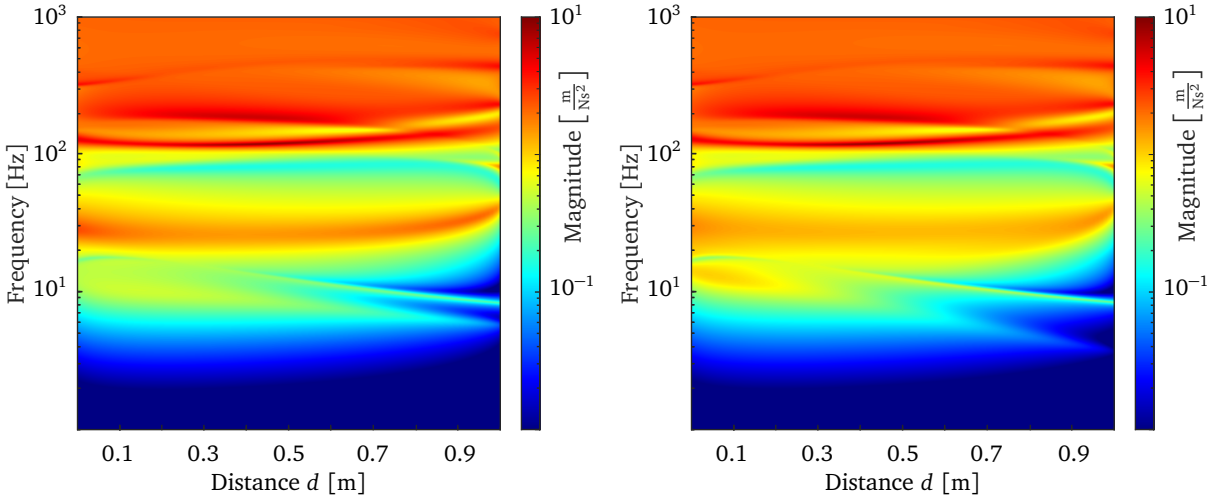

(c) With negative acceleration feedback controller. $g_{\mathrm{NAF},y/z} = 5 \cdot 10^4\,\mathrm{Nm}^{-1}$, $\zeta_{\mathrm{NAF},y/z} = 0.5$ and constant controller eigenfrequencies $\omega_{\mathrm{NAF},y} = 2\pi \cdot 22\,\mathrm{Hz}$ and $\omega_{\mathrm{NAF},z} = 2\pi \cdot 18\,\mathrm{Hz}$.

(d) With negative acceleration feedback controller. $g_{\mathrm{NAF},y/z} = 5 \cdot 10^4\,\mathrm{Nm}^{-1}$, $\zeta_{\mathrm{NAF},y/z} = 0.5$ and variable controller eigenfrequencies with $\omega_{\mathrm{NAF},y}$ tracking the second structural eigenfrequency of the robot and $\omega_{\mathrm{NAF},z}$ tracking the first eigenfrequency.

Figure 5.5: Campbell diagrams of the $\ddot{y}_{\mathrm{TCP}}/f_{\mathrm{TCP},y}$ transfer function during a straight horizontal trajectory with the flexible UR10 simulation model and different active vibration controllers applied.

However, the difference is quite small, such that it might be questionable if the tuning effort would be worth it in practice. This also shows that the NAF controller is quite robust against changing system dynamics, since it also performs quite well by just using constant controller eigenfrequencies.

These results also reveal a major issue for the external vibration damping approach: If the subject robot is affected by a lot of torque-ripple (like the UR10, see Fig. 4.4b), the external vibration controller will only damp the structural dynamics response of the system. However, since torque-ripple originates on the motor axis behind the typically large gear ratios of the joint drivetrains, it can not be affected by the external forces created at the TCP of the robot. The result is basically a rigid response of the robot following the disturbance oscillations on its motor axis according to its forward kinematics.

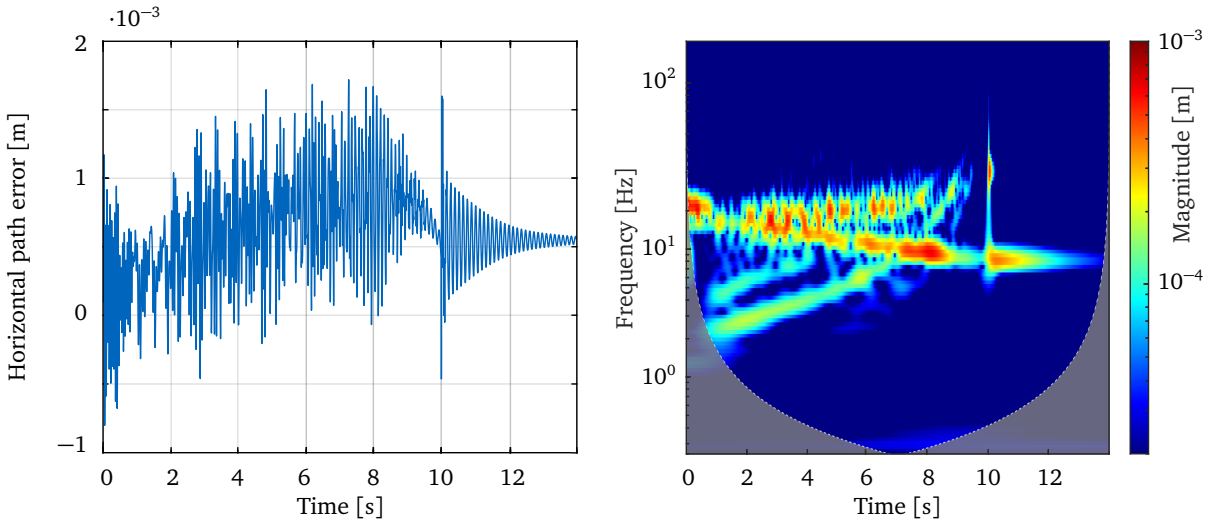

(a) Horizontal path error. **(b)** CWT of the horizontal path error.

Figure 5.6: Simulated horizontal path error at the TCP of the UR10 simulation model along a 1 m horizontal trajectory with 100 mms^{-1} without external vibration damping controller.

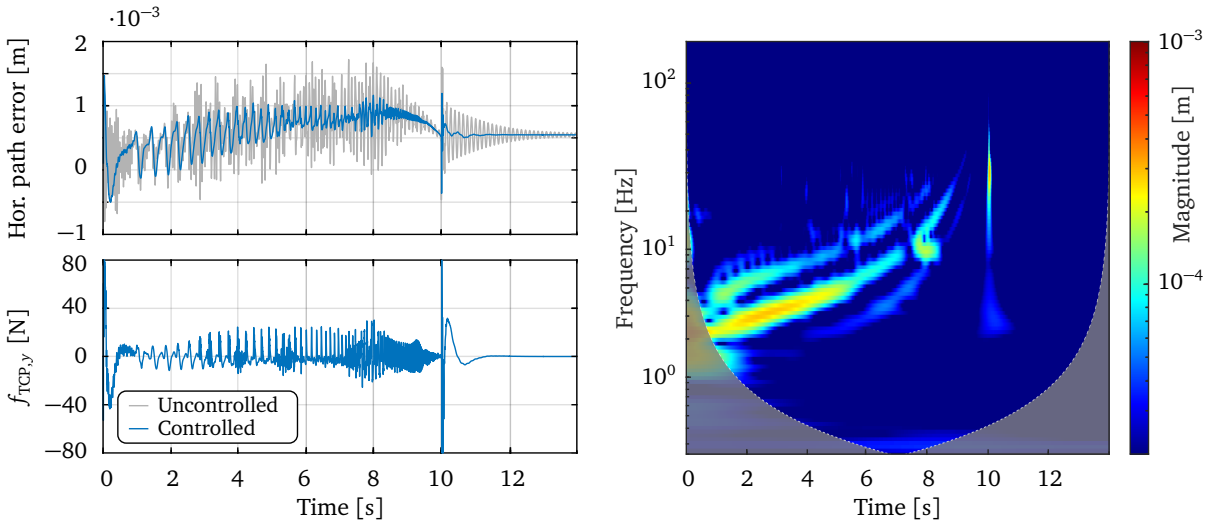

(a) Horizontal path error. **(b)** CWT of the horizontal path error.

Figure 5.7: Simulated horizontal path error at the TCP of the UR10 simulation model along a 1 m horizontal trajectory with 100 mms^{-1} with *direct velocity feedback* controllers.

On the other hand, what these simulation results have shown is that structural dynamics of a robot manipulator can be very effectively and easily attenuated using an external vibration approach. We have seen in section 2.1 and 4.3 that this would otherwise be a very difficult task for a control system that only uses the robots joint motors as inputs. External vibration damping might therefore still be an attractive alternative for robot manipulators that are less affected by torque-ripple and more affected by structural vibration issues.

An example for a robot that shows major issues due to its structural dynamics and link flexibilities is our CROPS robot, as already shown in section 4.2.1. The effectiveness of the external vibration damping approach is therefore tested on the CROPS robot in the following subsection.

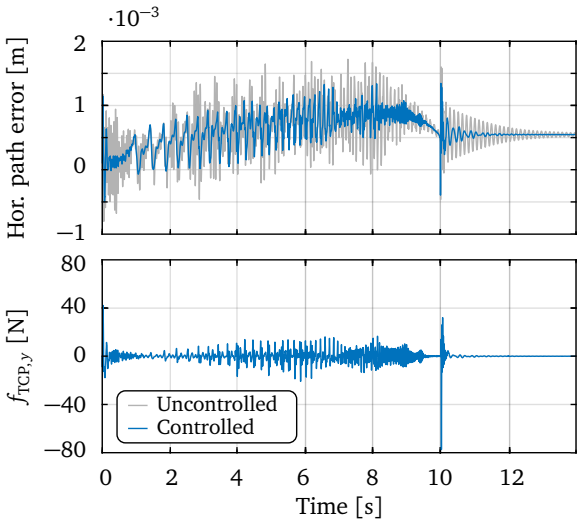

(a) (Top) Horizontal path error. (Bottom) Control force output.

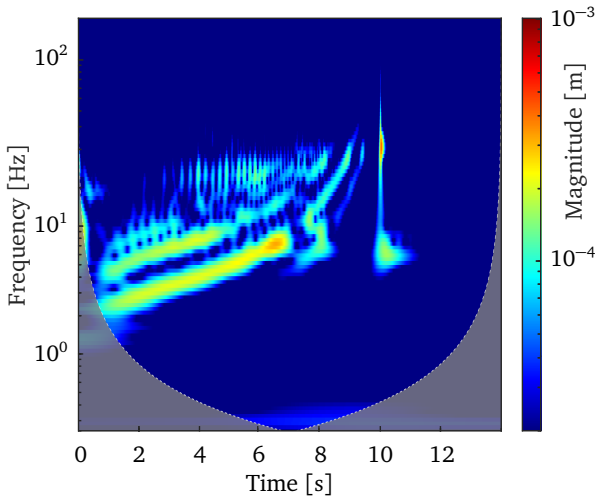

(b) CWT of the horizontal path error.

Figure 5.8: Simulated horizontal path error at the TCP of the UR10 simulation model along a 1 m horizontal trajectory with 100 mms^{-1} with *negative acceleration feedback* controllers with *constant controller eigenfrequencies*.

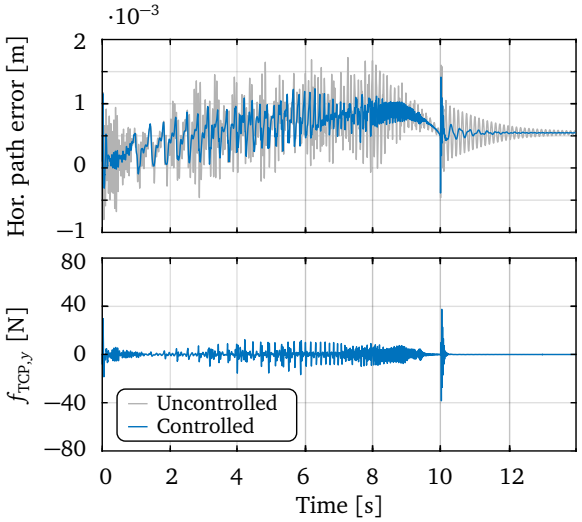

(a) Horizontal path error. (Bottom) Control force output.

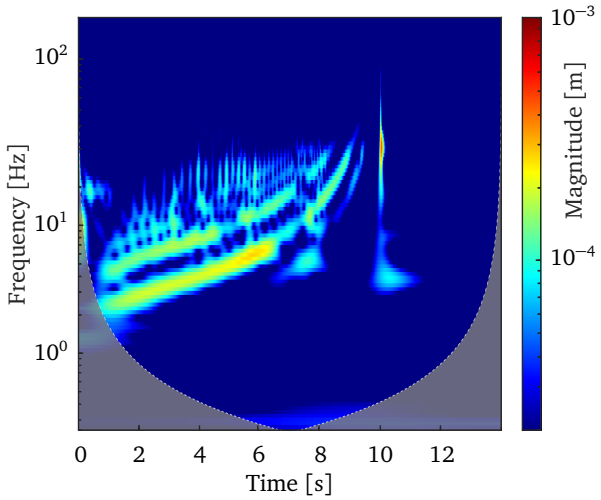

(b) CWT of the horizontal path error.

Figure 5.9: Simulated horizontal path error at the TCP of the UR10 simulation model along a 1 m horizontal trajectory with 100 mms^{-1} with *negative acceleration feedback* controllers with *variable controller eigenfrequencies*.

5.1.3 Experiments with the CROPS Robot

The actuator for the test with the CROPS robot is built following the design shown in Fig. 5.1. The magnet of the voice coil actuator is guided by two guide rails with ball bearings (Fig. 5.10b), with the moving assembly having a total mass of about $m_{VCA} = 1\,kg$. The displacement of the inertial mass x_{VCA} is measured using a *Micro Epsilon* triangulation laser sensor. The total possible displacement is 6 cm. Another triangulation laser sensor is attached to the actuator to measure the vertical path error at the TCP. A *PCB* 1 g acceleration sensor

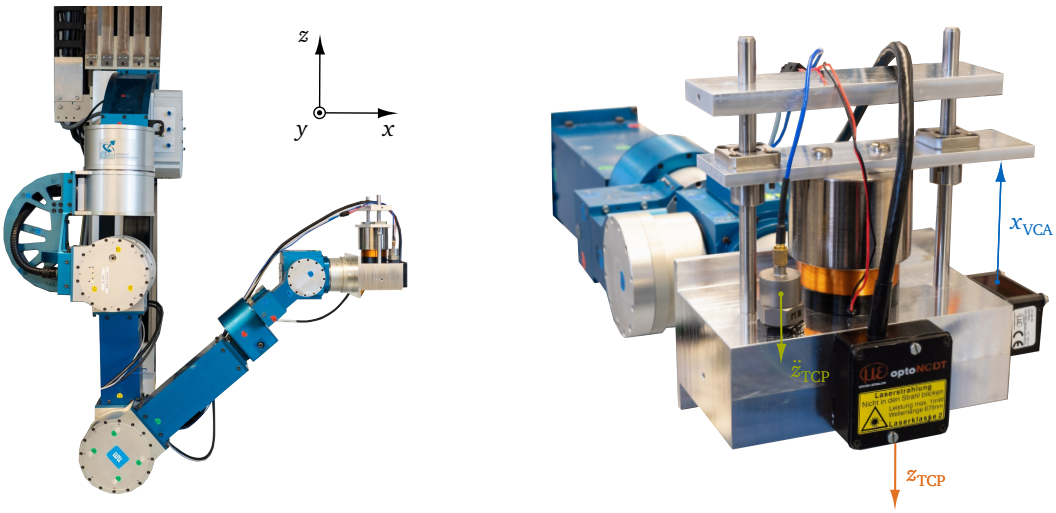

(a) The CROPS robot with an voice coil actuator for external vibration damping.

(b) Close up of the voice coil actuator.

Figure 5.10: Test setup for external vibration damping on the CROPS robot.

is used to measure the acceleration feedback for the external vibration damping controller. The entire assembly is mounted on an aluminum block, making the total mass of the actuator assembly about 4 kg.

The current for the voice coil is controlled using an *ELMO* motor driver with a PI controller as described in the last section. The *ELMO* controller clock rate is 10 kHz. The external vibration damping controller is implemented on a *dSpace* Microlab-Box and runs at 5 kHz. The Microlab-Box is the central controller that reads the acceleration signal through an analog lowpass filter with a built in ICP circuit, as well as the laser sensor via an analog connection. The desired current is also sent via a 10 V analog connection to the *ELMO*[4].

Actuator Dynamics

The force transfer function of the actuator is verified by measuring the transfer function from the desired force $f_{\text{VCA},d}$ to the acceleration $\ddot{x}_{\text{VCA}}$ of the permanent magnet with an additional acceleration sensor. The acceleration at the magnet is then proportional to the output force f_u of the higher level vibration damping controller.

The measurement of the transfer function is shown in Fig. 5.11, with the actuator being mounted on a heavy and isolated experimental table. As already mentioned, the guide rails introduce quite of a lot damping into the system (5.11 blue line). This can be somewhat mitigated by using a negative $g_{D,x}$ gain for the PD position controller of the actuator (5.11 red line). The virtual stiffness $g_{P,x}$ is set as low as possible without causing too many issues with stick-slip effects at the guide rail bearings. The overall achievable lower bandwidth limit is about 5 Hz and the upper limit is set at 80 Hz due to the tuning of the current controller. The current controller could be tuned more aggressively, however, since we are only interested in a frequency range of up to 50 Hz this would only introduce more noise into the system without any other benefit.

The actuator mostly behaves as expected. However, the high amount of friction introduced by the guide rails caused some problems, as I will discuss in the following. This is most likely due to the high number of balls used in the ball bearings, which are also lubri-

[4]See also appendix B for more details and advantages of using a setup with a *dSpace* Microlab-Box and *ELMO* motor driver with analog connections.

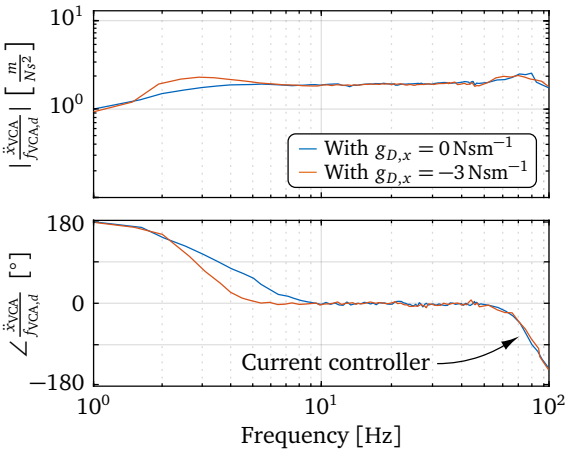

Figure 5.11: Measured transfer function from desired force to measured acceleration at the permanent magnet of the actuator prototype.

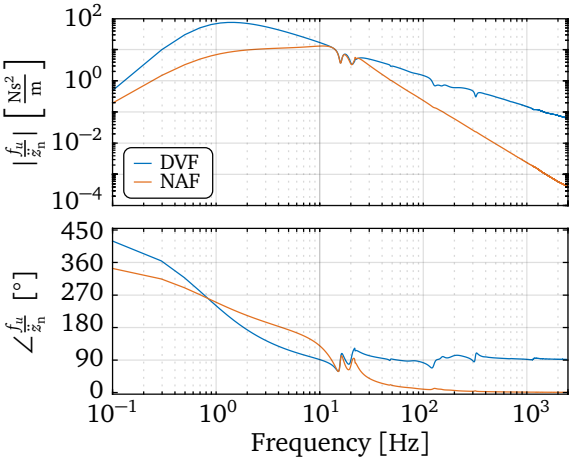

Figure 5.12: Simulated controller sensitivity function for a DVF and NAF controller applied in the z-direction of the UR10 model. Both controller are tuned to achieve a $-10\,\mathrm{dB}$ attenuation at the first structural eigenfrequency of the model.

cated with quite viscous grease.

Noise Sensitivity

Before we have a look at the experiments, I want to shortly touch on the issue of noise sensitivity, which will be relevant for the following results. In the above simulation section, the DVF controller seemed to perform slightly better than the NAF controller, without having a clear idea about how much gain is possible with each controller in practice. A good way to estimate the amplification of noise of each controller, which is one of the main limiting factors in a real mechatronic system, is the sensitivity transfer function from an additional disturbance at the input to the controller output.

Fig. 5.12 shows the linearized sensitivity transfer functions for a single DVF and NAF controller applied to the z-direction at the TCP of the simulation model. Both controllers are tuned such that they achieve a $-10\,\mathrm{dB}$ attenuation at the first structural eigenfrequency of the UR10 simulation model. We can see that the DVF controller has a consistently higher amplification of noise over a broad frequency range, while performing the same as the NAF controller at the targeted first structural eigenfrequency of the robot around 18 Hz. This can be explained by the DVF control structure broadly damping the entire system dynamics by just increasing the overall damping in the system, while the NAF controller can be specifically tuned to only affect the resonance frequency of interest.

By calculating the noise amplification factor as described in Appendix B for these specific sensitivity functions, we find that the DVF has an almost three times higher noise amplification than the NAF controller, while performing essentially the same. Assuming that the real system will get unstable as soon as a certain amount of noise amplification is present in the control-loop, this suggests that the DVF controller will actually perform slightly worse than the the NAF controller, because of the lower amounts of possible controller gains.

Closed-Loop Dynamics at the TCP

The closed-loop dynamics are measured the same way with hammer impacts as described in section 4.2.1. The robot is again moved through the same poses from completely stretched

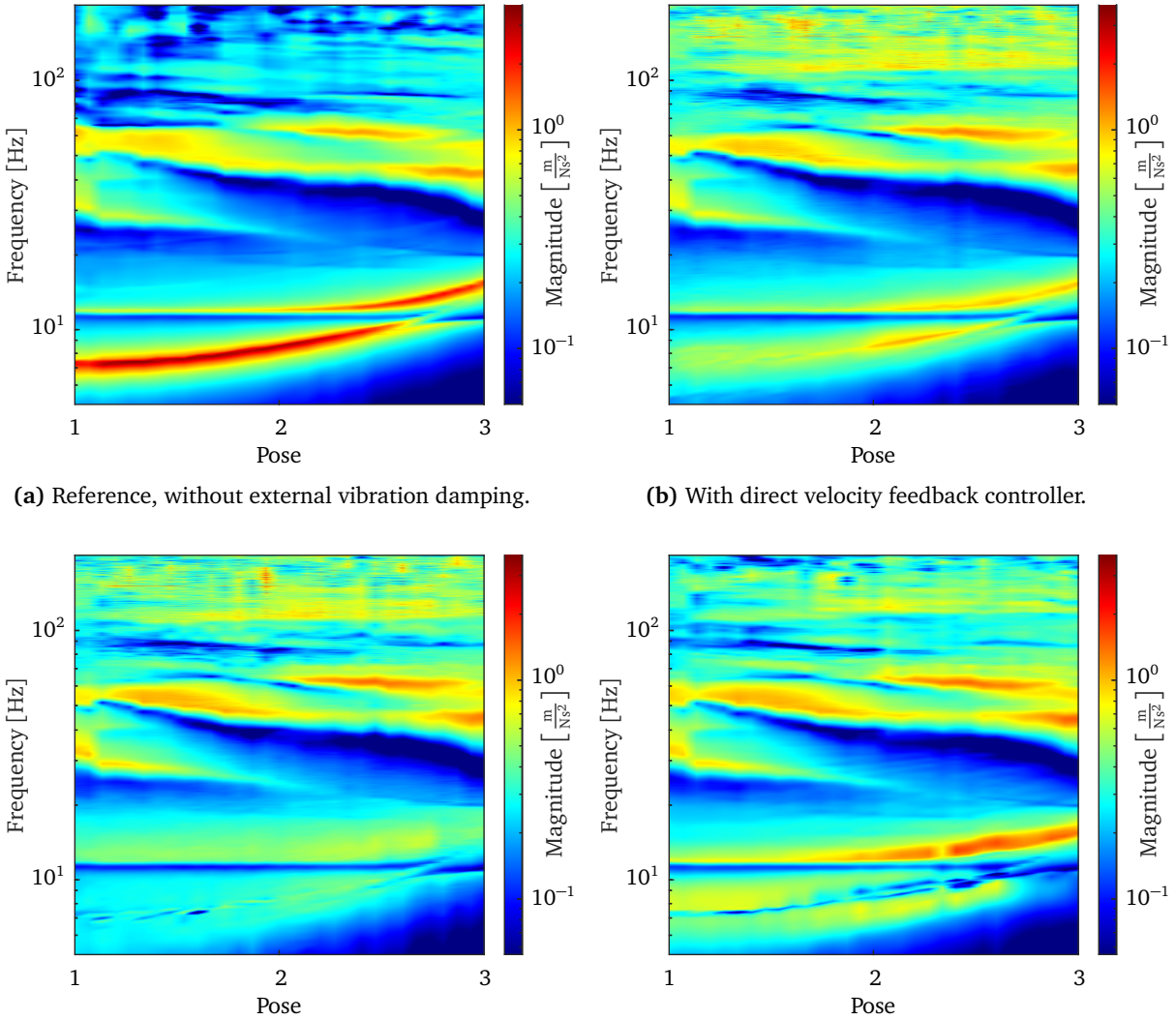

(a) Reference, without external vibration damping.

(b) With direct velocity feedback controller.

(c) With negative acceleration feedback controller, damping the first two eigenfrequencies.

(d) With tuned mass damper for the first eigenfrequency.

Figure 5.13: Campbell diagrams of the vertical driving point transfer function at the CROPS TCP $\ddot{z}_{\mathrm{TCP}}/f_{\mathrm{TCP},z}$. The transfer functions are recorded for 30 poses changing according to Fig. 4.11. The controllers are all re-tuned for each pose for best performance.

out to a completely retracted position as shown in Fig. 4.11. The resulting Campbell-diagrams are shown in Fig. 5.13.

It should be noted that the additional 4 kg of mass at the robots TCP already has quite a significant effect on the uncontrolled structural dynamics, Fig. 5.13a. Compared to the measurements in Fig. 4.17, the first mode's eigenfrequency is now changing with the pose and the modes over 30 Hz are already quite attenuated by the high amount of inertia added to the TCP of the robot.

Three different control strategies are tested:

- The first one is again the *velocity feedback controller*.
- The second one is the *negative acceleration feedback controller*. However, this time we are only controlling the z-direction at the the TCP of the robot. The controller is still tuned to attenuate the first two eigenfrequencies starting at 8 and 12 Hz, by using the

sum of two NAF controllers (3.84).

- The third controller uses the actuator as a *tuned mass damper*. For this controller, no acceleration feedback is used. The actuator is simply tuned with the $g_{P,x}$ and $g_{D,x}$ gains to have the same actuator eigenfrequency as the first structural eigenfrequency of the robot. The actuator therefore acts like a passive tuned mass damper with variable stiffness.

For the closed-loop measurements, the controllers are re-tuned for each robot pose to asses the best possible performance on the real systems. Meaning that for the DVF- and NAF controller the controller gains are increased until the system becomes unstable. The gains are then slightly reduced for the measurements. The controller eigenfrequencies for the NAF- and tuned mass damper controller are also set to the structural eigenfrequency of the current pose of the robot.

The results are plotted in Fig. 5.14. As expected, we can see that the DVF controller actually performance slightly worse than the NAF controller on the real system, most likely due to the higher noise amplification. The DVF controller is capable of attenuating the first two resonance peaks by up to −15 dB, with a bit worse performance once the robot passes the second main pose. The NAF controller performs constantly better with a maximum attenuation of up to −30 dB for the earlier poses.

The tuned mass damper controller is only able to attenuate the first structural eigenfrequency by design. A disadvantage of this approach is that, while being the most simple one, there is no active control over the amount of attenuation, which is determined by the mass of the permanent magnet. The tuned mass damper is actually able to attenuate the first structural eigenfrequency the best, which is visible by the thin blue line following the first eigenfrequency in Fig. 5.13d. However, the attenuation is so large that we get the typical two side resonances. The lower frequency side resonance is especially problematic, since lower frequencies will cause higher displacement amplitudes.

The tuned mass damper controller is therefore an even simpler alternative to the NAF controller. However, the main disadvantages are that the amount of attenuation has to be tuned by the mass of the permanent magnet in advance and that the controller can only attenuate one structural eigenfrequency at once. The main benefit is that the system does not need a higher-level active vibration damping controller with acceleration feedback to work, which reduces system complexity.

Step Response

For the next experiment, the CROPS robot performs a vertical trajectory of about 500 mm length at a constant velocity of 80 mm/s, Fig. 5.14a. The trajectory has a high jerk at the end, which acts like a step excitation on the TCP. Since the displacement can not be directly measured for this trajectory, we are going to have a look at the measured residual accelerations at the TCP, Fig. 5.14b - 5.14d. The acceleration signal is lowpass filtered in post with a cutoff frequency at 20 Hz to reduce the high frequency accelerations in the signal, since the low frequency content is more relevant for the actual mechanical displacements at the TCP.

We can see that the NAF controller performs better than the DVF controller, as we would expect according to the closed-loop transfer function measurements in Fig. 5.13. The tuned mass damper controller performs the worst, because of its lower frequency side resonance.

While the NAF and DVF controller are able to significantly reduce high amplitude oscillations at the high jerk points of the trajectory, they do not significantly reduce the residual vibration during the middle part of the trajectory. This is also observable when performing a more typical horizontal test trajectory, where neither controller has any significant effect on

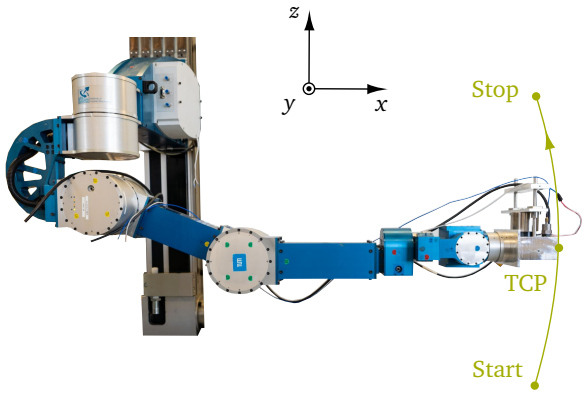

(a) Test setup for the step response trajectory.

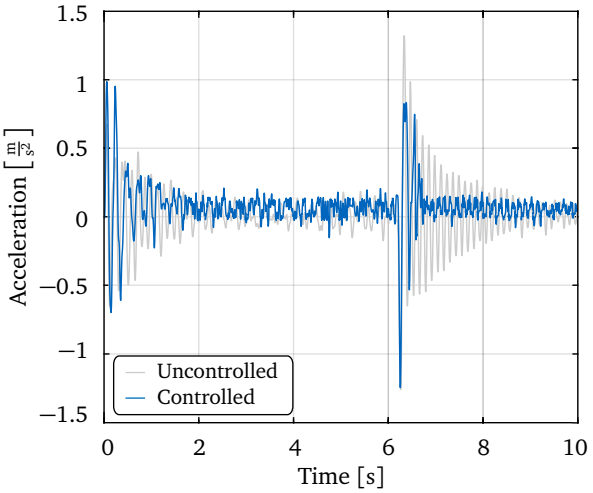

(b) Residual accelerations measured at the TCP with a direct velocity feedback controller.

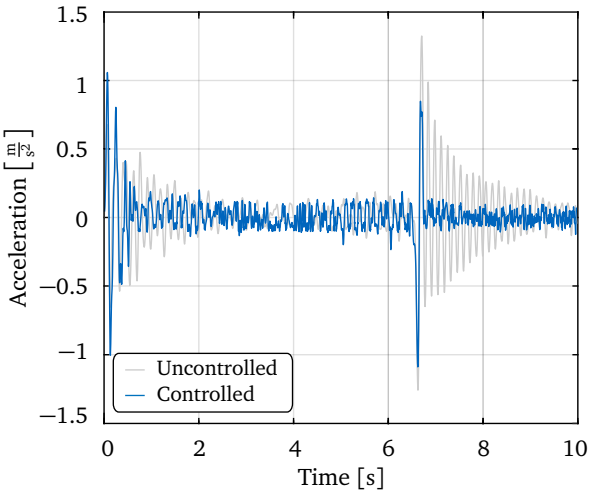

(c) Residual accelerations measured at the TCP with a negative acceleration feedback controller.

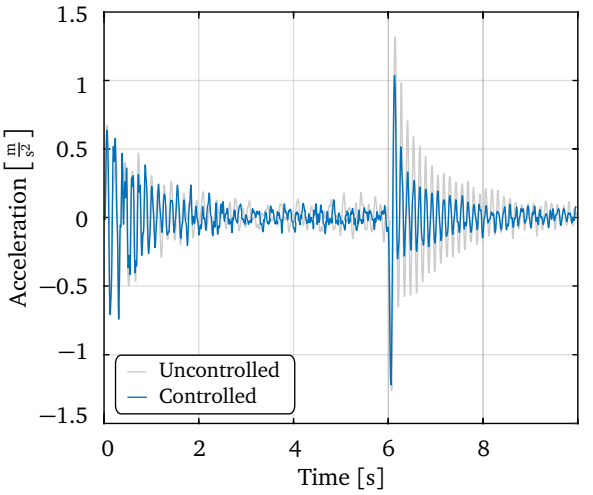

(d) Residual accelerations measured at the TCP with a tuned mass damper controller.

Figure 5.14: Step response experiment with the CROPS robot. The residual vibrations are measured at the TCP and lowpass filtered with a cutoff frequency at 20 Hz to have a better view on the lower frequency vibrations.

the path accuracy of the robot. This is initially rather surprising, since the CROPS robot actually has very little torque-ripple and should be a prime example for this external vibration damping approach.

The reason for this little effect during more typical motions is that there is actually only very little force needed to damp small structural vibrations. We can also see this in the simulation results in e.g. Fig. 5.9, where the control forces are very small outside of the high jerk points of the trajectory. This is a problem for the actuator, since it has to create rather small forces very precisely to damp the relatively low amplitude vibrations during normal operation. However, small actuator forces also mean that the friction at the actuator plays a larger role in the dynamics of the actuator, as I have already discussed above. This greatly degrades the force transmission of the actuator due to unmodeled friction and stick-slip effects at the guide rails. This is rather unfortunate, since the external vibration damping

approach seems to be quite effective for the CROPS robot in general, however, fails to produce good results for low amplitude disturbances and therefore high-accuracy applications, which is the purpose of this thesis.

Trajectory Tracking with External Disturbance

While this series of experiments was not effective to reduce the CROPS dynamic path tracking error during normal operation due to the limitations of the actuator, I still wanted to test the performance of the external vibration approach for a slightly different scenario that might not be too uncommon in practice: Most industrial robots are usually operated in larger assembly lines or factory environments that have a lot of environmental disturbances. Since a robot manipulator is just a large beam-like structure, it is quite susceptible to transferring disturbance forces from the base of the robot to its TCP, degrading its dynamic accuracy.

The test setup shown in Fig. 5.15a is designed to replicate this problem. The robot performs a horizontal trajectory of about 1 m length with a velocity of 65 mm/s. Additionally a shaker is placed next to its mounting table, causing a broadband disturbance force f_{dist} of up to 20 Hz, simulating environmental disturbance forces.

Fig. 5.15b - 5.15d shows the vertical tracking error measured with a *Micro Epsilon* triangulation sensor against a reference surface for the three same control approaches. We can see that even a light disturbance can cause quite large dynamic error amplitudes (gray lines). As expected, the NAF controller again performs the best at attenuating the larger vibration amplitudes.

It is also notable that the vertical path error of the CROPS robot is quite a lot less repeatable than the path error of e.g. the UR10 (cf. Fig. 4.7). This is probably due to the robot operating with 7 DOFs and the path planning algorithm always choosing a slightly different null space while moving backwards and forwards.

5.1.4 Discussion of Results

The results for the external vibration damping approach are a bit mixed. The simulation results did show that it is quite simple to effectively control the pose dependent structural dynamics of a robot manipulator with very little knowledge about the underlying system dynamics, which is a great advantage over most control strategies proposed for flexible robots (cf. section 2.1.3). Both the NAF, and the even simpler DVF, controller are very robust against modeling errors, thanks to the collocated control problem created by using both acceleration feedback and force input near the TCP of the robot.

However, even in simulation, the external vibration damping approach has its limitations when the robot experiences a lot of torque-ripple, which can not be effectively attenuated by an external force acting at the TCP.

When applying the external vibration damping approach to our CROPS robot, we achieved a maximum attenuation of up to −30 dB. This is actually a quite common result for structural vibration damping controllers applied to real systems, regardless of the underlying control strategy (cf. section 2.3). The reason for all of these control strategies applied to different problems all performing quite similar also became evident for this application: It is quite hard to build a force actuator that can both produce very high forces and still be very precise, since friction will start to degrade the actuator performance for small, precise motions. The accuracy of actuators is often within 1 % of their maximum output value for this reason, even for more expensive hardware.

I am confident that we could achieve better results in regards of reducing the dynamic tracking error during normal operation by downsizing the actuator and redesigning the guid-

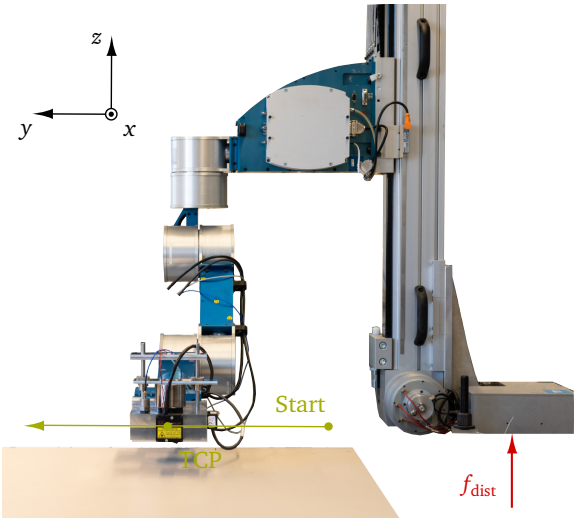

(a) Test setup for the step response trajectory.

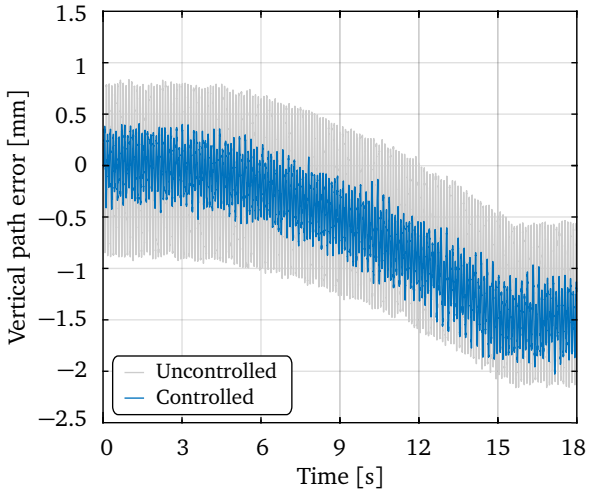

(b) Residual accelerations measured at the TCP with a direct velocity feedback controller.

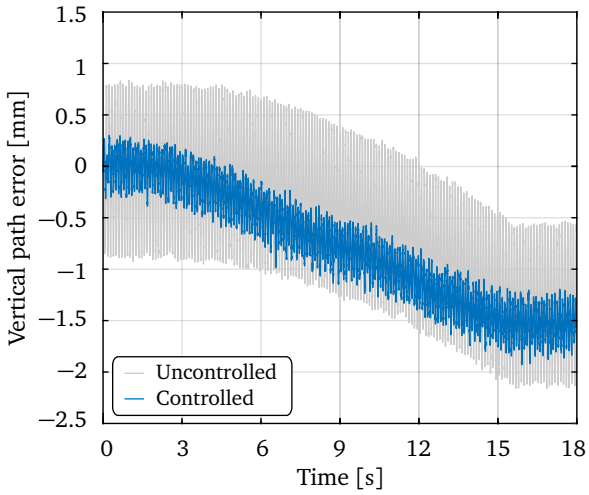

(c) Residual accelerations measured at the TCP with a negative acceleration feedback controller.

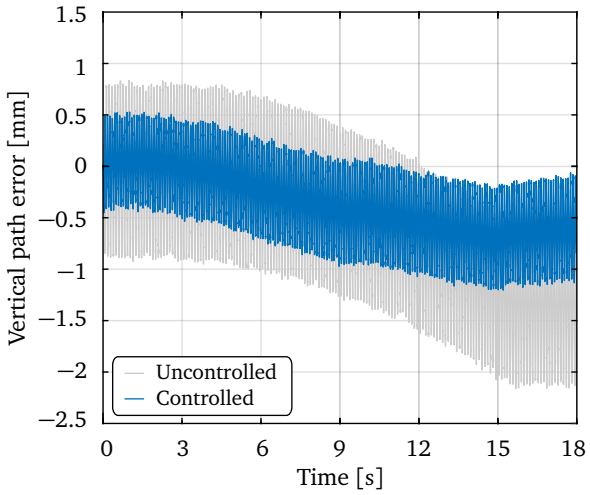

(d) Residual accelerations measured at the TCP with a tuned mass damper controller.

Figure 5.15: Step response experiment with the CROPS robot. The residual vibrations are measured at the TCP and lowpass filtered with a cutoff frequency at 20 Hz to have a better view on the lower frequency vibrations.

ing mechanism to reduce friction. The system would then no longer be able to effectively damp high jerk situations as shown in Fig. 5.14. However, these are not really relevant in practice, since most robots will plan a trajectory with as little jerk as possible anyway. Unfortunately, we were not able to build a second better prototype for the active vibration damping approach due to time restrictions in the project[5].

It might also be interesting to test a two stage system, with a larger actuator for the attenuation of high vibration amplitudes during high jerk and an additional smaller actuator for structural vibrations during normal operation.

Overall, the external vibration damping approach still seems to have potential to deal with tracking issues of robot manipulators which are specifically due to structural vibrations and will most likely be easier to implement, and more robust, than using the robots own

[5] and Covid-19...

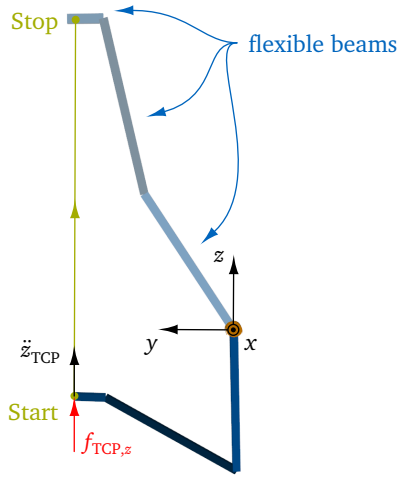

Figure 5.16: Simplified 2D robot model with three flexible beams using the lumped-parameter approach.

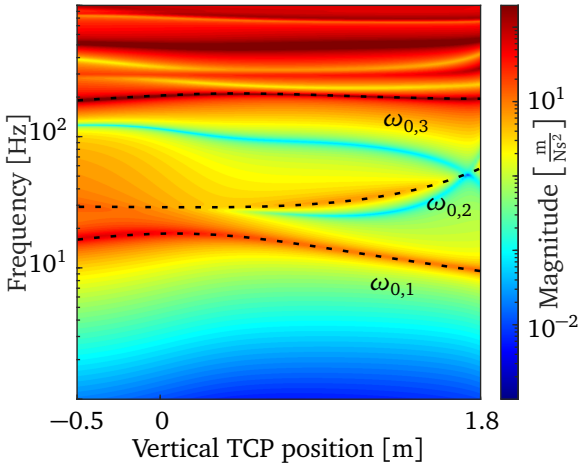

Figure 5.17: Campbell diagram of the driving point transfer function of the simplified 2D robot model in z-direction at the TCP over a vertical trajectory.

control system. The obvious downside is that this approach can not deal with the quasi-static error of the robot. This would either need to be dealt with by applying an absolute calibration method to the robot as described in section 2.1.1, or by adding additional actuators at the TCP that can compensate sag.

Appendix C describes the first version of such a stabilization system which used voice coil actuators to damp the dynamic error and a BLDC motor driven positioning system to compensate the quasi-static error.

5.1.5 A Word on Modern Control Methods

Until now, I only discussed classical vibration damping methods for the external vibration damping approach. The main reason for this is that this thesis was partially funded by an industry project and classical control methods have a better proven track record when applied to real systems. However, as a researcher, I was of course also interested in looking into any benefits that might be provided by modern control methods.

For this purpose, I supervised two student theses: The first one being the master's thesis of HARDER [125], who investigated Pole Placement, LQR and H_∞ controllers. The second one is the semester thesis of BODEIT [54], who investigated MPC, Sliding Mode Control, Eigenstructure Assignment, as well as Pole Placement with variable observer models.

This subsection is a short summary of our findings, which are documented in more detailed in their respective student theses.

Robot Model

Both theses used a simplified 2D version of the flexible robot model (Fig. 5.16), which was also the basis of our papers [48, 49]. The model consists of a 2D robot with 3 DOFs. All links are modeled as flexible beams, with the first two links being modeled as hollow rectangular magnesium beams with a 50x50 mm^2 outer and 45x22.5 mm^2 inner cross section and a length of 1 m. The third link has a length of 20 cm and the same profile. The links are modeled using the lumped-parameter approach described in section 3.2. The flexible joint model is the same as described before.

The robot performs a vertical test trajectory shown in Fig. 5.16. The driving point transfer function of interest is again in z-direction at the TCP. The corresponding Campbell-diagram without an external vibration damping controller is shown in Fig. 5.17. It is interesting to note that the structural dynamics behave quite similar to the UR10 robot model (cf. eg. Fig. 5.5a), although this robot model is of larger size and uses a different material for the beams. The reason for this is again the bad scalability of structural dynamics. Two tree like structures with similar morphology will always behave quite similar regardless of material and size.

The control problem is the same as before: Use acceleration feedback at the TCP $\ddot{z}_{\mathrm{TCP}}$ and the collocated force $f_{\mathrm{TCP},z}$ as the control variable to damp the structural dynamics of the robot during the test trajectory. We did not consider the actuator dynamics for the following results and just assumed that the control force can be directly applied from the controller output. However, all controllers needed to be designed such that the control force does not exceed the maximum control force of $f_{\max} = 80\,\mathrm{N}$.

Pole Placement, LQR and H_∞ Controller

The Pole Placement-, LQR- and H_∞ controllers were all designed 'by the book' using the corresponding Matlab toolboxes[6]. Modern control methods often require an observer model to recreate the necessary states of the system. In this case, we only use one acceleration sensor to generate the required states. In order to also test the robustness of these controllers, we decided to design them using one observer model linearized at the initial starting pose of the robot. Fig. 5.18a shows the full linearized model in blue. In practice, a full model can rarely be used, since it is quite unlikely to get a precise model of higher-order dynamics. It is also often not necessary to control a lot of higher modes in the system. In our case, we decided to include the first five modes into the observer model.

The general goal of all controllers was to increase the modal damping of the closed-loop system. We designed the desired poles by transforming the system matrix into the state space modal canonical form (3.65) and equally increasing the modal damping of all desired poles. We deliberately chose to not increase the eigenfrequencies of the closed-loop system to keep the performance more comparable to the classical approaches[7]. The controllers were then tuned such that they achieved the best performance over the entire trajectory of the robot, while also remaining stable.

Fig. 5.18b - d show the performance of these controller compared with a NAF controller, which is also only tuned at the first pose (NAF const.), and a second NAF controller, which is tuned to follow the changing eigenfrequencies (NAF variable). The NAF controllers are both designed for the first three eigenfrequencies of the robot. The plots Fig. 5.18b - d each follow the amplitude of the first, second and third eigenfrequency as shown in Fig. 5.17.

It immediately becomes apparent that the modern controllers all perform worse than the classical NAF controllers. The main reason for this is the lack of robustness of modern control methods, which heavily rely on precise observer models. Since we only designed the observer for the initial pose, there is an increasing mismatch between the observer and the real system dynamics when the robot starts moving upwards. In order to keep the controllers stable over the entire trajectory, we had to significantly reduce the desired damping ratios. Unfortunately, there is still no clear consensus about when and how modern control methods become unstable due to observer-plant mismatch.

In his semester thesis [54], my student BODEIT later also tried to use observer models which were updated along the robot trajectory to stay as close as possible to the changing

[6] Since I did not end up using these methods on the real prototype, I will not dive into the theory of these controllers. Modern control methods are very well established and we closely followed the common frameworks provided by books like [251, 261] and the corresponding Matlab toolboxes.

[7] Also, increasing the eigenfrequency of the desired closed-loop poles made the controllers even less robust.

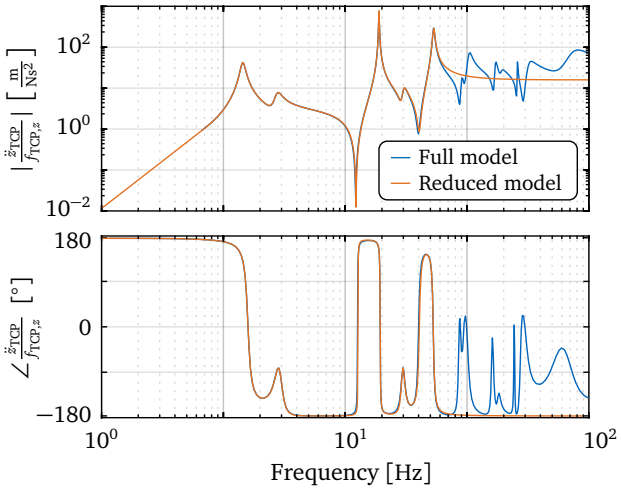

(a) Driving point transfer function at the starting position of the simplified 2D model with reduced model for the observer.

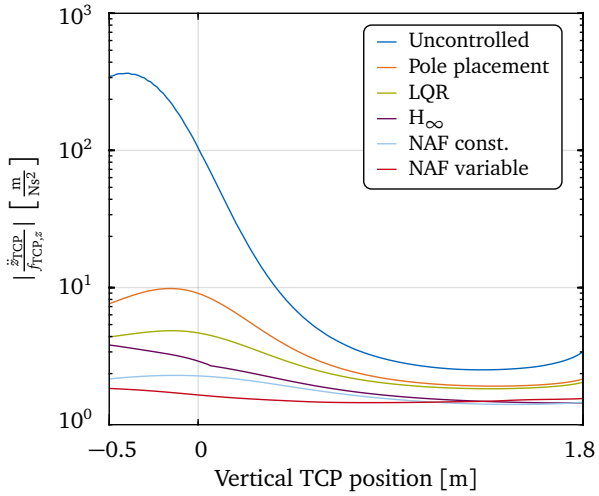

(b) Amplitude of the first structural eigenfrequency $\omega_{0,1}$.

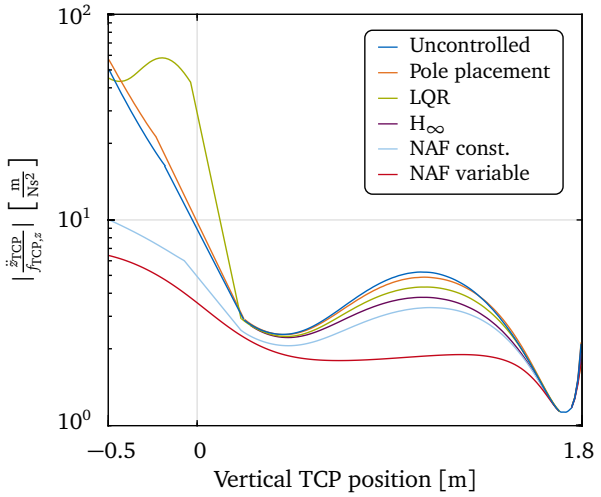

(c) Amplitude of the second structural eigenfrequency $\omega_{0,2}$.

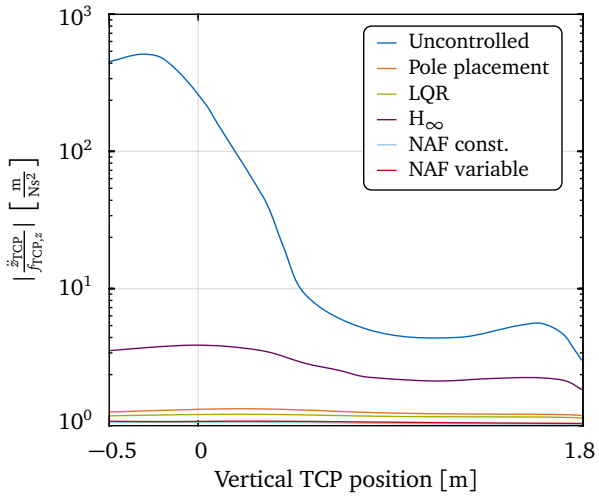

(d) Amplitude of the third structural eigenfrequency $\omega_{0,3}$.

Figure 5.18: Comparison of the performance of modern control methods as external vibration damping controllers applied to the simplified robot model. Fig. (b) to (d) each follows one eigenfrequency shown in Fig. 5.17. Adapted from my student HARDER's master's thesis [125].

dynamics of the system. Also with only unsatisfying results. The main reason for this is probably a second issue related to acceleration feedback: As we can see by the height of the amplitude peaks in Fig. 5.18a, the unmodeled higher-order system dynamics still contribute significantly to the overall system dynamics. This is a consequence of using accelerations as feedback, since an accelerance transfer function will remain roughly at the same order of magnitude for higher frequencies. This makes the control system quite susceptible to observer- and control-spillover due to unmodeled system dynamics. The larger contribution of the higher frequency resonance peaks make it much more likely for unforseen interactions to occur between unmodeled system dynamics and the control system. In contrast, a position feedback based control system is easier to handle, since the contribution of higher-order dynamics will quickly decrease for higher frequencies (see e.g. Fig. 3.9c). It is therefore much safer to ignore unmodeled higher-order system dynamics of a receptance. Unfortunately,

as explained earlier, we had to use acceleration feedback for our application for practical reasons.

MPC, Sliding Mode Control, Receptance/Accelerance Based Eigenstructure Assignment

Together with BODEIT, we also investigated further modern control methods, which I want to quickly summarize in the following:

- **Model Predictive Control**
  The MPC framework does not perform very well for systems with high frequency dynamics. Even when we tried to control a simple flexible beam, we needed to use a MPC update rate of 10^4 Hz to keep the system stable. Unfortunately, since MPC is very computationally intensive, this also meant that this controller would not be real-time capable. Additional issues arise when using acceleration feedback, since the MPC framework does not seem to handle systems with direct feedthrough very well. There are in fact very little publications available that try to use MPC for active vibration control. One of the only ones seems to be [211], which uses a laser vibrometer as feedback on a simple beam test rig and does only achieve a vibration attenuation of about -6 dB at the resonance peaks.

- **Sliding Mode Control**
  A sliding mode controller also becomes quite difficult to tune when dealing with higher-order systems, because of the large amount of parameters in the sliding-variable[8]. The controller worked quite well on a single flexible beam assuming full system knowledge. However, in our experience, the sliding mode controller was very unrobust when using reduced order models for the controller design or if there was any kind of unmodeled disturbance acting on the system.

- **Receptance/Accelerance Based Eigenstructure Assignment**
  Receptance based eigenstructure assignment (RBEA, see e.g. [222]) was stable on the robot model. However, it needed position feedback to work, meaning we had to integrate the acceleration feedback twice. This is an undesirable processing step which also does not deal well with noise in practice. Additionally, RBEA will modify the stiffness of the system in order to place the closed-loop poles. This has the effect of trying to hold the TCP of the robot in place when moving the robot arm. Instead, we also tested Accelerance Based Eigenstructure Assignment (ABEA) with acceleration feedback, which will modify the inertia of the system to place the closed-loop poles. This will no longer affect the quasi-static motion of the robot. However, ABEA has to deal with the same stability issues as the other modern methods, when using acceleration feedback. When placing the desired closed-loop poles by only increasing the modal damping, the controller will not modify the inertia of the system. This makes the controller significantly more robust, however, also quite similar to a simple direct velocity feedback controller.

Conclusions

All of the these methods worked very well in simulation when controlling simple systems with a low number of states and full system knowledge. Unfortunately, the task of controlling a time variant system with a high number of states and acceleration feedback seems to be quite difficult for most modern control methods for the above mentioned reasons. When we started to assume that we do not have full system knowledge, most methods stopped working

[8] Even using a simplified beam model with only three modes and therefore six states.

at all or performed significantly worse than the more simple classical control methods when applied to the robot model. Additionally, at this stage, we only worked with a simplified 2D robot model and did not even incorporate actuator dynamics, signal delay or sensor noise into the control system.

Considering all of these issues, and the high amount of effort needed to get these methods to work even in simulation, I decided to not proceed to implement them on the real system.

5.2 External Stabilization of Robot Manipulators

While the external vibration damping approach showed some promise in the previous section, it is questionable if the required path accuracy target of 20 μm can be achieved via this method. Especially if the robot is affected by a lot of torque-ripple.

As explained in Appendix C, with the UR10 robot we achieved better results using the external stabilization approach, which uses an additional set of actuators to stabilize the tool against any disturbances coming from the robot. However, the first version of our stabilization unit prototype used positioning tables moved by spindles, which were significantly affected by backlash and friction, and only achieved a 50 % reduction of the vertical path error. We tried to address these problems with the second version of the stabilization unit, by designing the entire actuator system in-house.

I will again start by explaining the actuator and controller design in subsection 5.2.1. Simulation results are discussed in subsection 5.2.2 and the experiments performed on the UR10 robot are shown in subsection 5.2.3.

The results of this section are also partially published in our paper [51].

5.2.1 Actuator and Controller Design

The underlying manufacturing process that motivates this thesis is affected the most by vertical disturbances in the z-direction (see Fig. 5.19) and inclination errors around the y-axis. The second prototype of the stabilization unit was therefore designed to stabilize these two DOFs.

Inspired by In-Body-Image-Stabilization systems (IBIS, see section 2.2), we used a plate as the stabilized platform, which is connected to the housing via two sets of springs, Fig. 5.19. The first set of springs k_z is aligned with the z-direction the stabilized platform. The second set of springs k_φ is attached to the corners of the platform, with the distance d_φ to its center of mass.

This setup allows us to design the mechanical system of the actuator for both desired DOFs as decoupled single harmonic oscillators. Moving the plate in the z-direction will only engage the vertical springs k_z for small displacements[9], since a vertical motion is orthogonal to the horizontal springs k_φ (see also Fig. 5.20.d for a more detailed view). In the same way, a rotation around the y-axis will only engage the horizontal springs k_φ, since the motion caused at the attachment points of the vertical springs k_z by a rotation φ_y is orthogonal to their alignment.

The platform is actuated by two vertical forces f_L and f_R, which have the distance of d_f to the center of mass of the stabilized platform. The equations of motion of the two stabilized

[9] This is quite valid here, since we are trying to stabilize the load in the 10 μm range.

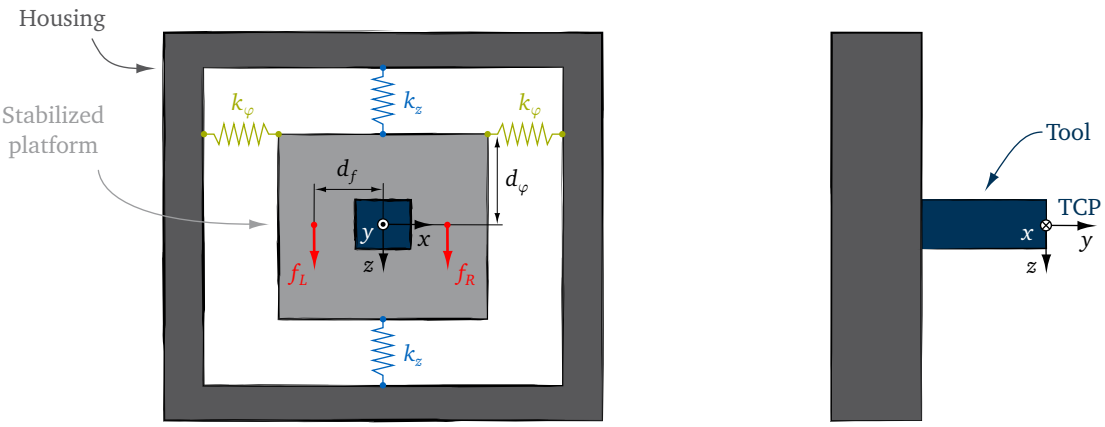

Figure 5.19: Concept of the stabilization unit.

DOFs z and φ_y are therefore:

$$m_{\mathrm{SP}}\ddot{z} + c_{\mathrm{SP},z}\dot{z} + 2k_z z = f_{\mathrm{SU}} \,, \tag{5.11}$$

$$J_{\mathrm{SP}}\ddot{\varphi}_y + c_{\mathrm{SP},\varphi}\dot{\varphi}_y + 2k_\varphi \varphi_y = \tau_{\mathrm{SU}} \,, \tag{5.12}$$

with the actuator forces at the stabilization unit

$$f_{\mathrm{SU}} = f_L + f_R \,, \tag{5.13}$$

$$\tau_{\mathrm{SU}} = 2d_f\,(f_L - f_R) \,. \tag{5.14}$$

The mechanical system of the actuator can therefore be designed as a single harmonic oscillator using the mass m_{SP} of the stabilized platform and vertical spring stiffnesses k_z for the z DOF, and the area moment of inertia J_{SP} and the horizontal spring stiffnesses k_φ for the rotational DOF φ_y. The mechanical system will also be affected by some amount of damping $c_{\mathrm{SP},z/\varphi}$, however, as we have learned from the actuator for the external vibration damping approach (see section 5.1.4), it is beneficial to minimize the damping due to friction as much as possible.

The controller of the stabilization unit will use a measured position reference from the process surface to stabilize the platform. For a position based control system, it would be beneficial to design the mechanical system as stiff as possible, since the dynamic terms coming from the inertia and damping in equation (5.11) and (5.12) would play a smaller role. E.g. tuning the mechanical system with an eigenfrequency at 100 Hz would simplify the control design for the desired control bandwidth of 50 Hz, since the system behaves quasi-statically and is completely dominated by the stiffness term. This would also reduce the influence of non-linear friction and stick-slip effects, since even for small displacements the system would need to mainly work against the linear stiffness of the spring. However, such a stiff system would also require very high control forces in order to move the platform.

Another disadvantage of using a very high spring stiffness is that the control system needs to be able to control the high frequency actuator resonance and provide the high actuator forces with high control gains, which are also more prone to instability due to the amplification of noise. This can somewhat be circumvented by using a simple feedforward model to determine the high control forces for quasi-static motions without feedback. However, even though the required model is quite simple, it still needs to be very accurate to not negatively influence the precision of the positioning system.

In our case, we performed a few preliminary tests on a simplified 1 DOF system to determine that an actuator eigenfrequency of 20 Hz is a good compromise for our application.

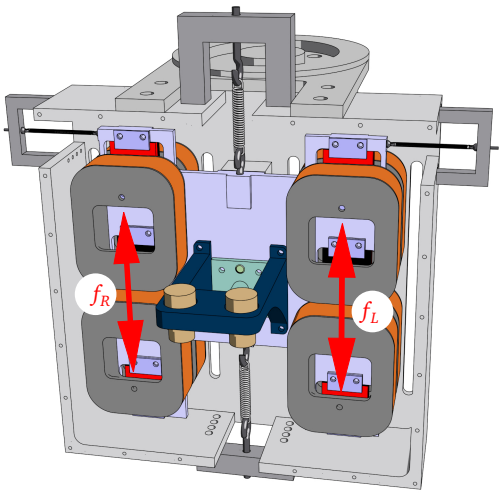

(a) Front view: Lorenz actuators.

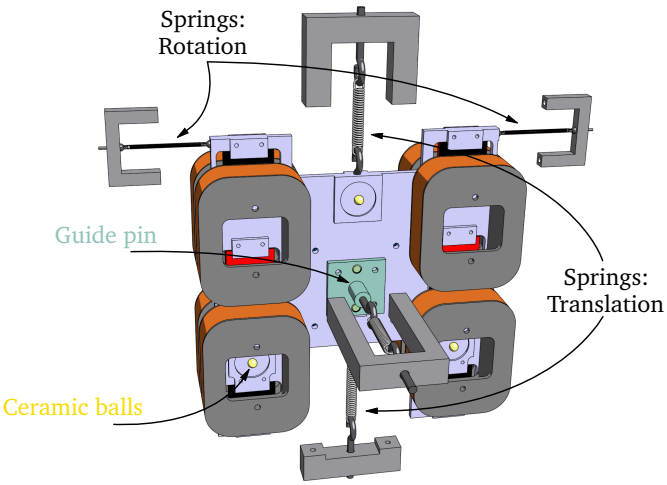

(b) Back view: Mechanical system.

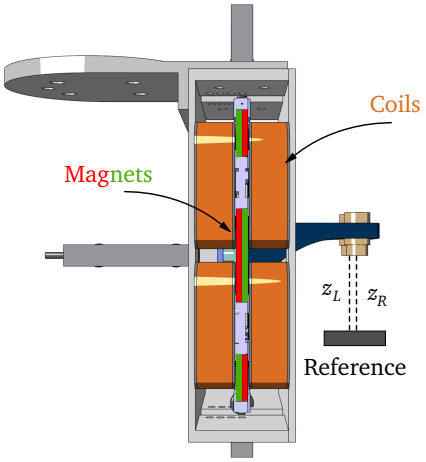

(c) Side view: Lorenz actuator.

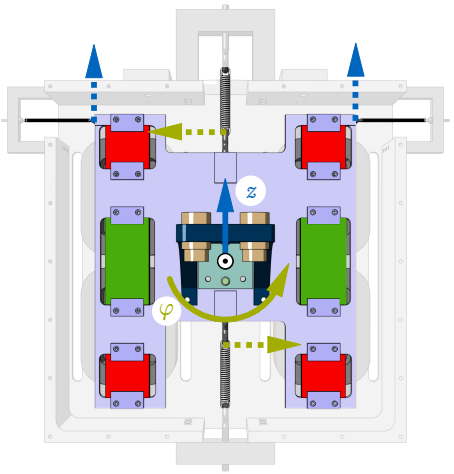

(d) Front view: Mechanical system.

Figure 5.20: Mechanical design and Lorenz actuators of the second version of the stabilization unit. Adapted from our paper [51].

Mechanical Design

The final mechanical design of the second stabilization unit prototype is shown in Fig. 5.20. The stabilized platform has a mass of $m_{SP} = 0.2\,\text{kg}$ and is attached to the housing via four springs as described above, Fig. 5.20.d. The stiffnesses of the vertical k_z and horizontal springs k_φ are chosen such that both DOFs have an eigenfrequency of 20 Hz.

The platform is pulled via a fifth spring on three ceramic bearing balls to only allow motion within the plane of the stabilized platform, Fig. 5.20.b. The fifth spring is again aligned orthogonally to the plane of motion, such that it does not contribute to the dynamics of the system for small displacements. In order to block all further undesired DOFs, a guide pin is attached to the front and back of the platform respectively. The guide pins glide in linear guides (not depicted in the figures) which only allow vertical displacements in the z-direction and rotations φ_y around the guide pin around the y-axis. This setup is again a compromise between mechanically blocking all unnecessary DOF and reducing friction

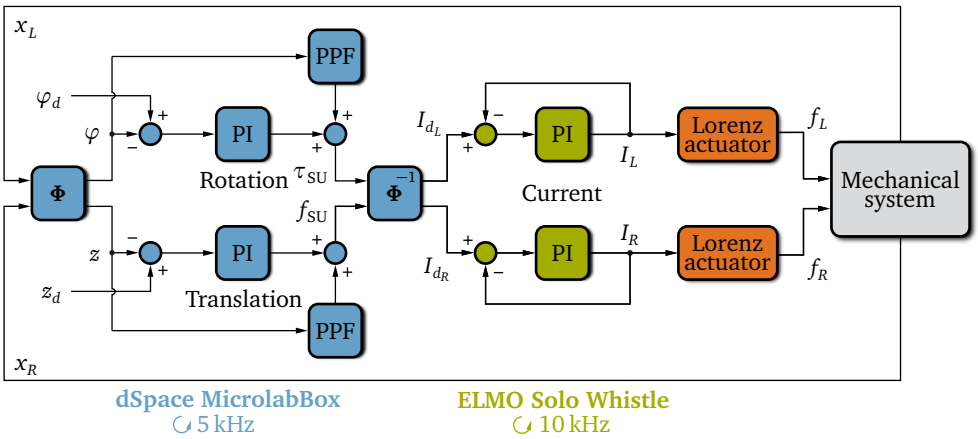

Figure 5.21: Mechanical design and Lorenz actuators of the second version of the stabilization unit. Adapted from our paper [51].

as much as possible, which is both important to simplify the control problem as much as possible[10].

The control forces f_L and f_R are realized with two Lorentz actuators. The actuators consists of three magnets each, which are embedded in the stabilized platform, Fig. 5.20.d. The housing holds four custom wound coils for each side, Fig. 5.20.a and 5.20.c. Each actuator is capable of producing a peak force of 70 N and continuous force of 20 N. The maximum displacement of the system is $z_{\max} = \pm 2.5\,\text{mm}$, which results in a maximum needed static force of $\sim 10\,\text{N}$ [11], when pushing the load against the full gravitational pull.

For the following studies, the tool is replaced by a dummy tool, which holds two *Micro Epsilon* eddy current sensors, which have a measurement range of 3 mm and a resolution of $3\,\mu\text{m}$ [258]. The sensors measure the left z_L and right z_R distance to a reference surface and have distance of $d_{\text{EC}} = 30\,\text{mm}$ between each other.

Controller Design

In order to design the controller, the stabilization unit is modeled in Simulink/Simmechanics and attached to the same flexible UR10 model as used in previous sections, Fig. 5.22. This step is important for the controller design, since we can asses the influence of the dynamic interaction between the robot's structural dynamics and joint controllers with the control system of the stabilization unit.

The final control structure is shown in Fig. 5.21. First, the measurement signals of the left z_L and right z_R eddy current sensors are transformed into the DOFs of the stabilization unit:

$$\begin{bmatrix} z \\ \varphi_y \end{bmatrix} = \underbrace{\begin{bmatrix} 0.5 & 0.5 \\ 1/d_{\text{EC}} & -1/d_{\text{EC}} \end{bmatrix}}_{\Phi} \begin{bmatrix} x_L \\ x_R \end{bmatrix}. \tag{5.15}$$

Since the equations of motion for both DOFs are completely decoupled from each other (5.11)(5.12), we can design the control law for each DOF separately. Let us start by applying

[10] I really want to stress here that experience has shown that it is very important to have a good mechanical and actuator design which simplifies the underlying control problem. There are a lot of powerful control methods that can achieve amazing things, however, all of them have their limitations, especially when faced with multiple bottlenecks from the rest of the mechatronic system. It is very unlikely that a control system can perform well, when the controller has to compensate for bad mechanical design with a lot of friction, stick-slip or backlash, a slow bus-communication system with a lot of delay and lost packages, high amount of sensor noise, slow controller clock-rates, unnecessarily complicated actuator dynamics, etc.

[11] An actuator eigenfrequency of 20 Hz at 0.2 kg mass results in a vertical stiffness of $2k_z = 3.16 \cdot 10^3\,\text{N/m}$.

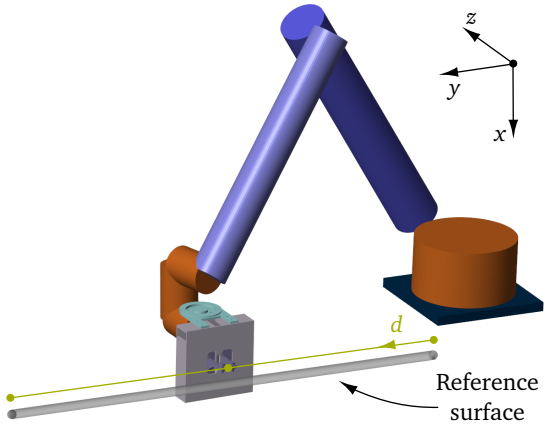

Figure 5.22: The flexible UR10 simulation model with the stabilization unit.

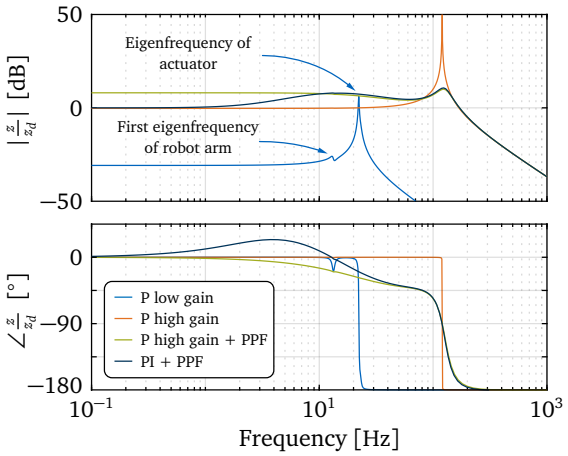

Figure 5.23: Closed-loop transfer function of the z-DOF with different controller gains. Adapted from our paper [51].

a simple P-controller to the z-DOF (5.11):

$$f_{\mathrm{SU}}(s) = g_{\mathrm{P,z}} \cdot (z(s) - z_d(s)) \ , \tag{5.16}$$

with z_d being the desired distance to the reference surface and $g_{P,z}$ the controller gain. Fig. 5.23 shows the closed-transfer function for the z-DOF. We can see even for very low $g_{P,z}$ gain (blue line) that the structural dynamics of the robot are barely visible in the closed-loop transfer function. The reason for this is that the control problem that we are investigating here is collocated with both the controller output f_{SU} and feedback z acting on the same DOF, which causes structural dynamics of the robot to show up as alternating pole-zero pairs in the closed-loop transfer function. Applying a simple P controller to this kind of control plant will cause the poles created by the dynamics of the structure to be pushed on their respective zeros with increasing amounts of gain, canceling out their dynamic contribution to the closed-loop transfer function. This is a very useful property when applying a collocated control problem to a dynamic structure [219][12]. In our case, we can see that very little gain is already enough that only the pole-zero pair of the first structural mode is still barely visable in the closed-loop transfer function (Fig. 5.23 blue line).

Increasing the gain further will cause the structural dynamics of the robot to completely cancel out, and only the pole caused by the the actuator dynamics (acting like a single harmonic oscillator) will be pushed to higher frequencies (Fig. 5.23 orange line). This will also cause the pole to further lose modal damping, because of the very low damping in the mechanical system. This is by design, since we want to avoid as much friction as possible in the actuator system. However, this leaves us with another problem: The very high resonance peak basically makes this kind of controller unusable, because of the very high amplitude oscillations in the step response of the system.

The control plant now acts like a simple single harmonic oscillator with very little damping. In theory, this kind of plant could be very easily controlled by using a PID controller, with the D part damping the high resonance peak. However, the amount of D gain needed for this to work would be so high that the system would never work in the presence of sensor noise.

In order to reduce the resonance peak, we can instead modify the control plant with a

[12] See also Appendix A.

PPF controller as described in section 3.3 (3.79):

$$f_{\mathrm{SU}}(s) = g_{\mathrm{P,z}} \cdot (z(s) - z_d(s)) \; + \; \frac{g_{PPF}}{s^2 + 2\zeta_{c,PPF}\omega_{c,PPF}s + \omega_{c,PPF}^2} \cdot z(s) \; , \tag{5.17}$$

with the PPF controller eigenfrequency $\omega_{c,PPF}$ set to the resonance frequency caused by the controller gain $g_{\mathrm{P,z}}$. The PPF damping ratio is again set to $\zeta_{c,PPF} = 0.5$ and the PPF gain g_{PPF} is increased until a suitable amount of damping is achieved.

The disadvantage of this approach is that the gain of the PPF controller will stack on the P controller and cause the steady state solution to overshoot (Fig. 5.23 green line). However, this can easily be fixed by adding an I part to the P controller to ensure steady state accuracy:

$$f_{\mathrm{SU}}(s) = \left(g_{\mathrm{P,z}} + \frac{g_{\mathrm{I,z}}}{s}\right) \cdot (z(s) - z_d(s)) + \frac{g_{PPF}}{s^2 + 2\zeta_{c,PPF}\omega_{c,PPF}s + \omega_{c,PPF}^2} \cdot z(s) \qquad \text{(SU } z \text{ controller)} \tag{5.18}$$

The controller for the inclination φ_y can be designed in the exact same way.

Note that not a lot of $g_{\mathrm{I,z}}$ gain is needed to achieve a stable controller with a usable bandwidth of around 2 Hz for precise tracking (Fig. 5.23 dark blue line). This might appear way too low at first glance, however, the goal of the tracking controller is not to be able to quickly track a desired distance z_d. For our application the desired distance z_d and inclination φ_y will almost always be set to a constant value and would only sometimes need to follow a relatively slow trajectory. The important property of the controller is its capability to reject disturbances coming from the robot, which we will investigate in the Simulation Results subsection 5.2.2.

Noise Sensitivity

However, let us first have a short look at two other important properties of this control approach. The first one is the noise sensitivity of the controller (5.18). The sensitivity function of the controller from a disturbance at the feedback z_n to the output of the controller f_{SU} is shown in Fig. 5.24 as the blue line. Let us compare the same sensitivity function to a PID controller that achieves the same amount of damping (Fig. 5.24 orange line).

We can see that the sensitivity function of the PID controller is significantly higher the sensitivity function of the SU z controller (5.18) in the higher frequency range. However, the higher frequency range is needed, since the micro controller has to operate with a sufficiently high enough clock-rate (in our case 5 kHz) to ensure the proper operation of the real discrete control system[13].

The high slope at higher frequencies of the PID controller's sensitivity function could be reduced by tuning the cut-off frequency of the lowpass filter (see pole at around 300 Hz) of the D part to lower frequencies. However, this would also negatively impact the damping capabilities of the PID controller. The lowpass filter of the PID controller of the sensitivity function shown in Fig. 5.24 is already tuned an the verge of affecting the PID controllers performance.

Using these sensitivity functions, we can calculate the noise amplification factor of both of these controllers (see Appendix B) and find that the PID controller has a 100 times higher noise amplification than the SU z controller derived in (5.18).

This high noise amplification factor is the main reason why we were not able to apply a PID controller on the real system to damp the high resonance peak of the actuator system.

[13] See Appendix B for more details about typical application issues of real control systems.

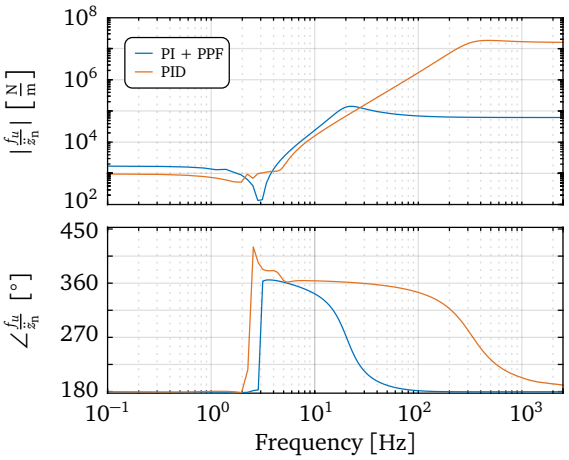

Figure 5.24: Sensitivity function of the SU z controller and a PID controller with the same amount of damping.

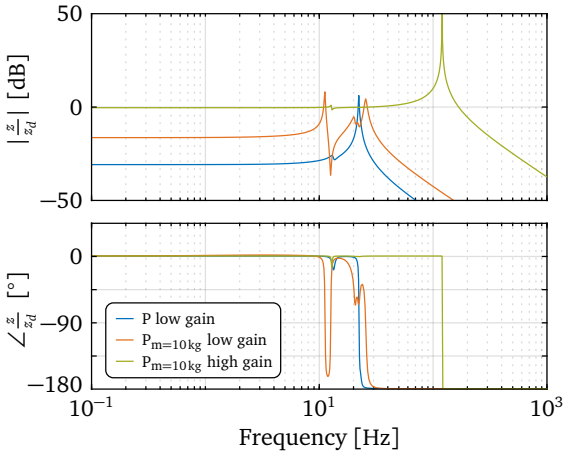

Figure 5.25: Closed-loop transfer function of the z-DOF with a stabilized load mass of $m_{SP} = 10\,\text{kg}$.

We also tried to apply other control strategies to damp the actuator resonance, however, none were as successful as the controller shown in (5.18)[14].

Scalability

In the following experiments, we will only stabilize a relatively low load of 0.2 kg. Let us therefore also investigate if this external stabilization approach is also scalable to higher stabilized masses. Fig. 5.25 again shows the closed-loop transfer function for the z DOF with a stabilized load of now 10 kg. The blue line shows the same transfer function with low P gain as in Fig. 5.23 with a stabilized mass of $m_{\text{SP}} = 0.2\,\text{kg}$. The orange line shows the closed-loop transfer function with the same amount of low P gain, however, with much higher stabilized mass of $m_{\text{SP}} = 10\,\text{kg}$ [15]. The stiffness of the actuator k_z is again designed to achieve a 20 Hz actuator eigenfrequency.

We can see that the heavier system has much further separated zero-pole pairs for the first and second eigenmode of the robots structural dynamics. However, applying the same amount of high P gain as before basically causes the system to almost behave exactly the same as before, with only the first pole-zero pair barely not canceling out (cf. Fig. 5.25 green line with Fig. 5.23 green line).

This suggests that the external stabilization approach would in theory work for any amount of reasonable stabilized mass m_{SP}. However, it should be noted that higher control forces would of course be needed to still achieve the same performance. This could be addressed by reducing the actuator eigenfrequency and therefore the amount of stiffness and actuator forces needed to move the system. This is probably fine, since the heavy system already needs quite high forces to be moved and the main motivation to use a high actuator eigenfrequency was to keep the linear stiffness forces more dominant than the non-linear friction effects.

[14] Even using the loop-shaping method for an H_∞ controller, which in theory allows to directly shape the sensitivity function, did not achieve better results on the real system.

[15] Note that the maximum load of the UR10 is also 10 kg. The real system would be even heavier, when accounting for the weight of the actuator system.

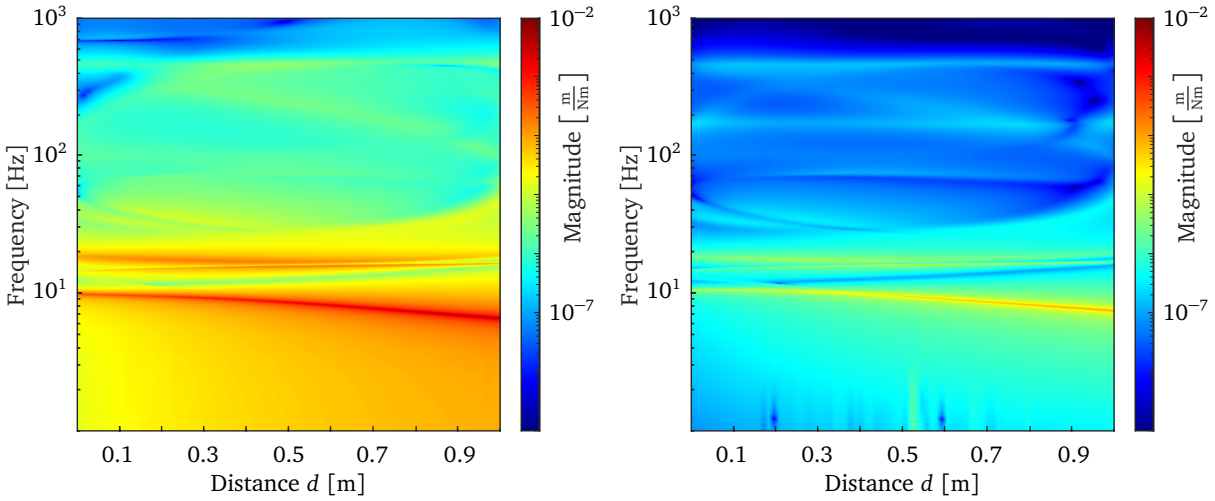

(a) Uncontrolled reference. **(b)** Stabilized.

Figure 5.26: Campbell-diagram of the transfer function from a disturbance at the motor torque $\tau_{m,2}$ of the second joint of the robot to the displacement at the stabilized load z.

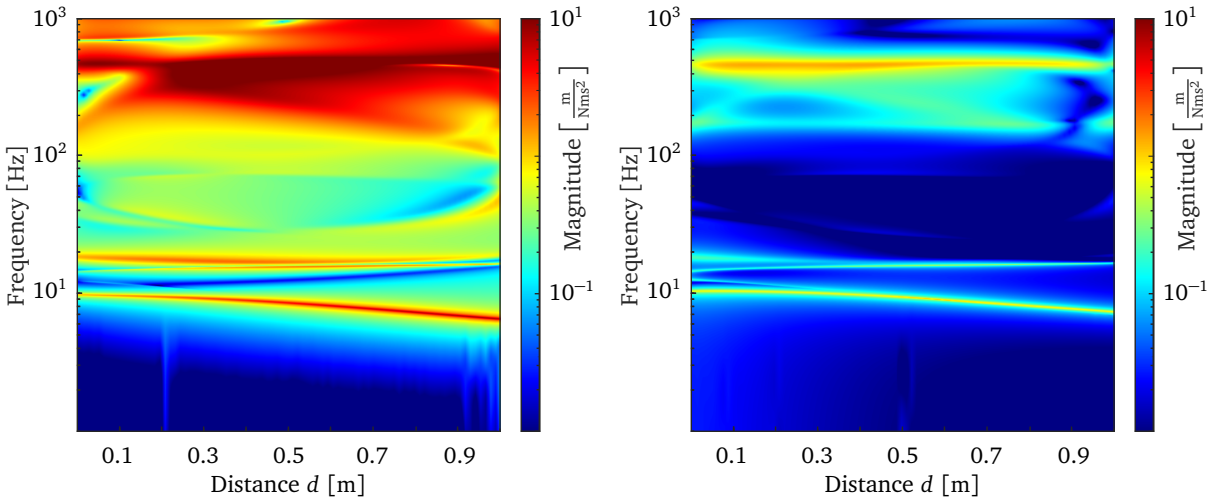

(a) Uncontrolled reference. **(b)** Stabilized.

Figure 5.27: Campbell-diagram of the transfer function from a disturbance at the motor torque $\tau_{m,2}$ of the second joint of the robot to the accelerations at the stabilized load $\ddot{z}$.

5.2.2 Simulation Results

Let us assess the performance of the system in simulation by letting the flexible UR10 model again perform the same 1 m long horizontal test trajectory with 100 mm/s speed. The robot again performs a high jerk stop after 10 s.

Disturbance Rejection

As already mentioned in the previous subsection, the designed controller only has a relatively low tracking bandwidth of 2 Hz (see Fig. 5.23 dark blue line). However, the more important property of the controller is its capability to stabilize the payload against external disturbances coming from the robot. We can quantify this by looking at the transfer function of

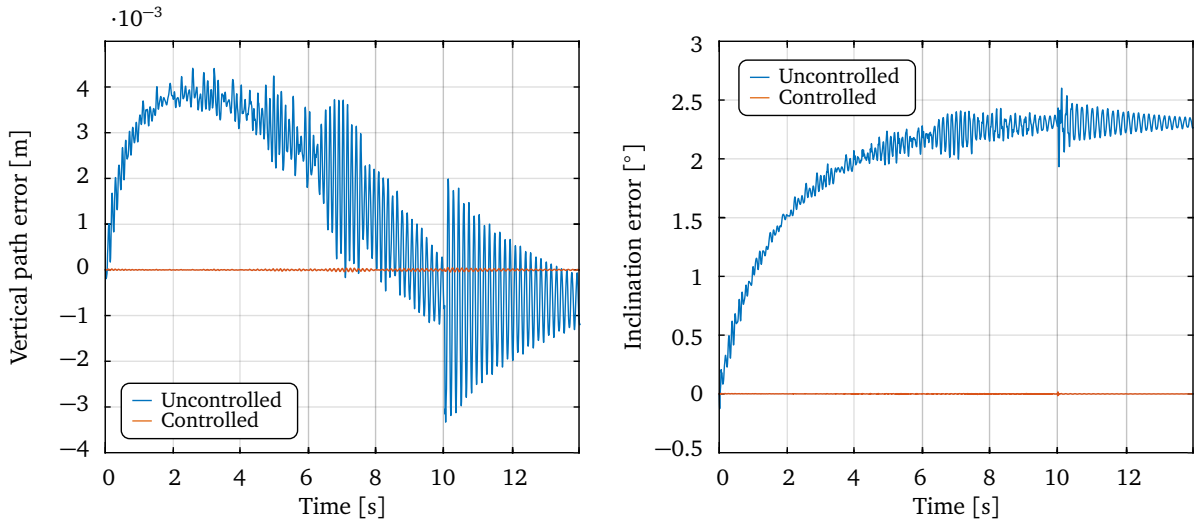

(a) Vertical path error at the stabilized tool.

(b) Inclination error at the stabilized tool.

Figure 5.28: Simulation of the tracking performance for the vertical z-DOF and inclination φ_y-DOF at the stabilized tool during a 1 m long horizontal test trajectory with 100 mm/s speed.

a disturbance acting on e.g. the motor torque of the second joint of the robot $\tau_{m,2}$ to the displacements z measured at the tool attached to the stabilization unit.

A Campbell-diagram of a set of these liniearized transfer functions, while following the trajectory shown in Fig. 5.22, is shown in Fig. 5.26b. Fig. 5.26a shows a reference with the actuators being blocked and the control system turned off.

We can see that by turning the stabilization on, the displacements z at the stabilized tool are almost completely decoupled from any disturbance acting on the second joint over the entire frequency range. Even at the resonance frequencies, the response is attenuated by almost two orders of magnitude.

We can get a better assessment of the performance in the higher frequency range by also looking at the same transfer function, but with accelerations $\ddot{z}$ as the output, Fig. 5.27. Which reveals the same results for the higher frequency region.

This suggests that, while the control system is only capable of following a change in desired distance z_d with a bandwidth of 2 Hz, the stabilized load is actually almost completely decoupled from any disturbance acting on the robot, which is ultimately the goal for a good high-precision tracking performance.

Tracking Performance

We can verify this assumption by looking at the tracking performance of the stabilization unit shown in Fig. 5.28. The uncontrolled reference (blue line) is simulated by blocking all the DOFs of the stabilization unit and turning the stabilization controllers off. We can see that the stabilization unit is capable of a large reduction of the tracking error from a RMSE of 2.43 mm to 14.6 μm for the vertical path error and a RMSE of 2.05° to 0.0011° for the inclination error, which is a reduction of two orders of magnitude in both cases.

The system is very robust against any kind of disturbances coming from the robot and barely interacts with its structural dynamics thanks to its collocated control design. Neither the torque-ripple from the joint motors, nor the large jerk excitation at the end of the trajectory effect the system. It is important to stress here that no model or any other prior knowledge about the robots dynamic behavior was required to design and tune the system. This suggests that a similar performance should be possible on the real system, as long as the

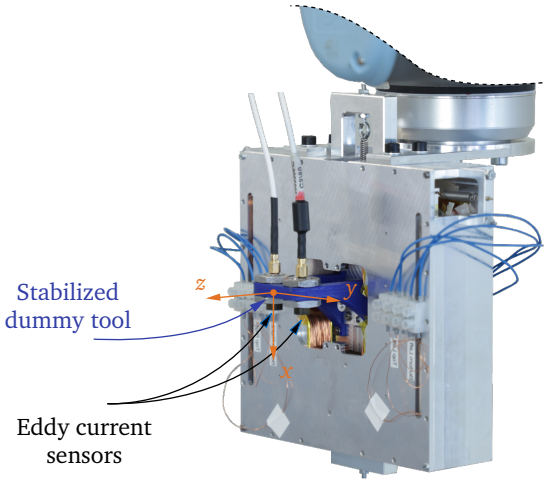

Figure 5.29: Second prototype of the stabilization unit.

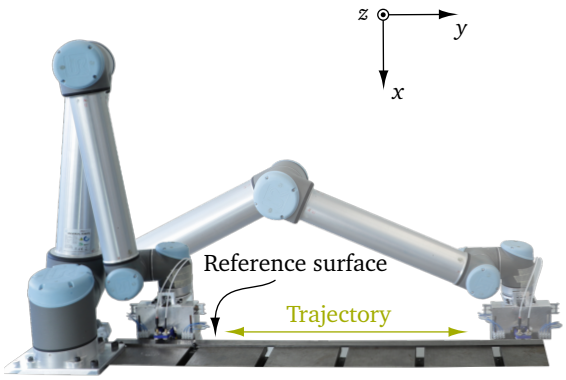

Figure 5.30: Test setup on the UR10 robot with the stabilization unit.

rest of the mechatronic system is build thoroughly enough.

5.2.3 Experiments on the UR10 Robot

The real system is shown in Fig. 5.29. The control system as shown in Fig. 5.21 is again run on a *dSpace* Microlab Box with a clock rate of 5 kHz. The desired forces for the left f_L and right f_R Lorentz actuator are again scaled with the motor constant and sent as desired currents via an 10 V analog connection to the PI current controller running on *ELMO* motor drivers at 10 kHz clock rate.

The PI current controllers on the ELMOs are tuned with a bandwidth of over 100 Hz, such that for our application

$$f_{L/R,d}\,\frac{1}{k_m} = I_{L/R,d} = I_{L/R} = \frac{1}{k_m}\,f_{L/R}\,, \tag{5.19}$$

which is also why I neglected the current controller for the control design in the previous subsection.

The eddy current sensors also send the measured position feedback $z_{L/R}$ via a 10 V analog connection to the Microlab Box.

Controller Tuning

The measured closed-loop transfer functions for both DOFs of the stabilization unit are shown in Fig. 5.31. The blue line with low P gain shows that the actuator system has its eigenfrequency at the desired value of around 20 Hz for both DOFs. The system is also well decoupled, as there is only one pole visible in both transfer functions. We can also see that the system has barely any damping because of the low-friction design of the actuator, which would cause an amplification of two orders of magnitude at the resonance peak without any additional control.

The tuning of the controllers works in the same steps as described in the previous subsection. The P gain is increased until the system starts to oscillate on the verge of instability. This is caused by the increased P gain pushing the resonance peak to higher frequencies and further decreasing the modal damping of the system. The PPF controller is then applied to

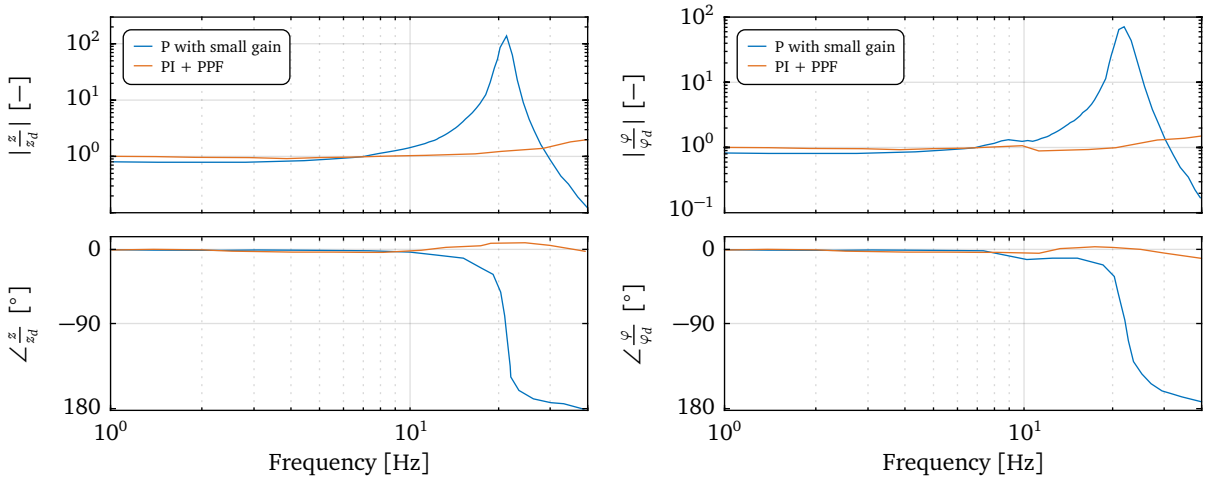

(a) Translational z-DOF.

(b) Rotational φ_y-DOF.

Figure 5.31: Measured closed-loop transfer function of the stabilization unit.

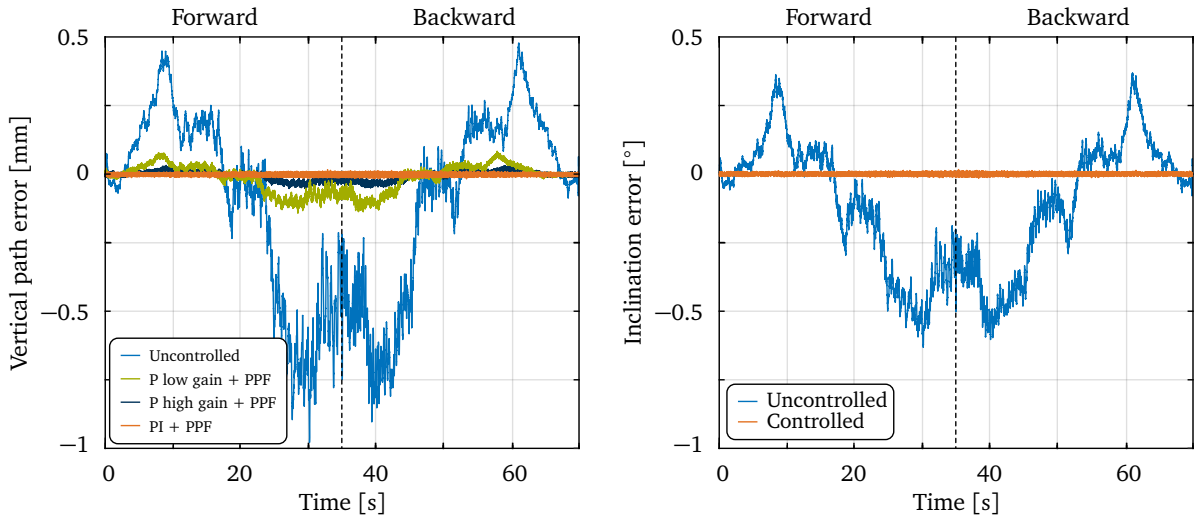

(a) Vertical path error at the stabilized tool with different controllers.

(b) Inclination error at the stabilized tool.

Figure 5.32: Measured tracking performance for the vertical z-DOF and inclination φ_y-DOF at the stabilized tool during a horizontal test trajectory with 30 mm/s speed.

this oscillation frequency to add damping. This process can be repeated a second time to further increase the bandwidth of the tracking controller. The final step is then the addition of the I part to ensure steady state precision.

The orange lines in Fig. 5.31 show the closed-loop transfer function after the tuning procedure. The achievable tracking bandwidth is even higher than in the simulation with about 20 Hz, which is thanks to the second tuning step. After the controller gains are found, the system can be safely turned on and off with the same gains without becoming unstable.

Tracking Performance

Fig . 5.32a shows the tracking performance for the z-DOF during the different steps of the tuning procedure. We can see how each tuning step gradually improves the tracking performance of the controller. I want to stress here again that most of the tracking improvement

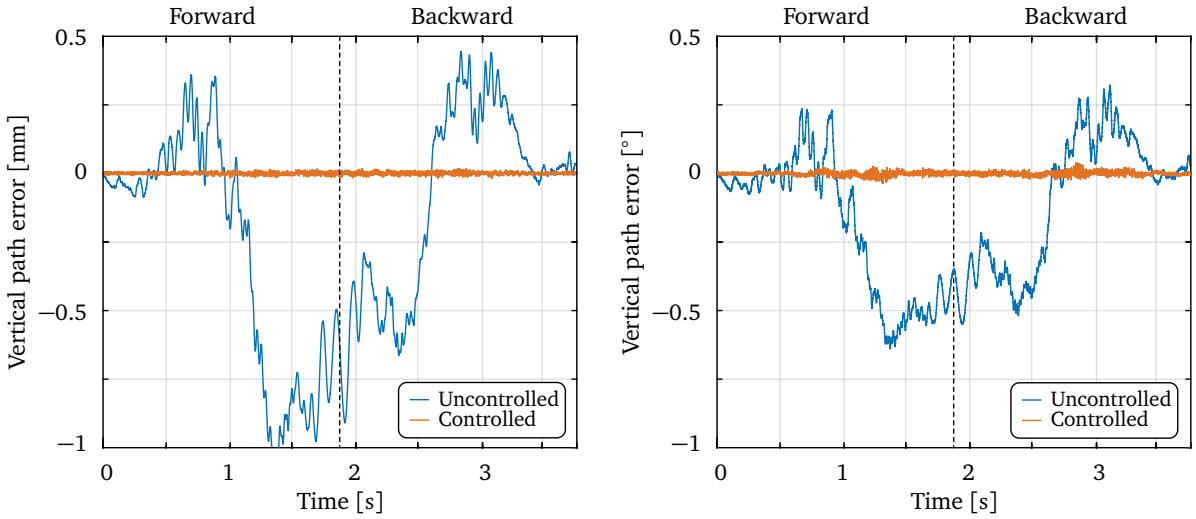

(a) Vertical path error at the stabilized tool.

(b) Inclination error at the stabilized tool.

Figure 5.33: Measured tracking performance for the vertical z-DOF and inclination φ_y-DOF at the stabilized tool during a horizontal test trajectory with 1 m/s speed.

does not come from the higher bandwidth tracking performance of the controller, but from the better disturbance rejection capabilities of the system as we have seen earlier.

For the test at 30 mm/s trajectory speed the system is able to reduce the RMSE from 0.36 mm to 2.49 μm for the vertical path error and the RMSE of the inclination error from 0.26 ° to 0.0025 °. Similar to the simulation results, this also corresponds to a reduction of the error by two orders of magnitude on the real system.

For the second test with a far quicker trajectory velocity of 1 m/s (Fig. 5.33), we get similar results: The RMSE of the vertical path error is reduced from from 0.36 mm to 3.33 μm and the RMSE of the inclination error is reduced from 0.26 ° to 0.0033 °.

The maximum error peaks of the vertical path error are in both cases below 15 μm, which meets the specifications for the path precision set in the introduction of this thesis. With a maximum displacement range of 5 mm and a precision of 15 μm, the stabilization unit achieves a precision of 0.3 % relative to its actuation range, which is significantly better than most tracking systems discussed in the State of the Art chapter 2.2. This is especially impressive considering that the stabilization unit is also attached to a moving robot and constantly exposed to dynamic disturbances coming from the robot.

The performance of the system is pretty much only limited by the noise floor of the eddy current sensors. Looking at the spectra of the vertical path and inclination error, Fig. 5.34, reveals that the system actually significantly undercuts the set goal from the introduction at −75 dB. This suggests that the maximum error peaks in e.g. Fig. 5.32a are just caused by sensor noise and that the physical displacement error of the system is actually even better than this. Lowpass-filtering the vertical path error of the 30 mm/s test at 100 Hz gives a maximum vertical error of 3 μm, which is exactly the claimed resolution of the *Micro Epsilon* eddy current sensors.

5.2.4 Discussion of Results

These are quite impressive results compared to most stabilization and tracking systems discussed in the State of the Art section 2.2 and 2.3. The better tracking systems usually achieve a precision of 1 % relative to their maximum motion range, while the second version of the

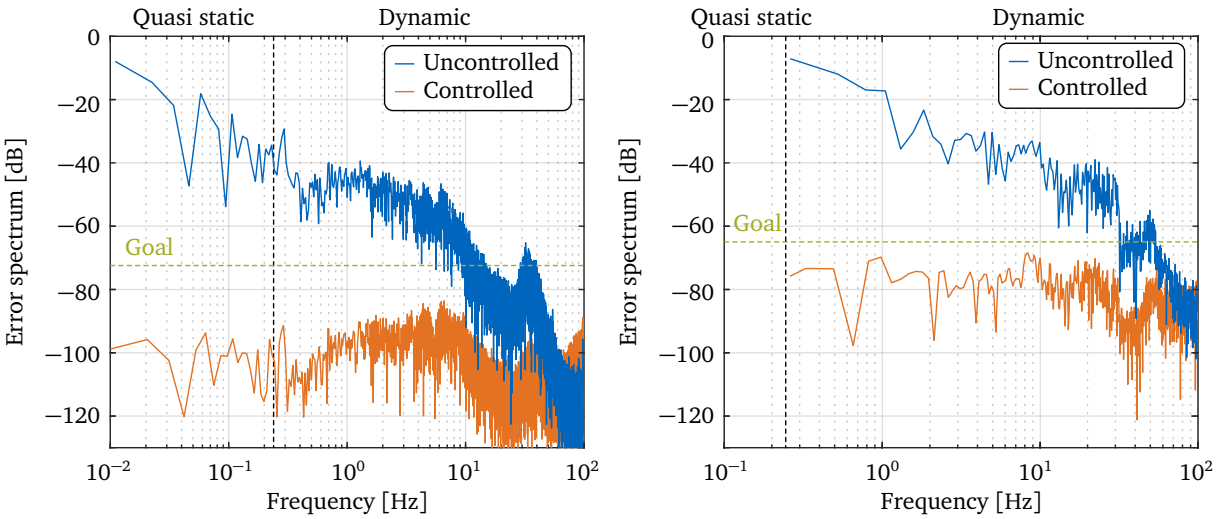

(a) Spectrum of the vertical error at 30 mm/s trajectory speed.

(b) Spectrum of the vertical error at 1 m/s trajectory speed.

Figure 5.34: Step response experiment with the CROPS robot. The residual vibrations are measured at the TCP and lowpass filtered with a cutoff frequency at 20 Hz to have a better view on the lower frequency vibrations.

stabilization unit accomplishes a relative precision between 0.3 % to 0.06 %. The better active vibration damping systems usually achieve a maximum attenuation between −30 dB to −40 dB at the resonance peaks. The stabilization unit manages to evenly attenuate most of the error spectrum, with an attenuation of the lower portion of the dynamic error spectrum by up to −70 dB (Fig. 5.34a).

The great advantage of using a stabilization unit with collocated sensor feedback at the TCP is that we do not need any significant knowledge about the underlying system dynamics of the robot itself. We also do not need to interface with the robot in any way. This makes this approach easily adaptable to other robot manipulators and also way easier to employ in an industrial setting in general.

However, while we got around having to use precise models of the robot's structural dynamics, the systems performance heavily relies on good sensor feedback from the relative motion at the robot's TCP. Acquiring this feedback is by no means a trivial task. In our case, we used two highly precise eddy-current sensors to measure position feedback relative to the process surface. However, depending on the application, this might not be as easily possible.

We already did some preliminary tests to get around this issue. In his semester thesis [253], my student SLIMAK investigated the use of a Kalman filter to generate the needed position feedback based on acceleration measurements at the TCP. This still worked well by reducing the maximum error peaks at the stabilization unit from 1 mm to 70 μm. However, failed it to achieve our 20 μm requirement. It was also an issue to eliminate drift from the fused sensor data over longer periods of operation. The drift issue might be circumvented by only controlling the dynamic error with the stabilization unit using acceleration feedback, while compensating the quasi-static error via an absolute compensation of the robot.

Chapter 6

Conclusions

The purpose of this thesis was to investigate external active vibration damping and stabilization approaches for high-precision applications of robot manipulators.

This goal was mainly motivated by a R&D project with *Boeing Research & Development*, which required us to improve the path tracking error of a UR10 robot from 1 mm to below 20 μm as a proof-of-concept. At these small displacements, the tracking error at the TCP of a robot is largely influenced by dynamic oscillations produced by the response of the robot's structural dynamics to excitation sources like torque-ripple at the individual robot joints.

The Influence of Structural Dynamics on Robots

For this reason, I first focused on gaining a better understanding of the influence of the structural dynamics of a robot manipulator on the performance of its control system.

We first built a detailed simulation model of a generic robot manipulator in Simulink as a development platform. The model includes the possibility of using position- or torque-controlled joints, disturbance sources like motor-cogging, flexible drivetrains and flexible links. The subcomponents of the model were verified using measurements from our humanoid walking robot *Lola* for the motor models and torque measurements of a *Franka* Panda robot to estimate stiffness and damping parameters for the flexible drivetrain. The global behavior of the model was then verified using measurements from a UR10 robot. The overall goal being to obtain a robot model with realistic global behavior depicting all relevant effects, however, without trying to exactly replicate the dynamics of our specific UR10 robot. Nevertheless, the model still showed great agreement with the measured driving points dynamics at the TCP of the UR10 robot for the first structural eigenfrequency.

We then used this model, as well as an experimental modal analysis of our harvesting robot CROPS, to investigated the pose dependent structural dynamics of robot manipulators. The main results being that the dynamics of a robot's mechanical system heavily depends on its current pose. Depending on the robot's mechanical design, there might also be several structural modes which can not be influenced by the robots own joint controllers.

We also tested the influence of motor position controlled robot joints on the structural dynamics at the robot's TCP. We found no noteworthy dynamic interactions, because of the typically high gear ratios used for industrial robots. This is an important result, since we consequently did not have to deal with any disruptive interactions between the robot's own control system and an external stabilization device mounted at its TCP.

Finally, we also investigated the influence of structural dynamics on position- and torque-controlled robot joints. We first tried to directly control the joint position of a robot joint test rig by closing the position-loop of a typical cascaded P-PI-PI motor controller using an absolute encoder mounted on the joint side of the gear. For this specific case, the achievable control bandwidth of such a joint position controller was about 2 Hz. We also found that the possible performance of this control setup is heavily influenced by the dynamics of the

flexible drivetrain and link. The typical approach to improve this behavior is to use a torque-controlled robot joint. We also investigated these type of robots with our robot simulation and measurements from a *Franka* Panda robot. One of the issues of using passivity based methods with a joint impedance controller to damp the structural response of a robot is that there are still certain poses at which the robot can not control the dynamics at the TCP. However, the main issue for these robots regarding high-precision path tracking is that their achievable torque-control bandwidth is still quite limited at about 10 Hz. Considering that we need to attenuate up to 50 Hz of the UR10's error spectrum, these low joint controller bandwidths will bottleneck any kind of higher-level control system, regardless of the specific control method.

This was one of the main reasons why we decided very early on in the R&D project with *Boeing* that we can not use the robot's own control system to achieve the required 20 μm tracking precision. Another reason was the sheer complexity of acquiring an accurate high-fidelity model of a robot's pose dependent structural dynamics, which would be needed for most control methods proposed by the literature for high-precision robot control.

External Active Vibration Damping

The external vibration damping approach utilizes a proof-mass actuator mounted near the TCP of the robot to generate a control force via the inertia of the moving actuator mass. A single acceleration sensor was used for feedback to keep the control problem collocated. Using acceleration feedback also has the advantage of not needing a reference point for the feedback measurement.

Usually, a proof-mass actuator is built using a set of mechanical leaf springs to guide the mass and keep it from drifting away. However, this way the actuator eigenfrequency is determined by the mechanical design of the actuator. In order to stay more flexible, I decided to not use leaf springs for our design of the proof-mass actuator. Instead, the actuator mass was guided using ball bearings and the mechanical spring was replaced by a PD controller. This way, the actuator dynamics could be tuned using the appropriate controller gains. The actuator achieved a usable force transfer bandwidth of 5 to 80 Hz. With the lower bandwidth limit being caused by limitations due to friction and the higher bandwidth limit by the lower-level current controller.

We first tested classical control approaches like direct velocity feedback (DVF), a negative acceleration feedback (NAF) controller with constant controller eigenfrequencies and a NAF controller with pose dependent controller eigenfrequencies. All of them performing quite similar in simulation. On the real system, the NAF controller performed the best by being slightly more robust to sensor noise, achieving a maximum attenuation of up to -30 dB of the pose dependent structural dynamics of the CROPS robot. The controllers were also able to significantly reduce the settling time of a step response excited by a sudden stop of the robot. The NAF controller again performed the best by reducing the settling time from c.a. 2 s to below 0.15 s. These results are comparable to the achievements of state of the art active vibration damping systems used in other application. Our system was also able to significantly reduce the dynamic oscillations caused by an additional external disturbance at the base of the robot during a horizontal trajectory.

However, the system failed to reduce the dynamic path tracking error of the CROPS robot during normal, undisturbed operation. The reason for this is that actually quite low and precise actuator forces are needed to further attenuate the structural dynamics during normal motions. The system is very capable of reducing large disturbances, however, is not precise enough to also attenuate small forces. This is a common problem in active vibration damping, where the better force actuators usually reach a precision of about 1 % relative to their maximum force. Below this limit, non-linear effects like friction and stick-slip start to effect the

performance of the actuator. This is probably also the reason why most of the better active vibration damping approaches reach a maximum attenuation of −30 dB to −40 dB, regardless of the used control method.

The most promising way to increase the performance of our system would therefore be to improve the accuracy of the proof-mass actuator. This could be done by again using low-stiffness spring leafs as guides instead of ball bearings to reduce friction. Another way could be to incorporate friction models in the actuator controller. However, the field of friction compensation is still a heavily researched topic. Instead of trying to improve the actuator, we could also use an additional smaller sized actuator that can be designed to be more precise by downsizing the maximum actuator force. The control system would then use the large size actuator to reduce large disturbances like sudden trajectory changes, and the smaller on would attenuate the structural dynamics during normal operation.

Finally, we also tested modern control methods like pole placement, LQR, H_∞, MPC, sliding mode control and receptance- or accelerance based eigenstructure assignment. However, our efforts of implementing these controllers never made it past the simulation stage. The main issue was their heavy reliance on accurate observer models for the control design. Without assuming perfect knowledge of the system dynamics at every possible pose, most of these methods were not robust enough because of the pose dependent structural dynamics of a robot manipulator. Many controllers were also quite sensitive to control- and observer-spillover, which was amplified by our reliance on acceleration feedback.

The external vibration damping approach overall showed promising results to effectively attenuate the structural dynamics of a robot manipulator. However, for high precision path tracking there are also other issues that have to be compensated. This approach could work well as a final addition to a robot manipulator that compensates the quasi-static error via an absolute calibration and only has little issues with motor-cogging. An active vibration system could then further improve the robots tracking performance by also reducing the dynamic error caused by structural dynamics. Another way to effectively employ this system would be in combination with another positioning system. The active vibration system would then reduce the higher frequency dynamic error and the slow positioning system would compensate the quasi-static error.

The first version of our stabilization unit prototype was based on this approach. However, the dynamic error of the UR10 robot is heavily dominated by motor-cogging frequencies below 10 Hz. These excitation frequencies are lower than the first structural eigenfrequency of the robot. Meaning that the main portion of the dynamic error of the UR10 is caused by the robots mechanical structure rigidly following the motor-cogging error produced on the motor side of the joints. Because of the commonly large gear ratios used in robot manipulators, there is no way for a proof-mass actuator attached near the robot's TCP to affect this type of error.

External Stabilization

The second version of the stabilization unit completely relied on a fast and precise mechanical positioning system, which stabilized a dummy tool against any external disturbances transferred through the robot's structure.

The system was inspired by in-body-image-stabilization (IBIS) systems commonly used to stabilize camera sensors. With the main difference being that our system also had to precisely track a desired trajectory, while actuating a higher stabilized mass. The system also needed to perform well on a moving robot without provoking any undesirable dynamic interactions between the robot and the stabilization system. The accuracy requirement of 20 μm tracking precision is also way more ambitious than for common IBIS systems.

Learning from our previous prototypes, we made sure that the mechanical design avoids non-linear friction effects as much as possible. The system was designed to stabilize one translational and one rotational DOF. The stabilized platform is mounted to the frame using five springs. Their arrangement ensures that both DOFs are decoupled and respectively act like a simple mechanical single harmonic oscillator (MSHO) with very little damping. All other DOF are mechanically blocked. The stabilized platform is actuated by two custom designed Lorentz-actuators, with position feedback being measured via two highly precise eddy-current sensors at the TCP relative to the process surface.

This setup again ensured that the control problem is collocated. We used our simulation model to verify that only very little control gain is needed to cancel out the entire dynamic contributions of the robot's structural dynamics. We further tested in simulation that this is also the case for higher stabilized loads of up to 10 kg. This indicates a good scalability of this approach, however, higher stabilized loads would also require more powerful actuators.

This simplified the control problem of the stabilization unit to two decoupled MSHO with low amount of damping. The controller of the stabilization unit is a combination of a PI controller with a positive position feedback (PPF) controller. The PPF controller is needed to introduce enough damping into the system. This approach was preferred to other control methods, because of the PPF controller's relatively low amplification of noise.

The tracking controller achieved a usable control bandwidth of 20 Hz on the real prototype. This is lower than the goal of 50 Hz, however, the desired motions relative to the process surface are usually quite simple and slow. The important property of the control system is the robustness against external disturbances transferred through the structure of the robot to the stabilized tool. The controller proved to be very robust in both the simulation and experimental results.

Mounted on a UR10 robot, the system was capable of reducing the vertical path error at the TCP from 1 mm to below 15 μm, with further analyses indicating that the real precision is in the region of 3 μm. The error spectrum was attenuated by up to -90 dB for the quasi-static error and up to -70 dB for the dynamic error. The system achieves a relatively even attenuation of the error up to 100 Hz. The stabilization unit only performed slightly worse at very high trajectory speeds of 1 m/s, while still being capable of keeping the maximum tracking error below 20 μm. The system also proved to be very robust against additional external disturbances, like hitting on the robot during operation.

These are very good results that even surpass the performance of most state of the art stabilization systems. However, it is important to keep in mind that the system heavily relies on precise sensor feedback and high controller clock rates. We also ensured to keep signal delay as low as possible by only using analog communications between the central controller and motor drivers.

Outlook

The active vibration damping approach showed some promise by being able to effectively attenuate the structural dynamics of a robot manipulator. However, it is not able to also affect other common sources of error, like sag or oscillations induced by low frequency motor-cogging. External active vibration damping for robot manipulators will therefore probably remain a promising, but niche application.

The external stabilization approach proved to be a very capable alternative to achieve a high precision tracking performance with robot manipulators.

As we have seen through the early stages of this thesis, it is still extremely difficult to further improve the precision of large industrial manipulators by relying on their own control system and motors. The reasons for this are the low achievable bandwidths of the joint

controllers, as well as the very challenging non-collocated control problem of trying to use the joint motors of a robot to precisely control the motion at the TCP in the $10\,\mu$m range. These type of controllers usually need very precise models of the entire transfer path from the motor torque to the motion at the TCP, which involves quite complex effects in the drivetrains, flexible joints and flexible links.

For this reason, I am of the firm believe that an additional stabilization device is currently one of the very few feasible approaches to achieve a path tracking precision in the $10\,\mu$m range with robot manipulators.

However, the stabilization unit developed in this thesis was just a small proof-of-concept device and still has further room of improvement. The main issue is the heavy reliance on precise position feedback at the TCP. This constraints the current stabilization unit to applications where the measurement of this feedback is actually possible. We already did some preliminary tests using acceleration feedback in combination with a Kalman filter with promising results. However, these sensor fusion approaches are still in need of further investigation.

The next issue is the scalability of the system to higher stabilized loads and the use of more DOFs. We tested in simulation that higher loads should be possible for the control concept, however, it might still be an issue to generate the needed control forces. Actuating more DOFs will also make it more difficult to mechanically decouple all stabilized DOFs. A new stabilization unit with more DOFs will therefore probably have to decouple these via its control system. All of these issues are currently being addressed in a follow-up project between the Chair of Applied Mechanics and *Boeing Research & Technology*.

Appendix A

Collocated and Non-Collocated Control with a 3 DOF Mechanical Oscillator

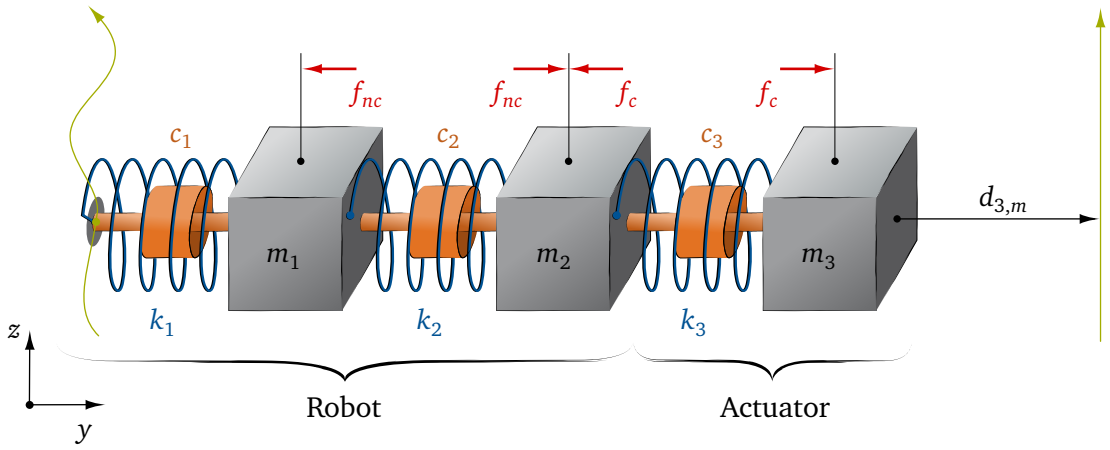

Figure A.1: The base of a 3 DOF mechanical oscillator (cf. Fig. 3.8) follows an arbitrary path in the z-y-plane. A control force f_c can be applied to the third m_3, which also causes a reaction force on the second mass m_2. Alternatively, a non-collocated control forces f_{nc} can also be applied between the first and second mass. The distance $d_{3,m}$ between the third mass and a desired path can be measured.

In this appendix, I will apply a simple collocated and non-collocated control strategy to the 3 DOF mechanical oscillator introduced in section 3.1.2. The intention is to give a bit more insight on why collocated control of dynamic structures is much more simple than non-collocated control. A good discussion about this topic can for example also be found in [219].

Control Problem

The exemplary control problem is shown in Fig. A.1. The base of the 3 DOF mechanical oscillator is now no longer fixed to the ground, but follows an arbitrary trajectory in the z-direction, while also oscillating in the y-direction. The 3 DOFs of the mechanical oscillator are still only movable in the y-direction. While the system is moving, we want to keep a desired distance $d_{3,d}$ of the third mass m_3 to a planned path, which is a measurable feedback input $d_{3,m}$.

The mass and stiffness parameters of the system (3.28) are given as:

$$\begin{aligned} m_1 &= 5\,\mathrm{kg} & k_1 &= 2 \cdot 10^4\,\mathrm{N/m} \\ m_2 &= 2\,\mathrm{kg} & k_2 &= 5 \cdot 10^3\,\mathrm{N/m} \\ m_3 &= 1\,\mathrm{kg} & k_3 &= 1 \cdot 10^3\,\mathrm{N/m} \end{aligned} \tag{A.1}$$

The damping matrix $\boldsymbol{C}$ of the system (3.28) is calculated using Rayleigh damping (3.53) with $\alpha = 0.1\,\mathrm{s}^{-1}$ and $\beta = 1 \cdot 10^{-5}\,\mathrm{s}$.

For the collocated control problem, we apply a control force f_c to the same mass m_3 from which we also measure the feedback. Since we have to generate the control force from within the system, there is also a reaction force acting on the second mass m_2. This setup is very similar to the stabilization unit discussed in section 5: The first two DOFs can be seen as a representation of the structural dynamics of the robot, while the third DOF is the actuator with the stabilized payload.

For the non-collocated control problem, we instead apply a control force f_{nc} between the first and second mass of the system. The control force therefore no longer acts on the same DOF as where we are measuring the feedback $d_{3,m}$. This setup can be similarly interpreted as the dual feedback joint position control method discussed in section 4.3: The motor torque is the non-collocated control force f_{nc} applied to the motor inertia represented by m_2. The spring k_3 and damper c_3 represent the compliance of the gear and the mass m_3 can be seen as the inertia of the robot arm. The feedback $d_{3,m}$ would then be the joint position feedback measured on the link side of the gear.

Collocated Control

The collocated controller is just a simple proportional gain:

$$f_c = g_{P,c} \cdot \left(d_{3,d} - d_{3,m}\right) \qquad \text{with} \quad f_{nc} = 0\,. \tag{A.2}$$

This can be interpreted as adding a virtual spring with stiffness $g_{P,c}$ between the third mass m_3 and the new boundary condition $d_{3,d}$ [1]. Note that the mechanical harmonic oscillator still only has three masses and therefore three DOF. However, instead of being completely fixed on the left- and the right-hand side, both boundary conditions are variable. The system therefore still only has three poles and two zeros.

Let us now analyze the performance of such a simple controller by step wise increasing the controller gain $g_{P,c}$ (and therefore the virtual stiffness). The closed-loop transfer function between the desired $d_{3,d}$ and measured distance $d_{3,m}$ is shown in Fig. A.2. Since input and output are acting on the same DOF, the resulting transfer function is a series of alternating poles and zeros (cf. Fig. 3.9c). We can see that by simply increasing the controller gain, the first and second pole of the system are pushed towards their corresponding zeros, while the third pole simply increases in frequency and loses some modal damping. This can be seen even better in the corresponding root-locus plot, Fig. A.3.

With $g_{P,c} = 1 \cdot 10^5\,\mathrm{Nm}^{-1}$ the two lower frequency pole-zero pairs almost cancel out and the third mass basically starts to behave like a single harmonic oscillator with a single spring being attached to the desired distance $d_{3,d}$ as a boundary condition. The resulting eigenfrequency approaches $\omega_{0,3} = \sqrt{g_{P,c}/m_3}$ with the closed-loop dynamics only being influenced by the controller gain and the third mass, ignoring the dynamics of the rest of the system. Further increasing the controller gain $g_{P,c}$ will only cause the third mass to more tightly follow the desired distance $d_{3,d}$ and the system to lose further modal damping, since the viscous damping of the system remains unchanged while the overall stiffness is increasing.

This can easily be interpreted as the increasing virtual stiffness $g_{P,c}$ - which attaches the third mass to the desired distance $d_{3,d}$ on the right-hand side - overpowering the spring stiffness k_3 on the left-hand side of the third mass, which consequently weakens the coupling

[1] With $d_{3,m}$ just being a different way of expressing the position x_3 of the third mass. It should also be noted that it is not exactly the same, since the force created by the virtual spring does not only act on the third mass m_3, but also on the second mass m_2 due to the reaction force created by the actuator being placed between those two masses. However, as we will see in the following, this makes no difference in terms of stability.

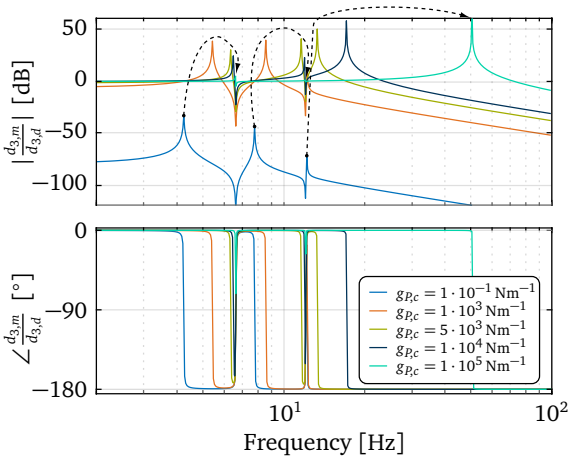

Figure A.2: Closed-loop transfer function of the collocated controller from desired distance $d_{3,d}$ to measured distance $d_{3,m}$ with different controller gains $g_{P,c}$.

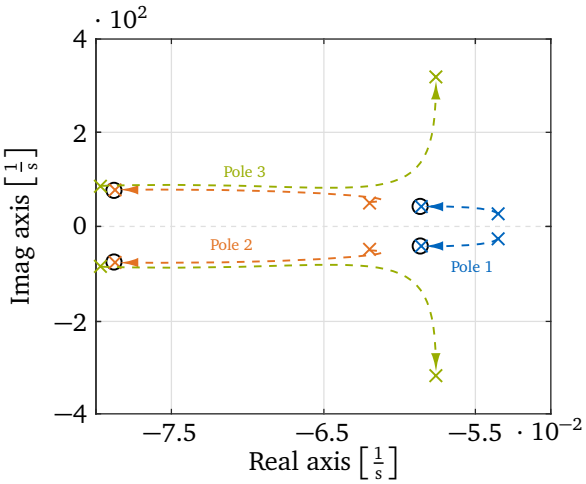

Figure A.3: Movement of the poles in a root-locus plot when increasing the gain of the collocated controller from $g_{P,c} = 1 \cdot 10^{-1}\,\mathrm{Nm}^{-1}$ to $1 \cdot 10^{5}\,\mathrm{Nm}^{-1}$.

of the third mass to the rest of the mechanical oscillator system. A lower spring stiffness k_3 would therefore cause this behavior to emerge earlier for lower virtual stiffnesses $g_{P,c}$, with the control system needing lower control gains and control forces to decouple the third mass from the rest of the system dynamics. A low stiffness of the actuator system is therefore a desirable property from a control perspective, which has some influence on the mechanical design of the stabilization unit in section 5.1.1.

In theory, we could increase the closed-loop bandwidth of the control system by just continuing to increase the controller gain $g_{P,c}$ with the system always remaining stable. Note that this can be done by designing the controller without any knowledge about the underlying system dynamics, which underlines the simplicity and strength of a collocated control setup. However, we would still need to deal with the increasing loss of modal damping by inducing additional damping via the control law. Additionally, in practice, the mechatronic system must be able to implement such a high virtual stiffness, which requires adequate controller clock-rates, low sensor noise, low system delay, high control forces and sufficiently fast actuator dynamics[2].

Non-Collocated Control

Let us now apply the same control law to the second mass of the system instead:

$$f_{nc} = g_{P,nc} \cdot \left(d_{3,d} - d_{3,m}\right) \qquad \text{with} \quad f_c = 0\,. \tag{A.3}$$

In contrast to the collocated control law (A.2), it is difficult to find a physical analogy to this non-collocated control approach. We are taking the feedback $d_{3,m}$ from the right-hand side of the third mass, however, the resulting force is acting on the second mass. This can be somewhat loosely interpreted as trying to enforce a stiffness $g_{P,nc}$ on the third mass by pushing on the second mass with the mechanical stiffness k_3 in between. Another analogy would be to try to balance an inverted pendulum with its base on your fingertip, while also trying to precisely follow a desired path with the other end of the pendulum.

Let us do the same analysis by again step wise increasing the control gain $g_{P,nc}$ while having a look at the closed-loop transfer function, Fig. A.4. Since input and output are no

[2] See the following Appendix B for a brief discussion about more practical aspects of real control systems.

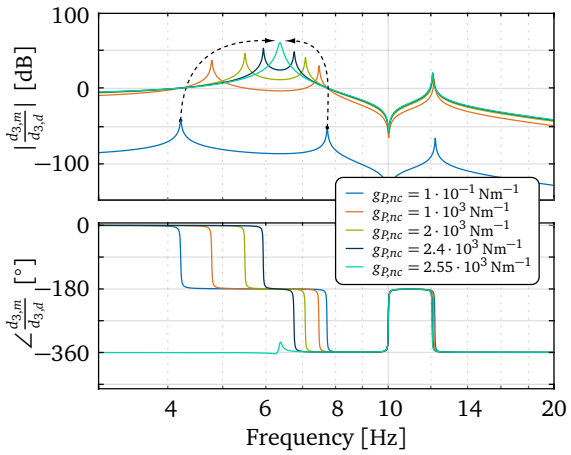

Figure A.4: Closed-loop transfer function of the non-collocated controller from desired distance $d_{3,d}$ to measured distance $d_{3,m}$ with different controller gains $g_{P,nc}$.

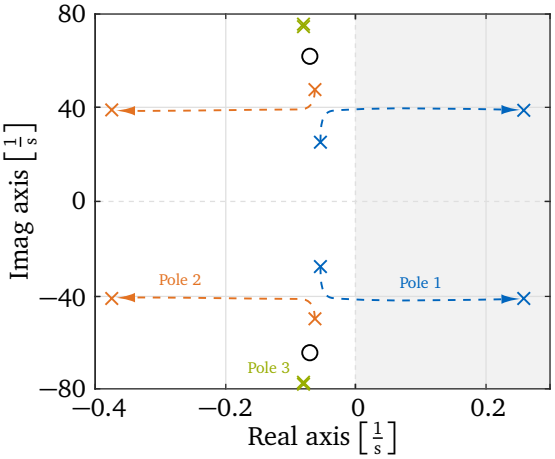

Figure A.5: Movement of the poles in a root-locus plot when increasing the gain of the non-collocated controller from $g_{P,c} = 1 \cdot 10^{-1}\,\mathrm{Nm}^{-1}$ to $2.55 \cdot 10^{3}\,\mathrm{Nm}^{-1}$.

longer collocated, we do no longer have an alternating series of zeros and poles (cf. Fig. 3.9b). Instead of pushing all poles to higher frequencies as before, already a small amount of gain causes the first and second pole to rapidly approach each other, while only the third pole slowly moves towards the only zero. At a gain of slightly above $g_{P,nc} = 2.5 \cdot 10^{3}\,\mathrm{Nm}^{-1}$, both poles approach the same frequency and the first pole becomes unstable. Further increasing the control gain $g_{P,nc}$ will cause both poles modal damping to increase rapidly, while their frequency remains the same with the system continuing to be unstable. This can again better be visualized with a root-locus plot, Fig. A.5.

As we are trying to enforce a higher stiffness between the third mass and the desired distance $d_{3,d}$ by pushing an the second mass, the system becomes unstable as soon as the mechanical compliance k_3 is no longer able to sustain the faster dynamics that we are trying to force through it. Note that we can still achieve a stable system with low closed-loop bandwidth. If we additionally induce damping via the control law to reduce the resonance peaks, we could still achieve a desirable closed-loop performance, however, with a quite slowly reacting system. This is a similar conclusion as with the dual feedback joint position control approach analyzed in section 4.3, where a low closed-loop control bandwidth could be an acceptable trade-off for higher accuracy via the joint side feedback.

For simultaneously precise and fast control performance with a non-collocated control setup, more modern control approaches are needed which take the underlying system dynamics into account for the control design. However, while this would not be very difficult for a simple academic example as shown here, this becomes increasingly harder for more complex real systems. The performance of such control methods often heavily rely on the quality of the identified system model, which is not an easy task if we want to achieve fast and precise non-collocated control of a complex mechatronic system like a robot manipulator. I go into more detail about the challenges of acquiring a high quality robot model in section 2.1.2 and 4.1. I also give a brief discussion about the limitations of modern control methods in respect to external vibration damping of robot manipulators in section 5.1.5.

Appendix B

Mechanical Single Harmonic Oscillator Test Rig

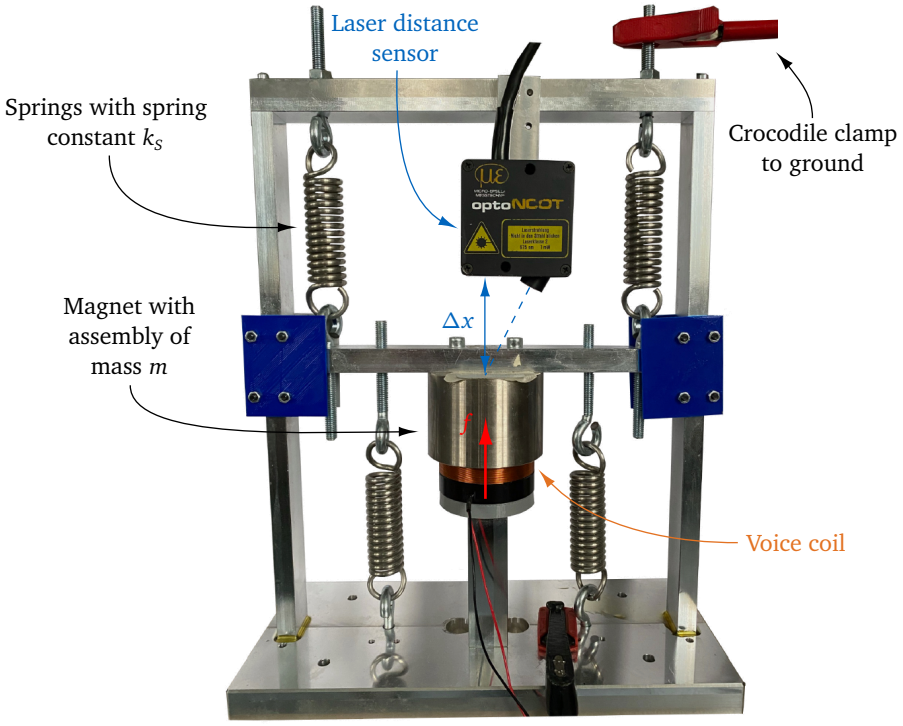

Figure B.1: Mechanical single harmonic oscillator test rig.

This appendix is based on the bachelor's thesis of my student MAICHER [181]. The goal of his thesis was to control a simple mechatronic system in order to investigate the influence of typical implementation issues like sensor noise, actuator limits and limited controller clock rates on different types of controllers.

In practice, simulations are useful to investigate control problems and test different control designs. However, rarely can these designs be directly implemented on real mechatronic systems, without significantly retuning the control parameters with often varying results. MAICHER showed in his bachelor's thesis that he could achieve the exact same performance for multiple types of controllers with the same controller gains in simulation and on the real micro controller. He admittedly only did this with a very simple system, however, his results were still very useful to me for the design of multiple prototypes and the general evaluation of control approaches. Which is why I want to summarize our results in this appendix.

The test rig is shown in Fig. B.1. The idea was to build a mechanical single harmonic oscillator, which has a very simple linear model as already described in Section 3.1.1. The test rig consists of a voice coil actuator (VCA), which can apply a force f to a cylindrical magnet

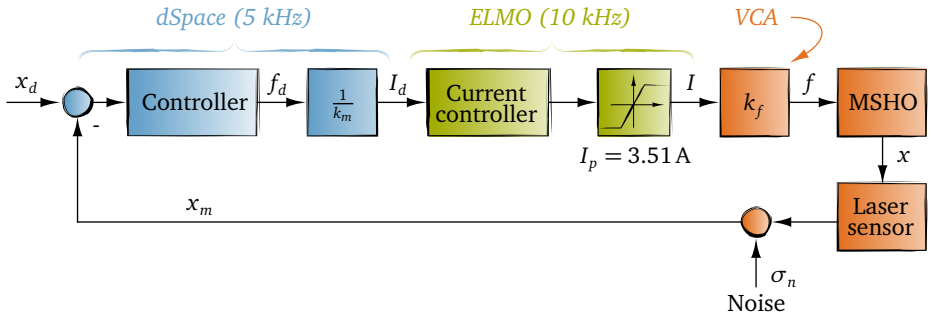

(a) Flowchart for the real system.

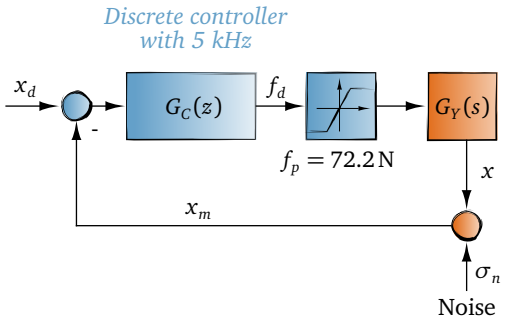

(b) Flowchart for the simulated system.

Figure B.2: Signal flow charts for the real and simulated system.

with mass $m_{\mathrm{Mag}} = 668\,\mathrm{g}$. The VCA can apply a continuous stall force of $f_c = 24.07\,\mathrm{N}$ and peak force of $f_p = 72.2\,\mathrm{N}$. The force constant is $k_f = 20.57\,\mathrm{N/A}$. The magnet is attached to the outer frame using four springs with the spring constant $k_S = 11.01\,\mathrm{N/m}$. The displacement of the mass is measured using a laser-triangulation sensor. The chassis of the test rig is connected to ground to reduce sensor noise.

The current of the VCA is controlled using an *ELMO* motor driver with a PI controller at 10 kHz. The position controller is implemented on a *dSpace* MicrolabBox at 5 kHz. The desired current for the ELMO and the measured position are sent via 10 V analog connections, Fig. B.2a.

System Model

The system was modeled using a second-order system by measuring the step response. We measured the applied current for the input, however, used the force constant k_f to model the receptance of the mechanical system:

$$G_Y(s) = \frac{1.99 \cdot 10^{-5}}{\frac{1}{218^2}s^2 + 2 \cdot 0.15 \cdot \frac{1}{218}s + 1} \frac{\mathrm{m}}{\mathrm{N}}, \tag{B.1}$$

which corresponds to a natural frequency of $\omega_0 = 218\,\mathrm{rad/s}$, damping ratio of $\zeta = 0.15$, total stiffness of $k = 75.38\,\mathrm{N/mm}$ and a mass of $m = 1.58\,\mathrm{kg}$. The stiffness and mass of the system are higher than expected. The additional inertia of the system can be explained by the additional weight of the spring assembly. It is also not clear how much the springs themselves

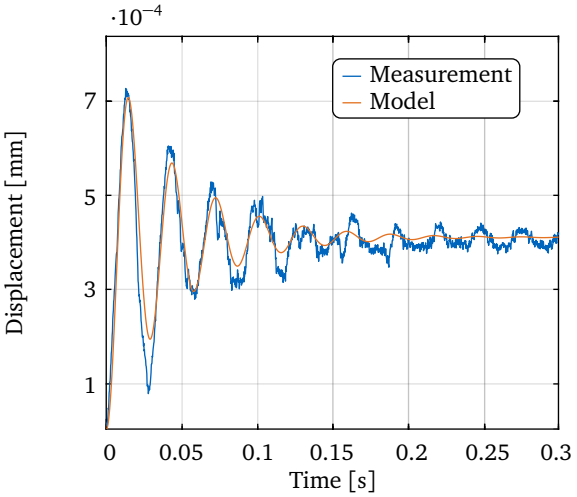

Figure B.3: Measured and modeled step response of the system. Adapted from my student's thesis [181].

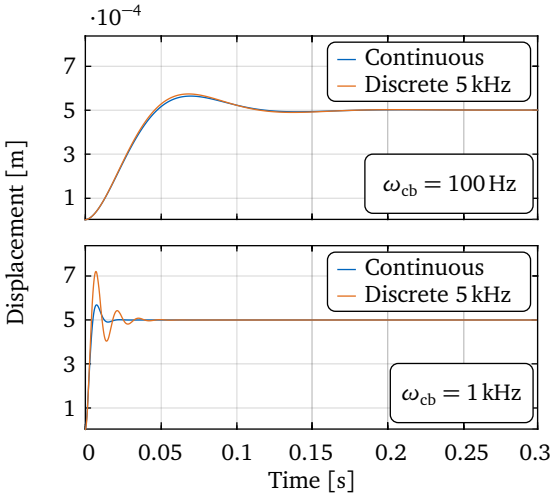

Figure B.4: Influence of the control bandwidth ω_{cb} on discrete controllers. Adapted from my student's thesis [181].

contribute to the overall inertia of the system[1].

The measured system and model response are plotted in Fig. B.3. The model matches the real system behavior quite well for larger amplitudes. For lower amplitudes, unmodeled friction effects like stick-slip start to affect the system response. This would make it quite difficult to control the system precisely with low desired amplitudes. However, the model is good enough to control large desired motions, as we will see in the following.

To simulate the system, all controllers were implemented as discrete controllers directly applying a control force to the identified system model (B.1). The reason for ignoring the actuator dynamics in this case is that we can achieve a bandwidth for the current controller of over 2 kHz, which is way beyond the achievable bandwidth of any higher-level position controller. We also found the force constant of $k_f = 20.57\,\mathrm{N/A}$ to be quite accurate. Meaning that $f \approx f_d$ for this application. In order to still consider the actuator limit, we included the corresponding peak force limit of $f_p = 72.2\,\mathrm{N}$ in our simulation, Fig. B.2b.

In the following, I will discuss a few important effects that can cause instability of the real system. We included these effects in our simple simulation model to design different types of controllers. The controllers were then implemented on the *dSpace* MicrolabBox with the exact same control parameters.

Numerical Integration and Discrete Controllers

The first effect that one should be aware of is the influence of numerical integration on simulation results. This is important for the design phase of simulation, since the numerical integration scheme itself can produce an unstable system response for a theoretically stable system. In general, the time step size of the numerical integration has to be small enough to still be able to depict the highest natural frequency of the simulated system. This critical step size varies depending on the exact integration scheme [124]. E.g. for the central difference method the simulation sampling frequency must be at least twice as high as the highest natural frequency in the system[2]. It is also generally recommended to keep the step size at

[1] This already underlines the difficulty of predicting system models just using data sheet information. Even with such a simple system we would be quite off with a system model only based on the known stiffness of the springs and weight of the sub components.

[2] In my experience, I would also recommend to always use fixed step-size methods to simulate actively controlled systems, since variable step-size integration schemes can keep unstable systems stable by inducing addi-

least ten times lower than the stability limit to ensure numerical accuracy [74].

More relevant for the practical application of controllers is the influence of discrete controllers on their closed loop stability. In order to be used on micro-controllers, control algorithms have to be implemented recursively using for example the Tustin transformation [208]. As the closed-loop control bandwidth ω_{cb} starts to approach the sampling frequency of the discrete controller ω_{cs}, the system response will start to be affected by the time-delay of the sampling process, which will cause the closed-loop system to lose damping [65]. In [179], it is recommended to use the following controller sampling frequency:

- $\omega_{cs} = 30 \cdot \omega_{cb}$ to $20 \cdot \omega_{cb}$ for an accurate approximation of a continuous controller.
- $\omega_{cs} = 5 \cdot \omega_{cb}$ to $20 \cdot \omega_{cb}$ will cause a discrete controller to visibly lose damping, however, is still mostly usable.
- $\omega_{cs} < 5 \cdot \omega_{cb}$ will cause most discrete control systems to become unstable.

In Fig. B.4, a discrete and continuous PID controller are simulated for our system. The discrete controller behaves almost the same for $\omega_{cs} = 50 \cdot \omega_{cb}$, however, significantly loses damping for $\omega_{cs} = 5 \cdot \omega_{cb}$.

Thankfully, the controller sampling frequency is less of a problem these days with even cheap micro-controllers being able to achieve quite high clock rates. However, it is still important to keep in mind that surprisingly high clock-rates are needed to get a similar performance to a continuous controller.

Actuator Dynamics and -Limit

The next limiting factor for most real mechatronic systems is the power of their actuators, which can have a large impact on the possible control bandwidth[3]. As also discussed in section 5.1.1, the dynamics and limitations of the actuators play a very important role for the achievable performance of a mechatronic system. In the case of our MSHO test rig, we did not have to consider additional dynamics, since the control plant is the actuator itself. The very fast dynamics of the current controller can be neglected as already discussed above. Meaning, we only have to consider the actuator limit of $f_p = 72.2\,\mathrm{N}$ in this case.

This was actually the most significant limiting factor for this test rig, causing almost all control methods to perform very similar with respect to the achievable settling time for a controlled step response. The actuator limit can be considered in the controller design by looking at the controller sensitivity function

$$G_{cs}(s) = \frac{f_d(s)}{x_d(s)} = \frac{G_C(s)}{1 + G_C(s)G_Y(s)}\,, \tag{B.2}$$

which can be used to check the produced control force f_d to a desired position x_d. The inclusion of actuator limits into the control design was also one of the main driving factors in the development of modern control techniques such as LQR.

Noise

Another very important factor is the amplification of sensor noise. This can again be estimated by using the controller sensitivity function $G_{cs}(s)$, since the measurement noise also

tional numerical damping due to their specific integration algorithms.

[3] E.g. moving a 1 kg mass with 1 kHz bandwidth by 1 mm needs peak forces of $\sim 1.5 \cdot 10^5$ N.

acts directly on the input of the controller. The standard deviation of the amplified noise at the controller output σ_{n,f_d} can be estimated by using the integral

$$\sigma^2_{n,f_d} = \int_{-\omega_{\mathrm{nb}}}^{\omega_{\mathrm{nb}}} |G_{\mathrm{cs}}(j\omega)|^2 \phi_n(\omega)\, \mathrm{d}\omega \,, \tag{B.3}$$

with ω_{nb} being the bandwidth of the noise and $\phi_n(\omega)$ the power spectral density function of the measurement noise. The noise amplification gain g_n can than be defined as the ratio between the standard deviation of the measurement noise and noise at the controller output [237]:

$$g_n = \frac{\sigma_{n,f_d}}{\sigma_n} \,. \tag{B.4}$$

As a rough rule of thumb, the standard deviation of the noise at the controller output σ_{n,f_d} should be kept below a third of the continuous force limit of the actuator to avoid noise peaks triggering a safety shut-down after a few seconds[4].

The bandwidth of the noise arriving at the control system will be half of the controller sampling frequency $\omega_{\mathrm{nb}} = 0.5 \cdot \omega_{\mathrm{cs}}$. As we have seen above, the controller sampling frequency ω_{cs} will usually be quite high in order to ensure a proper approximation of a continues control system. However, this also means that high frequency noise contained in the otherwise unused high bandwidth of the controller sampling system will significantly contribute to the overall standard deviation of the noise and therefore noise peaks at the controller output (B.3). It is therefore good practice to add a lowpass filter to any controller to ensure a roll-off of the controller transfer function after the desired controller bandwidth ω_{cb}, see Fig. B.5. This has the additional advantage of reducing any undesired interaction of the controller with unmodeled higher order system dynamics, which is especially a problem for modern controllers that rely on accurate system models.

The amplification of noise also has additional implications for the tuning of the PI current controller. We neglected to model the current controller because of the very high achievable control bandwidth. However, this does not mean that the current controller should be tuned to perform as fast as possible. Because of the limited actuator power, the possible closed-loop bandwidth of any position controller will be significantly lower than the possible bandwidth of the current controller. The current controller has to be fast enough to not negatively affect the overall system performance. However, tuning the controller any faster than that has no additional benefits for the system. In fact, an unnecessarily aggressive current controller will just add additional high frequency noise to system, potentially reducing the possible bandwidth of the higher-level position controller. In this case, we tuned the current controller such that the settling time of the step response was five times faster than the achievable settling time of the best position controller.

Signal Delay

Another important topic for the implementation of control systems I want to mention here is signal delay. We avoided this issue for this test rig, since all communication between the *dSpace* MicrolabBox and *ELMO* motor driver was handled using analog 10 V signals.

Analog communication has the advantage of being the fastest way to send signals, since there is very little additional processing involved. However, analog signals will be more susceptible to noise than digital communication interfaces. Digital bus communication solutions

[4]Noise peaks hitting the higher peak force limit will trigger an immediate shut-down for most motor drivers and should be avoided at all cost. If there is no such safety feature in the control system, such a high amplification of noise will usually cause instability quite quickly by high frequency noise being cut of by the physical limit of the actuator, which is usually an unconsidered non-linearity for most control systems.

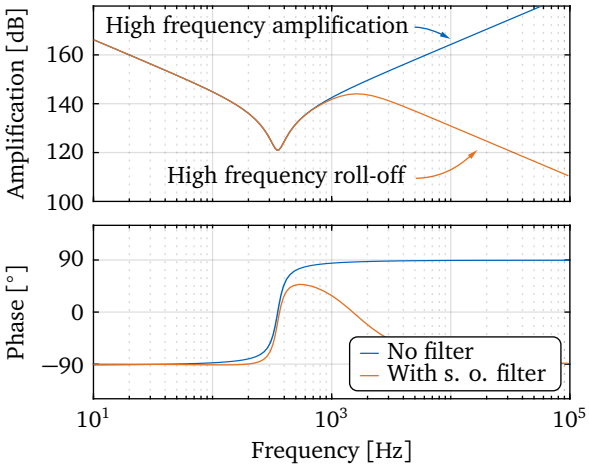

Figure B.5: Typical transfer function of a PID controller with a second order filter. Adapted from my students thesis [181].

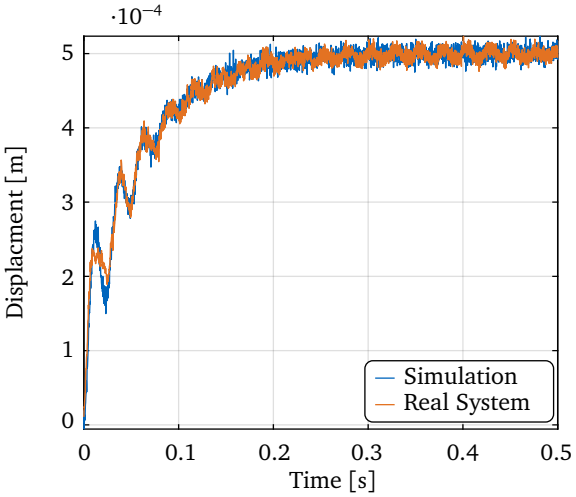

Figure B.6: Step response with a PID controller with the same parameters for simulation and the real test rig. Adapted from my students thesis [181].

have an advantage for large control systems that need to handle a lot of different signal communications between a large number of member devices, however, can also introduce significant signal delay. Similar to discrete controllers, the additional signal delay will cause the closed-loop system to lose damping and can lead to instability[5].

Example: PID Controller

In order to test whether we could achieve comparable results in the simulation as for the real test rig, MAICHERT designed multiple control approaches in simulation, while also modeling all the limiting factors discussed above. In the following, I want to quickly showcase his results for a simple PID controller as an example.

The transfer function of a PID controller is:

$$G_{\text{PID}}(s) = \left(g_p + \frac{g_D s}{T_D s + 1} + \frac{g_I}{s} \right) \cdot (x_d(s) - x_m(s)) \ , \tag{B.5}$$

with g_P, g_D, g_I being the gains of the PID controller respectively and T_D the time constant for a first order filter needed to implement the D-part on a real system. The controller gains are tuned in simulation using the Ziegler-Nichols method [310], which yields the controller gains:

$$\begin{aligned} g_P &= 14280 \ \text{N/m} \\ g_D &= 42.84 \ \text{Ns/m} \qquad \text{with} \quad T_D = 2.5 \cdot 10^{-4} \ \text{s} \\ g_I &= 1.09 \cdot 10^6 \ \text{N/ms} \end{aligned}$$

The exact same gains are applied to the simulated and real system. The results are shown in Fig. B.6. As we can see, both the test rig and simulated system behave exactly the same.

[5] It depends on the application if one should use analog signals or digital buses to communicate between devices. In my experience, CAN bus is basically unusable for high-performance control systems that need a lot of control bandwidth. On the other hand, more modern bus systems like EtherCAT can work quite a lot better, which is used for our harvesting robot CROPS and humanoid robot LOLA. However, we still needed to implement a delay compensation to improve the tracking performance of LOLA's joint controllers [268]. Since we needed to achieve a very high control bandwidth with the prototypes shown in this work, I decided to use analog communication signals as much as possible to reduce any kind of additional delay.

Conclusions

MAICHNER also tested PI-, I-PD, model based feedforward-, internal model-, positive position feedback- and posicast-controller. The simulation was always capable to give a very good prediction of the real behavior of the system for all feedback based controllers. However, for the model-based controllers the simulation results where less accurate. This is probably because the identified model used for the controller design does not perfectly match the real system, as seen in Fig. B.3. The simulation was also very usable to predict stability limits due to the amplification of noise or sensor delay.

These results underline how important it is to also consider sensor noise, signal delay and actuator dynamics / -limits in a simulation model to make proper predictions about the possible performance of the control system.

Appendix C

First Version of the Stabilization Unit

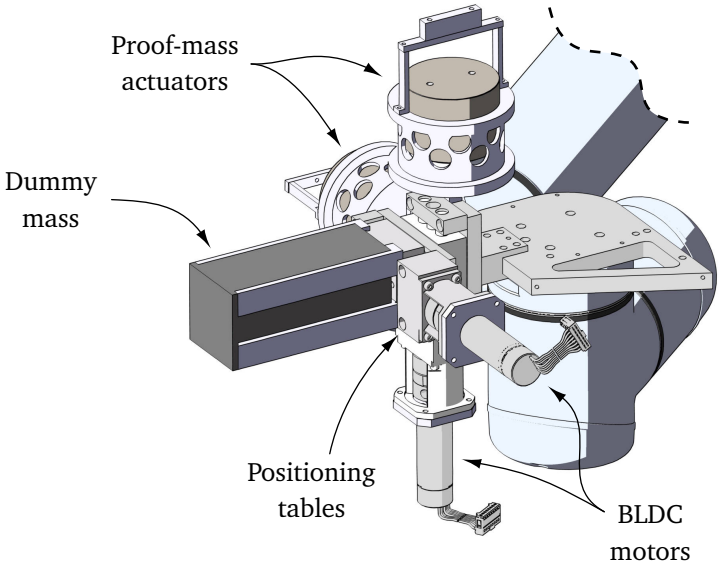

Figure C.1: First prototype of the stabilization unit. Two proof-mass actuators for the attenuation of high frequency vibrations. Two BLDC motors drive two positioning tables via spindles to compensate the quasi-static error.

The first version of the stabilization unit was part of a short project with *Boeing Research & Technology* in 2017 which was supposed to develop a working proof-of-concept prototype in a short period of time. The general idea of the prototype was to attenuate the dynamic error of the robot via active vibration damping methods using proof-mass actuators, Fig. C.1 (1). The quasi-static error was then supposed to be compensated with BLDC motor driven positioning tables, Fig. C.1 (2) and (3).

The main issue of this setup was that the dynamic error of the UR10 is still dominated by lower frequency vibrations caused by the transfer of torque-ripple. As we have seen in section 4.1.1, these excitation frequencies are mostly below the first structural eigenfrequency of the UR10 robot. This means that active vibration damping techniques which attenuate the structural dynamics of the robot are mostly ineffective in reducing these lower frequency vibrations. Additionally, the positioning system was also not designed to compensate errors above 1 Hz, since one of the main assumptions was that the dynamic error is purely caused by the excitation of the robots structural dynamics.

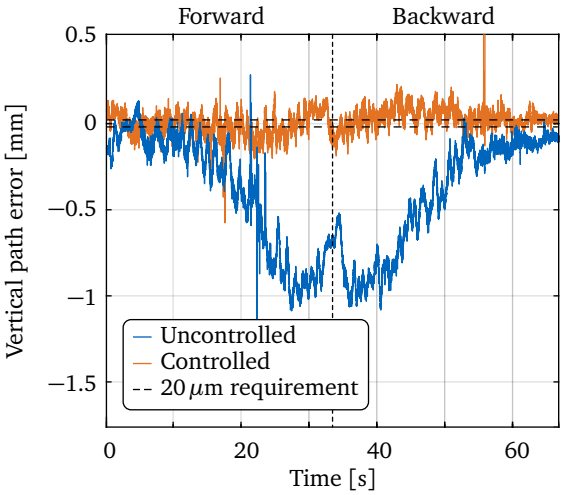

Figure C.2: Measured vertical path error during a horizontal trajectory using the UR10 robot with the first prototype of the stabilization unit.

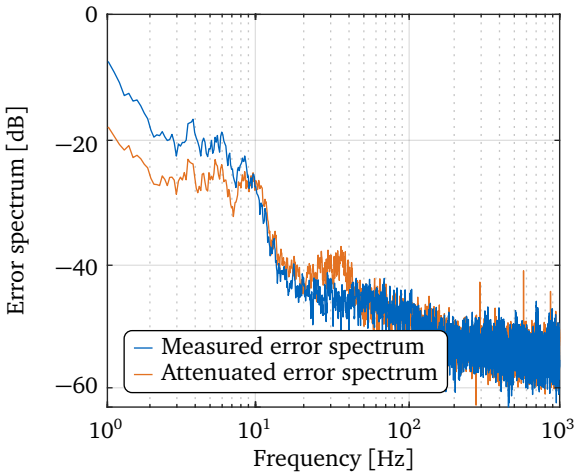

Figure C.3: Spectrum of the measured vertical path error at the UR10 robot. The reference value is 1 mm.

System Performance

With the proof-mass actuators mostly being ineffective in this specific case, we still tried to use the positioning system to compensate as much of the error as possible.

The control setup was similar to the one for the second version of the stabilization unit (see section 5.2): A laser sensor was used to measure position feedback from the process surface. A simple PI controller was then employed on a *dSpace* MicroLab Box to keep the vertical path error at zero. The desired position for the motors was then send via CAN-Bus to *ELMO* motor drivers to move the motors. The motors then moved two positioning tables via spindles to move the process tool.

Fig. C.2 shows the measured vertical path error with the stabilization unit mounted on a UR10 robot performing a horizontal trajectory. The tool is stabilized just using the PI controlled BLDC motors, with the proof-mass actuators turned off. The system is able to compensate the quasi-static error quite well, reducing the RMSE from 0.53 mm to 61.6 μm. The spectrum of the measured vertical path error is shown in Fig. C.3. The system is able to reduce the dynamic error below 10 Hz by −5 to −10 dB.

Conclusions

This is still a quite respectable results for a first prototype that only uses the positing system, which was not designed initially for highly dynamic motions. The key take-away points from this first prototype were:

- Specifically for the UR10 robot, the proof-mass actuators can only provide very little benefit via active vibration damping methods, since the main source of error is the direct transfer of low frequency torque-ripple through the robot's kinematic chain to the TCP.
- A position based stabilization system can reduce the quasi-static and dynamic error. However, the actuator system needed to be improved for better performance.
- The first bottleneck of the system was the quite unreliable and slow CAN-bus communication between the higher-level *dSpace* MicroLab Box and the lower-level *ELMO* motor

drivers. We addressed this for the second version of the stabilization unit by only using direct analog communication between devices.

- The spindles of the used positioning tables claim a positioning tolerance of 5 μm. However, this is only true when moving the spindle in one direction. The mechanical system still experiences a significant amount of backlash when changing directions, which had a quite significant impact on the dynamic performance of the positioning system. We therefore made it a top priority for the second stabilization unit to reduce friction, backlash and other deteriorating effects of the new mechanical system as much as possible.
- The noise levels of the used laser sensors where quite high and were also quite sensitive to EMI. We therefore used more precise eddy-current sensors for the new version of the stabilization unit.

Appendix D

Student List

In this appendix, I will give a list of all students I had the pleasure to work with during my time at the Chair of Applied Mechanics. I am happy to say that I did not have a single noteworthy bad experience with any of them and was very fortunate to supervise some truly outstanding students. The following list is in somewhat chronological order and will list their contributions to either this thesis or other projects I had the pleasure to work with them on:

- AHMED EL MAHMOUDI was hired as a student assistant for the first R&D project with *Boeing Research & Technology* in 2017 and helped a lot during the first conceptual design phase, as well as CAD design, testing and reporting of the first version of the stabilization unit. He later was also hired as a Ph.D. student and research assistant at the Chair of Applied Mechanics and became my office mate for the rest of my time at the chair. I am truly thankful for the time that we spend together and could not have wished for a better office partner.
- MIRZA BEGH was also hired in 2017 as a student assistant for the same project with *Boeing Research & Technology*. He helped implementing the controller for the first version of the stabilization unit on the *dSpace* Microlab Box, as well as tuning of the *ELMO* motor drivers, and performed many tests on the final prototype. He later moved on to start his Ph.D. in electrical engineering in Finland.
- MAHMUT FEVZI DOGAN was the third student assistant hired for the first version of the stabilization unit in 2017 and mainly helped with the CAD design of the first prototype.
- JULIEN KAMMERER was hired in 2017 to help with performing harvesting field tests in a green house with our harvesting robot CROPS. The project was in cooperation with the Gewächshauslaborzentrum Dürnast of the TUM School of Life Sciences. Afterwards, he developed a new gripper prototype for the harvest of sweet peppers in his semester thesis [143]. The new gripper was also tested in the field in a second project with the Gewächshauslaborzentrum Dürnast. The data gathered in both projects are part of our paper [123].
- LEONARDO VON LERCHENFELD was also hired in 2017 as a student assistant to help with the CROPS field tests.
- YILON SUN was briefly hired as a student assistant in 2017 to help with the programming of the PyFBS toolbox. He then moved on to start his Ph.D. at the Chair of Micro Technology and Medical Device Technology.
- JAN NALIVAIKA was hired in 2017 as a long term student assistant helping with multiple of my and other colleagues' projects.
- FRANCESCO TRAINOTTI did his semester thesis about the development of a proper FRF acquisition procedure for experimental dynamic substructuring under my supervision

in 2017 [273]. Although his thesis was about an unrelated topic for my later research topic, his results were still very useful to get experimental measurement experience in general. He later became a valuable long term student assistant for the Chair of Applied Mechanics and also started his Ph.D. in 2020 at our chair.

- SEBASTIAN FUDERER did his bachelor's thesis about the modal analysis of a robot manipulator in 2018 [100]. The data gathered during his thesis was used as a basis of our paper [46], which he co-authored. He later also helped with the measurements for the first modal analysis of our biped walking robot LOLA [52].

- LORENZ BAYERLEIN did his bachelor's thesis about an active vibration damping test rig in 2018 [38]. His thesis was helpful to get a first feeling about the typical implementation issues for active vibration damping techniques.

- STEFAN QIU did his bachelor's thesis in 2018 about a first version of the proof-mass actuator [220] shown in section 5.1.1. While the prototype of the final proof-mass actuator is quite different from the initial tests performed by QIU in his bachelor's thesis, his results were still very useful to test some early ideas for the actuator system.

- MARVIN OCHSENIUS was hired as a student assistant in 2018 to help in the first stages of the development of the Simulink robot model shown in section 4.1. He was also a co-author for our papers [48] and [47].

- CHENHONG HUANG did her semester thesis about the influence of structural dynamics on a position controlled robot joint test rig in 2018 [129]. Her measurement results were partially used for our paper [47] and section 4.3.1 in this thesis.

- STEFANIE ZIMMERMANN did her master's thesis about the dynamic modeling of robot manipulators for accuracy evaluation in 2018 [312]. Her thesis was in cooperation with ABB and used modeling techniques for flexible links in Dymola that we also later incorporated in our Simulink model (see section 4.1). She later also main-authored our paper [313] based on her master's thesis. She then moved on to work for ABB Robotics for two years and recently started to do her Ph.D. in Sweden.

- ELIAS SANIEWSKI did his semester thesis about developing a flexible multi body simulation in Simulink in 2019 [231]. This semester thesis was in a bit of an awkward spot, since Matlab did not yet had the new 'reduced order model' block for Simulink released and just provided a paper about a possible implementation of reduced order flexible bodies [191]. The method provided in this paper, however, did not produce very accurate results for higher order dynamics. The semester thesis of SANIEWSKI was still quite useful, since we learned a lot about the application of multi body systems in Simulink.

- RAPHAELA ALLGAYER was hired in 2019 as a student assistant to help me with the translation of the 'Experimental Vibration Analysis' course's script from German to English. She helped a lot by translating and transferring the old CoralDraw based figures to Inkscape.

- MARIE HARDER did her master's thesis about the simulation of external vibration damping approaches for flexible robot manipulators in 2019 [125]. HARDER showed in her thesis that modern control methods like pole placement, LQR or H_∞ control struggle quite a bit to produce good results compared to classical vibration damping methods under the assumption that there is not perfect model knowledge available. I discuss her results briefly in section 5.1.5.

- TOM PRAUTZSCH did his semester thesis about the simulation of torque controlled robots in Simulink in 2019 [216]. He then continued his work in 2020 with his master's thesis [217], which also looked into the influence flexible links on the structural dynamics of torque controlled robots. The results of his master's thesis are partially published in our paper [218], which he main-authored. Section 4.3.2 is also partially based on this paper. PRAUTZSCH was also of great help by cleaning up our flexible robot simulation model in Simulink.

- TOMAS SLIMAK was initially hired as a student assistant in 2019 to work on CAN-bus communication with dSpace. He later helped me to develop the second version of the stabilization unit for our second industry project with *Boeing Research & Technology Europe*. Afterwards, he was of great help during the follow up project about sensor fusion. He also did a semester thesis about using different sensor setups for the control of the stabilization unit [253] and is a co-author of our paper [51]. He now started his Ph.D. at the Chair of Applied Mechanics and develops a third version of the stabilization unit in cooperation with *Boeing Research & Technology Europe*.

- JENS BODEIT expended on HARDERS master's thesis by also looking into the feasibility of advanced control methods like MPC, sliding mode, or receptance based eigenstructure assignment for active vibration damping of robot manipulators in his semester thesis in 2020 [54]. Unfortunately, these methods also showed unsatisfactory results compared to classical control methods. I also briefly discuss his results in section 5.1.5.

- TAREK SENJAB was hired as a long term student assistant in 2020 and supported me for various industry projects like a beneficiary projects sponsored by BOEING.

- LUKAS MAICHER did his bachelor's thesis about the control of a single harmonic oscillator test rig in 2020 [181]. His results were very useful to expand our general knowledge about the implementation of control systems and I summarize his results in Appendix B. He now started to work as a student assistant for the new project with *Boeing Research & Technology Europe* under the supervision of TOMAS SLIMAK.

- NIKLAS HAIN started his semester thesis about the comparison of game engines for flexible multi body simulations in cooperation with *Boeing Research & Technology Europe* in 2021. The supervision of the thesis is now carried over by TOMAS SLIMAK.

Appendix E

Author Publication List

Related Publications as the Main-Author

[46] Berninger, T. F. C., Fuderer, S., and Rixen, D. J. "Modal Analysis of a 7 DoF Sweet Pepper Harvesting Robot". In: *Topics in Modal Analysis & Testing, Volume 8*. Springer International Publishing, May 2019. DOI: 10.1007/978-3-030-12684-1_16.

[47] Berninger, T. F. C., Huang, C., Ochsenius, M. A., and Rixen, D. J. "The Influence of Structural Dynamics on Cascaded Joint Position Control of a Flexible Beam with a Compliant Gear". In: *2019 19th International Conference on Control, Automation and Systems (ICCAS)*. IEEE, 2019. DOI: 10.23919/iccas47443.2019.8971640.

[48] Berninger, T. F. C., Ochsenius, M. A., and Rixen, D. J. "Evaluation of an External Vibration Damping Approach for Robot Manipulators Using a Flexible Multi Body Simulation". In: *2019 IEEE/ASME International Conference on Advanced Intelligent Mechatronics (AIM)*. IEEE, 2019. DOI: 10.1109/aim.2019.8868406.

[49] Berninger, T. F. C. and Rixen, D. J. "External Vibration Damping of a Robot Manipulator's TCP Using Acceleration Feedback". In: *PAMM* 19.1 (Nov. 2019). DOI: 10.1002/pamm.201900344.

[50] Berninger, T. F. C., Seiwald, P., Sygulla, F., and Rixen, D. J. "Evaluating the Mechanical Redesign of a Biped Walking Robot Using Experimental Modal Analysis". In: *Topics in Modal Analysis & Testing, Volume 8*. Ed. by Dilworth, B. J. and Mains, M. Cham: Springer International Publishing, 2022, pp. 45–52. DOI: 10.1007/978-3-030-75996-4_6.

[51] Berninger, T. F. C., Slimak, T., Weber, T., and Rixen, D. J. "An External Stabilization Unit for High-Precision Applications of Robot Manipulators". In: *2020 IEEE/RSJ International Conference on Intelligent Robots and Systems (IROS)*. 2020, pp. 4276–4282. DOI: 10.1109/IROS45743.2020.9341454.

[52] Berninger, T. F. C., Sygulla, F., Fuderer, S., and Rixen, D. J. "Experimental Analysis of Structural Vibration Problems of a Biped Walking Robot". In: *2020 IEEE International Conference on Robotics and Automation (ICRA)*. 2020, pp. 8726–8731. DOI: 10.1109/ICRA40945.2020.9197282.

Related Publications as a Co-Author

[218] Prautzsch, T., Berninger, T. F. C., and Rixen, D. J. "Investigation of Torque Controlled Robots with Flexible Links Using a Flexible Multibody Simulation". In: *2021 IEEE/ASME International Conference on Advanced Intelligent Mechatronics (AIM)*. 2021, pp. 638–644. DOI: 10.1109/AIM46487.2021.9517633.

[240] Seiwald, P., Wu, S.-C., Sygulla, F., Berninger, T. F. C., Staufenberg, N.-S., Sattler, M. F., Neuburger, N., Rixen, D., and Tombari, F. "LOLA v1.1 – An Upgrade in Hardware and Software Design for Dynamic Multi-Contact Locomotion". In: *2020 IEEE-RAS 20th International Conference on Humanoid Robots (Humanoids)*. 2021, pp. 9–16. DOI: 10.1109/HUMANOIDS47582.2021.9555790.

[268] Sygulla, F., Wittmann, R., Seiwald, P., Berninger, T., Hildebrandt, A.-C., Wahrmann, D., and Rixen, D. "An EtherCAT-Based Real-Time Control System Architecture for Humanoid Robots". In: *2018 IEEE 14th International Conference on Automation Science and Engineering (CASE)*. IEEE, Aug. 2018. DOI: 10.1109/coase.2018.8560532.

[313] Zimmermann, S. A., Berninger, T. F. C., Derkx, J., and Rixen, D. J. "Dynamic modeling of robotic manipulators for accuracy evaluation". In: *2020 IEEE International Conference on Robotics and Automation (ICRA)*. 2020, pp. 8144–8150. DOI: 10.1109/ICRA40945.2020.9197304.

Unrelated Publications

[112] Gille, M., Berninger, T. F. C., and Rixen, D. J. "Comparison of different Excitation Strategies in Operational Modal Analysis (OMA)". In: *PAMM* 19.1 (2019). DOI: 10.1002/pamm.201900392.

[123] Habegger, R., Bergamo, E., Schwab, W., Berninger, T. F. C., and Rixen, D. "Impact of intensive modification of sweet pepper plants on performance of end effectors for autonomous harvesting". In: *European Journal of Horticultural Science* 86.4 (Aug. 2021), pp. 354–359. DOI: 10.17660/ejhs.2021/86.4.2.

[156] Krinner, A., Tsunoda, W., Wagner, C., Berninger, T., Thümmel, T., and Rixen, D. "Simulation and Experimental Validation of a Misaligned Rotor in Journal Bearings using Different Levels of Detail". In: *Technische Mechanik* 37.2-5 (2017), pp. 450–459. ISSN: 0232-3869. DOI: 10.24352/UB.OVGU-2017-121.

[157] Krinner, A., Tsunoda, W., Wagner, C., Berninger, T., Thümmel, T., and Rixen, D. "Simulation and experimental validation of a misaligned rotor in journal bearings using different levels of detail". In: *12. Internationale Tagung Schwingungen in Rotierenden Maschinen (SIRM)*. Ed. by Ecker, H., Irretier, H., Liebichand, R., Markert, R., Nordmann, R., and Strackeljan, J. 2017.

[274] Trainotti, F., Berninger, T. F. C., and Rixen, D. J. "Using Laser Vibrometry for Precise FRF Measurements in Experimental Substructuring". In: *Conference Proceedings of the Society for Experimental Mechanics Series*. Springer International Publishing, June 2019. DOI: 10.1007/978-3-030-12184-6_1.

[275] Tsunoda, W., Wagner, C., Berninger, T., Thümmel, T., and Rixen, D. "Measurement Method of Damping Ratio as Stability Diagnosis for Rotor-Seal System with Fluidic Random Excitation". In: *The 5th International Education Forum on Environment and Energy Science*. 2016.

[285] Wagner, C., Berninger, T., Thümmel, T., and Rixen, D. "Rotordynamic effects in turbopumps for space propulsion systems - systems first minimal models and experimental validation". In: *Space Propulsion 2016 Conference*. 2016.

[286] Wagner, C., Tsunoda, W., Berninger, T., Thümmel, T., and Rixen, D. "Instability Prediction and Rotordynamic with Seals: Simulations Based on the Bulk-Flow Theory and Experimental Measurements". In: *Proceedings of the XVII International Symposium on Dynamic Problems of Mechanics*. ABCM, 2017.

[287] Wagner, C., Tsunoda, W., Berninger, T., Thümmel, T., and Rixen, D. “Simulative und experimentelle Vorhersage der Instabilität in Rotorsystemen mit Dichtungen”. In: *12. Internationale Tagung Schwingungen in Rotierenden Maschinen (SIRM)*. Ed. by Ecker, H., Irretier, H., Liebichand, R., Markert, R., Nordmann, R., and Strackeljan, J. 2017.

[288] Wagner, C., Tsunoda, W., Berninger, T., Thümmel, T., and Rixen, D. “Estimation of Rotordynamic Seal Coefficients Using Active Magnetic Bearing Excitation and Force Measurement”. In: *Lecture Notes in Mechanical Engineering*. Springer International Publishing, 2018. DOI: 10.1007/978-3-319-91217-2_1.

[289] Wagner, C., Tsunoda, W., Matsushita, O., Berninger, T., Thümmel, T., and Rixen, D. “Prediction of Instability in Rotor-Seal Systems using Forward Whirl Magnetic Bearing Excitation”. In: *Technische Mechanik* 37.2-5 (2017), pp. 358–366. ISSN: 0232-3869. DOI: 10.24352/UB.OVGU-2017-111.

Appendix F

Simulink Flexible Robot Simulation Library

This appendix presents the Simulink libraries and models that were developed by my students and I during my time at the chair. Most notably did PRAUTZSCH extend the library to also include torque control schemes in his semester- [216] and master's thesis [217]. He also already did a very good job of cleaning up and documenting the library. This appendix is therefore just copied from the appendix of his master's thesis [217].

The reader is referred to the figure captions for more information on the corresponding block, model or library. Only a selection of the implemented models and custom blocks are presented. The figures below, however, should provide a sufficient overview. The MATLAB & Simulink release used for this thesis is R2020a.

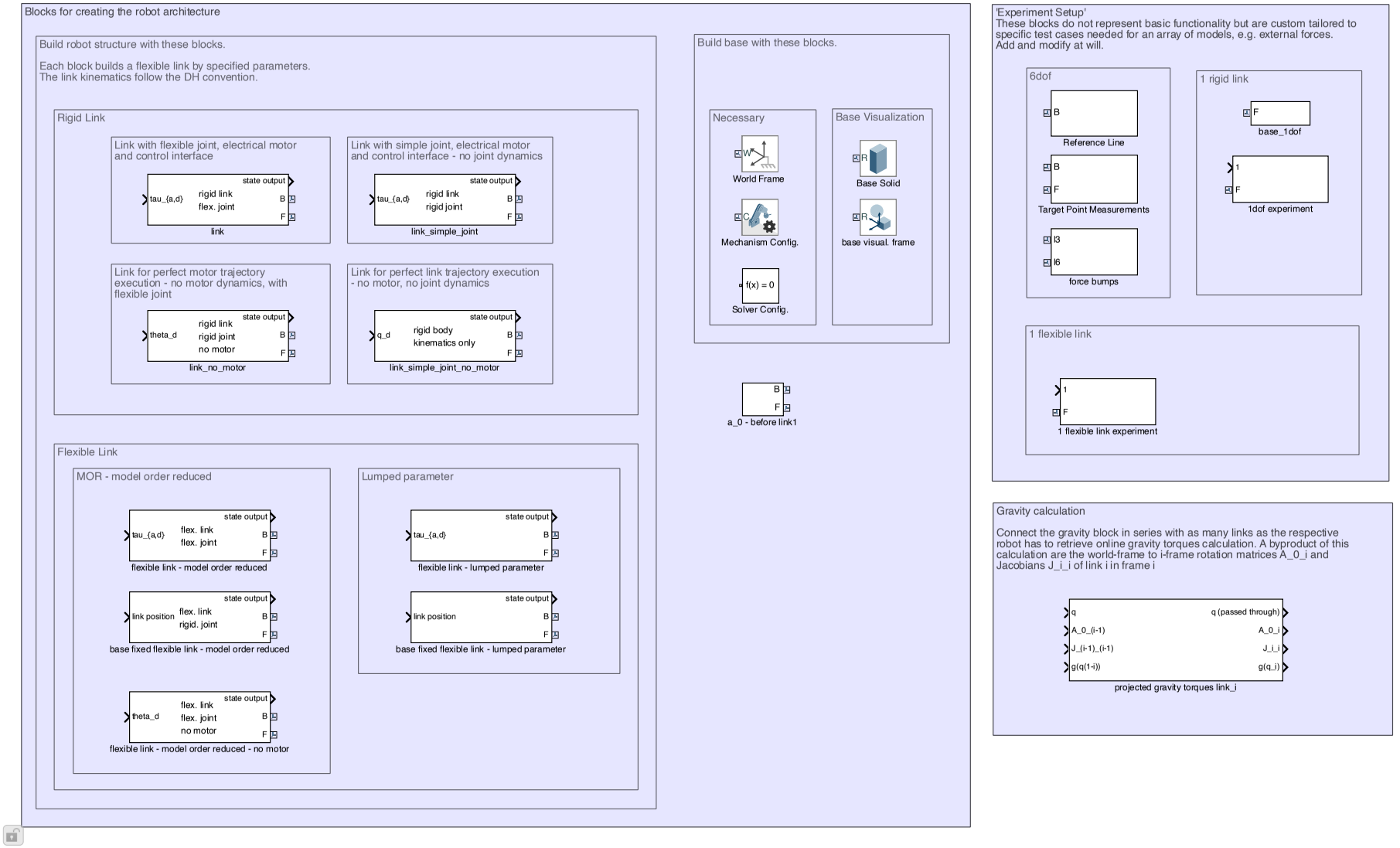

Figure F.1: Custom Simulink library containing all blocks for building a Simulink robot model and functions needed for online calculation of gravity and Jacobian terms. Additionally, an area is reserved for blocks needed for common simulation test cases ('Experiments') [217].

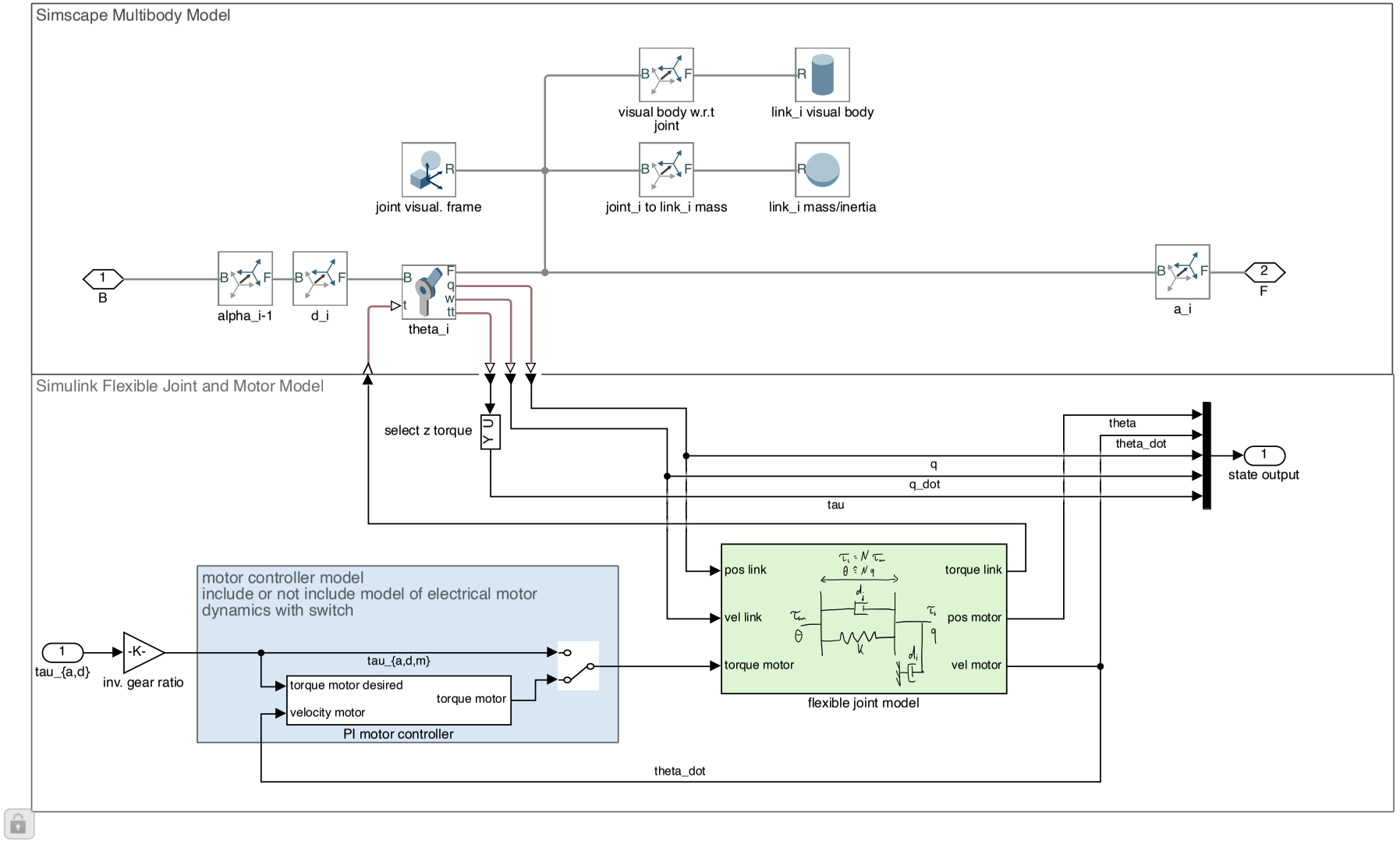

Figure F.2: Robot library block: **link**. Rotatory flexible-joint rigid-body link is connected to frame B according to the DH parameters as defined in the robot parameters. F is the frame for succeeding structures, e.g. links [217].

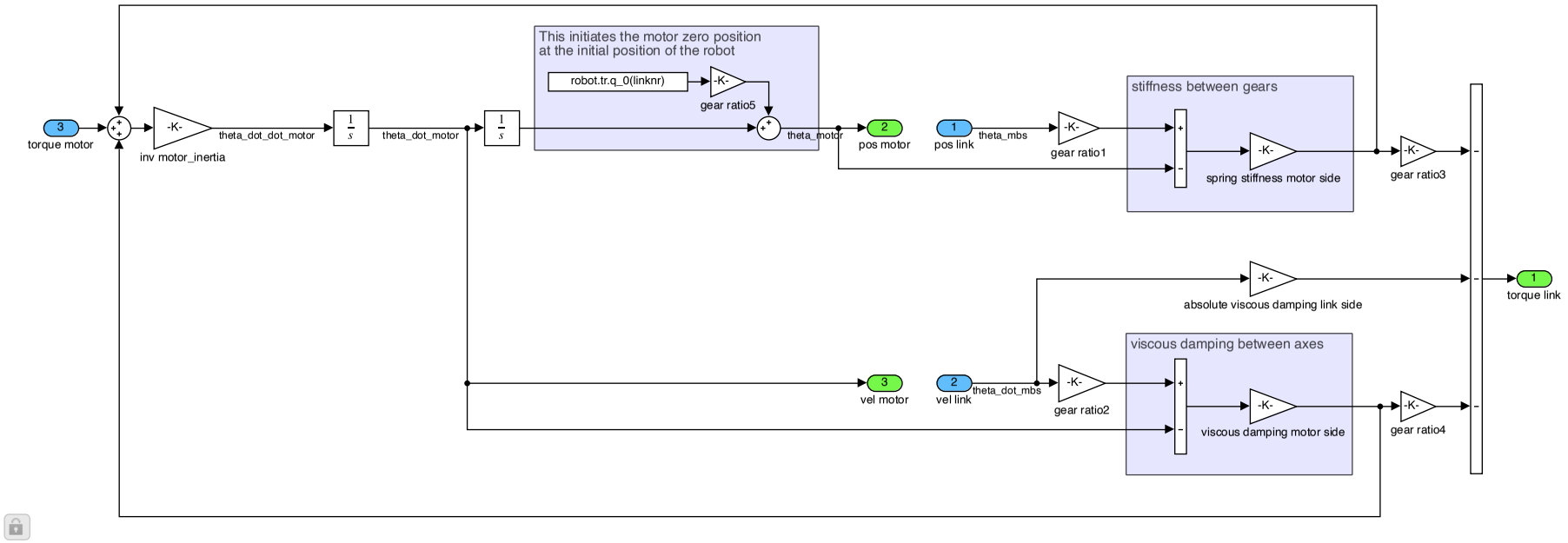

Figure F.3: Robot library block: **flexible link - model order reduced**. Rotatory flexible-joint flexible-body link is connected to frame B according to the DH parameters as defined in the robot parameters. F is the frame for succeeding structures, e.g. links. The flexible body dynamics is performed with a reduced order model [217].

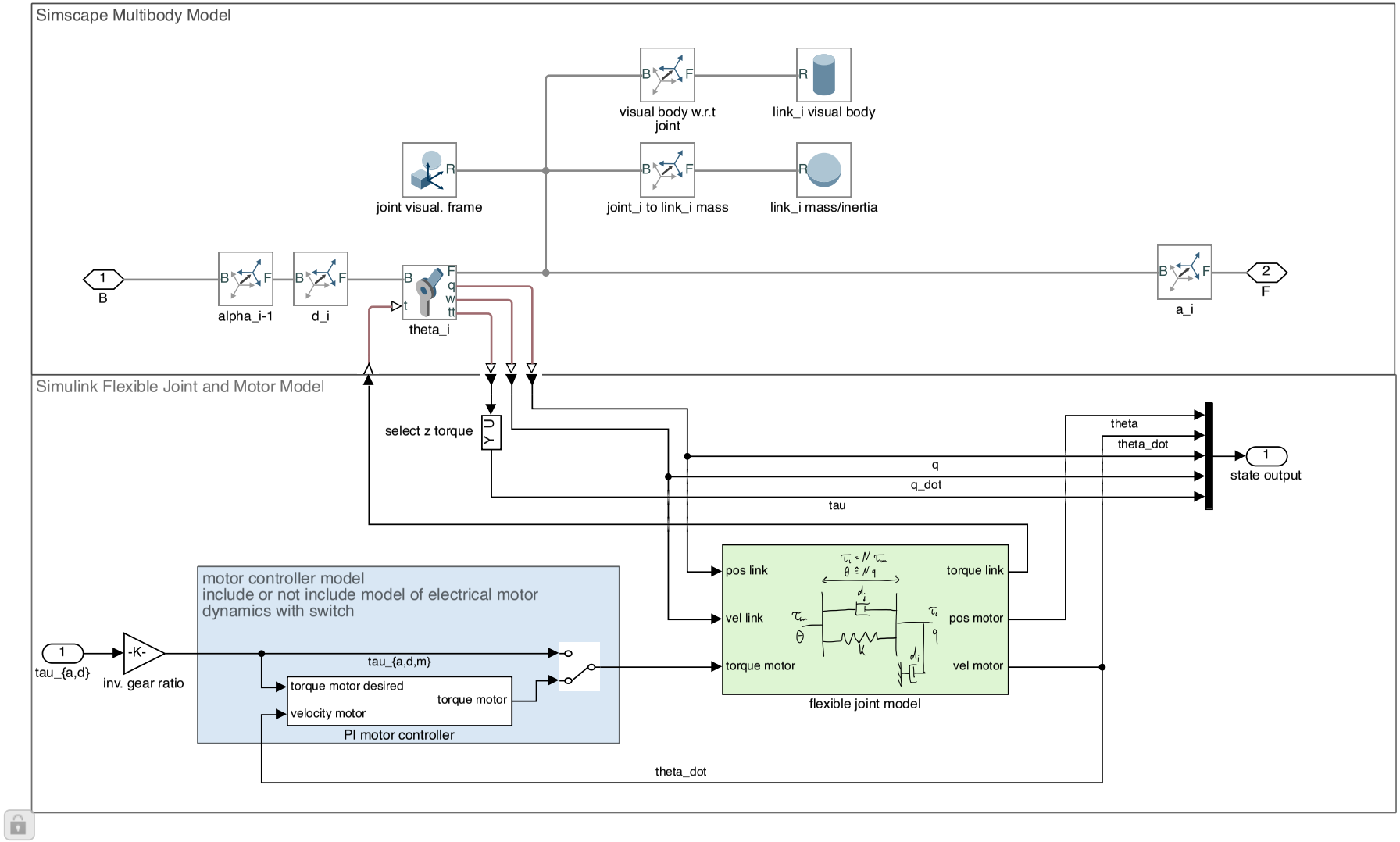

Figure F.4: Robot library subblock of any link block containing a motor model and **flexible joint model** [217].

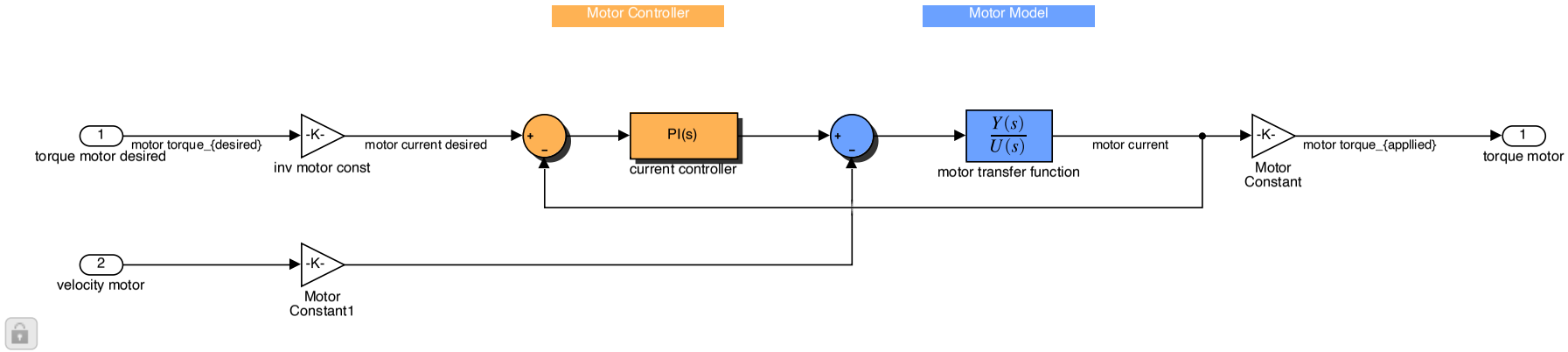

Figure F.5: Robot library subblock of any link block containing a motor model with a **PI motor controller** [217].

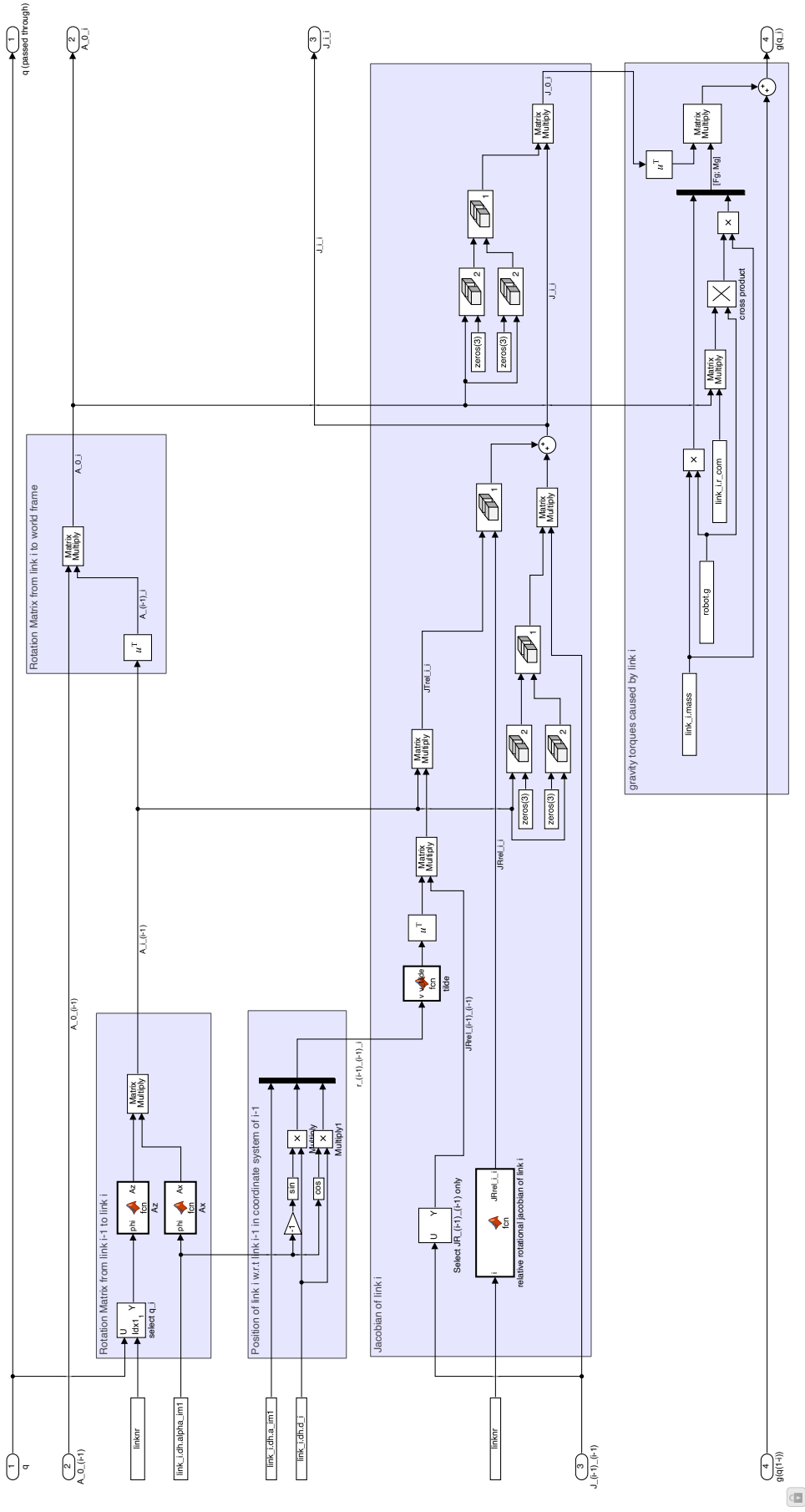

Figure F.6: Robot library block **gravity link i**. Online computation of rotation matrix and Jacobian with respect to the world frame in dependence on the current configuration and the preceding frame. The gravity forces and moments of the link are projected onto the robots degrees of freedom and added to the gravitational torques of preceding links. This computation assumes rigid link bodies [217].

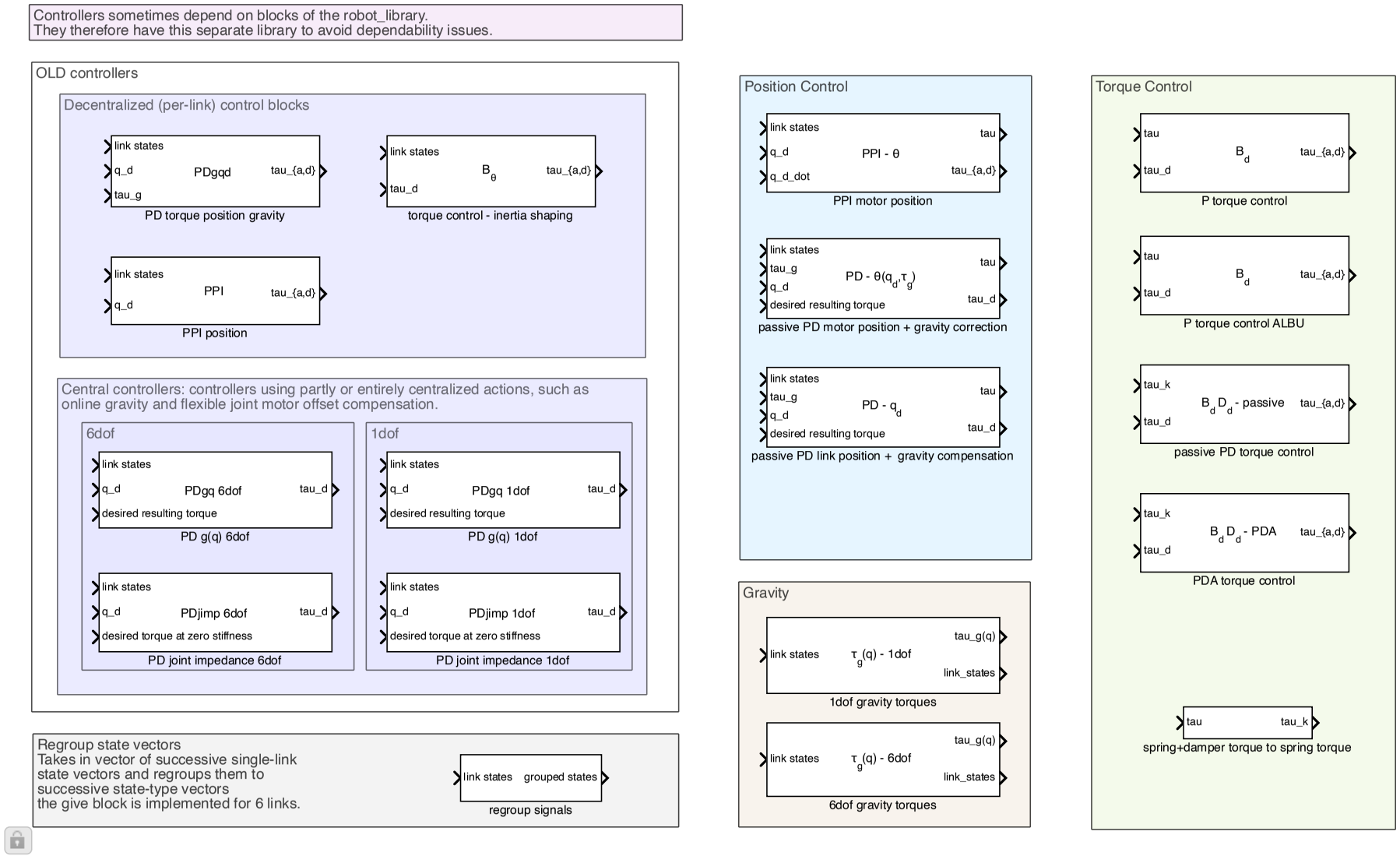

Figure F.7: Custom Simulink library containing all blocks for a selection of control strategies. This library was created in the preceding project (see “OLD controllers”) [217].

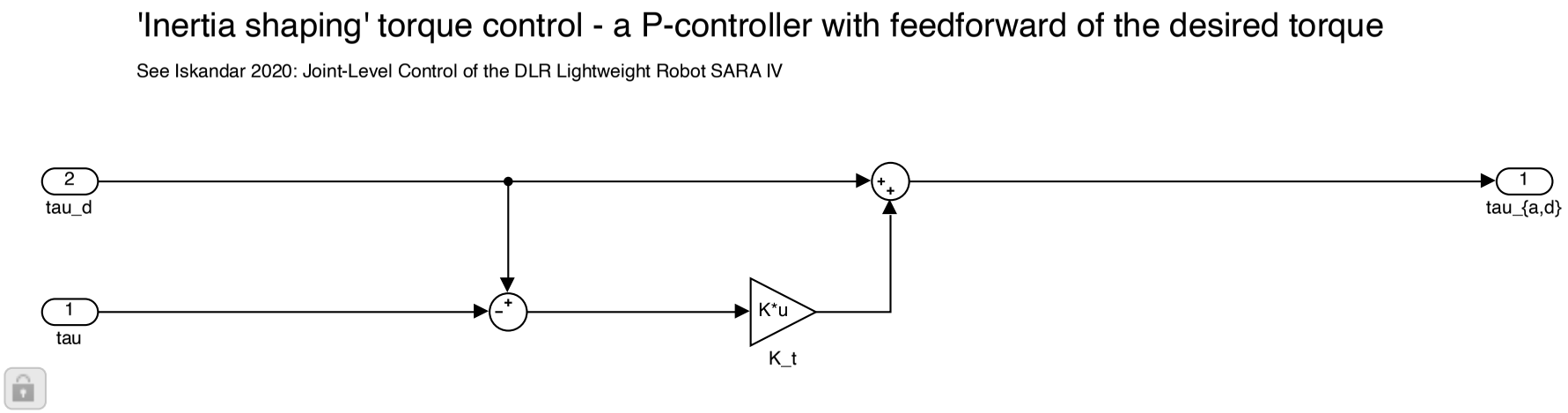

Figure F.8: Robot control library block **P torque control** [217].

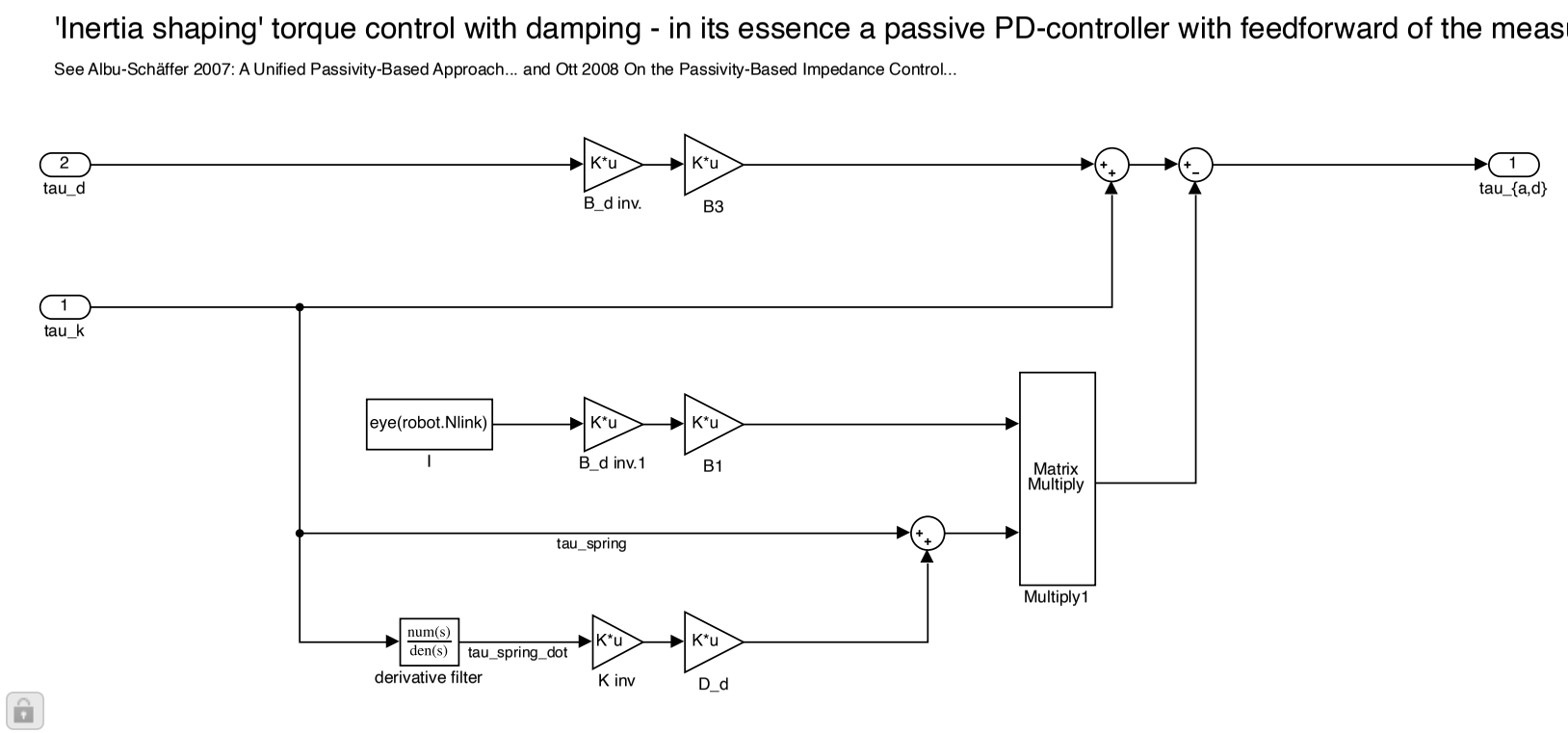

Figure F.9: Robot control library block **passive PD torque control** [217].

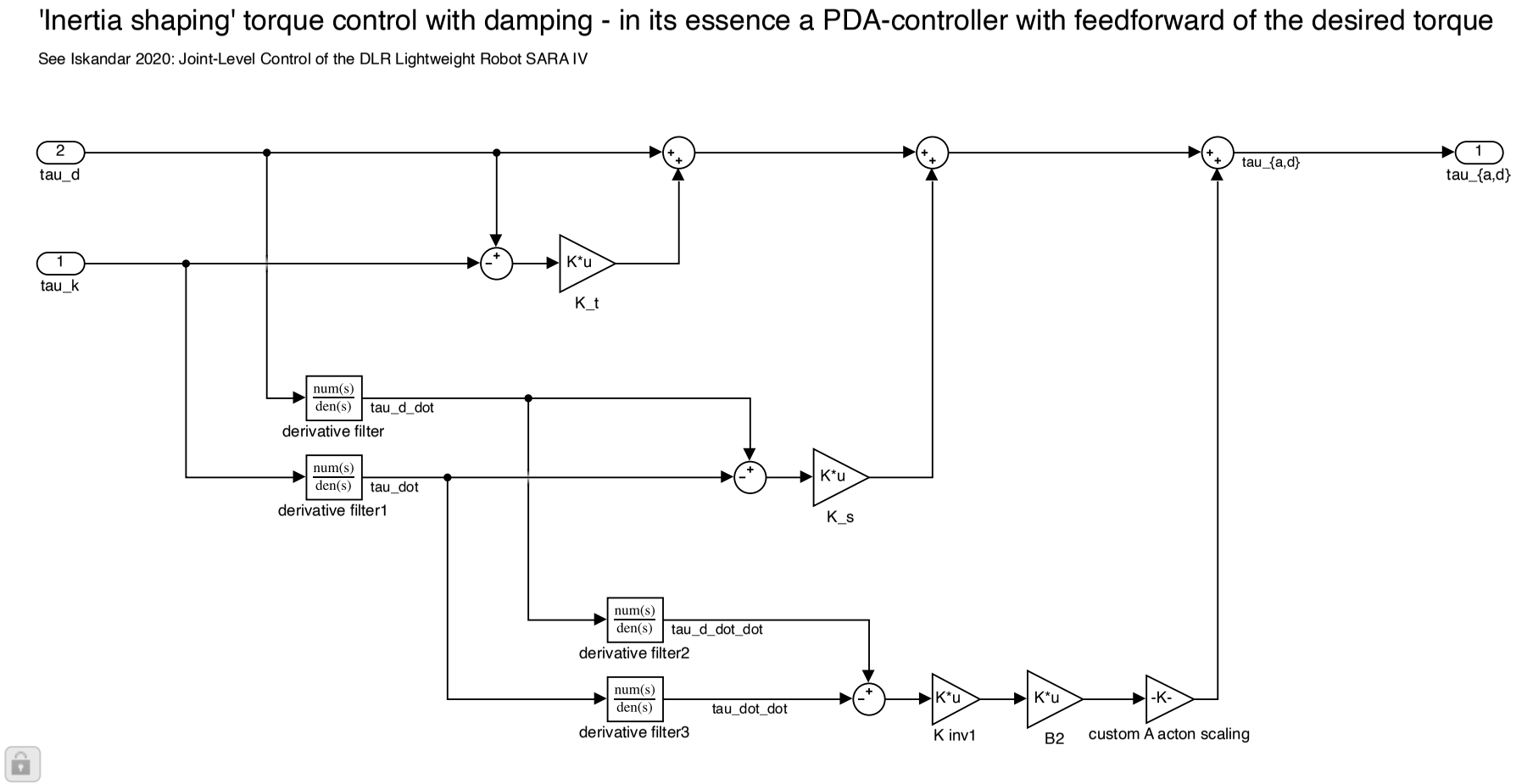

Figure F.10: Robot control library block **PDA torque control** [217].

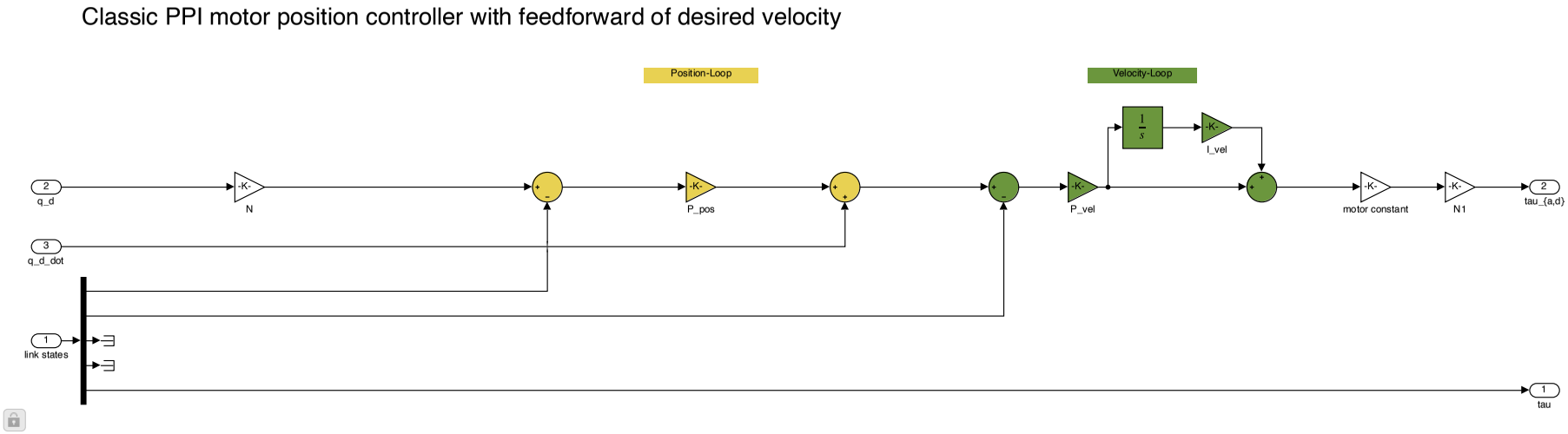

Figure F.11: Robot control library block **PPI motor position** [217].

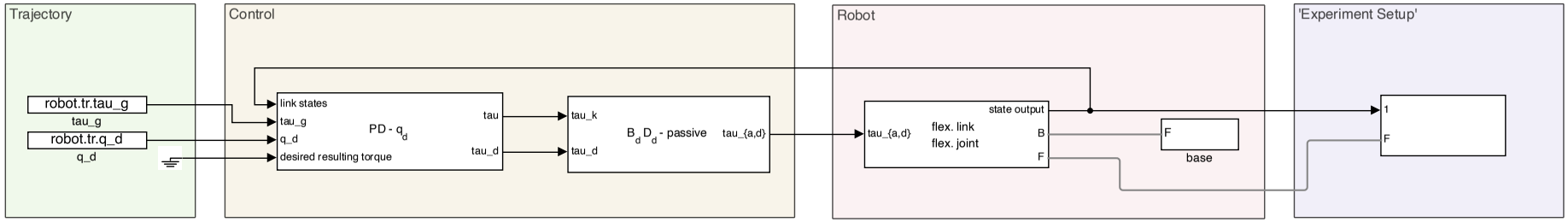

Figure F.12: Simulation model of a single link. The link block is interchangeable with any other link model block form the robot_library, e.g. a rigid link flexible joint block [217].

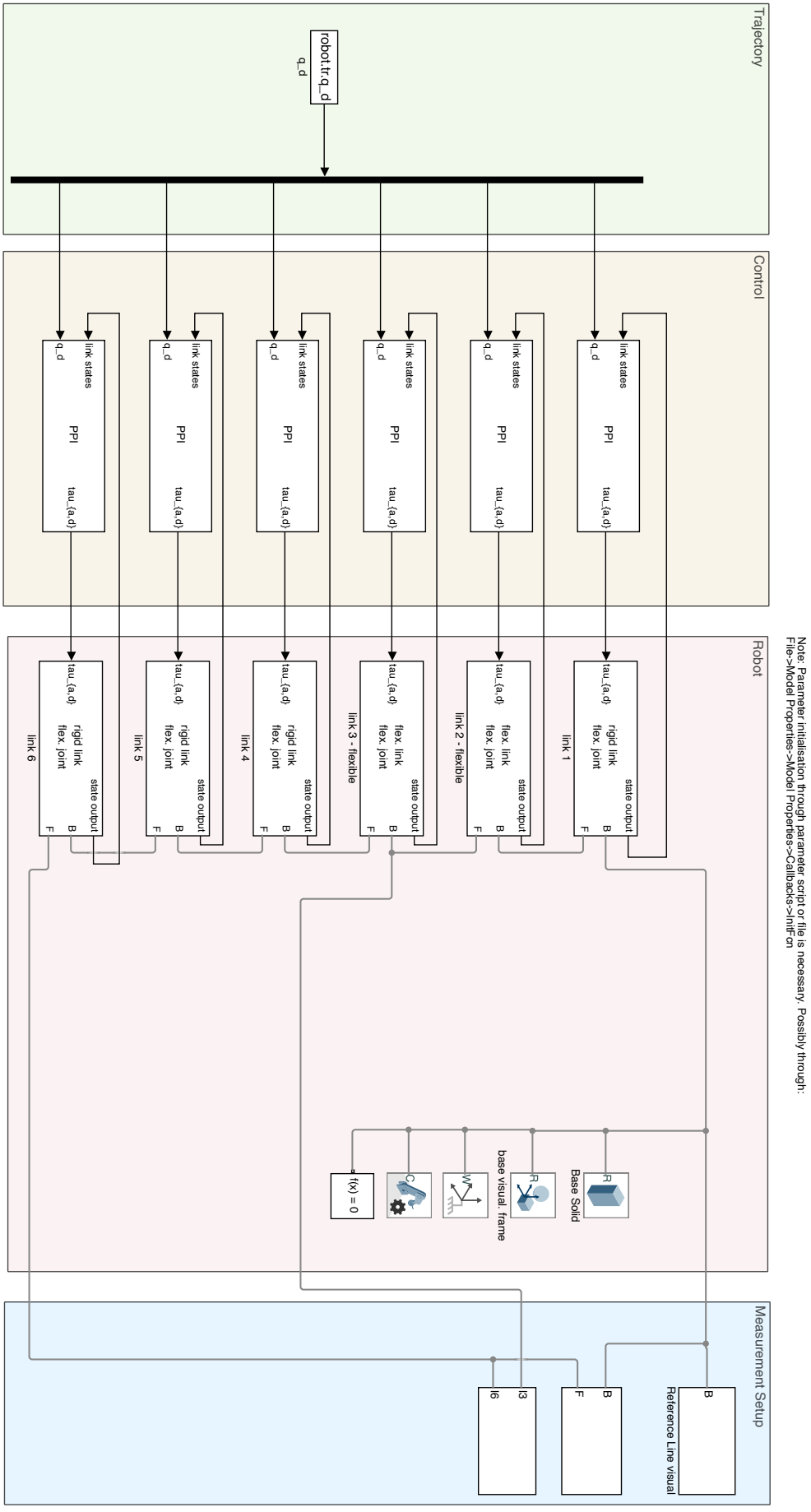

Figure F.13: Simulation model of the UR10 with PPI motor position control and flexible-joint flexible-body link simulation [217].

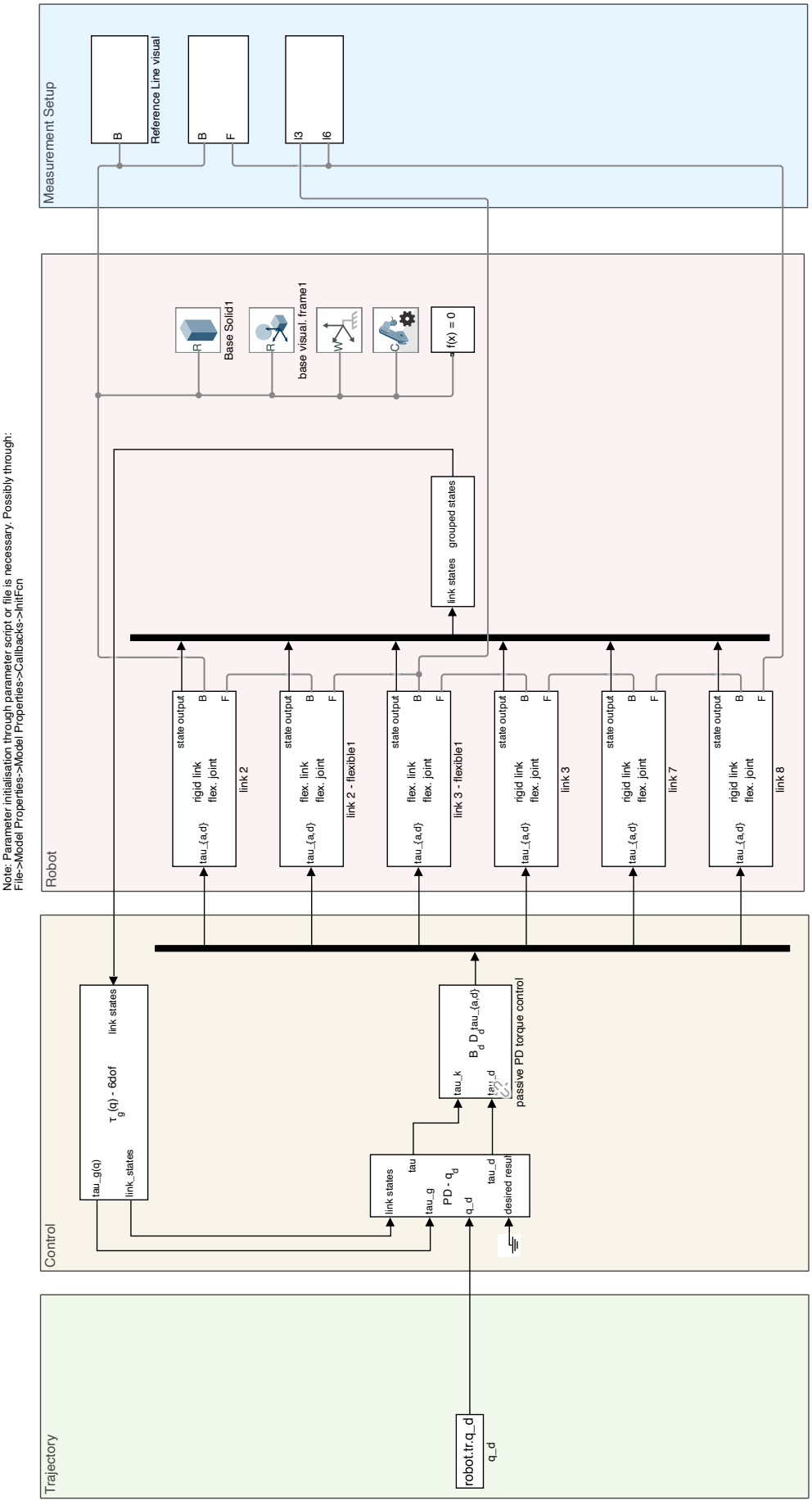

Figure F.14: Simulation model of the UR10 with PD joint impedance/position control and flexible-joint flexible-body link simulation [217].

Bibliography

[1] A. Kumar Poonama, B. S. and Sehgalc, V. K. “Active Vibration Control Of Structures Against Earthquakes Using ModernControl Theory”. In: *Asian Journal Of Civil Engineering (Building And Housing)* 8.3 (2007), pp. 283–299.

[2] *ABB absolute accuracy option*. URL: https://library.e.abb.com/ (visited on 01/05/2021).

[3] *ABB IRB 120 Product Specification*. URL: https://new.abb.com/products/robotics/de/industrieroboter/irb-120 (visited on 12/28/2020).

[4] *ABB IRB 1600 FlexPicker Product Specification*. URL: https://new.abb.com/products/robotics/de/industrieroboter/irb-1600 (visited on 01/06/2021).

[5] *ABB IRB 460 FlexPicker Product Specification*. URL: https://new.abb.com/products/robotics/de/industrieroboter/irb-360 (visited on 01/05/2021).

[6] *ABB IRB 4600 Product Specification*. URL: https://new.abb.com/products/robotics/de/industrieroboter/irb-4600 (visited on 12/21/2020).

[7] *ABB IRB 6700 Product Specification*. URL: https://new.abb.com/products/robotics/de/industrieroboter/irb-6700 (visited on 01/05/2021).

[8] Abele, E., Bauer, J., Hemker, T., Laurischkat, R., Meier, H., Reese, S., and von Stryk, O. “Comparison and validation of implementations of a flexible joint multibody dynamics system model for an industrial robot”. In: *CIRP Journal of Manufacturing Science and Technology* 4.1 (2011). Special Section on Innovative and Cognitive Manufacturing Engineering, pp. 38–43. ISSN: 1755-5817. DOI: 10.1016/j.cirpj.2011.01.006.

[9] Aguiar-Conraria, L. and Soares, M. J. “The continuous wavelet transform: Moving beyond uni-and bivariate analysis”. In: *Journal of Economic Surveys* 28.2 (2014), pp. 344–375.

[10] Ahmad, S. “Control of cooperative multiple flexible joint robots”. In: *IEEE Transactions on Systems, Man, and Cybernetics* 23.3 (1993), pp. 833–839. DOI: 10.1109/21.256553.

[11] Akhtar, M. T. and Mitsuhashi, W. “Improving performance of FxLMS algorithm for active noise control of impulsive noise”. In: *Journal of Sound and Vibration* 327.3-5 (Nov. 2009), pp. 647–656. DOI: 10.1016/j.jsv.2009.07.023.

[12] Albu-Schaffer, A., Eiberger, O., Grebenstein, M., Haddadin, S., Ott, C., Wimbock, T., Wolf, S., and Hirzinger, G. “Soft robotics”. In: *IEEE Robotics Automation Magazine* 15.3 (2008), pp. 20–30. DOI: 10.1109/MRA.2008.927979.

[13] Albu-Schaffer, A. and Hirzinger, G. “State feedback controller for flexible joint robots: a globally stable approach implemented on DLR’s light-weight robots”. In: *Proceedings. 2000 IEEE/RSJ International Conference on Intelligent Robots and Systems (IROS 2000) (Cat. No.00CH37113)*. Vol. 2. 2000, 1087–1093 vol.2. DOI: 10.1109/IROS.2000.893164.

[14] Albu-Schaffer, A. and Hirzinger, G. “Parameter identification and passivity based joint control for a 7 DOF torque controlled light weight robot”. In: *Proceedings 2001 ICRA. IEEE International Conference on Robotics and Automation (Cat. No.01CH37164)*. Vol. 3. 2001, 2852–2858 vol.3. DOI: 10.1109/ROBOT.2001.933054.

[15] Albu-Schaffer, A. and Hirzinger, G. “Cartesian impedance control techniques for torque controlled light-weight robots”. In: *Proceedings 2002 IEEE International Conference on Robotics and Automation (Cat. No.02CH37292)*. Vol. 1. 2002, 657–663 vol.1. DOI: 10.1109/ROBOT.2002.1013433.

[16] Albu-Schaffer, A., Ott, C., Frese, U., and Hirzinger, G. “Cartesian impedance control of redundant robots: recent results with the DLR-light-weight-arms”. In: *2003 IEEE International Conference on Robotics and Automation (Cat. No.03CH37422)*. Vol. 3. 2003, 3704–3709 vol.3. DOI: 10.1109/ROBOT.2003.1242165.

[17] Albu-Schaffer, A., Ott, C., and Hirzinger, G. “A passivity based Cartesian impedance controller for flexible joint robots - part II: full state feedback, impedance design and experiments”. In: *IEEE International Conference on Robotics and Automation, 2004. Proceedings. ICRA ’04. 2004*. Vol. 3. 2004, 2666–2672 Vol.3. DOI: 10.1109/ROBOT.2004.1307463.

[18] Albu-Schäffer, A., Ott, C., and Hirzinger, G. “Passivity based cartesian impedance control for flexible joint manipulators”. In: *IFAC Proceedings Volumes* 37.13 (2004). 6th IFAC Symposium on Nonlinear Control Systems 2004 (NOLCOS 2004), Stuttgart, Germany, 1-3 September, 2004, pp. 901–906. ISSN: 1474-6670. DOI: 10.1016/S1474-6670(17)31340-X.

[19] Albu-Schäffer, A., Ott, C., and Hirzinger, G. “A Unified Passivity-based Control Framework for Position, Torque and Impedance Control of Flexible Joint Robots”. In: *The International Journal of Robotics Research* 26.1 (2007), pp. 23–39. DOI: 10.1177/0278364907073776.

[20] Alkhatib, R. and Golnaraghi, M. F. “Active Structural Vibration Control: A Review”. In: *The Shock and Vibration Digest* 35.5 (Sept. 2003), pp. 367–383. DOI: 10.1177/05831024030355002.

[21] Allen, M. S., Rixen, D., Seijs, M. van der, Tiso, P., Abrahamsson, T., and Mayes, R. L. *Substructuring in Engineering Dynamics*. Springer International Publishing, 2020. DOI: 10.1007/978-3-030-25532-9.

[22] Aoustin, Y. and Formal’sky, A. “On the Feedforward Torques and Reference Trajectory for Flexible Two-Link Arm”. In: *Multibody System Dynamics* 3.3 (1999), pp. 241–265. DOI: 10.1023/a:1009875908235.

[23] Armstrong-Hélouvry, B. *Control of Machines with Friction* -. Berlin Heidelberg: Springer Science & Business Media, 2012. ISBN: 978-1-461-53972-8.

[24] Armstrong-Hélouvry, B., Dupont, P., and De Wit, C. C. “A survey of models, analysis tools and compensation methods for the control of machines with friction”. In: *Automatica* 30.7 (1994), pp. 1083–1138. ISSN: 0005-1098. DOI: 10.1016/0005-1098(94)90209-7.

[25] Asada, H., Ma, Z.-D., and Tokumaru, H. “Inverse Dynamics of Flexible Robot Arms: Modeling and Computation for Trajectory Control”. In: *Journal of Dynamic Systems, Measurement, and Control* 112.2 (June 1990), pp. 177–185. DOI: 10.1115/1.2896124.

[26] Atsumi, T., Okuyama, A., and Kobayashi, M. “Track-following Control Using Resonant Filter in Hard Disk Drives”. In: *2007 American Control Conference*. 2007, pp. 61–67. DOI: 10.1109/ACC.2007.4282597.

[27] B. Rebbechi, C. H. and Hansen, C. “Active Control Of Gearbox Vibration”. In: *ACTIVE 99*. 1999.

[28] Babu, P. R., Ramprasath, S., and Paranthagan, B. “Modeling and Dynamic Simulation of Permanent Magnet Brushless DC Motor (PMBLDCM) Drives”. In: *Mobile Communication and Power Engineering*. Springer Berlin Heidelberg, 2013, pp. 556–564. DOI: 10.1007/978-3-642-35864-7_86.

[29] Bac, C. W., Hemming, J., Barth, R., Wais, E., and Henten, E. J. V. “Performance Evaluation of a Haervesting Robot for Seweet Pepper”. In: *Journal ofField Robotics* 17 (2017), pp. 1–17.

[30] Baillargeon, B. P. and Vel, S. S. “Active Vibration Suppression of Sandwich Beams using Piezoelectric Shear Actuators: Experiments and Numerical Simulations”. In: *Journal of Intelligent Material Systems and Structures* 16.6 (June 2005), pp. 517–530. DOI: 10.1177/1045389x05053154.

[31] Balas, G. J. and Young, P. M. “Control design for variations in structural natural frequencies”. In: *Journal of Guidance, Control, and Dynamics* 18.2 (Mar. 1995), pp. 325–332. DOI: 10.2514/3.21387.

[32] Balas, M. J. “Direct velocity feedback control of large space structures”. In: *Journal of guidance and control* 2.3 (1979), pp. 252–253.

[33] Bang, J. S., Shim, H., Park, S. K., and Seo, J. H. “Robust Tracking and Vibration Suppression for a Two-Inertia System by Combining Backstepping Approach With Disturbance Observer”. In: *IEEE Transactions on Industrial Electronics* 57.9 (2010), pp. 3197–3206. DOI: 10.1109/TIE.2009.2038398.

[34] Barker, L. “Vector-algebra approach to extract Denavit–Hartenberg parameters of assembled robot arms”. In: *NASA Tech Paper* (1983).

[35] Bauchau, O. A. *Flexible Multibody Dynamics*. Springer Netherlands, 2011. DOI: 10.1007/978-94-007-0335-3.

[36] Bauomy, H. and El-Sayed, A. “Active control of a rectangular thin plate via negative acceleration feedback”. In: *Journal of Computational and Nonlinear Dynamics* 11.4 (2016).

[37] Baur, J., Dendorfer, S., Pfaff, J., Schutz, C., Buschmann, T., and Ulbrich, H. “Experimental friction identification in robot drives”. In: *2014 IEEE International Conference on Robotics and Automation (ICRA)*. IEEE, May 2014. DOI: 10.1109/icra.2014.6907744.

[38] Bayerlein, L. “Aufbau eines Prüfstandes zur aktiven Vibrationsdämpfung”. Bacherlorarbeit. Technische Universität München, 2018.

[39] Bayo, E. “Computed torque for the position control of open-chain flexible robots”. In: *Proceedings. 1988 IEEE International Conference on Robotics and Automation*. 1988, 316–321 vol.1. DOI: 10.1109/ROBOT.1988.12067.

[40] Baz, A. and Ro, J. “Active control of flow-induced vibrations of a flexible cylinder using direct velocity feedback”. In: *Journal of Sound and Vibration* 146.1 (1991), pp. 33–45.

[41] Behi, F. and Tesar, D. “Parametric identification for industrial manipulators using experimental modal analysis”. In: *IEEE Transactions on Robotics and Automation* 7.5 (1991), pp. 642–652. DOI: 10.1109/70.97876.

[42] Benassi, L. and Elliott, S. “Active vibration isolation using an inertial actuator with local displacement feedback control”. In: *Journal of Sound and Vibration* 278.4-5 (Dec. 2004), pp. 705–724. DOI: 10.1016/j.jsv.2003.10.065.

[43] Benosman, M., Boyer, F., Vey, G. L., and Primault, D. In: *Journal of Intelligent and Robotic Systems* 34.4 (2002), pp. 381–414. DOI: 10.1023/a:1019639517064.

[44] Benosman, M. and Vey, G. L. “Control of flexible manipulators: A survey”. In: *Robotica* 22.5 (Aug. 2004), pp. 533–545. DOI: 10.1017/s0263574703005642.

[45] Berninger, T. “Dezentrale Gelenkregelung für humanoide Roboter”. Masterthesis. Technische Universität München, 2016.

[46] Berninger, T. F. C., Fuderer, S., and Rixen, D. J. “Modal Analysis of a 7 DoF Sweet Pepper Harvesting Robot”. In: *Topics in Modal Analysis & Testing, Volume 8*. Springer International Publishing, May 2019. DOI: 10.1007/978-3-030-12684-1_16.

[47] Berninger, T. F. C., Huang, C., Ochsenius, M. A., and Rixen, D. J. “The Influence of Structural Dynamics on Cascaded Joint Position Control of a Flexible Beam with a Compliant Gear”. In: *2019 19th International Conference on Control, Automation and Systems (ICCAS)*. IEEE, 2019. DOI: 10.23919/iccas47443.2019.8971640.

[48] Berninger, T. F. C., Ochsenius, M. A., and Rixen, D. J. “Evaluation of an External Vibration Damping Approach for Robot Manipulators Using a Flexible Multi Body Simulation”. In: *2019 IEEE/ASME International Conference on Advanced Intelligent Mechatronics (AIM)*. IEEE, 2019. DOI: 10.1109/aim.2019.8868406.

[49] Berninger, T. F. C. and Rixen, D. J. “External Vibration Damping of a Robot Manipulator’s TCP Using Acceleration Feedback”. In: *PAMM* 19.1 (Nov. 2019). DOI: 10.1002/pamm.201900344.

[50] Berninger, T. F. C., Seiwald, P., Sygulla, F., and Rixen, D. J. “Evaluating the Mechanical Redesign of a Biped Walking Robot Using Experimental Modal Analysis”. In: *Topics in Modal Analysis & Testing, Volume 8*. Ed. by Dilworth, B. J. and Mains, M. Cham: Springer International Publishing, 2022, pp. 45–52. DOI: 10.1007/978-3-030-75996-4_6.

[51] Berninger, T. F. C., Slimak, T., Weber, T., and Rixen, D. J. “An External Stabilization Unit for High-Precision Applications of Robot Manipulators”. In: *2020 IEEE/RSJ International Conference on Intelligent Robots and Systems (IROS)*. 2020, pp. 4276–4282. DOI: 10.1109/IROS45743.2020.9341454.

[52] Berninger, T. F. C., Sygulla, F., Fuderer, S., and Rixen, D. J. “Experimental Analysis of Structural Vibration Problems of a Biped Walking Robot”. In: *2020 IEEE International Conference on Robotics and Automation (ICRA)*. 2020, pp. 8726–8731. DOI: 10.1109/ICRA40945.2020.9197282.

[53] Beudaert, X., Erkorkmaz, K., and Munoa, J. “Portable damping system for chatter suppression on flexible workpieces”. In: *CIRP Annals* 68.1 (2019), pp. 423–426. DOI: 10.1016/j.cirp.2019.04.010.

[54] Bodeit, J. “Erweiterte Regelungsmethoden zur externen Vibrationsdämpfung von Robotermanipulatoren”. Semesterarbeit. Technische Universität München, 2020.

[55] Bona, B. and Indri, M. “Friction Compensation in Robotics: an Overview”. In: *Proceedings of the 44th IEEE Conference on Decision and Control*. 2005, pp. 4360–4367. DOI: 10.1109/CDC.2005.1582848.

[56] Book, W. J. “Analysis of Massless Elastic Chains With Servo Controlled Joints”. In: *Journal of Dynamic Systems, Measurement, and Control* 101.3 (Sept. 1979), pp. 187–192. ISSN: 0022-0434. DOI: 10.1115/1.3426423.

[57] Book, W. and Loper, J. “Inverse dynamics for commanding micromanipulator inertial forces to damp macromanipulator vibration”. In: *Proceedings 1999 IEEE/RSJ International Conference on Intelligent Robots and Systems. Human and Environment Friendly Robots with High Intelligence and Emotional Quotients (Cat. No.99CH36289)*. IEEE. DOI: 10.1109/iros.1999.812763.

[58] Book, W. J. and Lee, S. H. “Vibration Control of a Large Flexible Manipulator by a Small Robotic Arm”. In: *1989 American Control Conference*. IEEE, June 1989. DOI: 10.23919/acc.1989.4790404.

[59] Bouhaddi, N. and Fillod, R. “A method for selecting master DOF in dynamic substructuring using the Guyan condensation method”. In: *Computers & Structures* 45.5 (1992), pp. 941–946. ISSN: 0045-7949. DOI: 10.1016/0045-7949(92)90052-2.

[60] Butterfield, A. J. and Woodard, S. E. “Measured spacecraft instrument and structural interactions”. In: *Journal of Spacecraft and Rockets* 33.4 (July 1996), pp. 556–562. DOI: 10.2514/3.26799.

[61] Byung-hoon Chang and Yoichi Hori. “Trajectory design considering derivative of jerk for head-positioning of disk drive system with mechanical vibration”. In: *Proceedings of the 2003 American Control Conference, 2003.* Vol. 5. 2003, 4335–4340 vol.5. DOI: 10.1109/ACC.2003.1240520.

[62] Canudas de Wit, C., Olsson, H., Astrom, K. J., and Lischinsky, P. “A new model for control of systems with friction”. In: *IEEE Transactions on Automatic Control* 40.3 (1995), pp. 419–425. DOI: 10.1109/9.376053.

[63] Casado, C. M., Sebastian, I. M. D. de, Poncela, A. V., and Lorenzana, A. “Implementation of passive and active vibration control on an in-service footbridge”. In: *Structural Control and Health Monitoring* 20.1 (June 2011), pp. 70–87. DOI: 10.1002/stc.471.

[64] Caughey, T. K. “Classical Normal Modes in Damped Linear Dynamic Systems”. In: *Journal of Applied Mechanics* 27.2 (June 1960), pp. 269–271. DOI: 10.1115/1.3643949.

[65] Chen. *Analog and digital control system design : transfer-function, state-space, and algebraic methods*. New York Oxford: Oxford University Press, 1993. ISBN: 978-0-195-31046-7.

[66] Chen, J. W. and Liu, T. S. “H/sub /spl infin// repetitive control for pickup head flying height in near-field optical disk drives”. In: *IEEE Transactions on Magnetics* 41.2 (2005), pp. 1067–1069. DOI: 10.1109/TMAG.2004.842018.

[67] Cheong, J., Chung, W. K., and Youm, Y. “Two-Step Controller for 3-D Flexible Link Manipulators: Bandwidth Modulation and Modal Feedback Approach”. In: *Journal of Dynamic Systems, Measurement, and Control* 124.4 (Dec. 2002), pp. 566–574. DOI: 10.1115/1.1514240.

[68] Childs, D. *Turbomachinery Rotordynamics*. Wiley, 1993. ISBN: 978-0-471-53840-0.

[69] Chiu, C. W., Chao, P. C. P., and Wu, D. Y. “Optimal design of magnetically actuated optical image stabilizer mechanism for cameras in mobile phones via genetic algorithm”. In: *IEEE Transactions on Magnetics* 43.6 (2007), pp. 2582–2584. ISSN: 00189464. DOI: 10.1109/TMAG.2007.893320.

[70] Cinquemani, S. and Resta, F. “Limits on the use of inertial actuators in active vibration control”. In: *9th International Conference on Computing, Communications and Control Technologies*. 2011, pp. 1–6.

[71] *CIPA Standard*. URL: http://www.cipa.jp/image-stabilization/index_e.html.

[72] Clough, R. W. and Penzien, J. *Dynamics of Structures*. McGraw-Hill College, 2003. ISBN: 978-0070113923.

[73] *Comprehensive list of typical robot manipulator applications*. URL: https://www.robots.com/applications (visited on 12/26/2020).

[74] Corless, R. M., Kaya, C. Y., and Moir, R. H. C. “Optimal residuals and the Dahlquist test problem”. In: *Numerical Algorithms* 81.4 (Nov. 2018), pp. 1253–1274. DOI: 10.1007/s11075-018-0624-x.

[75] CRAIG, R. R. and BAMPTON, M. C. C. “Coupling of substructures for dynamic analyses.” In: *AIAA Journal* 6.7 (July 1968), pp. 1313–1319. DOI: 10.2514/3.4741.

[76] Craig, R. R. and Kurdila, A. J. *Fundamentals of Structural Dynamics*. Berlin: Wiley, 2006. ISBN: 978-0471430445.

[77] Crocker, M. J., ed. *Handbook of Noise and Vibration Control*. John Wiley & Sons, Inc., Sept. 2007. DOI: 10.1002/9780470209707.

[78] Cros, J., Vinassa, J. M., Clenet, S., Astier, S., and Lajoie-Mazenc, M. “A novel current control strategy in trapezoidal EMF actuators to minimize torque ripples due to phases commutations”. In: *1993 Fifth European Conference on Power Electronics and Applications*. 1993, 266–271 vol.4.

[79] Dahl, P. “Inertial Beam Alignment Sensor and a Simplified Application”. In: *AIAA Guidance, Navigation, and Control Conference and Exhibit*. American Institute of Aeronautics and Astronautics, Aug. 2002. DOI: 10.2514/6.2002-5002.

[80] De Luca, A. “Feedforward/feedback laws for the control of flexible robots”. In: *Proceedings 2000 ICRA. Millennium Conference. IEEE International Conference on Robotics and Automation. Symposia Proceedings (Cat. No.00CH37065)*. Vol. 1. 2000, 233–240 vol.1. DOI: 10.1109/ROBOT.2000.844064.

[81] De Luca, A., Lucibello, P., Ulivi, and G. “Inversion techniques for trajectory control of flexible robot arms”. In: *Journal of Robotic Systems* 6.4 (1989), pp. 325–344. DOI: https://doi.org/10.1002/rob.4620060403.

[82] Deng, R. “Integrated 6-DOF Lorentz Actuator with Gravity Compensation for Vibration Isolation in in-Line Surface Metrology”. PhD thesis. TU Delft, 2017.

[83] Diaz, C. G., Paulitsch, C., and Gardonio, P. “Active damping control unit using a small scale proof mass electrodynamic actuator”. In: *The Journal of the Acoustical Society of America* 124.2 (Aug. 2008), pp. 886–897. DOI: 10.1121/1.2945167.

[84] *DLR LWR Robot*. URL: https://www.dlr.de/rm/en/desktopdefault.aspx/tabid-12464/%23gallery/29163#gallery/2916.

[85] Drapeau, V. and Wang, D. “Verification of a closed-loop shaped-input controller for a five-bar-linkage manipulator”. In: *[1993] Proceedings IEEE International Conference on Robotics and Automation*. 1993, 216–221 vol.3. DOI: 10.1109/ROBOT.1993.291847.

[86] Driggers, R. G., Kelley, M., and Cox, P. G. “National imagery interpretation rating system (NIIRS) and the probabilities of detection, recognition, and identification”. In: *Infrared Imaging Systems: Design, Analysis, Modeling, and Testing VII*. Ed. by Holst, G. C. SPIE, June 1996. DOI: 10.1117/12.241970.

[87] Du, H., Lim, M., and Liew, K. “A nonlinear finite element model for dynamics of flexible manipulators”. In: *Mechanism and Machine Theory* 31.8 (1996), pp. 1109–1119. ISSN: 0094-114X. DOI: https://doi.org/10.1016/0094-114X(96)84602-7.

[88] Dwivedy, S. K. and Eberhard, P. “Dynamic analysis of flexible manipulators, a literature review”. In: *Mechanism and Machine Theory* 41.7 (July 2006), pp. 749–777. DOI: 10.1016/j.mechmachtheory.2006.01.014.

[89] Dwivedy, S. K. and Eberhard, P. “Dynamic analysis of flexible manipulators, a literature review”. In: *Mechanism and Machine Theory* 41.7 (2006), pp. 749–777. ISSN: 0094-114X. DOI: 10.1016/j.mechmachtheory.2006.01.014.

[90] Egeland, O. and Gravdahl, J. T. *Modeling and Simulation for Automatic Control* -. Marine Cybernetics, 2002. ISBN: 978-8-292-35601-2.

[91] Ewins, D. J. *Modal testing : theory, practice, and application*. Baldock, Hertfordshire, England Philadelphia, PA: Research Studies Press, 2000. ISBN: 0863802184.

[92] Ewins, D. J. *Modal Testing: Theory, Practice and Application*. 2nd ed. Research Studies Press Ltd., 2000, p. 562. ISBN: 0 86380 218 4.

[93] Fanson, J. L. and Caughey, T. K. “Positive position feedback control for large space structures”. In: *AIAA Journal* 28.4 (Apr. 1990), pp. 717–724. DOI: 10.2514/3.10451.

[94] *Fanuc Arc Mate 100iD/16S Product Specification*. URL: https://www.fanuc.eu/de/en/robots/robot-filter-page/arc-welding/arcmate-100id-16s (visited on 12/24/2020).

[95] Fisk, J. W. and Rue, A. K. “Confidence Limits for the Pointing Error of Gimbaled Sensors”. In: *IEEE Transactions on Aerospace and Electronic Systems* AES-2.6 (1966), pp. 648–654. DOI: 10.1109/TAES.1966.4501957.

[96] Flint, E., Evert, M., Anderson, E., and Flannery, P. “Active/passive counter-force vibration control and isolation systems”. In: *2000 IEEE Aerospace Conference. Proceedings (Cat. No.00TH8484)*. Vol. 4. 2000, 285–298 vol.4. DOI: 10.1109/AERO.2000.878440.

[97] Focchi, M., Medrano-Cerda, G. A., Boaventura, T., Frigerio, M., Semini, C., Buchli, J., and Caldwell, D. G. “Robot impedance control and passivity analysis with inner torque and velocity feedback loops”. In: *Control Theory and Technology* 14.2 (May 2016), pp. 97–112. DOI: 10.1007/s11768-016-5015-z.

[98] *Franka Panda Product Specification*. URL: https://wiredworkers.io/wp-content/uploads/2019/12/Panda_FrankaEmika_ENG.pdf.

[99] Fuderer, S. “Modalanalyse eines Roboterarmes”. Bachelorarbeit. Technische Universität München, 2018.

[100] Fuderer, S. “Modalanalyse eines Roboterarmes”. Bachelorarbeit. Technische Universität München, 2018.

[101] Fuentes, A. T., Kipfmueller, M., and Prieto, M. A. “6 DOF articulated-arm robot and mobile platform: Dynamic modelling as Multibody System and its validation via Experimental Modal Analysis.” In: *IOP Conference Series: Materials Science and Engineering* 257.1 (2017). ISSN: 1757899X. DOI: 10.1088/1757-899X/257/1/012008.

[102] Fukuda, T. and Kuribayashi, Y. “Flexibility control of elastic robotic arms and its application to contouring control”. In: *Proceedings. 1984 IEEE International Conference on Robotics and Automation*. Vol. 1. 1984, pp. 540–545. DOI: 10.1109/ROBOT.1984.1087206.

[103] FUKUDA, T. and ARAKAWA, A. “Modeling and control characteristics for a two-degrees-of-freedom coupling system of flexible robotic arms.” In: *JSME international journal* 30.267 (1987), pp. 1458–1464. DOI: 10.1299/jsme1987.30.1458.

[104] Gardonio, P. and Elliott, S. J. “Modal response of a beam with a sensor–actuator pair for the implementation of velocity feedback control”. In: *Journal of sound and vibration* 284.1-2 (2005), pp. 1–22.

[105] Ge, S. S., Lee, T. H., and Wang, Z. P. “Model-free regulation of multi-link smart materials robots”. In: *IEEE/ASME Transactions on Mechatronics* 6.3 (2001), pp. 346–351. DOI: 10.1109/3516.951372.

[106] Ge, S. S., Lee, T. H., and Zhu, G. “Asymptotically stable end-point regulation of a flexible SCARA/Cartesian robot”. In: *IEEE/ASME Transactions on Mechatronics* 3.2 (1998), pp. 138–144. DOI: 10.1109/3516.686682.

[107] George, L. E. and Book, W. J. “Inertial Vibration Damping Control for a Flexible Base Manipulator”. In: *Dynamic Systems and Control*. ASME, 2002. DOI: 10.1115/imece2002-33533.

[108] Geradin, M. *Mechanical vibrations : theory and application to structural dynamics*. Hoboken, New Jersey: Wiley, 2014. ISBN: 978-1-118-90020-8.

[109] Géradin, M. and Cardona, A. *Flexible multibody dynamics: a finite element approach*. New York: John Wiley, 2001. ISBN: 9780471489900.

[110] Gerson, G. “Tracking Systems”. In: *Precision Stabilization and Tracking Systems for Acquisition, Pointing, and Control Applications* (1996).

[111] Ghorbel, F. H., Gandhi, P. S., and Altpeter, F. “COn the Kinematic Error in Harmonic Drive Gears”. In: *Transactions of the ASME: Journal of Mechanical Design* 123 (2001).

[112] Gille, M., Berninger, T. F. C., and Rixen, D. J. “Comparison of different Excitation Strategies in Operational Modal Analysis (OMA)”. In: *PAMM* 19.1 (2019). DOI: 10.1002/pamm.201900392.

[113] Ginani, L. S. and Motta, J. M. S. T. “Theoretical and practical aspects of robot calibration with experimental verification”. In: *Journal of the Brazilian Society of Mechanical Sciences and Engineering* 33.1 (Mar. 2011), pp. 15–21. DOI: 10.1590/s1678-58782011000100003.

[114] GOH, C. J. and CAUGHEY, T. K. “On the stability problem caused by finite actuator dynamics in the collocated control of large space structures”. In: *International Journal of Control* 41.3 (Mar. 1985), pp. 787–802. DOI: 10.1080/00207185089611163.

[115] Good, M. C., Sweet, L. M., and Strobel, K. L. “Dynamic Models for Control System Design of Integrated Robot and Drive Systems”. In: *Journal of Dynamic Systems, Measurement, and Control* 107.1 (Mar. 1985), pp. 53–59. DOI: 10.1115/1.3140707.

[116] Grandia, R., Farshidian, F., Ranftl, R., and Hutter, M. “Feedback MPC for Torque-Controlled Legged Robots”. In: *2019 IEEE/RSJ International Conference on Intelligent Robots and Systems (IROS)*. 2019, pp. 4730–4737. DOI: 10.1109/IROS40897.2019.8968251.

[117] Greenway, B. “Robot accuracy”. In: *Industrial Robot: An International Journal* 27.4 (Aug. 2000), pp. 257–265. DOI: 10.1108/01439910010372136.

[118] Griffiths, D., Aubert, A., Green, E. R., and Ding, J. “A Technique for Relating Vehicle Structural Modes to Stiffness as Determined in Static Determinate Tests”. In: *SAE Technical Paper Series*. SAE International, May 2003. DOI: 10.4271/2003-01-1716.

[119] Guelman, M., Kogan, A., Kazarian, A., Livne, A., Orenstein, M., Michalik, H., and Arnon, S. “Acquisition and pointing control for inter-satellite laser communications”. In: *IEEE Transactions on Aerospace and Electronic Systems* 40.4 (2004), pp. 1239–1248. ISSN: 00189251. DOI: 10.1109/TAES.2004.1386877.

[120] Guilluy, W., Beghdadi, A., and Oudre, L. “A performance evaluation framework for video stabilization methods”. In: *2018 7th European Workshop on Visual Information Processing (EUVIP)*. IEEE, Nov. 2018. DOI: 10.1109/euvip.2018.8611729.

[121] Gurgul, M. *Industrial Robots and Cobots - Everything You Need to Know about Your Future Co-worker*. Michał Gurgul., 2018. ISBN: 978-8-395-25131-3.

[122] GUYAN, R. J. “Reduction of stiffness and mass matrices”. In: *AIAA Journal* 3.2 (Feb. 1965), pp. 380–380. DOI: 10.2514/3.2874.

[123] Habegger, R., Bergamo, E., Schwab, W., Berninger, T. F. C., and Rixen, D. “Impact of intensive modification of sweet pepper plants on performance of end effectors for autonomous harvesting”. In: *European Journal of Horticultural Science* 86.4 (Aug. 2021), pp. 354–359. DOI: 10.17660/ejhs.2021/86.4.2.

[124] Hairer, E. and Wanner, G. *Solving Ordinary Differential Equations II*. Springer Berlin Heidelberg, 1996. DOI: 10.1007/978-3-642-05221-7.

[125] Harder, M. “Multi-Sensor-Based On Line Contact and Parameter Estimation of a Robotic Arm”. Masterarbeit. Technische Universität München, 2019.

[126] Hilkert, J. M. “Inertially Stabilized Platform Technology Concepts and Principles”. In: *IEEE Control Systems* 28.1 (2008), pp. 26–46. ISSN: 1066033X. DOI: 10.1109/MCS.2007.910256.

[127] Holtz, J. and Springob, L. “Identification and compensation of torque ripple in high-precision permanent magnet motor drives”. In: *IEEE Transactions on Industrial Electronics* 43.2 (1996), pp. 309–320. DOI: 10.1109/41.491355.

[128] Hongchao Zhao and Degang Chen. “Exact and stable tip trajectory tracking for multi-link flexible manipulator”. In: *Proceedings of 32nd IEEE Conference on Decision and Control*. 1993, 1371–1376 vol.2. DOI: 10.1109/CDC.1993.325413.

[129] Huang, C. “Einfluss der Strukturdynamik auf die Regelung eines Robotergelenkprüfstandes”. Semesterthesis. Technische Universität München, 2019.

[130] “Hubble Space Telescope Precision Pointing Control System”. In: *J. Guidance* 11.2 (1988), pp. 119–123. ISSN: 07315090. DOI: 10.2514/6.1986-1981.

[131] Hutter, M., Gehring, C., Jud, D., Lauber, A., Bellicoso, C. D., Tsounis, V., Hwangbo, J., Bodie, K., Fankhauser, P., Bloesch, M., Diethelm, R., Bachmann, S., Melzer, A., and Hoepflinger, M. “ANYmal - a highly mobile and dynamic quadrupedal robot”. In: *2016 IEEE/RSJ International Conference on Intelligent Robots and Systems (IROS)*. IEEE, Oct. 2016. DOI: 10.1109/iros.2016.7758092.

[132] Huyanan, S. and Sims, N. D. “Vibration Control Strategies for Proof-mass Actuators”. In: *Journal of Vibration and Control* 13.12 (Dec. 2007), pp. 1785–1806. DOI: 10.1177/1077546307080031.

[133] IRONS, B. “Structural eigenvalue problems - elimination of unwanted variables”. In: *AIAA Journal* 3.5 (May 1965), pp. 961–962. DOI: 10.2514/3.3027.

[134] Iskandar, M., Ott, C., Keppler, M., Eiberger, O., Albu-Schaffer, A., and Dietrich, A. “Joint-Level Control of the DLR Lightweight Robot SARA IV”. In: *2020 International Conference on Intelligent Robots and Systems (IROS)*. IEEE.

[135] Isogai, M., Arai, F., and Fukuda, T. “Modeling and vibration control with neural network for flexible multi-link structures”. In: *Proceedings 1999 IEEE International Conference on Robotics and Automation (Cat. No.99CH36288C)*. Vol. 2. 1999, 1096–1101 vol.2. DOI: 10.1109/ROBOT.1999.772465.

[136] Iwasaki, M., Seki, K., and Maeda, Y. “High-Precision Motion Control Techniques: A Promising Approach to Improving Motion Performance”. In: *IEEE Industrial Electronics Magazine* 6.1 (2012), pp. 32–40. DOI: 10.1109/MIE.2012.2182859.

[137] Jacobus, R. and Serna, M. “Modal analysis of a three dimensional flexible robot”. In: *Proceedings of the 1994 IEEE International Conference on Robotics and Automation* (1994), pp. 2962–2967. DOI: 10.1109/ROBOT.1994.350889.

[138] Jahns, T. M. “Motion control with permanent-magnet AC machines”. In: *Proceedings of the IEEE* 82.8 (1994), pp. 1241–1252. DOI: 10.1109/5.301686.

[139] Jalili, N. “A Comparative Study and Analysis of Semi-Active Vibration-Control Systems”. In: *Journal of Vibration and Acoustics* 124.4 (Sept. 2002), pp. 593–605. DOI: 10.1115/1.1500336.

[140] Jia, H., Li, J., Xiang, G., Wang, J., Xiao, K., and Han, Y. “Modeling and analysis of pure kinematic error in harmonic drive”. In: *Mechanism and Machine Theory* 155 (2021), p. 104122. ISSN: 0094-114X. DOI: https://doi.org/10.1016/j.mechmachtheory.2020.104122.

[141] Jiang, Z.-H. “Impedance Control of Flexible Robot Arms with Parametric Uncertainties”. In: *Journal of Intelligent and Robotic Systems* 42.2 (Feb. 2005), pp. 113–133. DOI: 10.1007/s10846-005-0933-x.

[142] Jin-Soo Kim, Suzuki, K., Konno, A., and Uchiyama, H. “Force control of constrained flexible manipulators”. In: *Proceedings of IEEE International Conference on Robotics and Automation*. Vol. 1. 1996, 635–640 vol.1. DOI: 10.1109/ROBOT.1996.503846.

[143] Kammerer, J. “Weiterentwicklung eines Endeffektors zur Automatisierten Ernte von Paprika”. Semesterarbeit. Technische Universität München, 2018.

[144] Kammerer, J. “Weiterentwicklung eines Endeffektors zur Automazisierten Ernte von Paprika”. Semesterarbeit. Technische Universität München, 2018.

[145] Karan, B. and Vukobratović, M. “Calibration and accuracy of manipulation robot models—An overview”. In: *Mechanism and Machine Theory* 29.3 (Apr. 1994), pp. 479–500. DOI: 10.1016/0094-114x(94)90130-9.

[146] Kelemen, M. and Bagchi, A. “Modeling and feedback control of a flexible arm of a robot for prescribed frequency-domain tolerances”. In: *Automatica* 29.4 (1993), pp. 899–909. ISSN: 0005-1098. DOI: https://doi.org/10.1016/0005-1098(93)90095-B.

[147] Khalil, W. and Boyer, F. “An efficient calculation of computed torque control of flexible manipulators”. In: *Proceedings of 1995 IEEE International Conference on Robotics and Automation*. Vol. 1. 1995, 609–614 vol.1. DOI: 10.1109/ROBOT.1995.525351.

[148] Khalil, W. and Gautier, M. “Modeling of mechanical systems with lumped elasticity”. In: *Proceedings 2000 ICRA. Millennium Conference. IEEE International Conference on Robotics and Automation. Symposia Proceedings (Cat. No.00CH37065)*. Vol. 4. 2000, 3964–3969 vol.4. DOI: 10.1109/ROBOT.2000.845349.

[149] Khorrami, F. “Adaptive nonlinear control for end-effector position tracking of multilink flexible manipulators with embedded active materials”. In: *Proceedings of 1994 33rd IEEE Conference on Decision and Control*. Vol. 1. 1994, 103–108 vol.1. DOI: 10.1109/CDC.1994.411038.

[150] Kienholz, D. A. “Active alignment and vibration control system for a large airborne optical system”. In: *Smart Structures and Materials 2000: Damping and Isolation*. Ed. by Hyde, T. T. SPIE, Apr. 2000. DOI: 10.1117/12.384586.

[151] Kim, B. K., Chung, W. K., and Ohba, K. “Design and Performance Tuning of Sliding-Mode Controller for High-Speed and High-Accuracy Positioning Systems in Disturbance Observer Framework”. In: *IEEE Transactions on Industrial Electronics* 56.10 (2009), pp. 3798–3809. DOI: 10.1109/TIE.2009.2028357.

[152] Kim, M. H., Kim, H. Y., Kim, H. C., Ahn, D., and Gweon, D. “Design and Control of a 6-DOF Active Vibration Isolation System Using a Halbach Magnet Array”. In: *IEEE/ASME Transactions on Mechatronics* 21.4 (2016), pp. 2185–2196. DOI: 10.1109/TMECH.2016.2539349.

[153] Kim, S.-H. *Electric motor control: DC, AC and BLDC motors*. OCLC: ocn965339831. Cambridge, Massachusetts: Elsevier, 2017. ISBN: 9780128121382.

[154] Koh, Y. J., Lee, C., and Kim, C. “Video Stabilization Based on Feature Trajectory Augmentation and Selection and Robust Mesh Grid Warping”. In: *IEEE Transactions on Image Processing* 24.12 (2015), pp. 5260–5273. DOI: 10.1109/TIP.2015.2479918.

[155] Konstanzer, P. and Enenkl, B. “Recent advances in Eurocopter’s passive and active vibration control”. In: *American Helicopter Society 64th Annual Forum*. 2008.

[156] Krinner, A., Tsunoda, W., Wagner, C., Berninger, T., Thümmel, T., and Rixen, D. “Simulation and Experimental Validation of a Misaligned Rotor in Journal Bearings using Different Levels of Detail”. In: *Technische Mechanik* 37.2-5 (2017), pp. 450–459. ISSN: 0232-3869. DOI: 10.24352/UB.OVGU-2017-121.

[157] Krinner, A., Tsunoda, W., Wagner, C., Berninger, T., Thümmel, T., and Rixen, D. “Simulation and experimental validation of a misaligned rotor in journal bearings using different levels of detail”. In: *12. Internationale Tagung Schwingungen in Rotierenden Maschinen (SIRM)*. Ed. by Ecker, H., Irretier, H., Liebichand, R., Markert, R., Nordmann, R., and Strackeljan, J. 2017.

[158] Krishnamurthy, K. and Yang, L. “Dynamic modeling and simulation of two cooperating structurally-flexible robotic manipulators”. In: *Robotica* 13.4 (1995), pp. 375–384. DOI: 10.1017/S0263574700018804.

[159] Krishnan, H. “An approach to regulation of contact force and position in flexible-link constrained robots”. In: *1995 IEEE International Conference on Systems, Man and Cybernetics. Intelligent Systems for the 21st Century*. Vol. 3. 1995, 2087–2092 vol.3. DOI: 10.1109/ICSMC.1995.538087.

[160] Krishnan, R. *Permanent Magnet Synchronous and Brushless DC Motor Drives* -. Justus-Liebig-Universität Gießen: Taylor & Francis, 2009. ISBN: 978-0-824-75384-9.

[161] *Kuka iiwa*. URL: https://www.kuka.com/en-de/products/robot-systems/industrial-robots/lbr-iiwa.

[162] *Kuka KR 4 Agilus Product Specification*. URL: https://www.kuka.com/de-de/produkteleistungen/robotersysteme/industrieroboter/kr-4-agilus (visited on 12/28/2020).

[163] Kumar, R., Berkelman, P., Gupta, P., Barnes, A., Jensen, P. S., Whitcomb, L. L., and Taylor, R. H. “Preliminary experiments in cooperative human/robot force control for robot assisted microsurgical manipulation”. In: *Proceedings 2000 ICRA. Millennium Conference. IEEE International Conference on Robotics and Automation. Symposia Proceedings (Cat. No.00CH37065)*. Vol. 1. 2000, 610–617 vol.1. DOI: 10.1109/ROBOT.2000.844120.

[164] Kuntze, H.-B. and Jacubasch, A. “Control algorithms for stiffening an elastic industrial robot”. In: *IEEE Journal on Robotics and Automation* 1.2 (1985), pp. 71–78. DOI: 10.1109/jra.1985.1087011.

[165] Leang, K. K. and Devasia, S. “Feedback-Linearized Inverse Feedforward for Creep, Hysteresis, and Vibration Compensation in AFM Piezoactuators”. In: *IEEE Transactions on Control Systems Technology* 15.5 (2007), pp. 927–935. DOI: 10.1109/TCST.2007.902956.

[166] Lee, H.-H. “New Dynamic Modeling of Flexible-Link Robots”. In: *Journal of Dynamic Systems, Measurement, and Control* 127.2 (Dec. 2003), pp. 307–309. ISSN: 0022-0434. DOI: 10.1115/1.1902843.

[167] Lee, T., Ge, S., and Wang, Z. “Adaptive robust controller design for multi-link flexible robots”. In: *Mechatronics* 11.8 (2001), pp. 951–967. ISSN: 0957-4158. DOI: 10.1016/S0957-4158(00)00062-3.

[168] Leventhall, H. G. and L.Wong. “A Review of Active Attenuation And Development of An Active Attenuator”. In: *HSE Contract Research Report* (1988).

[169] Lew, J. Y. and Book, W. J. “Hybrid control of flexible manipulators with multiple contact”. In: *[1993] Proceedings IEEE International Conference on Robotics and Automation*. 1993, 242–247 vol.2. DOI: 10.1109/ROBOT.1993.292153.

[170] Lew, J. and Moon, S.-M. “A simple active damping control for compliant base manipulators”. In: *IEEE/ASME Transactions on Mechatronics* 6.3 (2001), pp. 305–310. DOI: 10.1109/3516.951368.

[171] Li, H., Zheng, S., and Ning, X. “Precise Control for Gimbal System of Double Gimbal Control Moment Gyro Based on Cascade Extended State Observer”. In: *IEEE Transactions on Industrial Electronics* 64.6 (2017), pp. 4653–4661. DOI: 10.1109/TIE.2017.2674585.

[172] Lightcap, C., Hamner, S., Schmitz, T., and Banks, S. “Improved Positioning Accuracy of the PA10-6CE Robot with Geometric and Flexibility Calibration”. In: *IEEE Transactions on Robotics* 24.2 (2008), pp. 452–456. DOI: 10.1109/TRO.2007.914003.

[173] Lin, S. .-., Tosunoglu, S., and Tesar, D. “Control of a six-degree-of-freedom flexible industrial manipulator”. In: *IEEE Control Systems Magazine* 11.3 (1991), pp. 24–30. DOI: 10.1109/37.75575.

[174] Liou, Y. A., Lin, P. P., Lindeke, R. R., and Chiang, H. “Tolerance specification of robot kinematic parameters using an experimental design technique—the Taguchi method”. In: *Robotics and Computer-Integrated Manufacturing* 10.3 (June 1993), pp. 199–207. DOI: 10.1016/0736-5845(93)90055-o.

[175] LIU, C. and FORWARD, R. “Electronic damping of resonance in gimbal structures”. In: *22nd Structures, Structural Dynamics and Materials Conference*. American Institute of Aeronautics and Astronautics, Apr. 1981. DOI: 10.2514/6.1981-556.

[176] Liu, Q., Li, H., Wang, W., Peng, C., and Yin, Z. “Analysis and Experiment of 5-DOF Decoupled Spherical Vernier-Gimballing Magnetically Suspended Flywheel (VGMSFW)”. In: *IEEE Access* 8 (2020), pp. 111707–111717. DOI: 10.1109/ACCESS.2020.3001144.

[177] Looke, T. D., Bayoumi, M. M., and Farooq, M. “Simulation of computed torque controllers for flexible manipulators”. In: *[1991] Proceedings of the 34th Midwest Symposium on Circuits and Systems*. 1991, 505–508 vol.1. DOI: 10.1109/MWSCAS.1991.252206.

[178] Luca, A. D. and Siciliano, B. “Explicit dynamic modeling of a planar two-link flexible manipulator”. In: *29th IEEE Conference on Decision and Control*. IEEE, 1990. DOI: 10.1109/cdc.1990.203652.

[179] Lunze, J. *Regelungstechnik 2*. Springer Berlin Heidelberg, 2016. DOI: 10.1007/978-3-662-52676-7.

[180] Lyuminarsky, Igor and Lyuminarsky, Stanislav. "Kinematic error of a harmonic drive". In: *MATEC Web Conf.* 224 (2018), p. 01039. DOI: 10.1051/matecconf/201822401039.

[181] Maicher, L. "Comparison of control strategies for a mechanical system under consideration of implementation limitations". Bachelor's Thesis. Technische Universität München, 2020.

[182] Malik, A. A. and Bilberg, A. "Collaborative robots in assembly: A practical approach for tasks distribution". In: *Procedia CIRP* 81 (2019), pp. 665–670. DOI: 10.1016/j.procir.2019.03.173.

[183] Mason, S., Righetti, L., and Schaal, S. "Full dynamics LQR control of a humanoid robot: An experimental study on balancing and squatting". In: *2014 IEEE-RAS International Conference on Humanoid Robots*. IEEE, Nov. 2014. DOI: 10.1109/humanoids.2014.7041387.

[184] Mason, S., Rotella, N., Schaal, S., and Righetti, L. "Balancing and walking using full dynamics LQR control with contact constraints". In: *2016 IEEE-RAS 16th International Conference on Humanoid Robots (Humanoids)*. IEEE, Nov. 2016. DOI: 10.1109/humanoids.2016.7803255.

[185] MASTEN, M. K. "Inertially stabilized platforms for optical imaging systems". In: *IEEE Control Systems Magazine* 28.1 (2008), pp. 47–64. DOI: 10.1109/MCS.2007.910201.

[186] Matsuno, F., Kim, E., and Sakawa, Y. "Dynamic hybrid position/force control of a flexible manipulator which has two degrees of freedom and flexible second link". In: *Proceedings IECON '91: 1991 International Conference on Industrial Electronics, Control and Instrumentation*. 1991, 1031–1036 vol.2. DOI: 10.1109/IECON.1991.239149.

[187] Medbery, J. D. and Germann, L. M. "Specification of precision optical pointing systems". In: *Structures Sensing and Control*. Ed. by Breakwell, J. and Varadan, V. K. SPIE, Oct. 1991. DOI: 10.1117/12.46597.

[188] Megahed, S. M. and Hamza, K. T. "Modeling and simulation of planar flexible link manipulators with rigid tip connections to revolute joints". In: *Robotica* 22.3 (2004), pp. 285–300. DOI: 10.1017/S0263574703005587.

[189] Messner, W. C. "Classical control revisited: Variations on a theme". In: *2008 10th IEEE International Workshop on Advanced Motion Control*. 2008, pp. 15–20. DOI: 10.1109/AMC.2008.4516034.

[190] Miljkovic, D. "Review of Active Vibration Control". In: *MIPRO*. 2009.

[191] Miller, S., Saares, T., Van Weddingen, Y., and Wendlandt, J. "Modeling Flexible Bodies with Simscape Multibody Software". In: (2017).

[192] Moallem, M., Patel, R. V., and Khorasani, K. "An observer-based inverse dynamics control strategy for flexible multi-link manipulators". In: *Proceedings of 35th IEEE Conference on Decision and Control*. Vol. 4. 1996, 4112–4117 vol.4. DOI: 10.1109/CDC.1996.577415.

[193] Moberg, S. "Modeling and Control of Flexible Manipulators". dissertation. Linköping University, 2010.

[194] Moberg, S., Wernholt, E., Hanssen, S., and Brogårdh, T. “Modeling and Parameter Estimation of Robot Manipulators Using Extended Flexible Joint Models”. In: *Journal of Dynamic Systems, Measurement, and Control* 136.3 (Feb. 2014). DOI: 10.1115/1.4026300.

[195] Mondal, S., Mitra, A., and Chattopadhyay, M. “Mathematical modeling and simulation of Brushless DC motor with ideal Back EMF for a precision speed control”. In: *2015 IEEE International Conference on Electrical, Computer and Communication Technologies (ICECCT)*. 2015, pp. 1–5. DOI: 10.1109/ICECCT.2015.7225944.

[196] Moon, S., Geonha Lee, Lee, J., Yangkyu Park, Minyoung Yun, and Lee, J. “Microactuator for autofocus and optical image stabilization in mobile phone cameras using unleveled comb electrodes”. In: *2016 International Conference on Optical MEMS and Nanophotonics (OMN)*. 2016, pp. 1–2. DOI: 10.1109/OMN.2016.7565886.

[197] Morris, A. S. and Madani, A. “Quadratic optimal control of a two-flexible-link robot manipulator”. In: *Robotica* 16.1 (1998), pp. 97–108.

[198] Moulin, H. C. and Bayo, E. “Accuracy of discrete models for the inverse dynamics of flexible arms, feasible trajectories”. In: *29th IEEE Conference on Decision and Control*. 1990, 531–532 vol.2. DOI: 10.1109/CDC.1990.203653.

[199] Naganathan, G. and Soni, A. “An analytical and experimental investigation of flexible manipulator performance”. In: *Proceedings. 1987 IEEE International Conference on Robotics and Automation*. Vol. 4. 1987, pp. 767–773. DOI: 10.1109/ROBOT.1987.1087962.

[200] Nagarajan, S. and Turcic, D. A. “Lagrangian Formulation of the Equations of Motion for Elastic Mechanisms With Mutual Dependence Between Rigid Body and Elastic Motions: Part II—System Equations”. In: *Journal of Dynamic Systems, Measurement, and Control* 112.2 (June 1990), pp. 215–224. DOI: 10.1115/1.2896128.

[201] Neat, G. W., Melody, J. W., and Lurie, B. J. “Vibration attenuation approach for spaceborne optical interferometers”. In: *IEEE Transactions on Control Systems Technology* 6.6 (1998), pp. 689–700. DOI: 10.1109/87.726529.

[202] Newman, W. S., Birkhimer, C. E., Horning, R. J., and Wilkey, A. T. “Calibration of a Motoman P8 robot based on laser tracking”. In: *Proceedings 2000 ICRA. Millennium Conference. IEEE International Conference on Robotics and Automation. Symposia Proceedings (Cat. No.00CH37065)*. Vol. 4. 2000, 3597–3602 vol.4. DOI: 10.1109/ROBOT.2000.845292.

[203] Niskanen, M., Silven, O., and Tico, M. “Video Stabilization Performance Assessment”. In: *2006 IEEE International Conference on Multimedia and Expo*. IEEE, July 2006. DOI: 10.1109/icme.2006.262522.

[204] Nof, S. Y. *Handbook of Industrial Robotics* -. New York: John Wiley & Sons, 1999. ISBN: 978-0-471-17783-8.

[205] NOGUCHI, S. and DOHMEKI, H. “Study on high precision positioning of actuator system integrating PMSM with ball screw”. In: *Journal of the Japan Society of Applied Electromagnetics and Mechanics* 27.1 (2019), pp. 134–139. DOI: 10.14243/jsaem.27.134.

[206] Nubiola, A. and Bonev, I. A. “Absolute calibration of an ABB IRB 1600 robot using a laser tracker”. In: *Robotics and Computer-Integrated Manufacturing* 29.1 (Feb. 2013), pp. 236–245. DOI: 10.1016/j.rcim.2012.06.004.

[207] Ohr, J., Moberg, S., Wernholt, E., Hanssen, S., Pettersson, J., Persson, S., and Sadertavallaey, S. “Identification of Flexibility Parameters of 6-axis Industrial Manipulator Models”. In: *ISMA 2006*. 2006.

[208] Oppenheim, A. *Discrete-time signal processing*. Upper Saddle River, NJ: Pearson, 2010. ISBN: 978-0-13-198842-2.

[209] Ott, C., Albu-Schaffer, A., Kugi, A., and Hirzinger, G. “On the Passivity-Based Impedance Control of Flexible Joint Robots”. In: *IEEE Transactions on Robotics* 24.2 (2008), pp. 416–429. DOI: 10.1109/TRO.2008.915438.

[210] Ott, C., Albu-Schaffer, A., Kugi, A., Stamigioli, S., and Hirzinger, G. “A passivity based Cartesian impedance controller for flexible joint robots - part I: torque feedback and gravity compensation”. In: *IEEE International Conference on Robotics and Automation, 2004. Proceedings. ICRA ’04. 2004*. Vol. 3. 2004, 2659–2665 Vol.3. DOI: 10.1109/ROBOT.2004.1307462.

[211] Oveisi, A., Hosseini-Pishrobat, M., Nestorović, T., and Keighobadi, J. “Observer-based repetitive model predictive control in active vibration suppression”. In: *Structural Control and Health Monitoring* 25.5 (Feb. 2018), e2149. DOI: 10.1002/stc.2149.

[212] Park, C. J., Han, C. Y., Lim, S. C., Park, J. H., and Lee, D. K. “Image Stabilization for Camera Module”. Patent 8,218,016 B2 (US). June 2012.

[213] Paulitsch, C., Gardonio, P., and Elliott, S. J. “Active Vibration Damping Using an Inertial, Electrodynamic Actuator (DETC2005-84632)”. In: *Journal of Vibration and Acoustics* 129.1 (July 2006), pp. 39–47. DOI: 10.1115/1.2349537.

[214] Peeters, B. and Van Der Auweraer, H. “PolyMAX: a revolution in operational modal analysis.” In: *International Operational Modal Analysis Conference (IOMAC)*. 2005, p. 13. ISBN: 9788781606000.

[215] Pfaff, J., Baur, J., and Schütz, C. “Design of Drive Units for Agricultural Robots”. In: *International Conference of Agricultural Engineering*. 2014.

[216] Prautzsch, T. “Simulation of a Torque-Controlled Robot with Flexible Joints”. Semesterarbeit. Technische Universität München, 2020.

[217] Prautzsch, T. “The Influence of Flexible Links on Torque Controlled Robots”. Masterarbeit. Technische Universität München, 2020.

[218] Prautzsch, T., Berninger, T. F. C., and Rixen, D. J. “Investigation of Torque Controlled Robots with Flexible Links Using a Flexible Multibody Simulation”. In: *2021 IEEE/ASME International Conference on Advanced Intelligent Mechatronics (AIM)*. 2021, pp. 638–644. DOI: 10.1109/AIM46487.2021.9517633.

[219] Preumont, A. *Vibration Control of Active Structures: An Introduction*. Springer, 2002.

[220] Qiu, S. “Control of a proof-mass actuator”. Bacherlorarbeit. Technische Universität München, 2019.

[221] Rafieian, F., Liu, Z., and Hazel, B. “Dynamic model and modal testing for vibration analysis of robotic grinding process with a 6DOF flexible-joint manipulator”. In: *2009 IEEE International Conference on Mechatronics and Automation, ICMA 2009*. 2009, pp. 2793–2798. ISBN: 9781424426935. DOI: 10.1109/ICMA.2009.5246491.

[222] Ram, Y. M. and Mottershead, J. E. “Receptance Method in Active Vibration Control”. In: *AIAA Journal* 45.3 (Mar. 2007), pp. 562–567. DOI: 10.2514/1.24349.

[223] Rayleigh, J. *The Theory of Sound, second edition*. Dover, 1896.

[224] Redding, D. C. and Breckenridge, W. G. “Optical modeling for dynamics and control analysis”. In: *Journal of Guidance, Control, and Dynamics* 14.5 (Sept. 1991), pp. 1021–1032. DOI: 10.2514/3.20745.

[225] Rioul, O. and Duhamel, P. “Fast algorithms for discrete and continuous wavelet transforms”. In: *IEEE transactions on information theory* 38.2 (1992), pp. 569–586.

[226] Robert H. Cannon, J. and Schmitz, E. “Initial Experiments on the End-Point Control of a Flexible One-Link Robot”. In: *The International Journal of Robotics Research* 3.3 (1984), pp. 62–75. DOI: 10.1177/027836498400300303.

[227] Rohlfing, J., Elliott, S., and Gardonio, P. “Feedback compensator for control units with proof-mass electrodynamic actuators”. In: *Journal of Sound and Vibration* 331.15 (July 2012), pp. 3437–3450. DOI: 10.1016/j.jsv.2012.03.010.

[228] Rossi, M., Zuo, K., and Miang, D. “Issues in the design of passive controllers for flexible link robots”. In: *Proceedings of the 1994 IEEE International Conference on Robotics and Automation*. 1994, 321–326 vol.1. DOI: 10.1109/ROBOT.1994.351275.

[229] Roy Craig, J. “Coupling of substructures for dynamic analyses - An overview”. In: *41st Structures, Structural Dynamics, and Materials Conference and Exhibit*. American Institute of Aeronautics and Astronautics, Apr. 2000. DOI: 10.2514/6.2000-1573.

[230] Saiki, K., Hara, A., Sakata, K., and Fujimoto, H. “A Study on High-Speed and High-Precision Tracking Control of Large-Scale Stage Using Perfect Tracking Control Method Based on Multirate Feedforward Control”. In: *IEEE Transactions on Industrial Electronics* 57.4 (2010), pp. 1393–1400. DOI: 10.1109/TIE.2009.2030212.

[231] Saniewski, E. “Aufbau einer flexiblen Mehrkörpersimulation in Simulink”. Semesterthesis. Technische Universität München, 2019.

[232] Sarkar, P., Yamamoto, M., and Mohri, A. “Numerical method to minimize tracking error of multi-link elastic robot”. English. In: *Innovations in Theory, Practice and Applications*. Ed. by Anon. Vol. 1. IEEE, 1998, pp. 685–690.

[233] Schempf, H. *Comparative design, modeling, and control analysis of robotic transmissions*. Massachusetts Institute of Technology and Woods Hole Oceanographic Institution, 1990. DOI: 10.1575/1912/5431.

[234] Schroeder, M. “Synthesis of low-peak-factor signals and binary sequences with low autocorrelation (Corresp.)” In: *IEEE Transactions on Information Theory* 16.1 (1970), pp. 85–89. DOI: 10.1109/TIT.1970.1054411.

[235] Schuetz, C., Pfaff, J., Sygulla, F., Rixen, D., and Ulbrich, H. “Motion Planning for Redundant Manipulators in Uncertain Environments based on Tactile Feedback”. In: *IEEE/RSJ International Conference on Intelligent Robots and Systems*. This is a preprint of an article published in the proceedings of IEEE IROS. The final authenticated version is available online at: https://doi.org/10.1109/IROS.2015.7354290. IEEE, 2015. DOI: 10.1109/IROS.2015.7354290.

[236] Schuetz, C., Ponn, T., Sygulla, F., Rixen, D., and Ulbrich, H. “Proprioceptive Estimation of External Joint Torques at a 9-DOF Manipulator”. In: *International Conference on Multibody System Dynamics (IMSD)*. Montreal, Canada, May 2016.

[237] Segovia, V. R., Hägglund, T., and Åström, K. “Measurement noise filtering for PID controllers”. In: *Journal of Process Control* 24.4 (Apr. 2014), pp. 299–313. DOI: 10.1016/j.jprocont.2014.01.017.

[238] Seijs, M. van der. “Experimental Dynamic Substructuring Analysis and Design Strategies for Vehicle Development”. PhD thesis. TU Delft, 2016.

[239] Seiwald, P., Sygulla, F., Staufenberg, N.-S., and Rixen, D. “Quintic Spline Collocation for Real-Time Biped Walking-Pattern Generation with variable Torso Height”. In: *IEEE-RAS 19th International Conference on Humanoid Robots (Humanoids)*. Toronto, Canada, Oct. 2019, pp. 56–63. DOI: 10.1109/Humanoids43949.2019.9035076.

[240] Seiwald, P., Wu, S.-C., Sygulla, F., Berninger, T. F. C., Staufenberg, N.-S., Sattler, M. F., Neuburger, N., Rixen, D., and Tombari, F. “LOLA v1.1 – An Upgrade in Hardware and Software Design for Dynamic Multi-Contact Locomotion”. In: *2020 IEEE-RAS 20th International Conference on Humanoid Robots (Humanoids)*. 2021, pp. 9–16. DOI: 10.1109/HUMANOIDS47582.2021.9555790.

[241] Setareh, M. “Floor vibration control using semi-active tuned mass dampers”. In: *Canadian Journal of Civil Engineering* 29.1 (Feb. 2002), pp. 76–84. DOI: 10.1139/l01-063.

[242] Seyfferth, W., Maghzal, A. J., and Angeles, J. “Nonlinear modeling and parameter identification of harmonic drive robotic transmissions”. In: *Proceedings of 1995 IEEE International Conference on Robotics and Automation*. Vol. 3. 1995, 3027–3032 vol.3. DOI: 10.1109/ROBOT.1995.525714.

[243] Shabana, A. A. *Dynamics of multibody systems*. Cambridge University Press, 2009. DOI: 10.1017/cbo9781107337213.

[244] Shah, V. N. and Raymund, M. “Analytical selection of masters for the reduced eigenvalue problem”. In: *International Journal for Numerical Methods in Engineering* 18.1 (Jan. 1982), pp. 89–98. DOI: 10.1002/nme.1620180108.

[245] Shan, J., Liu, H.-T., and Sun, D. “Slewing and vibration control of a single-link flexible manipulator by positive position feedback (PPF)”. In: *Mechatronics* 15.4 (May 2005), pp. 487–503. DOI: 10.1016/j.mechatronics.2004.10.003.

[246] Sharf, I. “Active Damping of a Large Flexible Manipulator With a Short-Reach Robot”. In: *Journal of Dynamic Systems, Measurement, and Control* 118.4 (1996), p. 704. DOI: 10.1115/1.2802346.

[247] Shiakolas, P., Conrad, K., and Yih, T. “On the Accuracy, Repeatability, and Degree of Influence of Kinematics Parameters for Industrial Robots”. In: *International Journal of Modelling and Simulation* 22.4 (Jan. 2002), pp. 245–254. DOI: 10.1080/02286203.2002.11442246.

[248] Siciliano, B. *Springer handbook of robotics*. Berlin: Springer, 2016. ISBN: 978-3-319-32552-1.

[249] Siciliano, B., Sciavicco, L., Villani, L., and Oriolo, G. *Robotics - Modelling, Planning and Control*. London: Springer London, 2010. ISBN: 978-1-849-96634-4.

[250] SINGH, M. P., MATHEU, E. E., and SUAREZ, L. E. “ACTIVE AND SEMI-ACTIVE CONTROL OF STRUCTURES UNDER SEISMIC EXCITATION”. In: *Earthquake Engineering & Structural Dynamics* 26.2 (1997), pp. 193–213.

[251] Skogestad, S. *Multivariable feedback control : analysis and design*. Hoboken, NJ: John Wiley, 2005. ISBN: 9780470011676.

[252] Slamani, M., Nubiola, A., and Bonev, I. “Assessment of the positioning performance of an industrial robot”. In: *Industrial Robot: An International Journal* 39.1 (Jan. 2012), pp. 57–68. DOI: 10.1108/01439911211192501.

[253] Slimak, T. “Sensor Fusion for External Robot Stabilization”. Semesterarbeit. Technische Universität München, 2020.

[254] Song, G., Schmidt, S., and Agrawal, B. “Experimental robustness study of positive position feedback control for active vibration suppression”. In: *Journal of guidance, control, and dynamics* 25.1 (2002), 179a–182.

[255] Song, G., Vlattas, J., Johnson, S. E., and Agrawal, B. N. “Active vibration control of a space truss using a lead zirconate titanate stack actuator”. In: *Proceedings of the Institution of Mechanical Engineers, Part G: Journal of Aerospace Engineering* 215.6 (June 2001), pp. 355–361. DOI: 10.1243/0954410011533356.

[256] Song, M., Baek, H., Park, N., Park, K., Yoon, T., Park, Y., and Lim, S. “Development of Small Sized Actuator With Compliant Mechanism for Optical Image Stabilization”. In: *IEEE Transactions on Magnetics* 46.6 (2010), pp. 2369–2372. DOI: 10.1109/TMAG.2010.2042288.

[257] *Sony Alpha 1 Specifications*. URL: https://www.sony.co.uk/electronics/interchangeable-lens-cameras/ilce-1/specifications.

[258] *Spec sheet for Micro Epsilon eddy current sensors*. URL: https://www.micro-epsilon.com/download/products/cat--eddyNCDT--en.pdf (visited on 01/04/2021).

[259] Spong, M. W. “Modeling and Control of Elastic Joint Robots”. In: *Journal of Dynamic Systems, Measurement, and Control* 109.4 (Dec. 1987), pp. 310–318. DOI: 10.1115/1.3143860.

[260] Spong, M. W. “Adaptive control of flexible joint manipulators”. In: *Systems & Control Letters* 13.1 (July 1989), pp. 15–21. DOI: 10.1016/0167-6911(89)90016-9.

[261] Stengel, R. *Optimal control and estimation*. New York: Dover Publications, 1994. ISBN: 9780486682006.

[262] Subudhi, B. and Morris, A. “Dynamic modelling, simulation and control of a manipulator with flexible links and joints”. In: *Robotics and Autonomous Systems* 41.4 (Dec. 2002), pp. 257–270. DOI: 10.1016/s0921-8890(02)00295-6.

[263] Sumega, M., Zoššák, Š., Varecha, P., and Rafajdus, P. “Sources of torque ripple and their influence in BLDC motor drives”. In: *Transportation Research Procedia* 40 (2019), pp. 519–526. DOI: 10.1016/j.trpro.2019.07.075.

[264] Sweet, L. and Good, M. “Redefinition of the robot motion-control problem”. In: *IEEE Control Systems Magazine* 5.3 (Aug. 1985), pp. 18–25. DOI: 10.1109/mcs.1985.1104955.

[265] Sygulla, F. and Rixen, D. J. “A Force Control Scheme for Biped Robots to Walk over Uneven Terrain Including Partial Footholds”. In: *Preprint - submitted* (2019). DOI: 10.13140/RG.2.2.19012.68487.

[266] Sygulla, F. “Dynamic Robot Walking on Unknown Terrain: Stabilization and Multi-Contact Control of Biped Robots in Uncertain Environments”. PhD thesis. Technical University of Munich, 2021.

[267] Sygulla, F., Schuetz, C., and Rixen, D. “Adaptive Motion Control in Uncertain Environments using Tactile Feedback”. In: *IEEE International Conference on Advanced Intelligent Mechatronics (AIM)*. This is a pre-print of an article published in the proceedings of IEEE AIM. The final authenticated version is available online at: https://doi.org/10.1109/AIM.2016.7576946. IEEE, 2016.

[268] Sygulla, F., Wittmann, R., Seiwald, P., Berninger, T., Hildebrandt, A.-C., Wahrmann, D., and Rixen, D. “An EtherCAT-Based Real-Time Control System Architecture for Humanoid Robots”. In: *2018 IEEE 14th International Conference on Automation Science and Engineering (CASE)*. IEEE, Aug. 2018. DOI: 10.1109/coase.2018.8560532.

[269] Talib, E., Shin, J.-H., and Kwak, M. K. “Designing multi-input multi-output modal-space negative acceleration feedback control for vibration suppression of structures using active mass dampers”. In: *Journal of Sound and Vibration* 439 (2019), pp. 77–98.

[270] Teague, E. H., How, J. P., and Parkinson, B. W. “Control of Flexible Structures Using GPS: Methods and Experimental Results”. In: *Journal of Guidance, Control, and Dynamics* 21.5 (Sept. 1998), pp. 673–683. DOI: 10.2514/2.4299.

[271] Theodore, R. J. and Ghosal, A. “Robust control of multilink flexible manipulators”. In: *Mechanism and Machine Theory* 38.4 (2003). NaCOMM99, the National Conference on Machines and Mechanisms, pp. 367–377. ISSN: 0094-114X. DOI: 10.1016/S0094-114X(02)00125-8.

[272] Tomei, P. “A simple PD controller for robots with elastic joints”. In: *IEEE Transactions on Automatic Control* 36.10 (1991), pp. 1208–1213. DOI: 10.1109/9.90238.

[273] Trainotti, F. “Development of a proper FRF acquisition procedure for Experimental Dynamic Substructuring”. Semesterarbeit. Technische Universität München, 2018.

[274] Trainotti, F., Berninger, T. F. C., and Rixen, D. J. “Using Laser Vibrometry for Precise FRF Measurements in Experimental Substructuring”. In: *Conference Proceedings of the Society for Experimental Mechanics Series*. Springer International Publishing, June 2019. DOI: 10.1007/978-3-030-12184-6_1.

[275] Tsunoda, W., Wagner, C., Berninger, T., Thümmel, T., and Rixen, D. “Measurement Method of Damping Ratio as Stability Diagnosis for Rotor-Seal System with Fluidic Random Excitation”. In: *The 5th International Education Forum on Environment and Energy Science*. 2016.

[276] Ulbrich, H., Baur, J., Pfaff, J., and Schuetz, C. “Design and Realization of a Redundant Modular Multipurpose Agricultural Robot”. In: *Proceedings of the XVII International Symposium on Dynamic Problems of Mechanics (DINAME)*. 2015.

[277] *UR 10 DH and inertia parameters.* URL: https://www.universal-robots.com/articles/ur/application-installation/dh-parameters-for-calculations-of-kinematics-and-dynamics/.

[278] *UR 10 DH and inertia parameters.* URL: https://www.harmonicdrive.net/_hd/content/catalogs/pdf/csf-gh-catalog.pdf.

[279] *UR 10 Product Specification*. URL: https://www.universal-robots.com/media/50880/ur10_bz.pdf (visited on 12/24/2020).

[280] *US Air Force SIBR Project about a multi-axis precision seeker-laser pointing gimbal.* URL: https://www.merio.fr/en (visited on 01/03/2021).

[281] *US Air Force SIBR Project about a multi-axis precision seeker-laser pointing gimbal.* URL: https://www.sbir.gov/node/870337 (visited on 01/02/2021).

[282] Vér, I. L. and Beranek, L. L., eds. *Noise and vibration control engineering: principles and applications*. 2nd ed. OCLC: ocm57557703. Hoboken, N.J: Wiley, 2006. ISBN: 9780471449423.

[283] Vu, V.-H., Liu, Z., Thomas, M., and Hazel, B. “Modal analysis of a light-weight robot with a rotating tool installed at the end effector”. In: *Proceedings of the Institution of Mechanical Engineers, Part C: Journal of Mechanical Engineering Science* 231.9 (Dec. 2015), pp. 1664–1676. DOI: 10.1177/0954406215619451.

[284] Vukosavic, S. N. *Electrical Machines* -. Berlin-Heidelberg: Springer New York, 2014. ISBN: 978-1-489-98890-4.

[285] Wagner, C., Berninger, T., Thümmel, T., and Rixen, D. “Rotordynamic effects in turbopumps for space propulsion systems - systems first minimal models and experimental validation”. In: *Space Propulsion 2016 Conference*. 2016.

[286] Wagner, C., Tsunoda, W., Berninger, T., Thümmel, T., and Rixen, D. “Instability Prediction and Rotordynamic with Seals: Simulations Based on the Bulk-Flow Theory and Experimental Measurements”. In: *Proceedings of the XVII International Symposium on Dynamic Problems of Mechanics*. ABCM, 2017.

[287] Wagner, C., Tsunoda, W., Berninger, T., Thümmel, T., and Rixen, D. “Simulative und experimentelle Vorhersage der Instabilität in Rotorsystemen mit Dichtungen”. In: *12. Internationale Tagung Schwingungen in Rotierenden Maschinen (SIRM)*. Ed. by Ecker, H., Irretier, H., Liebichand, R., Markert, R., Nordmann, R., and Strackeljan, J. 2017.

[288] Wagner, C., Tsunoda, W., Berninger, T., Thümmel, T., and Rixen, D. “Estimation of Rotordynamic Seal Coefficients Using Active Magnetic Bearing Excitation and Force Measurement”. In: *Lecture Notes in Mechanical Engineering*. Springer International Publishing, 2018. DOI: 10.1007/978-3-319-91217-2_1.

[289] Wagner, C., Tsunoda, W., Matsushita, O., Berninger, T., Thümmel, T., and Rixen, D. “Prediction of Instability in Rotor-Seal Systems using Forward Whirl Magnetic Bearing Excitation”. In: *Technische Mechanik* 37.2-5 (2017), pp. 358–366. ISSN: 0232-3869. DOI: 10.24352/UB.OVGU-2017-111.

[290] Wernholt, E. and Moberg, S. “Nonlinear gray-box identification using local models applied to industrial robots”. In: *Automatica* 47.4 (Apr. 2011), pp. 650–660. DOI: 10.1016/j.automatica.2011.01.021.

[291] Wie, B. “Experimental demonstration of a classical approach to flexible structure control”. In: *Journal of Guidance, Control, and Dynamics* 15.6 (Nov. 1992), pp. 1327–1333. DOI: 10.2514/3.11393.

[292] Wriggers, P. *Nonlinear Finite Element Methods*. Berlin Heidelberg: Springer Science & Business Media, 2008. ISBN: 978-3-540-71000-4.

[293] Wu, W. and Liu, T. “Frequency-shaped sliding mode control for flying height of pickup head in near-field optical disk drives”. In: *IEEE Transactions on Magnetics* 41.2 (Feb. 2005), pp. 1061–1063. DOI: 10.1109/tmag.2004.842020.

[294] Wu, Y. and Zou, Q. “Iterative Control Approach to Compensate for Both the Hysteresis and the Dynamics Effects of Piezo Actuators”. In: *IEEE Transactions on Control Systems Technology* 15.5 (2007), pp. 936–944. DOI: 10.1109/TCST.2007.899722.

[295] Yamano, M., Konno, A., and Uchiyama, M. “Experiments on capturing a floating object by two flexible manipulators”. In: *Proceedings 2000 ICRA. Millennium Conference. IEEE International Conference on Robotics and Automation. Symposia Proceedings (Cat. No.00CH37065)*. Vol. 1. 2000, 482–487 vol.1. DOI: 10.1109/ROBOT.2000.844101.

[296] Yang, D.-H., Shin, J.-H., Lee, H., Kim, S.-K., and Kwak, M. K. “Active vibration control of structure by active mass damper and multi-modal negative acceleration feedback control algorithm”. In: *Journal of Sound and Vibration* 392 (2017), pp. 18–30.

[297] Yang, T. W., Xu, W. L., and Tso, S. K. In: *Dynamics and Control* 11.1 (2001), pp. 5–24. DOI: 10.1023/a:1017954615442.

[298] Yang, Z. and Sadler, J. “Prediction of the dynamic response of flexible manipulators from a modal database”. In: *Mechanism and Machine Theory* 32.6 (1997), pp. 679–689. ISSN: 0094-114X. DOI: https://doi.org/10.1016/S0094-114X(97)83002-9.

[299] Ye, S. H., Wang, Y., Ren, Y. J., and Li, D. K. "Robot Calibration Using Iteration and Differential Kinematics". In: *Journal of Physics: Conference Series* 48 (Oct. 2006), pp. 1–6. DOI: 10.1088/1742-6596/48/1/001.

[300] Yocum, J. F. and Slafer, L. I. . "Control System Design in the Presence of Severe Structural Dynamics Interactions". In: *Journal of Guidance and Control* 1.2 (Mar. 1978), pp. 109–116. DOI: 10.2514/3.55752.

[301] *Youtube video about Lola's hardware upgrade.* URL: https://www.youtube.com/watch?v=mpDqMFppT68&t (visited on 09/12/2020).

[302] *Youtube video showcasing Lola's multi-contact capabilities.* URL: https://www.youtube.com/watch?v=gUNZ0AmLiWU.

[303] Yu, H. and Liu, T. S. "Sliding Mode Control Using Virtual Eigenvalue Method for Compact Optical Image Stabilization Actuators". In: *IEEE Transactions on Magnetics* 44.11 (2008), pp. 4074–4077. DOI: 10.1109/TMAG.2008.2002787.

[304] Yue, S., Tso, S., and Xu, W. "Maximum-dynamic-payload trajectory for flexible robot manipulators with kinematic redundancy". In: *Mechanism and Machine Theory* 36.6 (2001). International Conference on Graphs and Mechanics, pp. 785–800. ISSN: 0094-114X. DOI: 10.1016/S0094-114X(00)00059-8.

[305] Yuh, J. and Young, T. "Dynamic Modeling of an Axially Moving Beam in Rotation: Simulation and Experiment". In: *Journal of Dynamic Systems, Measurement, and Control* 113.1 (Mar. 1991), pp. 34–40. DOI: 10.1115/1.2896355.

[306] Yunfeng Li and Horowitz, R. "Active vibration control of a PZT actuated suspension in hard disk drives". In: *Proceedings of the 2002 American Control Conference (IEEE Cat. No.CH37301)*. Vol. 2. 2002, 1366–1371 vol.2. DOI: 10.1109/ACC.2002.1023211.

[307] Zhou, S. and Shi, J. "Active Balancing and Vibration Control of Rotating Machinery: A Survey". In: *The Shock and Vibration Digest* 33.5 (Sept. 2001), pp. 361–371. DOI: 10.1177/058310240103300501.

[308] Zhu, G. and Ge, S. S. "A model-free approach for regulation of multi-link flexible robots". In: *Proceedings of the 1997 American Control Conference (Cat. No.97CH36041)*. Vol. 3. 1997, 1417–1421 vol.3. DOI: 10.1109/ACC.1997.610660.

[309] Zhu, G., Ge, S., and Lee, T. "Simulation studies of tip tracking control of a single-link flexible robot based on a lumped model". In: *Robotica* 17.1 (1999), pp. 71–78. DOI: 10.1017/S0263574799000971.

[310] Ziegler, J. G., Nichols, N. B., et al. "Optimum settings for automatic controllers". In: *trans. ASME* 64.11 (1942).

[311] Zienkiewicz, O. C., Taylor, R. L., Taylor, R. L., and Zhu, J. Z. *The Finite Element Method - Its Basis and Fundamentals*. Oxford: Butterworth-Heinemann, 2013. ISBN: 978-1-856-17633-0.

[312] Zimmermann, S. "Dynamic modeling of robotic manipulators for accuracy evaluation". Master's Thesis. Technische Universität München, 2018.

[313] Zimmermann, S. A., Berninger, T. F. C., Derkx, J., and Rixen, D. J. "Dynamic modeling of robotic manipulators for accuracy evaluation". In: *2020 IEEE International Conference on Robotics and Automation (ICRA)*. 2020, pp. 8144–8150. DOI: 10.1109/ICRA40945.2020.9197304.

[314] Zohoor, H. and Kakavand, F. "Timoshenko versus Euler–Bernoulli beam theories for high speed two-link manipulator". In: *Scientia Iranica* 20.1 (2013), pp. 172–178. ISSN: 1026-3098. DOI: https://doi.org/10.1016/j.scient.2012.12.016.